ATTACHMENT, SELECTION, AND TRANSFORMATION OF PREBIOTIC MOLECULES ON BRUCITE [$Mg(OH)_2$] AND THE IMPLICATIONS FOR CHEMICAL EVOLUTION AT HYDROTHERMAL SYSTEMS

by

Charlene F. Estrada

A dissertation submitted to The Johns Hopkins University in conformity with the requirements for the degree of Doctor of Philosophy

Baltimore, Maryland

September, 2014

Abstract

Serpentinite-hosted hydrothermal vents may have been plausible environments for the origins of life. Mineral assemblages within hydrothermal fields may have selected and concentrated biomolecules, although little is known about molecular interactions at these mineral surfaces. I investigated the adsorption of aspartate and ribose at the surface of brucite [$Mg(OH)_2$], a major mineral phase at serpentinite-hosted hydrothermal vents. I characterized the attachment of these molecules onto a synthetic brucite powder with Mg^{2+} and Ca^{2+} using batch adsorption experiments. I observed that Mg^{2+} inhibits both aspartate and ribose adsorption, whereas Ca^{2+} enhances adsorption onto the brucite surface. I used surface complexation modeling to predict that both aspartate and ribose attach as cooperative calcium-ligand complexes onto brucite.

To further investigate the cooperative effect of Ca^{2+} on biomolecule adsorption, I introduced an equimolar mixture of aspartate, glycine, lysine, leucine, and phenylalanine to the brucite surface, both with and without Ca^{2+}. Without Ca^{2+}, up to 8.9 % aspartate and ~5 % each of the remaining four amino acids adsorbed onto brucite. When Ca^{2+} was added, I observed that between 5.7 to 20 times more aspartate (37.3 %) adsorbed onto brucite compared with the remaining four amino acids (~3 % each). These results, when combined with the previous study, suggest that aspartate selectively adsorbs onto brucite as a cooperative calcium-aspartate complex.

The behavior of biomolecules at high temperatures is essential for evaluating whether hydrothermal systems may have been suitable environments for life's origins.

However, the geochemical complexities of a hydrothermal system could significantly affect this process. I characterized aspartate decomposition at 200 ºC and 15.5 bars for 24 hours in inert gold capsules with controlled redox state, added ammonia, and brucite. I determined that the initial experimental conditions significantly affect the decomposition of aspartate. Biomolecule decomposition may be a more complicated process within hydrothermal systems, which may contribute a diverse array of organic species to early Earth.

First reader (thesis advisor): Dimitri A. Sverjensky

Second reader: Robert M. Hazen

Acknowledgments

This work has been possible with the gracious help and support of many individuals at the Johns Hopkins University Department of Earth and Planetary Sciences and the Geophysical Laboratory at the Carnegie Institution of Washington. I particularly thank my thesis advisor, Dr. Dimitri Sverjensky whose guidance, patience, and overwhelming support in every area of this work has made my experience during this Ph. D. program both pleasant and exciting. Dimitri challenged the limits of what I expected I could do while simultaneously encouraging me that I could achieve almost anything. He has made me a stronger person and scientist, and I will always be grateful.

I also thank Dr. Bob Hazen, my supervisor at the Geophysical Laboratory. Bob's unwavering enthusiasm for science is contagious, and I always look forward to our discussions. His mentorship has been invaluable, and I feel inspired to continue my scientific career with the optimism, passion, and determination that he has imparted to me.

Over the three years that I have worked at the Geophysical Laboratory, I have come to think of my colleagues at the Carnegie Institution of Washington as my second family. My experience at the Geophysical Laboratory has been one of the happiest times of my life. I particularly thank Drs. George Cody, Dionysis Foustoukos, Irena Mamajanov, Chris Glein, John Armstrong, Paul Goldey, and Tim Strobel who have taken time from their own schedules to help me with my experiments. I also thank Drs. Andrew Steele, Bjørn Mysen, Karen Rogers, Jim Cleaves, and the Carnegie Institution of Washington Support Staff for their invaluable discussions and support during this work.

I am also grateful to the professors and staff at Johns Hopkins University who have encouraged me from the first day I began my Ph.D. program. In particular, I thank Drs. Alan Stone, Colin Norman, John Ferry, Ben Passey, and Bill Ball, who served as members on my committee. I also thank Drs. Naomi Levin, Ken Livi, Jocelyne DiRuggiero, and Tom Wright for their kind advice.

I am also indebted to my current and former research group members both at the Department of Earth and Planetary Sciences and the Geophysical Laboratory for their animated discussion and advice regarding my experimental techniques, results, and theoretical predictions. I specifically thank Namhey Lee, Alyssa Adcock, Clare Flynn, Patrick Griffin, David Azzolini, Branden Harrison, Jihua Hao, Fang Huang, Katya Klochko, Adrian Villegas-Jimenez, Xiaoming Liu, and Cécile Feuillie. I also thank Caroline and Christopher Jonsson who, as my first mentors at the Geophysical Laboratory, taught me how to conduct most of the experiments presented in this work. I am unimaginably grateful for their hard work in teaching me, and their work with me has been an inspiration over these past five years.

I am extremely grateful to my friend and colleague Dr. Bob Downs who was my first mentor in science. I believe that much of my success today is a result of his mentorship. If I had not walked into his office that day at the University of Arizona, my journey in science would have never been the same. My experience at the Carnegie Institution and JHU are direct results of my work with Bob Downs, and I hope that one day I can pay forward the kindness he has shown me by becoming the same type of mentor.

I thank my friends for making me a better and stranger person. I'm grateful to Jen McAlonan, Brian Olnick, Kelsey Wright, Corinne Warren, and Will Genschow. I also thank my best friend, my cat Rio, who has eaten my physical chemistry homework, sat on my laptop as I wrote these chapters, and purred in my ear (yes, *my ear*) as I practiced my thesis presentation. Throughout my time in this Ph.D. program, he has kept me sane, and acted as a not-so-subtle reminder that there is more to life than work.

Most importantly, I thank my family for helping me every step of the way in this endeavor. I especially thank my parents, Antonio and Barbara Estrada, for their unwavering support of everything I have done. I thank my brother, Eric and his wonderful growing family, and my sister, Gloria. I thank my grandmother, Shirley Polk. I am also grateful to my grandparents, Sharon and Don Ridlen, and my mother, Janis Ridlen, who are all missed. This thesis is dedicated my family for everything they have done to make me who I am today. I love you all!

All of the chapters included in this thesis were a collaborative effort. The contributions of those who have made each chapter possible are listed below.

Chapter 2

This chapter was co-authored with Dimitri Sverjensky, Manuel Pelletier, Angélina Razafitianamaharavo, and Robert Hazen. In our adsorption studies, we suspected that aspartate was adsorbing onto the edge surfaces of brucite. Drs. Manuel Pelletier and Angélina Razafitianamaharavo at the Université de Lorraine measured the specific edge surface area of our synthetic brucite powder with a novel low-pressure Ar adsorption method. This enabled us to calculate the amount of aspartate adsorption per m^2 of brucite. I am also grateful to Cécile Feuillie, Namhey Lee, Alyssa Adcock, Adrian

Villegas-Jimenez, John Armstrong, Paul Goldey, Tim Strobel, Stephen Hodge, and Steven Coley for their supportive discussions and assistance in the laboratory.

Chapter 3

This chapter was co-authored with Alyssa Adcock, Dimitri Sverjensky, Manuel Pelletier, Angélina Razafitianamaharavo, and Robert Hazen. As a summer intern at the Geophysical Laboratory, Alyssa conducted nearly half of the ribose adsorption experiments. Alyssa's tremendous amount of work in a short amount of time became the foundation for this chapter. I am also grateful to Cécile Feuillie, Namhey Lee, George Cody, Adrian Villegas-Jimenez, John Armstrong, Paul Goldey, Tim Strobel, Stephen Hodge, and Steven Coley for their supportive discussions and assistance in the laboratory.

Chapter 5

This chapter was co-authored with Irena Mamajanov, Dimitri Sverjensky, Jihua Hao, George Cody, and Robert Hazen. Dr. Irena Mamajanov analyzed samples with Ultra-High Performance Liquid Chromatography-Mass Spectrometry on numerous occasions and helped us determine the identity and concentration of organic species that had formed from the decomposition of aspartate. George Cody provided us with expertise on conducting high temperature experiments involving gold capsules, and during several discussions, he suggested possible reaction mechanisms and explanations to account for the products we detected. Jihua Hao calculated the speciation of the aqueous fluid in our experiments using the program EQ3 to estimate variables that we were unable to measure during our experiments, including solution pH, $CO_{2(g)}$ concentrations, and the extent of Mg^{2+} complexing, which hold important implications for our interpretation of the data. I am also extremely grateful to Dionysis Foustoukos who helped me with several of the experimental methods and analyzed the samples with ion chromatography. I also thank Chris Glein, Namhey Lee, Paul Goldey, and John Armstrong for useful discussions and aid in the laboratory.

Thank you, everyone, for this experience. I had a wonderful time!

Contents

List of Tables

CHAPTER 2.

CHAPTER 3.

CHAPTER 4.

CHAPTER 5.

List of Figures

CHAPTER 2.

CHAPTER 3.

CHAPTER 4.

CHAPTER 5.

Chapter 1

Introduction

The evolution of complex biomolecules that can store energy or replicate DNA is a crucial process in scenarios for life's origins. These macromolecules may have emerged through the polymerization of simpler prebiotic species such as sugars and amino acids that may have been produced on early Earth (Miller, 1953; Gabel and Ponnamperuma, 1967; Deamer and Pashley, 1989; Hennet et al., 1992; Jalbout et al., 2007; Cleaves et al., 2008; Kim et al., 2011). Mineral surfaces could have facilitated the assembly of complex organic species by selecting and concentrating the constituent biomolecules through adsorption (Goldschmidt, 1952; Schoonen et al., 2004; Hazen, 2006; Cleaves et al., 2012). The total dissolved ionic profile of an aqueous environment affects the adsorption of a biomolecule because the mineral-water interface significantly changes with respect to pH and ionic strength due to surface protonation reactions. A particular prebiotic environment containing a specific mineral assemblage may therefore selectively concentrate biomolecules essential for the emergence of proteins, RNA, and DNA.

Hydrothermal vents have been suggested as possible host environments for life's origins because the mixing of hot, reducing vent fluids with cold seawater may have created thermal and redox gradients favorable for the abiotic synthesis of organic molecules (Baross and Hoffman, 1985; Shock, 1990; Hennet et al., 1992; Shock and

Canovas, 2010). Serpentinite-hosted hydrothermal systems are different types of hydrothermal environments that are characterized by alkaline (pH 9-11), low-temperature (70-150 ºC) vents fluids (Kelley et al., 2001; 2005) in contrast to the conventional acidic, high temperature, “black-smoker” hydrothermal systems. In addition to a magmatic heat source, these hydrothermal systems are driven by the exothermic hydration of olivine into serpentinite (Kelley et al., 2002; 2005). Due to the more moderate temperatures, serpentinite-hosted hydrothermal vents have been proposed as a more conducive hydrothermal environment for the emergence of life (Holm et al., 2006; Sleep et al., 2011). Moreover, greenstone sequences as old as 3.8 Ga at the Isua Formation (Dymek et al., 1988) and 3.5 Ga at the Pilbara Craton (Van Kranendonk et al., 2007) may provide evidence that serpentinite-hosted hydrothermal activity occurred on the early Earth.

If serpentinite-hosted hydrothermal systems were prevalent on early Earth and conditions were favorable toward the synthesis of simple biomolecules, the mineral assemblages within these hydrothermal environments may have concentrated and polymerized organic species. Whereas most studies that focus on biomolecule adsorption at the mineral-water interface involve well-characterized oxide or clay minerals with high surface areas, very few investigate rock-forming minerals that were likely present at plausible prebiotic environments. For example, ferrobrucite [$(Fe,Mg)(OH)_2$] is a major product of serpentinization (Bach et al., 2006), and the magnesium endmember of brucite [$Mg(OH)_2$] precipitates as a stable phase at serpentinite-hosted hydrothermal vents from ferrobrucite as hydrogen fugacity becomes limited (Bach et al., 2006; McCollom and Bach, 2009). Except for a study by Pokrovsky and coworkers (2005), there are no investigations of biomolecule adsorption at the brucite-water interface.

In this work, I characterized the adsorption of the amino acid aspartate onto the surface of a synthetic, powdered brucite with batch adsorption experiments and surface complexation modeling. Aspartate is a biomolecule that has been identified in relative abundance (387 nM) at the Logatchev serpentinite-hosted hydrothermal vent (Klevenz et al., 2010), and it has been synthesized under mineral-buffered hydrothermal conditions (Hennet et al., 1992). I added variable aspartate concentrations (2 to 300 μM) to 10 g•L^{-1} brucite. I conducted batch experiments at four ionic strengths that resulted from different concentrations of Mg^{2+} and Ca^{2+} present: "low-Mg^{2+} experiments" ($[Mg^{2+}]= 0.7\text{x}10^{-3}$ M, $[Ca^{2+}]= 0$ M); "high-Mg^{2+} experiments" ($[Mg^{2+}]= 5.8\text{x}10^{-3}$ M, $[Ca^{2+}]= 0$ M); "low-Ca^{2+} experiments" ($[Mg^{2+}]= 0.9\text{x}10^{-3}$ M $[Ca^{2+}]= 1.0\text{x}10^{-3}$ M); and "high-Ca^{2+} experiments" ($[Mg^{2+}]= 1.0\text{x}10^{-3}$ M $[Ca^{2+}]= 4.0\text{x}10^{-3}$ M). I analyzed aspartate adsorption and characterized the equilibrium between the brucite surface in water and aspartate solutions between pH 9.8 and 10.3. I used a predictive extended triple-layer model or ETLM (Sverjensky and Sahai, 1996; Sverjensky, 2003; 2005; Sverjensky and Fukushi, 2006) to propose reaction stoichiometries between the brucite surface and adsorbing species that are consistent with the adsorption data at all experimental conditions. As a result of this wide range of ionic strengths, pH conditions, and initial aspartate concentrations, it became possible to characterize aspartate and Ca^{2+} adsorption at the brucite-water interface with a unique set of surface reactions.

Another key precursor molecule in origins of life scenarios is the monosaccharide ribose, which is a constituent molecule in nucleotides, RNA and DNA. Holm and coworkers (2006) have proposed that brucite may scavenge phosphate from the surrounding environment, and if it also adsorbs ribose, the nucleoside adenosine triphosphate (ATP) may form at the surface. With the exception of studies by Hashizume and colleagues (2007; 2010), however, ribose-mineral interactions have not been quantitatively studied. To better evaluate the potential role of brucite and serpentinite-hosted hydrothermal systems could have on the assembly of nucleic acids, I analyzed the adsorption of ribose onto brucite with batch adsorption experiments. I performed four sets of batch adsorption experiments at different ionic strengths that were dependent on Mg^{2+} and Ca^{2+} concentrations. Between pH 9.8 and 10.3 I investigated ribose adsorption at "low Mg^{2+}" concentrations ($[Mg^{2+}]= 0.6x10^{-3}$ M, $[Ca^{2+}]= 0$ M); "high Mg^{2+}" concentrations ($[Mg^{2+}]= 5.8x10^{-3}$ M, $[Ca^{2+}]= 0$ M); "low Ca^{2+}" concentrations ($[Mg^{2+}]= 0.9x10^{-3}$ M $[Ca^{2+}]= 1.0x10^{-3}$ M); and "high Ca^{2+}" concentrations ($[Mg^{2+}]= 0.6x10^{-3}$ M $[Ca^{2+}]= 4.2x10^{-3}$ M). During all experiments, I added variable initial concentrations of ribose between 5 and 200 μM to 10 $g \cdot L^{-1}$ brucite. I proposed possible reaction stoichiometries between the adsorbing species and brucite surface with the ETLM that were consistent with the adsorption data. I also applied surface reactions that had been proposed for the brucite-aspartate system, among them involving the attachment of calcium onto brucite. Therefore, the ETLM established for the brucite-water interface has been successfully applied toward the prediction of ribose and aspartate adsorption at variable pH conditions, biomolecule concentrations, and ionic strengths.

A key result I observed in both the aspartate and ribose adsorption experiments was that after adding high concentrations of Ca^{2+} ($4x10^{-3}$ M), the amount of surface adsorption of both biomolecules approximately doubled. This substantial increase in biomolecule adsorption may hold strong implications for the amplifying effect of Ca^{2+} on the attachment and concentration of prebiotic molecules onto mineral surfaces. This positive effect has been previously observed by Franchi and coworkers (2003), where the addition of Ca^{2+} increased the adsorption of nucleic acids on kaolinite and montomorillonite. This increase in adsorption may have been caused by the formation of a cooperative calcium-ligand complex, where the calcium ion acts as a bridge between the biomolecule and clay surface. The formation of calcium-ligand complexes, and calcium-amino acid complexes in particular, may reveal an important mechanism by which calcium-binding proteins have formed on early Earth.

Calcium-binding proteins, which are found in all three domains of life, achieve a wide range of cellular functions, including signaling, glycolysis, and apoptosis. The calcium ion in this family of proteins is typically bound to acidic or polar amino acids such as glutamate or aspartate. This preference of Ca^{2+} may have evolved early in Earth's history, and a selective mechanism where amino acids adsorb at the mineral-water interface as cooperative calcium-ligand surface complexes may have led to this preference. To further investigate this possible selective effect, I conducted batch adsorption experiments involving the attachment of equimolar mixtures of the amino acids aspartate, glycine, lysine, leucine, and phenylalanine onto brucite. I performed three sets of experiments with the initial concentrations of the amino acid mixture varying from 10 to 150 µM at pH 10.2 with no Ca^{2+} added. I then evaluated the adsorption of the amino acid mixture onto brucite with an additional three sets of experiments with $4.1x10^{-3}$ M Ca^{2+} added. The wide range of functional groups between the five amino acids studied may allow me to discern advantages of a particular amino acid in forming surface species and selectively adsorbing onto the brucite surface as a cooperative calcium-ligand complex. Moreover, this work may hold implications for the importance of calcium-rich environments, such as serpentinite-hosted hydrothermal vents, when considering mineral surfaces in origins of life scenarios.

Hydrothermal vents have been a central environment considered in the context of the experiments I performed in these studies, although all investigations were conducted at 25 ºC and 1 bar. A primary challenge in conducting experiments at hydrothermal conditions is the stability of aqueous biomolecules, particularly aspartate, at high temperatures. Cox and Seward (2007) have characterized the possible reaction pathways of aqueous aspartate in water from 120 to 180 ºC. Others investigations, however, have established that aqueous aspartate rapidly decomposes in water at temperatures above 200 ºC (Bernhardt et al., 1984; Miller and Bada, 1988; Bada et al., 1995). These experiments were conducted without consideration of the reducing conditions or mineral assemblages that characterize hydrothermal systems. Thermodynamic predictions established that the redox state of the system strongly influences amino acid stability at high fluid temperatures (Shock, 1990; Shock and Canovas, 2010). Experiments conducted by Andersson and Holm (2000), as well as Novikov and Copley (2013), included hydrothermal mineral assemblages as redox buffers at high temperatures. The authors of these studies observed that the reaction pathways for amino acids at redox-controlled hydrothermal conditions are complex and in general, decomposition rates are lower when mineral assemblages are added. A recent study by Lee and coworkers (2014) determined that between 150 and 200 ºC, the decomposition products of glutamate significantly decreased when the concentration of $H_{2(aq)}$ was fixed at $13x10^{-3}$ M. These reaction conditions reflect those found at serpentinite-hosted hydrothermal vents (Kelley et al., 2001; 2005), and because it is structurally similar to glutamate, aspartate may also remain stable within this type of system at sufficiently reducing conditions.

In the final investigation of this study, I calculated that aspartate is thermodynamically stable relative to its decomposition products at 200 ºC and 15.5 bars at reducing conditions where $[H_{2(aq)}]= 10x10^{-3}$ to $20x10^{-3}$ M and $[NH_4^+]= 2.4x10^{-3}$ M. I investigated the stability and reaction pathways of aspartate over these conditions with inert gold capsules over 24 hours. Furthermore, I performed a second set of experiments with brucite added, both with and without NH_4^+ and $H_{2(aq)}$, in order to evaluate whether the addition of this mineral affects the reaction pathways of aspartate at high temperatures. The conditions investigated in this study are relevant in serpentinite-hosted hydrothermal vent environments (Kelley et al., 2001; 2005). This work is the first attempt to investigate amino acid stability and transformation pathways at fixed reducing conditions with a well-characterized mineral surface. The results I report from this study may provide novel insight on the possible interactions between aspartate, its decomposition products, and brucite at hydrothermal conditions and further elucidate the potential role of hydrothermal systems in promoting the emergence of biological complexity on early Earth.

References

Andersson E. and Holm N. G. (2000) The stability of some selected amino acids under attempted redox constrained hydrothermal conditions. *Orig. Life Evol. Biosph.* **30**, 9–23.

Bach W., Paulick H., Garrido C. J., Ildefonse B., Meurer W. P. and Humphris S. E. (2006) Unraveling the sequence of serpentinization reactions: Petrography, mineral chemistry, and petrophysics of serpentinites from MAR 15°N (ODP Leg 209, Site 1274). *Geophys. Res. Lett.* **33**, 1–4.

Bada J. L., Miller S. L. and Zhao M. (1995) The stability of amino acids at submarine hydrothermal vent temperatures. *Orig. Life Evol. Biosph.* **25**, 111–118.

Baross J. A. and Hoffman S. E. (1985) Submarine hydrothermal vents and associated gradient environments as sites for the origin and evolution of life. *Orig. Life Evol. Biosph.* **15**, 327–345.

Bernhardt G., Lüdemann H.-D., Jaenicke R., König H., and Stetter K. O. (1984) Biomolecules are unstable under "black smoker" conditions. *Naturwissenschaften* **71**, 583–586.

Cleaves H. J., Chalmers J. H., Lazcano A., Miller S. L. and Bada J. L. (2008) A Reassessment of prebiotic organic synthesis in neutral planetary atmospheres. *Orig. Life Evol. Biosph.* **38**, 105–115.

Cleaves H. J., Michalkova Scott A., Hill F. C., Leszczynski J., Sahai N. and Hazen R. M. (2012) Mineral–organic interfacial processes: Potential roles in the origins of life. *Chem. Soc. Rev.* **41**, 5502-5525.

Cox J. S. and Seward T. M. (2007) The hydrothermal reaction kinetics of aspartic acid. *Geochim. Cosmochim. Acta* **71**, 797-820.

Deamer D. and Pashley R. M. (1989) Amphiphilic components of the Murchison carbonaceous chondrite- surface properties and membrane formation. *Orig. Life Evol. Biosph.* **19**, 21–38.

Dymek R. F., Brothers S. C. and Schiffries C. M. (1988) Petrogenesis of ultramafic metamorphic rocks from the 3800 Ma Isua Supracrustal Belt, West Greenland. *J. Petrol.* **29**, 1353–1397.

Franchi M., Ferris J. P. and Gallori E. (2003) Cations as mediators of the adsorption of nucleic acids on clay surfaces in prebiotic environments. *Orig. Life Evol. Biosph.* **33**, 1–16.

Gabel N. W. and Ponnamperuma C. (1967) Model for origin of monosaccharides. *Nature* **216**, 453–455.

Goldschmidt V. M. (1952) Geochemical aspects of the origin of complex organic molecules on the Earth, as precursors to organic life. *New Biol.* **12**, 97–105.

Hashizume H. and Theng B. K. G. (2007) Adenine, adenosine, ribose and 5′-Amp adsorption to allophane. *Clay Clay Miner.* **55**, 599–605.

Hashizume H., van der Gaast S. and Theng B. K. G. (2010) Adsorption of adenine, cytosine, uracil, ribose, and phosphate by Mg-exchanged montmorillonite. *Clay Miner.* **45**, 469–475.

Hazen R. M. (2006) Presidential Address to the Mineralogical Society of America, Salt Lake City, October 18, 2005: Mineral surfaces and the prebiotic selection and organization of biomolecules. *Am. Mineral.* **91**, 1715–1729.

Hennet R., Holm N. G. and Engel M. H. (1992) Abiotic synthesis of amino-acids under hydrothermal conditions and the origin of life - a perpetual phenomenon. *Naturwissenschaften* **79**, 361–365.

Holm N. G., Dumont M., Ivarsson M. and Konn C. (2006) Alkaline fluid circulation in ultramafic rocks and formation of nucleotide constituents: A hypothesis. *Geochem. Trans.* **7**, 1–13.

Jalbout A. F., Abrell L., Adamowicz L., Polt R., Apponi A. J. and Ziurys L. M. (2007) Sugar synthesis from a gas-phase formose reaction. *Astrobiology* **7**, 433–442.

Kelley D. S., Baross J. A. and Delaney J. R. (2002) Volcanoes, fluids, and life at mid-ocean ridge spreading centers. *Annu. Rev. Earth Planet. Sci.* **30**, 385–491.

Kelley D. S., Karson J. A., Blackman D. K., Früh-Green G. L., Butterfield D. A., Lilley M. D., Olson E. J., Schrenk M. O., Roe K. K., Lebon G. T., Rivizzigno P., and the AT3-60 Shipboard Party (2001) An off-axis hydrothermal vent field near the Mid-Atlantic Ridge at 30[deg] N. *Nature* **412**, 145–149.

Kelley D. S., Karson J., Fruh-Green G., Yoerger D., Shank T., Butterfield D., Hayes J., Schrenk M., Olson E., Proskurowski G., Jakuba M., Bradley A., Larson B., Ludwig K., Glickson D., Buckman K., Bradley A., Brazelton W., Roe K., Elend M., Delacour A., Bernasconi S., Lilley M., Baross J., Summons R. and Sylva S. (2005) A serpentinite-hosted ecosystem: The Lost City hydrothermal field. *Science* **307**, 1428–1434.

Kim H.-J., Ricardo A., Illangkoon H. I., Kim M. J., Carrigan M. A., Frye F. and Benner S. A. (2011) Synthesis of carbohydrates in mineral-guided prebiotic cycles. *J. Am. Chem. Soc.* **133**, 9457–9468.

Klevenz V., Sumoondur A., Ostertag-Henning C. and Koschinsky A. (2010) Concentrations and distributions of dissolved amino acids in fluids from Mid-Atlantic Ridge hydrothermal vents. *Geochem. J.* **44**, 387–397.

Lee N., Foustoukos D. I., Sverjensky D. A., Cody G. D. and Hazen R. M. (2014) The effects of temperature, ph and redox state on the stability of glutamic acid in hydrothermal fluids. *Geochim. Cosmochim. Acta*. In Press.

McCollom T. M. and Bach W. (2009) Thermodynamic constraints on hydrogen generation during serpentinization of ultramafic rocks. *Geochim. Cosmochim. Acta* **73**, 856–875.

Miller S. L. (1953) A production of amino acids under possible primitive Earth conditions. *Science* **117**, 528–529.

Miller S. L. and Bada J. L. (1988) Submarine hot springs and the origin of life. *Nature* **334**, 609–611.

Novikov Y. and Copley S. D. (2013) Reactivity landscape of pyruvate under simulated hydrothermal vent conditions. *PNAS* **110**, 13283-13288.

Pokrovsky O. S., Schott J. and Castillo A. (2005) Kinetics of brucite dissolution at 25°C in the presence of organic and inorganic ligands and divalent metals. *Geochim. Cosmochim. Acta* **69**, 905–918.

Schoonen M., Smirnov A. and Cohn C. (2004) A perspective on the role of minerals in prebiotic synthesis. *AMBIO* **33**, 539–551.

Shock E. L. (1990) Geochemical constraints on the origin of organic compounds in hydrothermal systems. *Orig. Life Evol. Biosph.* **20**, 331–367.

Shock E. L. and Canovas P. (2010) The potential for abiotic organic synthesis and biosynthesis at seafloor hydrothermal systems. *Geofluids* **10**, 161–192.

Sleep N. H., Bird D. K. and Pope E. C. (2011) Serpentinite and the dawn of life. *Philos. Trans. R. Soc. Lond., B* **366**, 2857–2869.

Sverjensky D. A. (2005) Prediction of surface charge on oxides in salt solutions: Revisions for 1:1 (M+L−) electrolytes. *Geochim. Cosmochim. Acta* **69**, 225–257.

Sverjensky D. A. (2003) Standard states for the activities of mineral surface sites and species. *Geochim. Cosmochim. Acta* **67**, 17–28.

Sverjensky D. A. and Fukushi K. (2006) Anion adsorption on oxide surfaces: Inclusion of the water dipole in modeling the electrostatics of ligand exchange. *Environ. Sci. Technol.* **40**, 263–271.

Sverjensky D. A. and Sahai N. (1996) Theoretical prediction of single-site surface-protonation equilibrium constants for oxides and silicates in water. *Geochim. Cosmochim. Acta* **60**, 3773–3797.

Van Kranendonk M. J., Hugh Smithies R., Hickman A. H. and Champion D. C. (2007)

Review: secular tectonic evolution of Archean continental crust: interplay between horizontal and vertical processes in the formation of the Pilbara Craton, Australia. *Terra Nova* **19**, 1–38.

Chapter 2

Interaction between L-aspartate and the brucite [$Mg(OH)_2$]-water interface

The interaction of biomolecules at the mineral-water interface could have played a prominent role in the prebiotic emergence of more complex organic species in life's origins. In one scenario, serpentinite-hosted hydrothermal vents may have acted as a suitable environment for this process to occur, although little is known about biomolecule-mineral interactions in this system. We used batch adsorption experiments and surface complexation modeling to study the interaction of L-aspartate onto a thermodynamically stable product of serpentinization, brucite [$Mg(OH)_2$], over a wide range of initial aspartate concentrations at four ionic strengths that resulted from the presence of [Mg^{2+}] and [Ca^{2+}]. We observed that up to 1.0 μmol of aspartate adsorbed per m^2 of brucite at pH~10.2 and low Mg^{2+} concentrations (0.7×10^{-3} M), but surface adsorption decreased at high Mg^{2+} concentrations (5.8×10^{-3} M). At high Ca^{2+} concentrations (4.0×10^{-3} M), surface adsorption of aspartate doubled (to 2.0 $\mu mol \cdot m^{-2}$), with Ca^{2+} adsorption at 29.6 $\mu mol \cdot m^{-2}$. We used the extended triple-layer model (ETLM) to construct a quantitative thermodynamic model of the adsorption data. We proposed

three surface reactions involving the adsorption of aspartate ($HAsp^-$) and/or Ca^{2+} onto brucite:

$2>SOH + H^+ + HAsp^- = >SOH_2^+>SAsp^- + H_2O$,

$>SOH + HAsp^- + Ca^{2+} = >SO^-\_Ca(HAsp)^+ + H^+$,

and

$>SOH + Ca^{2+} + 2H_2O = >SOH_2^+\_ Ca(OH)_2 + H^+$.

Our prediction of brucite particle surface charge with the ETLM indicates that the surface becomes more negative with increasing Mg^{2+}, creating an unfavorable electrostatic environment for a negatively-charged aspartate molecule to adsorb. In contrast, our addition of Ca^{2+} to the system resulted in Ca^{2+} adsorption and development of positive surface charge. Our prediction of surface speciation of aspartate on brucite with Ca^{2+} revealed that the calcium-aspartate complex is the predominant surface aspartate species, which suggests that the increase in aspartate adsorption with Ca^{2+} is primarily driven by calcium adsorption. The cooperative effect of Ca^{2+} and the negative effect of Mg^{2+} on aspartate adsorption onto brucite indicate that serpentinite-hosted hydrothermal fluids provide an ideal environment for these interactions to take place.

This paper is currently under review in Geochimica et Cosmochimica Acta.

Authors: Charlene F. Estrada, Dimitri A. Sverjensky, Manuel Pelletier, Angélina Razafitianamaharavo, and Robert M. Hazen

1. Introduction

The origin of life on early Earth is a geochemical sequence of emergent steps involving increasing complexity (Hazen, 2005). Among the first of these steps is the synthesis of prebiotic organic molecules in the midst of Archean atmosphere, ocean, and lithologies. The emergence of simple molecules such as amino acids and sugars may have occurred under a variety of plausible Archean environments (Ponnamperuma and Pering, 1966; Deamer and Pashley, 1989; Hennet et al., 1992; Holm and Andersson, 2005; Jalbout et al., 2007; Cleaves et al., 2008; Kim et al., 2011). Far less is known about the selection, concentration, and self-organization of these biomolecules into macromolecular systems from dilute solutions.

Mineral surfaces may provide the means by which simple biomolecules self-organize. The mineral-water interface is known to concentrate biomolecules through adsorption (Jonsson et al., 2009; Jonsson et al., 2010; Cleaves et al., 2012). Mineral surfaces change significantly with shifts in pH owing to surface protonation reactions. Adsorption behavior can be complex because it has been observed that the predominant adsorbing species of an organic molecule may not exist under natural conditions in bulk water (Geiger, 2009; Malin et al., 2009). A mineral surface may possibly have a catalytic role by concentrating an organic species with polarized functional groups and facilitating reactions among other adsorbed species. Accordingly, mineral surfaces may potentially play a key role in the origin of life, whereby the mineral-water interface provides sites for the selection, concentration, and self-organization of biomolecules (Goldschmidt, 1952; Hazen, 2006; Cleaves et al., 2012).

Hydrothermal vent systems have been discussed as plausible environments for the origin of life by providing suitable templates for macromolecular assembly (Baross and Hoffman, 1985; Shock and Canovas, 2010; Sleep et al., 2011). The disequilibria established by mixing hot, hydrothermal fluids (<350 ºC) with the overlying cold seawater (2 ºC) in the system may drive the formation of some carbon-based, prebiotic molecules (Shock and Schulte, 1998; Shock and Canovas, 2010). A remarkably different type of hydrothermal system, known as the Lost City hydrothermal field, was discovered off the Mid-Ocean Ridge Axis (Kelley et al., 2001). The Lost City hydrothermal vent belongs to a class of hydrothermal systems that undergo serpentinization, which involves the hydration of magnesium-rich olivine to serpentine and ferro-brucite (Bach et al., 2006), according to the reaction:

$$Mg_{1.8}Fe_{0.2}SiO_4 + 3H_2O \rightarrow Mg_{2.85}Fe_{0.15}Si_2O_5(OH)_4 + Mg_{0.75}Fe_{0.25}(OH)_2 \quad (1)$$

Serpentinite-hosted hydrothermal vents such as the Lost City hydrothermal field release fluids that contain up to 19 mM and 4 mM of H_2 and CH_4, respectively (Kelley et al., 2005; Proskurowski et al., 2006). The mixing of these hydrothermal fluids with seawater creates a strong redox gradient that may promote the formation of key prebiotic molecules (Holm et al., 2006; Shock and Canovas, 2010). Furthermore, vent fluids from serpentinite-hosted hydrothermal systems are low temperature (<70 ºC), and thermodynamic modeling experiments suggest that biomolecule synthesis may be more favorable at lower mixing temperatures between hydrothermal fluids and ambient seawater (Shock and Schulte, 1998; Shock and Canovas, 2010).

There is some geological evidence that serpentinite-hosted hydrothermal systems may have developed early on the submarine floor prior to appearance of the first cellular lifeform, which may have emerged at 3.48 Ga (Noffke et al., 2013). Greenstone sequences discovered at the Isua Formation (3.8 Ga) and the Pilbara Formation (3.5 Ga) have been interpreted to indicate hydrothermal alteration (Dymek et al., 1988; Van Kranendonk et al., 2007; Shibuya et al., 2010). It has been suggested from these localities and the presence of Archean komatiites that the oceanic crust on early Earth was more ultramafic compared to today's mafic, basalt-hosted seafloor (Herzberg et al., 2010; Van Kranendonk, 2010). Depending on the prevalence of the ultramafic host rock, serpentinite-hosted hydrothermal fields may have been prolific on the Archean seafloor.

A major, thermodynamically stable mineral of the first sequence of serpentinization is ferro-brucite [$Mg_{0.75}Fe_{0.25}(OH)_2)$]. In the second sequence of the serpentinization reaction, the ferrous iron in this mineral controls the amount of $H_{2(aq)}$ produced from the system as magnetite is subsequently precipitated:

$$(Mg_xFe_y)(OH)_2 \rightarrow (Mg_xFe_{y-3z})(OH)_2 + zFe_3O_4 + zH_{2(aq)} + z2H_2O \qquad (2)$$

It has been proposed that as this reaction proceeds to the right, the amount of $H_{2(aq)}$ flowing through the system becomes limited, and the brucite in the serpentinite-hosted hydrothermal field approaches the magnesium endmember (Bach et al., 2006; McCollom and Bach, 2009). Holm and coworkers (2006; 2012) have also suggested that magnesium plays a role in stabilizing prebiotic biomolecules such as proteins and nucleic acids, and as the primary constituent of brucite, magnesium may promote the formation of more complex molecules at the mineral-water interface within a serpentinite-hosted hydrothermal system.

Previous studies of brucite surface chemistry have focused on the precipitation and dissolution kinetics of brucite (Hostetler, 1963; Schott, 1981; Jordan and

Rammensee, 1996; Pokrovsky and Schott, 2004; Pokrovsky et al., 2005; Kudoh et al., 2006). Pokrovsky and Schott (2004) measured the surface charge of a natural ground sample of brucite in aqueous solution at variable ionic strength and pH in order to constrain the protonation constants with the constant capacitance surface complexation model. Dissolution and precipitation experiments also determined the solubility product (pK°_{sp}) of the brucite dissolution reaction

$$Mg(OH_2)_s = Mg^{2+}_{(aq)} + 2OH^{-}_{(aq)} \tag{3}$$

giving $pK^{o}_{sp}=10.4 \pm 0.05$.

In comparison to the amount of work on the dissolution of brucite, few studies exist on the adsorption of biomolecules onto the brucite surface over a wide range of conditions. The majority of adsorption investigations have focused on the attachment of inorganic ions, such as Pu(IV) and Cu(II) onto the brucite surface (Farr et al., 2000; Wu et al., 2007; Farr et al., 2007). Pokrovsky et al. (2005) have studied the effect of a wide range of organic molecules, including oxalate, citrate, glycine, xylose, and catechol, on brucite dissolution and precipitation. The authors determined that these biomolecules had an effect only at concentrations greater than about $1x10^{-2}$ M at neutral to weakly alkaline pH conditions. It was also suggested that the organic molecules adsorb onto the brucite surface through an inner-sphere attachment, represented by the surface reaction:

$$>MgOH_2^{+} + L^{n-} = >MgL^{1-n} + H_2O \tag{4}$$

where L^{n-} denotes the aqueous species of ligand, L. One of these ligands, citrate, was found to adsorb onto brucite in amounts as high as 0.4 $\mu mol•m^{-2}$ (Pokrovsky et al., 2005). In another study that characterized the adsorption of citrate in the presence of Pu(IV), a maximum of approximately 0.4 $\mu mol•m^{-2}$ citrate adsorption was observed (Farr et al. , 2000). The effect of alkaline earth cations on brucite dissolution has also been investigated (Pokrovsky et al., 2005), indicating that at concentrations of at least 1x10^{-2} M and at a pH of 4.9, Ca^{2+} increases the brucite dissolution rate. They assumed that the increase in brucite dissolution rate was caused by the formation of a bidentate or monodentate mononuclear complex between Ca^{2+} and the brucite surface. The efficient adsorption of an inorganic or organic molecule in large amounts may have weakened surface bonds and shifted the charge at the brucite-water interface such that there was an observable change in the dissolution rate (Pokrovsky et al., 2005).

In this study, we characterize the adsorption of the amino acid L-aspartate ($C_4H_7NO_4$) onto powdered brucite, [$Mg_{1.0}(OH)_2$]. Aspartate is a polar amino acid with three protonation sites: two carboxyl groups and one amine group. The adsorption of aspartate has been previously well-characterized on titanium dioxide (Giacomelli et al., 1995; Roddick-Lanzilotta and McQuillan, 2000; Jonsson et al., 2010), calcium carbonate (Hazen et al., 2001), kaolinite (Ikhsan et al., 2004) and alumina (Greiner et al., 2014). However, there are no studies on the adsorption of aspartate on brucite under the effects of variable divalent cation concentrations (Mg^{2+} and Ca^{2+}), biomolecule concentration, and pH conditions. Additionally, aspartate was chosen as a hydrothermally relevant biomolecule, both because it has been observed at the relatively high concentration of 387 nM at the Logatchev serpentinite-hosted hydrothermal field (Klevenz et al., 2010), and it has been synthesized under mineral-buffered, simulated hydrothermal conditions (Hennet et al., 1992; Holm and Andersson, 2005). Aspartate also play a key role in the citric acid cycle, the evolution of which may be a critical emergent step in the origin of life (Wächtershäuser, 1990; Meléndez-Hevia et al., 1996).

The aim of this study is to evaluate the potential role that serpentinite-hosted hydrothermal minerals play in concentrating and selecting fundamental prebiotic molecules from a dilute aqueous environment. In this framework, we characterize the extent and possible importance of this interaction with a combination of batch adsorption experiments at 25 ºC and 1 bar and surface complexation modeling. Further, we attempt to elucidate the effects that common dissolved ions, such as Mg^{2+} and Ca^{2+}, have on the interaction between aspartate and the brucite-water interface so that we may make predictions of the behavior of key mineral surface reactions in plausible prebiotic aqueous environments.

2. Materials and Methods

2.1. Brucite Synthesis

We synthesized a microcrystalline brucite powder using a precipitation method previously reported by Henrist and coworkers (2003) and Lu and coworkers (2004). With 18.2 MΩcm Milli-Q water (Millipore), we prepared a 2.0 M $MgCl_2$ solution (99.99 % Alfa Aesar dry ampoules under Ar gas) and a solution containing 2.0 M NH_4OH (Sigma-Aldrich, 25 wt. % solution) in a 250 mL Pyrex reaction vessel. We added the $MgCl_2$ solution dropwise to the reaction vessel at a rate of approximately 2.5 $mL \bullet min^{-1}$ using a graduated buret while we vigorously stirred the NH_4OH solution and kept it at a constant temperature of 45 ± 3 ºC. During the addition of $MgCl_2$ to the NH_4OH solution, the following precipitation reaction has been proposed to take place (Lu et al., 2004):

$$MgCl_2 + 2NH_4OH \rightarrow Mg(OH)_2 + 2NH_4Cl \tag{5}$$

After the precipitation reaction, we set the sealed reaction vessel aside to cool at room temperature for 3 days. We then separated the precipitate from the mother fluid and thoroughly washed it of the soluble NH_4Cl byproduct by mixing and centrifuging the solid with Milli-Q water for a minimum of 3 times. We halted the washing process when the fluid, after centrifugation, became cloudy, which was evidence that the brucite was beginning to dissolve. We then dried the precipitate on a Corning PC-420D hot plate at 135 ºC for 1 hour.

2.2. Hydrothermal Treatment

Studies by Henrist and coworkers (2003) and Lu and colleagues (2004) observed that when synthetic brucite is subjected to water >100 ºC in a sealed vessel over an extended period of time that its morphology and crystallinity improves. We carried out a hydrothermal aging treatment on our synthetic brucite by sealing the untreated precipitate in Milli-Q water within a PTFE-lined stainless steel reaction vessel (Col-Int-Tech). We heated the vessel at 150 ºC for 3 days (Fisher Scientific Isotherm Furnace ±2 ºC), and after cooling the brucite/water solution to room temperature, we dried the powder at 135 ºC (Corning Hot Plate). We stored the hydrothermally treated brucite powder in a glass vial under an Ar gas atmosphere at 25 ºC.

SEM imaging (JEOL 8500F) revealed that the untreated brucite has a crystal habit characterized by rosettes of rough, circular and oblong platelets (Fig. 1a), whereas the hydrothermally-treated brucite is distinguished by clusters of lamellar, hexagonal platelets (Fig. 1b). Additionally, the powder XRD (Bruker D2 Phaser) pattern of the hydrothermally-treated brucite demonstrates higher intensity peaks in the case of reflection (001) and reduced intensity for the (100), (101) and (111) reflections (Fig. 2), which is consistent with powder XRD patterns collected under ambient conditions that have been archived at the International Centre for Diffraction Data (http://icdd.com). Together these observations may be interpreted as evidence that the hydrothermal treatment process enhanced the crystallinity in the basal direction by reducing terraces and kink sites and improving hexagonal morphology.

2.3. Brucite Specific Surface Area

The surface area of the synthetic brucite powder was first characterized by the multi-point BET N_2 adsorption method (Micromeritics, Norcross, GA, USA) to obtain a specific surface area of 17.6 ± 0.1 $m^2 \bullet g^{-1}$. A high proportion of this measured surface area most likely represents the prominent (001) basal surface, although the distribution between the basal and lateral (edge) surfaces cannot be determined with the classical N_2 gas adsorption method. This distinction is important because previous adsorption studies involving minerals that have surfaces with hydroxyl functional groups similar to brucite, including gibbsite, geothite, illite, and kaolinite conclude that only lateral surfaces are active in the protonation and deprotonation reactions that can lead to molecular adsorption (Prélot et al., 2003; Sayed-Hassan et al., 2006; Liu et al., 2013). If the lateral surfaces primarily adsorb aspartate, it is necessary to determine the surface area specific to these edge faces.

We characterized the edge-specific surface area (ESA) with low-pressure argon gas adsorption, performed at the Laboratoire Interdisciplinaire des Environnements Continentaux (Vandœuvre les Nancy, France). We obtained surface reactivity data using a laboratory-constructed, quasi-equilibrium volumetric apparatus coupled with the Derivative Isotherm Summation (DIS) procedure (Villiéras et al., 1997). We used argon low-pressure quasi-equilibrium volumetry to estimate the extension of the lateral and basal faces of brucite (ultra-high purity argon, 99.9996 % Air Liquide). Consistent basal- and edge-specific surface areas were previously obtained with this technique for several lamellar minerals including talc, kaolinite, illite, lamellar silica, saponite, and smectites (Villiéras et al., 2002; Michot and Villiéras, 2002; Eypert-Blaison et al., 2002; Tournassat et al., 2003; Sayed-Hassan et al., 2005; Sayed-Hassan et al., 2006; Perronnet et al., 2007). As argon is mostly sensitive to the structural parameters of a surface, textural and surface properties of other minerals have also been investigated, including goethite, anatase, and manganese dioxides (Prélot et al., 2003; Stevanovic et al., 2010; Ali Ahmad et al., 2012).

During our analysis of brucite, the BET-derived formalism was used. A total of 877.1 mg of powdered brucite was introduced to the adsorption cell and outgassed for 18 hours at 110°C under a residual pressure of 10^{-3} Pa. Between 2000 to 3500 points were recorded with high accuracy in the domain of relative pressure lower than 0.15. Due to the large amount of data acquired by the quasi-equilibrium method, the total derivative adsorption isotherm as a function of the logarithm of relative pressure was calculated from the experimental high-resolution adsorption isotherm (Fig. 3). These derivative curves can be considered as fingerprints of the interactions between surface adsorption sites and the gas probes, where $\ln(P/P_0)$ corresponds to adsorption free energy scales graduated in $-KT$. With this representation, it was simpler to distinguish the different peaks that correspond to the surface groups or domains of similar adsorption sites on the brucite surface. The experimental derivative adsorption isotherm is simulated by the summation of several local theoretical derivative adsorption isotherms (Villiéras et al., 1992; Villiéras et al., 1997). Each local isotherm is characterized by three parameters: (1) the normal interaction between the surface and the adsorbed molecules, (2) the lateral interactions between two neighboring adsorbed molecules, "ω", and (3) the amount of argon gas adsorbed onto each domain at the monolayer state "V_m". Normal interactions depend on the position of the derivative isotherm maxima on the $\ln(P/P_0)$ axis and the intensity of lateral interaction. The peak position is proportional to the adsorption energy. The monolayer capacity, V_m, is given by the area of the peak. The lateral interaction is linked to the half-height width of the local derivative isotherm (ω/KT), and this parameter relates information about the heterogeneity of the considered adsorption domain.

From the application of the DIS procedure (Fig. 3), and using the parameters of each local derivative isotherm (Table 1), we assign local derivative isotherms 1 and 2 to the basal brucite faces and isotherms 3 and 4 to the lateral faces. These assignments are reasonable in comparison with results obtained for other clay minerals and layer silicates (Villiéras et al., 2002; Michot and Villiéras, 2002; Eypert-Blaison et al., 2002; Sayed-Hassan et al., 2005; Sayed-Hassan et al., 2006). We have calculated a surface area of 19.8 ± 0.2 $m^2 \bullet g^{-1}$ with Ar gas, which is comparable to the BET determined by N_2 gas (17.6 $m^2 \bullet g^{-1}$). We have estimated that 89.5 % of the surface area is represented by basal brucite surfaces, whereas 10.5 % is represented by lateral brucite surfaces. When the brucite particles are roughly considered as plates with square, basal faces, our estimated basal and lateral surface areas can be tested to derive the particle thickness (t) and length (l) using the equations

$$\mathrm{l} = \frac{4}{\rho\,.S_l} \tag{6}$$

and

$$\mathrm{t} = \frac{2}{\rho\,.S_b} \tag{7}$$

where ρ is the density of brucite (2.39 g•cm^{-3}) and S_l and S_b are the lateral and basal surface areas, respectively . Using the specific surface area obtained with N_2 gas (Sb=15.7 m^2•g^{-1} and S_l=1.9 m^2•g^{-1}), we calculated an average plate length of 881 nm and thickness of 53 nm. These values appear to consistent with those represented by the SEM image of brucite in Fig. 1b., where the particle length varies between 0.1 to 1 µm and the thickness is approximately 30 to 50 nm. We therefore consider 1.9 m^2•g^{-1} to accurately represent the ESA of the lateral surface of our brucite sample.

2.4. Batch Adsorption Experiments

We prepared each batch sample with a 10.0 ± 0.5 g•L^{-1} solid concentration of brucite combined with variable concentrations of aspartate, ranging from 2-300 µM, in 15 mL sterile Falcon tubes. The pH of each sample was strongly buffered by the brucite powder, and the pH of immersion (pH_{IMM}) lay between pH=10.2-10.3 when no additional Mg^{2+} was introduced to the system. We studied four ionic strengths that resulted from the dissolution of Mg^{2+} from brucite and our addition of either $MgCl_2$ or $CaCl_2$ to the aqueous phase. We investigated:

1) a "low Mg^{2+} concentration" with no Ca^{2+} present ($[Mg^{2+}]=0.7\times10^{-3}$ M, I= 2.1×10^{-3} M);
2) a "high Mg^{2+} concentration" with no Ca^{2+} present ($[Mg^{2+}]= 0.6\times10^{-3}$ M, $[MgCl_2]= 5.2\times10^{-3}$ M, I= 17.4×10^{-3} M) ;

3) a “low Ca^{2+} concentration” in the presence of $[Mg^{2+}]= 0.9x10^{-3}$ M ($[CaCl_2]= 1.0x10^{-3}$ M, I= $5.8x10^{-3}$ M);

and

4) a “high Ca^{2+} concentration” in the presence of $[Mg^{2+}]=1.0x10^{-3}$ M ($[CaCl_2]= 4.0x10^{-3}$ M, I=$15.2x10^{-3}$ M).

Previous work suggested that elevated concentrations of Ca^{2+} and some biomolecules ($>10^{-2}$ M) may affect the dissolution of brucite in aqueous solution (Pokrovsky et al., 2005). Accordingly, we studied a relatively low concentration of both Ca^{2+} ($\leq 4.0x10^{-3}$ M) and aspartate ($\leq 0.3x10^{-3}$ M) to avoid this potential complication.

Preliminary adsorption experiments conducted over multiple periods of time indicate that aspartate adsorption onto brucite reaches a steady state within 16 hours. In this study, we placed the batch samples on a test tube rotator at 40 rpm (25 ± 1 ºC, 1 bar) for 22 hours to ensure that the brucite-aspartate suspension had reached a steady state. We then measured the pH of the brucite-aspartate suspension with a combination glass electrode (Thermo-Electron, Orion 8103BNUWP) that had been calibrated prior to the experiment with NIST standardized buffers that referred to pH values of 4, 7, and 10 (Fischer Scientific). Each sample was constantly purged with Ar gas during exposure to air to avoid contamination by CO_2. We centrifuged the samples for 10 minutes with a relative centrifugal force of 1073g (Fisher Scientific accuSpin 400) and separated the liquid supernatant from the solid brucite.

We analyzed the concentration of the aspartate, Mg^{2+} and Ca^{2+} in the supernatant with ion chromatography. We used a Dionex ICS-5000 system equipped with a DP dual pump, AS-AP autosampler, ED electrochemical detector and Chromeleon 6.8 software

(Dionex Corporation, Sunnyvale, CA, USA). The analyte passed through an AminoPAC10 column that is packed with a hydrophobic, polymeric, pellicular resin, where the aspartate present in the supernatant was removed from the bulk fluid via gradient anion exchange separation at pH values between 12 to 14. Following separation, the relative analyte concentration was determined by integrated pulsed amperometric detection (IPAD), a method that irreversibly oxidizes the amino and hydroxyl groups of the aspartate to then be detected with the working gold electrode of the ED electrochemical detector (Clarke et al., 1999; Jandik et al., 2000). The Mg^{2+} and Ca^{2+} present in the supernatant passed through an IonPac CS12A column packed with a hydrophobic resin containing a carboxylate functional group that separated the ions through cation exchange (Jensen et al., 1993). A CD conductivity detector with electrolytic suppression then analyzed the cations. For each cation and amino acid application, a chromatogram containing a peak that is unique to aspartate, Mg^{2+} and Ca^{2+} was produced for every batch sample. The concentration of the cation or amino acid in the analyte was determined from the area beneath its peak, which was integrated with the software Chromeleon 6.8.

Prior to analyzing the supernatant with the IC, we measured a set of standards for Mg^{2+}, Ca^{2+}, and aspartate, which resulted in a linear correlation between the area under the peak and concentration. We standardized for each set of samples by calibrating the IC within two hours of analyzing the first supernatant of the batch adsorption experiment.

We analyzed the samples with ion chromatography in triplicate and determined the mean concentration of aspartate remaining in the liquid supernatant within ±1 standard error (σ_M). It was necessary to analyze the aspartate samples in triplicate because, with the Mg^{2+} batch adsorption experiments in particular, low amounts of aspartate adsorption (<10 %) were initially detected, and collecting data in triplicate better constrained accurate aspartate adsorption values. It was not necessary for us to analyze Ca^{2+} adsorption data in triplicate because initial measurements found that Ca^{2+} adsorbed onto brucite in large amounts (>10 %) and we calculated that ±1 σ standard deviation was equal to about 8 % of the adsorption data. From the analytical concentrations of aspartate and Ca^{2+} we determined the surface adsorption, (Γ_{ads}, $\mu mol \cdot m^{-2}$) of aspartate or Ca^{2+} on brucite, according to:

$$\Gamma_{\mathrm{ads}} = \frac{[X]_0 - [X]_{\mathrm{aq}}}{C_s A_s} \tag{8}$$

In which C_s is the solid concentration and A_s is the lateral edge surface area of brucite. We report Γ_{ads} as an isotherm, as a function of $[X]_{aq}$, the remaining aspartate in the liquid supernatant.

2.5. Surface Complexation Modeling Approach

We integrated experimental isotherm data with a predictive triple layer model that uses Born solvation and crystal chemical theory known as the extended triple-layer model or ETLM (Sverjensky and Sahai, 1996; Sahai and Sverjensky, 1997; Sverjensky, 2003; Sverjensky, 2005; Sverjensky and Fukushi, 2006). Unlike other solid-water interface models, the ETLM predicts the electrical work resulting from the release of water dipoles during inner-sphere adsorption. We carried out calculations for the ETLM iteratively with the computer code GEOSURF (Sahai and Sverjensky, 1998). We estimated a pH_{PZC}=10.5 from observations of pH_{IMM} in our batch adsorption experiments. Speciation reactions involving aqueous aspartate have been previously calculated and have been found to be consistent with those determined from potentiometric titration data (De Robertis et al., 1991; Jonsson et al., 2010). We obtained both protonation and electrolyte adsorption parameters for the brucite surface from a regression of previously published surface titration data (Pokrovsky and Schott, 2004). As illustrated by Fig. 4, we fit this data with the ETLM using parameters that were derived from a constant capacitance model (C= 500 μF•cm^{-2}), where pH_{PZC} =11.0, site density (N_s)=10 sites•nm^{-2}, and BET surface area = 9.2 m^2•g^{-1} were reported for the titration study at 1.0x10^{-2} M NaCl and 1.0 M NaCl. The protonation and electrolyte adsorption parameters were then recalculated for our estimated pH_{PZC}, lateral A_s, and N_s using the methods detailed in a previous publication, and these values are displayed in Table 2 (Sverjensky, 2003; Sverjensky, 2005).

Site densities can also be estimated from the number of broken bonds at the surface consistent with experimental site densities measured by tritium exchange experiments (Koretsky et al., 1998). Accordingly, we have calculated site densities for the lateral surfaces (100), (010), (110), and (111) by examining the broken bonds of each possible idealized surface with the program CrystalMaker (Palmer, 2009). With this method, we calculated a minimum possible site density of 9.7 sites•nm^{-2} and a maximum possible site density of 20.0 sites•nm^{-2} for the lateral surfaces (Table 3). In order to fit the Ca^{2+} adsorption data at high and low Ca^{2+} concentrations in combination with aspartate adsorption data, we needed a site density of 38 sites•nm^{-2}. This value is greater than what has been calculated for the idealized surfaces, but it appears to be the most appropriate site density for the aspartate-brucite system. Surface imperfections such as step and kink sites and the dissolution of Mg^{2+} in the aqueous system may explain why it is necessary for us to adopt a higher site density. It was established that biomolecule concentrations of at least 10^{-2} M may affect the dissolution of a natural, ground sample of brucite (Pokrovsky et al., 2005). However, it may be that our pure, synthetic brucite sample is susceptible to dissolution at lower concentrations of aspartate, and this may contribute to the increased site density.

With the protonation and electrolyte adsorption parameters established, we proposed surface reactions for the adsorption of aspartate onto brucite in a hypothetical 10^{-3} M NaCl system and fit the reactions to the experimental data (Table 2). The data has been collected at four distinct ionic strengths with different dissolved ions present and a variable pH range, thus thoroughly testing our proposed surface reactions and permitting the selection of a small number of reactions to successfully predict the adsorption of aspartate onto brucite.

3. Results and Discussion

3.1. Aspartate Adsorption onto Brucite at Low Mg^{2+} Concentrations

The adsorption data for aspartate onto brucite as a function of aspartate concentrations at low Mg^{2+} concentrations (0.7×10^{-3} M) is displayed in Fig. 5a, and all aspartate adsorption data is reported in Table 4. Aspartate surface adsorption at a pH value of 10.3 ± 0.05 increases steadily as a function of $[Asp]_{aq}$ from 1-145 μM and flattens off at the highest concentration of 275 μM. The error reported in Fig. 5 is ±1 σ_M of each mean Γ_{ads} and $[Asp]_{aq}$ value reported. The amount of aspartate adsorption lies between 8.4×10^{-2} and 1.0 μmol•m^{-2}. This range of surface adsorption generally corresponds to 16.4 to 3.6 % aspartate adsorption, where the percentage of adsorbed aspartate decreases with increasing surface adsorption. As a consequence, the reported error substantially increases with Γ_{ads} and $[Asp]_{aq}$.

As previously discussed, it is thought that only the lateral brucite surfaces are active in adsorption reactions; however, we are unable to distinguish whether there is one lateral surface that is more prominently adsorbing aspartate than any other. A crystallographic examination of the idealized lateral surfaces (100), (110), (111), and (010) has revealed that there are two distinct terminations on the three-coordinated hydroxyl group: a geminal site ($>Mg(OH)_2$) where two bonds are broken, and a bridging site ($>MgOH$), where a single bond is broken at the surface. Whether the aspartate molecule binds at a geminal or bridging reaction site cannot be distinguished by the ETLM because there is no difference in the electrical work that results from the proposed surface reactions in Table 2 at either site. Therefore to avoid ambiguity, we will display surface reactions occurring at the (100) brucite plane as an example surface only, and henceforth regard the neutral brucite surface as “>SOH”.

Analysis of the data in Fig. 5a with the ETLM suggests a surface reaction represented by the stoichiometry

$$2{>}SOH + H^+ + HAsp^- = {>}SOH_2^+{>}SAsp^- + H_2O \qquad (9)$$

It can be observed in Fig. 5b that this reaction results in a close fit to the experimental data within the analytical uncertainties. This surface reaction can be interpreted to involve a bidentate mononuclear, or “leaning” configuration, where there are two points of attachment onto the brucite surface: one that is hydrogen-bonded and one that is inner-sphere (Fig. 6). The hydrogen bond occurs between one oxygen atom of the γ-carboxylate group and the $–OH_2^+$ functional group attached to a surface Mg atom, which can be represented by the bond >SOH$^{\cdots}$O-C. At the inner-sphere point of attachment, we suggest that the doubly deprotonated aspartate molecule bonds to a magnesium atom through a ligand exchange reaction with the α-carboxylate group, which can be represented by the bond >S-O-C.

The reaction in Eq. (9) corresponds to the equilibrium constant

$$^{*}K^{0}_{>SOH_2^+>SAsp^-} = \frac{a_{>SOH_2^+>SAsp^-} a_{>H_2O}}{a^2{}_{>SOH}\, a_{HAsp^-}\, a_{H^+}} 10^{\frac{F\Delta\psi_{r,9}}{2.303RT}} \qquad (10)$$

where the superscript "*" indicates the reaction is expressed relative to the >SOH surface and "0" refers to a hypothetical 1.0 molal standard state (Sverjensky, 2003). The value $\Delta\psi_{r,9}$ represents the electrical work involved in Eq. (9). The electrical work includes a contribution from the movement of water dipoles off the brucite surface according to $\Delta\psi_{r=}$ $-n_{H2O}(\psi_{0-}\ \psi_{\beta})$, where n_{H2O} are the number of water molecules on the right-hand side of the reaction. In Eq. (9), n_{H2O}= 1, which results in $\Delta\psi_{r,9} = \psi_0 - \psi_\beta$.

3.2. Aspartate Adsorption onto Brucite at High Mg^{2+} Concentrations

The brucite dissolution reaction characterized in Eq. (3) can be rewritten as

$$Mg(OH)_2 + 2H^+ = Mg^{2+} + 2H_2O \qquad (11)$$

where the equilibrium constant of Eq. (11) can be expressed as

$$\log K = \frac{a_{Mg^{2+}}}{a^2_{H^+}} \qquad (12)$$

For our pure, synthetic brucite we calculated equilibrium constants of logK=17.3 ± 0.06 and logK= 17.3 ± 0.01 for the brucite-aspartate and brucite-water batch experiments ($[Mg^{2+}]=0.7\times10^{-3}$ M), respectively. These values for the logK are close to the value of 17.6 ± 0.5 previously determined for a ground, natural sample of brucite (Pokrovsky and

Schott, 2004). In Fig. 7a, we plot the steady-state activity ratio, where the activity coefficient of Mg^{2+} was calculated with GEOSURF, as a function of solution pH for our batch adsorption experiments. We observe that the activity ratio in Eq. (12) does not change as a function of pH. Therefore, we assume that brucite is in equilibrium with the aqueous phase during our batch adsorption experiments. If brucite is in equilibrium with the aqueous phase, the addition of Mg^{2+} to a brucite-aspartate batch experiment should decrease solution pH while maintaining the equilibrium constant illustrated by Fig. 7a. In Fig. 7b, we plot the activity ratio obtained by brucite-aspartate batch adsorption experiments conducted in the presence of 5.8×10^{-3} M Mg^{2+} (5.2×10^{-3} M $MgCl_2$ plus 0.6×10^{-3} M Mg^{2+} dissolved from brucite) as a function of solution pH. As predicted, pH decreases (pH_{IMM}= 9.9 ± 0.1) and the average activity ratio of logK= 17.2 ± 0.04, is consistent within the range of uncertainty of the previously calculated logK.

The aspartate surface adsorption data for the batch experiment conducted at high Mg^{2+} concentrations is displayed as an isotherm along with the data from the low-Mg^{2+} batch experiment in Fig. 8a. Aspartate adsorption at high Mg^{2+} concentrations occurs at an ionic strength of 17.4×10^{-3} M and lies between 1.7×10^{-2} and 0.6 $\mu mol \cdot m^{-2}$. In comparison with the adsorption data obtained under low Mg^{2+} concentrations, aspartate surface adsorption decreases by a factor of about 1.5. Using the model developed above with the surface reaction in Eq. (9), we obtained a fit to both the high- and low-Mg^{2+} data at pH=9.9 and pH=10.3, respectively, in Fig 8b. There is little discrepancy between the predicted curves and the experimental data within analytical uncertainty. The close agreement provided by the “leaning” aspartate species from Eq. (9) is consistent with experimental data at two distinct ionic strengths resulting from different experimental Mg^{2+} concentrations, which lends support to the use of the surface reaction in Eq. (9).

3.3. Aspartate Adsorption onto Brucite in the Presence of Ca^{2+}

Isotherms of aspartate surface adsorption onto brucite in the presence of low and high Ca^{2+} concentrations are shown in Fig. 9a. The low-Ca^{2+} experiments refer to a Ca^{2+} concentration of 1.0×10^{-3} M together with a Mg^{2+} concentration of 0.9×10^{-3} M at a pH of 10.2 ± 0.02. Surface adsorption lay between 4.3×10^{-2} and 1.8 $\mu mol \bullet m^{-2}$. High-Ca^{2+} experiments refer to a Ca^{2+} concentration of 4.0×10^{-3} M and a Mg^{2+} concentration of 1.0×10^{-3} M at a pH of 10.2 ± 0.05. Surface adsorption was observed to increase at high Ca^{2+} concentrations, where Γ_{ads} lay between 0.1 and 2.1 $\mu mol \bullet m^{-2}$. This range of Γ_{ads} corresponds to between 56.4 and 17.1 % aspartate adsorption, respectively.

Aspartate surface adsorption is significantly greater in the presence of Ca^{2+} compared to the batch adsorption experiments conducted with only Mg^{2+} (see Fig. 5a). In particular, when aspartate adsorbs onto brucite with high Ca^{2+} concentrations, Γ_{ads} increases two-fold. In addition to this remarkable amount of aspartate adsorption, a significant amount of Ca^{2+} has been observed to adsorb onto brucite as illustrated by Fig. 10a. The amount of Ca^{2+} surface adsorption averages 21.6 ± 1.8 $\mu mol \bullet m^{-2}$ (41.8 %) for the low-Ca^{2+} experiments and 29.6 ± 2.3 $\mu mol \bullet m^{-2}$ (14.4 %) for the high-Ca^{2+} experiments. The error of $\pm 1\ \sigma$ corresponds to an uncertainty of approximately 8 % of Ca^{2+} adsorption. All calcium adsorption data is reported in Table 5.

To develop a model of the surface adsorption of aspartate in Fig. 9a and Ca^{2+} in Fig. 10a, we combined the surface reaction in Eq. (9) with two surface reactions involving Ca^{2+}. The first surface reaction involves the formation of a calcium- aspartate complex:

$$>SOH + HAsp^{-} + Ca^{2+} = >SO^{-}\_CaHAsp^{+} + H^{+} \qquad (13)$$

This reaction can be interpreted as adsorption of a monodentate outer-sphere species on the brucite surface. This species is illustrated in Fig. 11a. The second reaction involves the adsorption of a hydrated calcium complex:

$$>SOH + Ca^{2+} + 2H_2O = >SOH_2^{+}\_\ Ca(OH)_2 + H^{+} \qquad (14)$$

that can be interpreted as a monodentate outer-sphere surface species shown in Fig. 11b.

In Fig. 11a, the calcium-aspartate outer-sphere species may attach through an electrostatic interaction between a negatively-charged surface site and the calcium atom that carries a local positive charge after complexing with the aspartate α-carboxylate group (>SO···Ca-O-C). Franchi and colleagues (2003) observed enhanced adsorption of nucleic acids on the clay minerals montmorillonite and kaolinite in the presence of Ca^{2+}. The authors concluded that a similar configuration involving calcium-aspartate complexes occurred where the Ca^{2+} atom would act as a "bridge" between the organic species and the clay-water interface (Franchi et al., 2003). We propose that this calcium-aspartate species adsorbs in addition to the "leaning" aspartate species illustrated in Fig. 6. The equilibrium constant of the surface reaction in Eq. (13) is expressed as

$$^{*}K^{0}_{>SO^{-}\_Ca(HAsp)^{+}} = \frac{a_{>SO^{-}\_(HAsp)^{+}}a_{H^{+}}}{a_{>SOH}\,a_{HAsp^{-}}\,a_{Ca^{2+}}}\,10^{\frac{F\Delta\psi_{r,13}}{2.303RT}} \qquad (15)$$

where the value $\Delta\psi_{r,13} = -\psi_0 + \psi_\beta$.

In Fig. 11b, the calcium outer-sphere species attaches to a protonated surface site by a single hydrogen bond through the hydroxyl group (>SOH···OH-CaOH). Here, the equilibrium constant of the surface reaction proposed in Eq. (14) is

$$^{*}K^{0}_{>SOH_2^+\_Ca(OH)_2} = \frac{a_{>SOH_2^+\_Ca(OH)_2}\, a_{H^+}}{a_{>SOH}\, a_{Ca^{2+}}\, a^{2}_{H_2O}}\, 10^{\frac{F\Delta\psi_{r,14}}{2.303RT}} \tag{16}$$

where $\Delta\psi_{r,14} = \psi_0$. The surface reactions in Eq. (9) and (13-14) were combined to fit the aspartate adsorption data at low and high Ca^{2+} concentrations at pH=10.2 and pH=10.3, respectively, in Fig. 9b. The calculated curve at pH=10.2 for the low Ca^{2+} concentration agrees with the adsorption data within analytical uncertainty. The curve calculated for the high Ca^{2+} concentration, although in overall agreement with the isotherm shape, is a bit low compared with all of the data points except for the highest surface coverage, but is consistent with the data within ±2.5 σ_M or approximately 7 % uncertainty.

We predicted curves for Ca^{2+} adsorption as a function of initial aspartate concentration, $[Asp]_0$, as shown in Fig 10b. In this figure, there are two data points in the high-Ca^{2+} experiments that are elevated above the curve calculated with the surface reaction in Eq. (14). However, the average surface adsorption of Ca^{2+} calculated by the curve for the high-Ca^{2+} experiment is 28.1 $\mu mol \cdot m^{-2}$, which falls well within our calculated uncertainty of the average experimental Γ_{ads} of Ca^{2+}, 29.6 ± 2.3 $\mu mol \cdot m^{-2}$. Therefore, we consider the Ca^{2+} surface adsorption curves predicted by the reactions in Eqs. (13-14) to be in acceptable agreement with the bulk of the data collected at low and high Ca^{2+} concentrations. We thus regard the surface reactions proposed by Eqs. (9) and (13-14) as sufficiently characterizing the aspartate-brucite and Ca^{2+}-brucite adsorption system with respect to different ionic strengths, pH conditions, divalent cation concentrations and initial aspartate concentrations.

3.4. Prediction of Brucite Particle Surface Charge

The significant increase in aspartate adsorption with Ca^{2+} and its decrease with $MgCl_2$ addition suggest that the particle surface charge of brucite shifted relative to the experimental conditions we investigated (Table 1). We therefore calculated the particle surface charge by predicting the ζ-potential of the brucite surface with the ETLM as a function of $[Asp]_0$ for each type of batch experiment. In these calculations, we assumed that the ζ-potential was equal to the potential at the start of the diffuse layer (Ψ_d) in the ETLM. As shown in Fig. 11, we predicted that ζ-potential was neutral to slightly negative for the low-Mg^{2+} experiment, and it decreased with increasing $[Mg^{2+}]$. This could be a result of decreased pH with added $MgCl_2$, which may directly affect the brucite surface charge. Moreover, we did not observe Mg^{2+} adsorption on brucite, although we added $MgCl_2$ to the system. In Eq. (7), we also predicted the doubly-deprotonated aspartate molecule, Asp^{2-}, adsorbed onto brucite. A decrease in surface particle charge could create an unfavorable electrostatic environment for Asp^{2-} to adsorb onto brucite, which reflects our observation of decreased aspartate adsorption with added $MgCl_2$. In Fig. 11, we modeled a reversal of the ζ-potential with Ca^{2+}. This calculation of positive particle surface charge reflects the ETLM reactions in Eqs. (11) and (13) where calcium adsorbs onto the brucite surface resulting in a net positive surface charge.

The cooperative metal-aspartate complex, $CaHAsp^{+}$, may enable the aspartate molecule to adsorb in greater amounts. We predicted the distribution of the two adsorbing aspartate species in Eqs. (9) and (13) with the ETLM at both low and high Ca^{2+} concentrations as a function of $[Asp]_0$ in Fig. 13. At both Ca^{2+} concentrations, we observed that the calcium-aspartate outer-sphere species overwhelmingly predominates, whereas very little of the surface adsorption can be represented by the “leaning” aspartate species. This result may provide further evidence that calcium forms the predominant surface species, and the formation of a calcium-aspartate complex serves to enhance the adsorption of aspartate.

It can be interpreted from Eq. (13) that a calcium-aspartate complex forms at the brucite-water interface. We plot the predicted distribution of aqueous aspartate species that can be represented by calcium-aspartate complexes as a function of $[Asp]_0$ at both low Ca^{2+} concentrations (Fig. 14a) and high Ca^{2+} concentrations (Fig. 14b). Fig. 13 illustrates that up to 25.8 % and 6.5 % of the aqueous aspartate species are represented by the $CaAsp^0$ species at high Ca^{2+} and low Ca^{2+} concentrations, respectively, which indicates that calcium-aspartate aqueous complexes are predicted to readily form. However, whereas the neutral $CaAsp^0$ species predominates in aqueous solution, the aqueous $CaHAsp^+$ species does not exceed 0.5 % at low Ca^{2+} concentrations and 2 % at high Ca^{2+} concentrations. Nevertheless, the $CaHAsp^+$ species is predicted to predominate as a surface species, which illustrates the tendency for the mineral-water interface to adsorb organic species that may not always predominate in bulk water (Geiger, 2009; Malin et al., 2009).

It is possible that because aspartate is a polar, negatively-charged amino acid, it may readily form a cooperative calcium-aspartate complex, and that leads to advantageous surface adsorption on brucite. A similar amino acid, such as glutamate ($C_5H_9NO_4$), may also form such a complex with Ca^{2+}, and follow a similar pattern of increased surface adsorption. Likewise, Ca^{2+} may not strongly bond to a positively-charged amino acid such as lysine ($C_6H_{14}N_2O_2$) and competitively adsorb on the brucite surface with aspartate. Whether Ca^{2+} may either cooperatively or competitively affect the surface adsorption of a particular organic molecule onto brucite is worth future investigation.

3.5. Prediction of Aspartate Adsorption in Lost City Fluids

We propose that an ideal natural environment for the adsorption of aspartate to occur to the greatest extent on brucite would have elevated concentrations of Ca^{2+} and little or no Mg^{2+} present. Serpentinite-hosted hydrothermal systems provide such an environment, not only due to the ionic composition of the vent fluids, but also the occurrence of both brucite and possibly aspartate (Kelley et al., 2001; Shock and Canovas, 2010). The vent fluids at the Lost City hydrothermal field are reported to have high concentrations of Ca^{2+} (23.3×10^{-3} M) relative to a 0 M Mg^{2+} endmember composition over a pH range between 9.0 and 9.8 (Kelley et al., 2002). In Fig. 15, we invoke the surface reactions in Eqs. (9), and (13-14) to predict the surface adsorption of aspartate in Lost City vent fluids at 25 ºC and 1 bar, where the major ions Na^{+}, Cl^{-}, Ca^{2+} and SO_4^{2-} are reported by Kelley and coworkers (2002). Surface adsorption is predicted at pH values of 9.8 and 10.2. In both cases, we predict that aspartate surface adsorption in the presence of the Lost City vent fluids are analogous to what we have observed in the high Ca^{2+} experiments, although at relatively high aspartate concentrations, surface adsorption continues to steadily increase rather than flatten: it is 1.8 $\mu mol \bullet m^{-2}$ at a pH of 10.2 and 3.6 $\mu mol \bullet m^{-2}$ at a pH of 9.8 when $[Asp]_0$ is equal to 300 μM.

The predictions made for aspartate adsorption in the presence of the Lost City vent fluids are at ambient conditions. However, it is possible that the ETLM predictions could be extrapolated to higher temperatures in future studies if experiments are conducted under more plausible hydrothermal temperatures and pressures. It also may be that vent fluids in a Lost City–type hydrothermal field may mix with cold seawater to approximately ambient temperatures. This low-temperature environment may hold an ideal Ca^{2+}/Mg^{2+} ratio that may promote favorable aspartate adsorption onto brucite. Moreover, aspartate or any of its aqueous species might more readily form in this type of environment due to the disequilibria from the mixing of different fluids (Shock and Canovas, 2010). Therefore, the results both observed and predicted in this study appear to be highly relevant for natural serpentinite-hosted hydrothermal systems.

4. Concluding Remarks

In this study, we performed batch adsorption experiments to evaluate the adsorption of aspartate onto brucite under conditions relevant to low-temperature serpentinite-hosted hydrothermal systems. We studied low Mg^{2+} ($0.7x10^{-3}$ M), high Mg^{2+} ($5.2x10^{-3}$ M), low Ca^{2+} ($1x10^{-3}$ M), and high Ca^{2+} ($4x10^{-3}$ M) concentrations at 25º C and 1 bar. Results indicated that aspartate adsorption increases with the addition of Ca^{2+}, whereas it decreases with the addition of Mg^{2+}. We used the extended triple-layer model to characterize the adsorption of aspartate onto the brucite surface. A total of three surface reactions were proposed to describe the data. One reaction involves a bidentate mononuclear surface species attaching through the α- and γ-carboxylate groups, which can be thought of as adopting a “leaning” configuration on the surface. A second reaction requires the formation of a calcium-aspartate complex. This complex may attach as a monodentate outer-sphere species through an electrostatic interaction between the calcium atom and a negatively-charged brucite surface site. The third reaction involves the adsorption of a hydrated calcium complex onto the positively-charged surface through a hydrogen bond as a monodentate outer-sphere species.

We tested the surface complexation model against the data collected at four different ionic strengths, variable initial aspartate concentrations, and different pH conditions, depending on the amount of Mg^{2+} in the system. Additionally, we fit data for calcium adsorption as a function of initial aspartate concentration. In each case, the surface reactions we proposed with the ETLM are consistent within the estimated experimental uncertainties. The success of these comparisons provides strong support for the use of the three surface reactions for aspartate and calcium adsorption onto brucite in a surface complexation model.

The decrease of aspartate adsorption with the addition of Mg^{2+} reflects the decrease in particle surface charge, predicted by the ζ-potential, and the unfavorable interaction between a negatively-charged aspartate molecule and a negatively-charged surface. The significant increase in aspartate adsorption with Ca^{2+} is a result of the favorable adsorption of calcium onto brucite and the formation of the cooperative calcium-aspartate complex that binds as an outer-sphere species onto the surface. This conclusion is indicated by the predominance of the calcium-aspartate outer-sphere species over the “leaning” species at both Ca^{2+} concentrations. As a result of a large amount of calcium adsorption, the brucite particle surface charge becomes positive, as indicated by the ζ-potential. The characterization of aspartate adsorption onto brucite with both batch adsorption experiments and surface complexation modeling has better elucidated the behavior of the brucite-water interface and brucite-aspartate interactions. Furthermore, we suggest that our experimental results are relevant to serpentinite-hosted hydrothermal vents, a plausible early Earth environment. It can be expected that such an environment may strongly favor aspartate adsorption on brucite. In this way, the result of this work contributes to a fundamental understanding of the role of the brucite-water interface in the emergence of complex biochemistry and the geochemical origin of life.

Acknowledgements

We would like to thank Cécile Feuillie, Namhey Lee, Alyssa K. Adcock, Timothy Strobel, Dionysis Foustoukos, Paul Goldey, John Armstrong, Adrian Villegas-Jimenez, Stephen Hodge and Steven Coley for their invaluable expertise and advice throughout this project. We thank the National Science Foundation, the NASA Astrobiology Institute, the Deep Carbon Observatory, and the Carnegie Institution for Science for support of this research.

References

Ali Ahmad M., Prélot B., Razafitianamaharavo A., Douillard J.-M., Zajac J., Dufour F., Durupthy O., Chanéac C. and Villiéras F. (2012) Influence of morphology and crystallinity on surface reactivity of nanosized anatase TiO2 studied by adsorption techniques. 1. The use of gaseous molecular probes. *J. Phys. Chem., C* **116**, 24596–24606.

Bach W., Paulick H., Garrido C. J., Ildefonse B., Meurer W. P. and Humphris S. E. (2006) Unraveling the sequence of serpentinization reactions: Petrography, mineral chemistry, and petrophysics of serpentinites from MAR 15°N (ODP Leg 209, Site 1274). *Geophys. Res. Lett.* **33**.

Baross J. A. and Hoffman S. E. (1985) Submarine hydrothermal vents and associated gradient environments as sites for the origin and evolution of life. *Orig. Life Evol. Biosph.* **15**, 327–345.

Clarke A. P., Jandik P., Rocklin R. D., Liu Y. and Avdalovic N. (1999) An integrated amperometry waveform for the direct, sensitive detection of amino acids and amino sugars following anion-exchange chromatography. *Anal. Chem.* **71**, 2774–2781.

Cleaves H. J., Chalmers J. H., Lazcano A., Miller S. L. and Bada J. L. (2008) A reassessment of prebiotic organic synthesis in neutral planetary atmospheres. *Orig. Life Evol. Biosph.* **38**, 105–115.

Cleaves H. J., Michalkova Scott A., Hill F. C., Leszczynski J., Sahai N. and Hazen R. M. (2012) Mineral–organic interfacial processes: Potential roles in the origins of life. *Chem. Soc. Rev.* **41**, 5502-5525.

De Robertis A., De Stefano C. and Gianguzza A. (1991) Salt effects on the protonation of L-histidine and L-aspartic acid: A complex formation model. *Thermochim Acta* **177**, 39–57.

Deamer D. and Pashley R. M. (1989) Amphiphilic Components of the Murchison Carbonaceous Chondrite - Surface-Properties and Membrane Formation. *Origins Life Evol B* **19**, 21–38.

Dymek R. F., Brothers S. C. and Schiffries C. M. (1988) Petrogenesis of ultramafic metamorphic rocks from the 3800 Ma Isua Supracrustal Belt, West Greenland. *J. Petrol.* **29**, 1353–1397.

Eypert-Blaison C., Villiéras F., Michot L. J., Pelletier M., Humbert B., Ghanbaja J. and Yvon J. (2002) Surface heterogeneity of kanemite, magadiite and kenyaite: a high-resolution gas adsorption study. *Clay Miner.* **37**, 531–542.

Farr J. D., Neu M. P., Schulze R. K. and Honeyman B. D. (2007) Plutonium uptake by brucite and hydroxylated periclase. *J. Alloy. Compd.* **444-445**, 533–539.

Farr J. D., Schulze R. K. and Honeyman B. D. (2000) Aqueous Pu (IV) sorption on brucite. *Radiochim. Acta* **88**, 675–680.

Franchi M., Ferris J. P. and Gallori E. (2003) Cations as mediators of the adsorption of nucleic acids on clay surfaces in prebiotic environments. *Orig. Life Evol. Biosph.* **33**, 1–16.

Geiger F. M. (2009) Second Harmonic Generation, Sum Frequency Generation, and χ (3): Dissecting environmental interfaces with a nonlinear optical swiss army knife. *Annu. Rev. Phys. Chem.* **60**, 61–83.

Giacomelli C. E., Avena M. J. and De Pauli C. P. (1995) Aspartic acid adsorption onto TiO_2 particles surface. Experimental data and model calculations. *Langmuir* **11**, 3483–3490.

Goldschmidt V. M. (1952) Geochemical aspects of the origin of complex organic molecules on the Earth, as precursors to organic life. *New Biol.* **12**, 97–105.

Greiner E., Kumar K., Sumit M., Giuffre A., Zhao W., Pedersen J. and Sahai N. (2014) Adsorption of L-glutamic acid and L-aspartic acid to γ-Al_2O_3. *Geochim. Cosmochim. Acta* **133**, 142–155.

Hazen R. M. (2005) *Genesis: The Scientific Quest for Life's Origin*, Joseph Henry Press, Washington, DC.

Hazen R. M. (2006) Presidential address to the Mineralogical Society of America, Salt Lake City, October 18, 2005: Mineral surfaces and the prebiotic selection and organization of biomolecules. *Am. Mineral.* **91**, 1715–1729.

Hazen R. M., Filley T. and Goodfriend G. (2001) Selective adsorption of L- and D-amino acids on calcite: Implications for biochemical homochirality. *PNAS* **98**, 5487–5490.

Hennet R., Holm N. G. and Engel M. H. (1992) Abiotic synthesis of amino-acids under hydrothermal conditions and the origin of life - a perpetual phenomenon. *Naturwissenschaften* **79**, 361–365.

Henrist C., Mathieu J., Vogels C., Rulmont A. and Cloots R. (2003) Morphological study of magnesium hydroxide nanoparticles precipitated in dilute aqueous solution. *J. Cryst. Growth* **249**, 321–330.

Herzberg C., Condie K. and Korenaga J. (2010) Thermal history of the Earth and its petrological expression. *Earth Planet. Sci. Lett.* **292**, 79–88.

Holm N. G. (2012) The significance of Mg in prebiotic geochemistry. *Geobiology* **10**, 269–279.

Holm N. G. and Andersson E. (2005) Hydrothermal simulation experiments as a tool for studies of the origin of life on earth and other terrestrial planets: A review.

Astrobiology **5**, 444–460.

Holm N. G., Dumont M., Ivarsson M. and Konn C. (2006) Alkaline fluid circulation in ultramafic rocks and formation of nucleotide constituents: a hypothesis. *Geochem. Trans.* **7**, 1–13.

Hostetler P. B. (1963) The stability and surface energy of brucite in water at 25 degrees C. *Am. J. Sci.* **261**, 238–258.

Ikhsan J., Johnson B. B., Wells J. D. and Angove M. J. (2004) Adsorption of aspartic acid on kaolinite. *J. Colloid Interface Sci.* **273**, 1–5.

Jalbout A. F., Abrell L., Adamowicz L., Polt R., Apponi A. J. and Ziurys L. M. (2007) Sugar synthesis from a gas-phase formose reaction. *Astrobiology* **7**, 433–442.

Jandik P., Pohl C., Barreto V. and Avdalovic N. (2000) Anion exchange chromatography and integrated amperometric detection of amino acids. In *Amino acid analysis protocols* Humana Press, New Jersey. pp. 63–85.

Jensen D., Weiss J., Rey M. A. and Pohl C. A. (1993) Novel weak acid cation-exchange column. *J. Chromatogr., A* **640**, 65–71.

Jonsson C. M., Jonsson C. L., Estrada C. F., Sverjensky D. A., Cleaves H. J. II and Hazen R. M. (2010) Adsorption of L-aspartate to rutile (α-TiO_2): Experimental and theoretical surface complexation studies. *Geochim. Cosmochim. Acta* **74**, 2356–2367.

Jonsson C. M., Jonsson C. L., Sverjensky D. A., Cleaves H. J. and Hazen R. M. (2009) Attachment of L-glutamate to rutile (α-TiO_2): A potentiometric, adsorption, and surface complexation Study. *Langmuir* **25**, 12127–12135.

Jordan G. and Rammensee W. (1996) Dissolution rates and activation energy for dissolution of brucite (001): A new method based on the microtopography of crystal surfaces. *Geochim. Cosmochim. Acta* **60**, 5055–5062.

Kelley D. S., Baross J. A. and Delaney J. R. (2002) Volcanoes, fluids, and life at mid-ocean ridge spreading centers. *Annu. Rev. Earth Planet. Sci.* **30**, 385–491.

Kelley D. S., Karson J. A., Fruh-Green G. L., Yoerger D. R., Shank T. M., Butterfield D. A., Hayes J. M., Schrenk M. O., Olson E. J., Proskurowski G., Jakuba M., Bradley A., Larson B., Ludwig K., Glickson D., Buckman K., Bradley A.S., Brazelton W.J., Roe K., Elend M.J., Delacour A., Bernasconi S.M., Lilley M.D., Baross J.A., Summons R.T., and Sylva S.P. (2005) A serpentinite-hosted ecosystem: the Lost City hydrothermal field. *Science* **307**, 1428-1434.

Kelley D. S., Karson J., Blackman D., Frueh-Green G., Butterfield D., Lilley M., Olson E., Schrenk M., Roe K., Lebon G., Rivizzigno P., and the AT3-60 Shipboard Party (2001) An off-axis hydrothermal vent field near the Mid-Atlantic Ridge at 30 degrees N. *Nature* **412**, 145–149.

Kim H.-J., Ricardo A., Illangkoon H. I., Kim M. J., Carrigan M. A., Frye F. and Benner S. A. (2011) Synthesis of carbohydrates in mineral-guided prebiotic cycles. *J. Am. Chem. Soc.* **133**, 9457–9468.

Klevenz V., Sumoondur A., Ostertag-Henning C. and Koschinsky A. (2010) Concentrations and distributions of dissolved amino acids in fluids from Mid-Atlantic Ridge hydrothermal vents. *Geochem. J.* **44**, 387.

Koretsky C. M., Sverjensky D. A. and Sahai N. (1998) A model of surface site types on oxide and silicate minerals based on crystal chemistry; implications for site types and densities, multi-site adsorption, surface infrared spectroscopy, and dissolution kinetics. *Am. J. Sci.* **298**, 349–438.

Kudoh Y., Kameda J. and Kogure T. (2006) Dissolution of brucite on the (001) surface at neutral pH: In situ atomic force microscopy observations. *Clay Clay Miner.* **54**, 598–604.

Liu X., Cheng J., Sprik M., Lu X. and Wang R. (2013) Understanding surface acidity of gibbsite with first principles molecular dynamics simulations. *Geochim. Cosmochim. Acta* **120**, 487–495.

Lu J., Qiu L. and Qu B. (2004) Controlled growth of three morphological structures of magnesium hydroxide nanoparticles by wet precipitation method. *J. Cryst. Growth* **267**, 676–684.

Malin J. N., Holland J. G. and Geiger F. M. (2009) Free energy relationships in the electric double layer and alkali earth speciation at the fused silica/water interface. *J. Phys. Chem., C* **113**, 17795–17802.

McCollom T. M. and Bach W. (2009) Thermodynamic constraints on hydrogen generation during serpentinization of ultramafic rocks. *Geochim. Cosmochim. Acta* **73**, 856–875.

Meléndez-Hevia E., Waddell T. G. and Cascante M. (1996) The puzzle of the Krebs citric acid cycle: Assembling the pieces of chemically feasible reactions, and opportunism in the design of metabolic pathways during evolution. *J. Mol. Evol.* **43**, 293–303.

Michot L. J. and Villiéras F. (2002) Assessment of surface energetic heterogeneity of synthetic Na-saponites. The role of layer charge. *Clay Miner.* **37**, 39–57.

Noffke N., Christian D., Wacey D. and Hazen R. M. (2013) Microbially induced sedimentary structures recording an ancient ecosystem in the ca. 3.48 billion-year-old Dresser Formation, Pilbara, Western Australia. *Astrobiology* **13**, 1103–1124.

Palmer D. (2009) CrystalMaker for Mac OS X, 8.2. 2. *CrystalMaker Software Limited: Oxfordshire*.

Perronnet M., Villiéras F., Jullien M., Razafitianamaharavo A., Raynal J. and Bonnin D. (2007) Towards a link between the energetic heterogeneities of the edge faces of smectites and their stability in the context of metallic corrosion. *Geochim. Cosmochim. Acta* **71**, 1463–1479.

Pokrovsky O. S. and Schott J. (2004) Experimental study of brucite dissolution and precipitation in aqueous solutions: surface speciation and chemical affinity control. *Geochim. Cosmochim. Acta* **68**, 31–45.

Pokrovsky O. S., Schott J. and Castillo A. (2005) Kinetics of brucite dissolution at 25°C in the presence of organic and inorganic ligands and divalent metals. *Geochim. Cosmochim. Acta* **69**, 905–918.

Ponnamperuma C. and Pering K. (1966) Possible abiogenic origin of some naturally occurring hydrocarbons. *Nature* **209**, 979–982.

Prélot B., Villiéras F., Pelletier M., Gérard G., Gaboriaud F., Ehrhardt J.-J., Perrone J., Fedoroff M., Jeanjean J., Lefèvre G., Mazerolles L., Pastol J.-L., Rouchaud J.-C. and Lindecker C. (2003) Morphology and surface heterogeneities in synthetic goethites. *J. Colloid Interface Sci.* **261**, 244–254.

Proskurowski G., Lilley M. D., Kelley D. S. and Olson E. J. (2006) Low temperature volatile production at the Lost City Hydrothermal Field, evidence from a hydrogen stable isotope geothermometer. *Chem. Geol.* **229**, 331–343.

Roddick-Lanzilotta A. D. and McQuillan A. J. (2000) An in situ Infrared spectroscopic study of glutamic acid and of aspartic acid adsorbed on TiO_2: Implications for the biocompatibility of titanium. *J. Colloid Interface Sci.* **227**, 48–54.

Sahai N. and Sverjensky D. A. (1998) GEOSURF: A computer program for modeling adsorption on mineral surfaces from aqueous solution. *Comput. Geosci.* **24**, 853–873.

Sahai N. and Sverjensky D. A. (1997) Solvation and electrostatic model for specific electrolyte adsorption. *Geochim. Cosmochim. Acta* **61**, 2827–2848.

Sayed-Hassan M., Villiéras F., Gaboriaud F. and Razafitianamaharavo A. (2006) AFM and low-pressure argon adsorption analysis of geometrical properties of phyllosilicates. *J. Colloid Interface Sci.* **296**, 614–623.

Sayed-Hassan M., Villiéras F., Razafitianamaharavo A. and Michot L. J. (2005) Role of exchangeable cations on geometrical and energetic surface heterogeneity of kaolinites. *Langmuir* **21**, 12283–12289.

Schott H. (1981) Electrokinetic studies of magnesium hydroxide. *J. Pharm. Sci.* **70**, 486–489.

Shibuya T., Komiya T., Nakamura K., Takai K. and Maruyama S. (2010) Highly alkaline, high-temperature hydrothermal fluids in the early Archean ocean.

Precambrian Res. **182**, 230–238.

Shock E. L. and Canovas P. (2010) The potential for abiotic organic synthesis and biosynthesis at seafloor hydrothermal systems. *Geofluids* **10**, 161–192.

Shock E. L. and Schulte M. D. (1998) Organic synthesis during fluid mixing in hydrothermal systems. *J. Geophys. Res.* **103**, 28513.

Sleep N. H., Bird D. K. and Pope E. C. (2011) Serpentinite and the dawn of life. *Philos. Trans. R. Soc. Lond., B* **366**, 2857–2869.

Stevanovic S., AliAhmad M., Razafitianamaharavo A., Villiéras F., Odile B., Prélot B., Zajac J., Douillard J.-M. and Chanéac C. (2010) Evidences for the relationship between surface structure and reactivity of goethite nanoparticles based on advanced molecular-probe methods. *Adsorption* **16**, 185–195.

Sverjensky D. A. (2005) Prediction of surface charge on oxides in salt solutions: Revisions for 1:1 (M+L−) electrolytes. *Geochim. Cosmochim. Acta* **69**, 225–257.

Sverjensky D. A. (2003) Standard states for the activities of mineral surface sites and species. *Geochim. Cosmochim. Acta* **67**, 17–28.

Sverjensky D. A. and Fukushi K. (2006) A predictive model (ETLM) for As(III) adsorption and surface speciation on oxides consistent with spectroscopic data. *Geochim. Cosmochim. Acta* **70**, 3778–3802.

Sverjensky D. A. and Sahai N. (1996) Theoretical prediction of single-site surface-protonation equilibrium constants for oxides and silicates in water. *Geochim. Cosmochim. Acta* **60**, 3773–3797.

Tournassat C., Neaman A., Villiéras F., Bosbach D. and Charlet L. (2003) Nanomorphology of montmorillonite particles: Estimation of the clay edge sorption site density by low-pressure gas adsorption and AFM observations. *Am. Mineral.* **88**, 1989–1995.

Van Kranendonk M. J. (2010) Two types of Archean continental crust: Plume and plate tectonics on early Earth. *Am. J. Sci.* **310**, 1187–1209.

Van Kranendonk M. J., Hugh Smithies R., Hickman A. H. and Champion D. C. (2007) Review: secular tectonic evolution of Archean continental crust: Interplay between horizontal and vertical processes in the formation of the Pilbara Craton, Australia. *Terra Nova* **19**, 1–38.

Villiéras F., Cases J. M., François M., Michot L. J. and Thomas F. (1992) Texture and surface energetic heterogeneity of solids from modeling of low pressure gas adsorption isotherms. *Langmuir* **8**, 1789–1795.

Villiéras F., Michot L. J., Bardot F., Cases J. M., François M. and Rudziński W. (1997)

An improved derivative isotherm summation method to study surface heterogeneity of clay minerals. *Langmuir* **13**, 1104–1117.

Villiéras F., Michot L. J., Bardot F., Chamerois M., Eypert-Blaison C., François M., Gérard G. and Cases J.-M. (2002) Surface heterogeneity of minerals. *C. R. Geosci.* **334**, 597–609.

Wächtershäuser G. (1990) Evolution of the first metabolic cycles. *PNAS* **87**, 200–204.

Wu W.-X., Shao L., Chen J.-F. and Lu S.-C. (2007) Investigation on mechanisms of Cu^{2+} immobilization by brucite. *Fresen. Environ. Bull.* **16**, 29–33.

Fig. 1. SEM image of synthesized brucite (a) before hydrothermal treatment where oblong platelets are clustered in rosettes and (b) after hydrothermal treatment where platelets are hexagonal in lamellar clusters (scale= 1 μM).

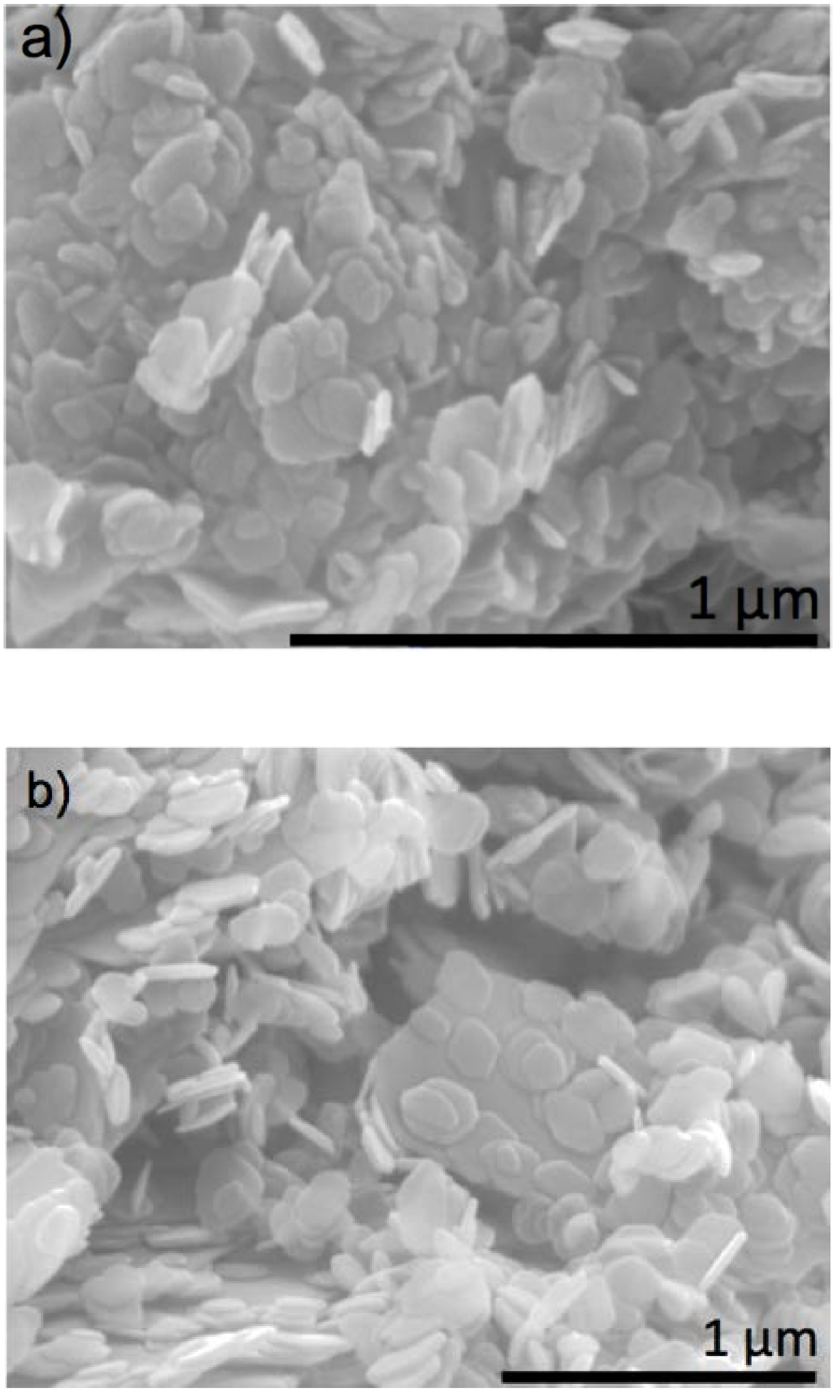

Fig. 2. Power XRD pattern of synthesized brucite that has been untreated (blue) and hydrothermally treated (black). *(hkl)* reflections are indexed by the red symbols.

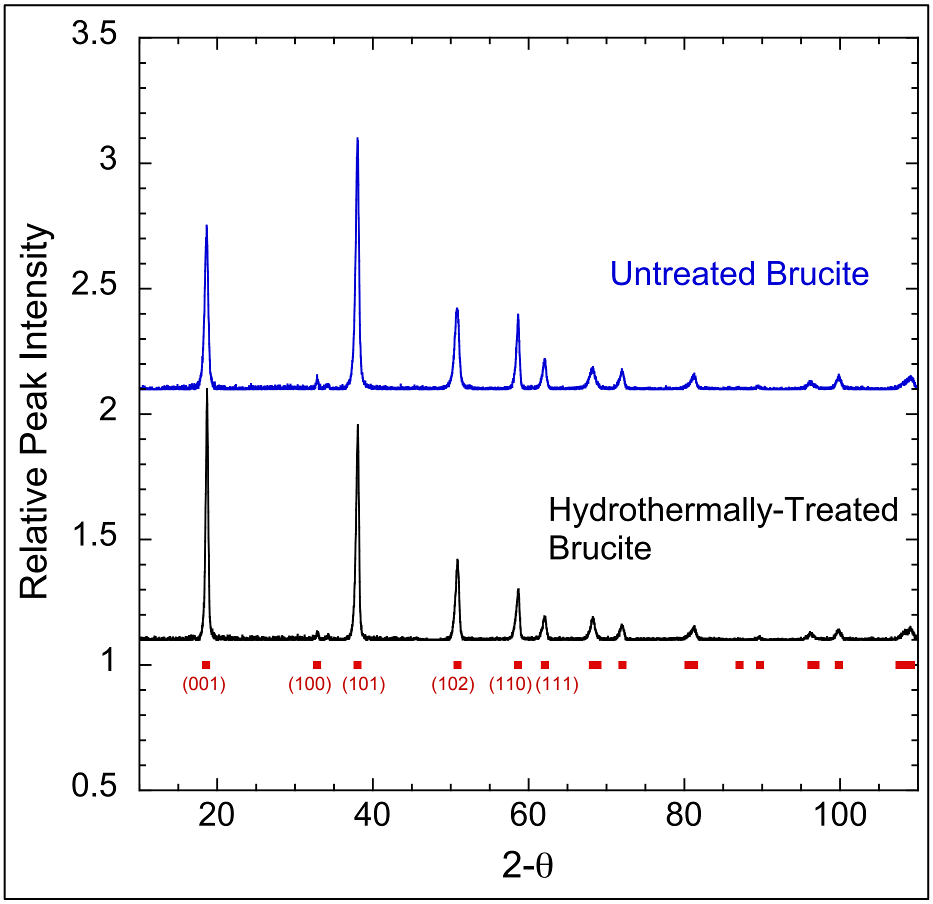

Fig. 3. Experimental derivative argon adsorption obtained at 77 K for brucite plotted against relative pressure for simulated isotherms using the derivative isotherm summation (DIS) method. The full gray line represents the experimentally obtained curve, the black-dotted line is the calculated curve, and the dotted lines are the adsorption domains obtained with the DIS procedure. Domains 1 and 2 are attributed to the basal faces, and domains 3 and 4 are attributed to lateral faces.

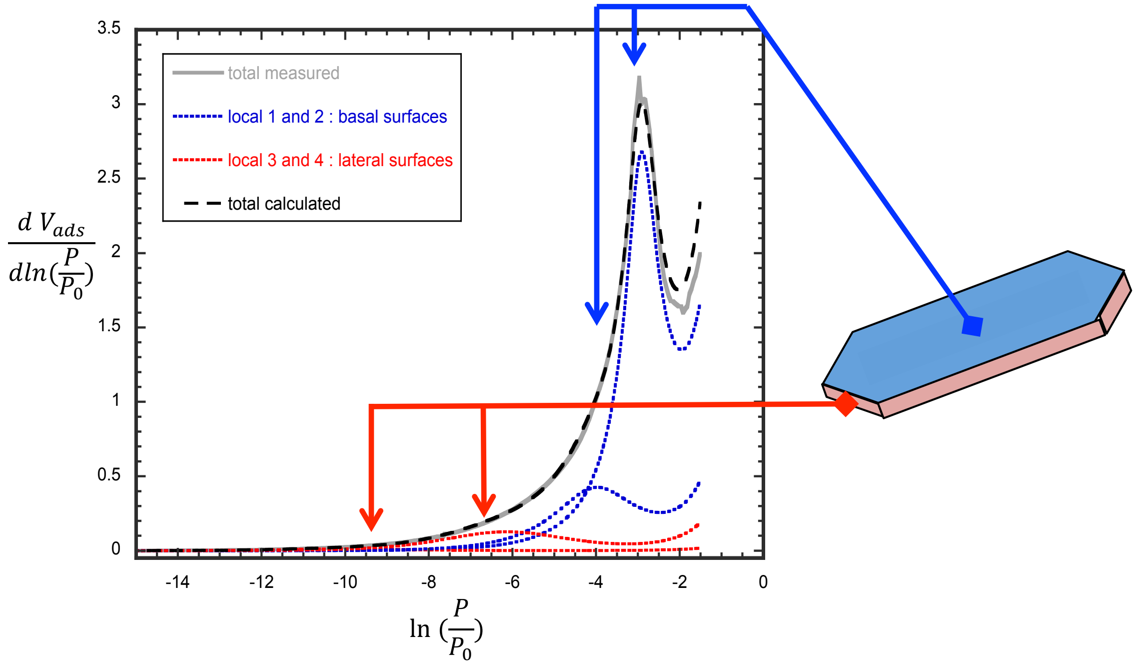

Fig. 4. Surface titration data of brucite at 25ºC as function of pH determined by Pokrovsky et al. (2004). Red data symbols represent experimental data collected at 1.0 M NaCl and blue data symbols represent data collected at 1.0 x10^{-2} M NaCl. Dashed curves are calculated fits to the experimental data using the ETLM. $\log K_1$= 10.0, $\log K_2$= 12.0, $\log K^*_{Na^+}$= -9.6, $\log K^*_{Cl^-}$= -12.2, A_s= 9.2 $m^2 \cdot g^{-1}$ and N_s=10 sites•nm^{-2}.

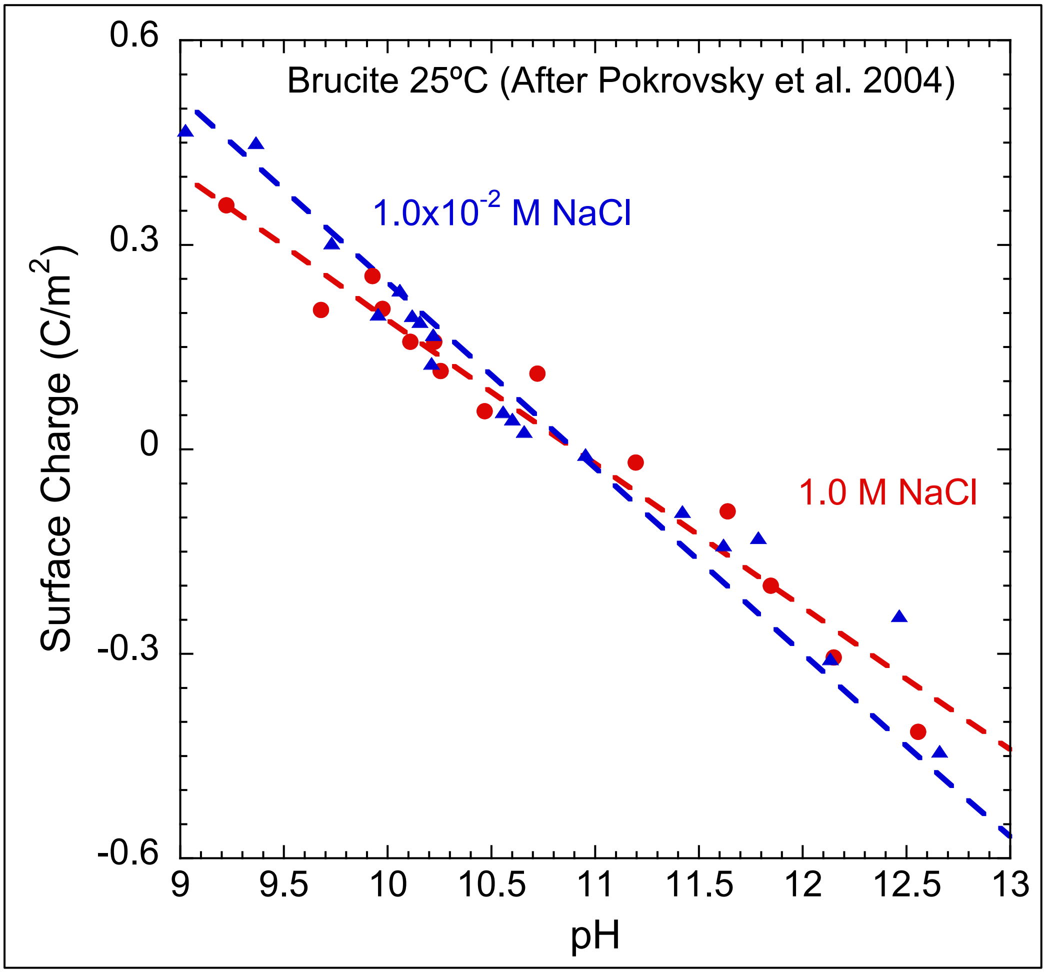

Fig. 5. (a) Adsorption of aspartate on brucite as a function of aspartate concentration remaining in solution in the presence of a low Mg^{2+} concentration (Mg^{2+}=$0.7x10^{-3}$ M) and (b) theoretical model of aspartate adsorption at pH=10.3 (dashed curve) calculated using the parameters in Table 2. Symbols represent experimental data that are the average of a triplicate run and horizontal and vertical error bars are ±1 standard error from the average.

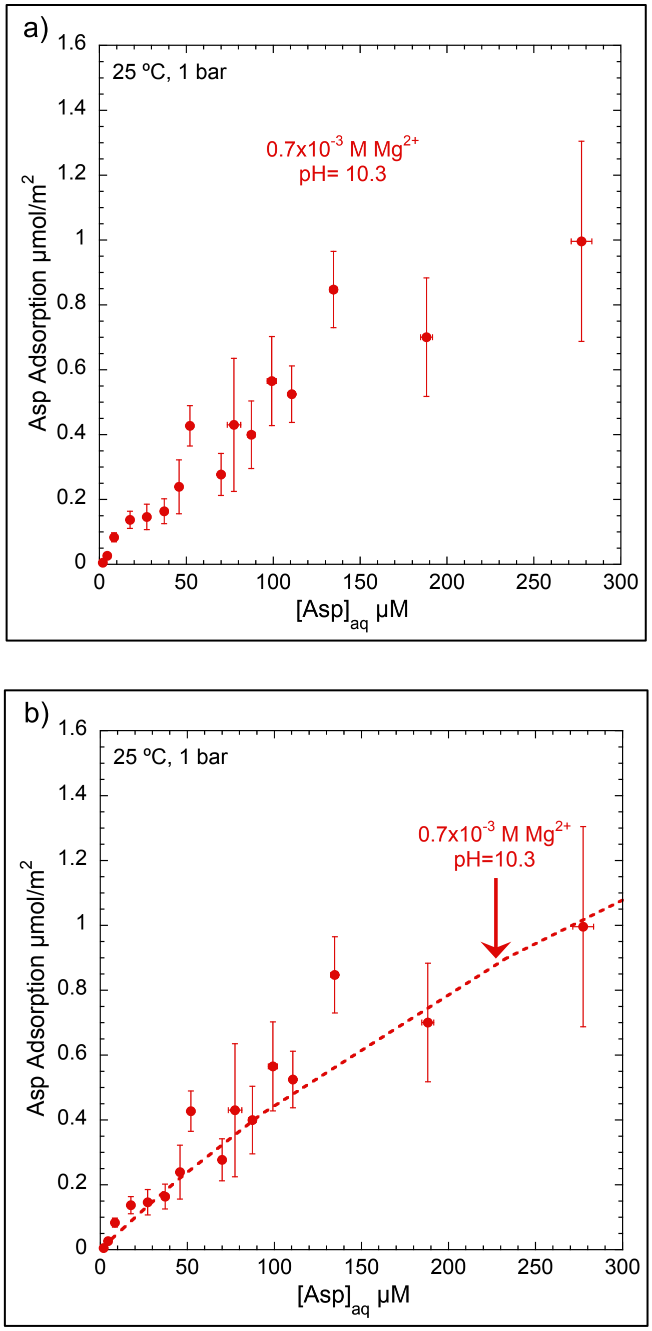

Fig. 6. Possible representation of the surface species predicted by surface complexation calculations using the parameters in Table 2 where aspartate attaches onto brucite as bidentate mononuclear, or "leaning" species. Aspartate attaches onto (100) brucite through a bond between a magnesium atom and the α-carboxylate group (>S-O-C) and a hydrogen bond between the γ-carboxylate group and a protonated surface site (>SOH···C=O). Red spheres represent oxygen, yellow spheres are magnesium, tan spheres are hydrogen, black spheres are carbon, and pale blue spheres are nitrogen atoms.

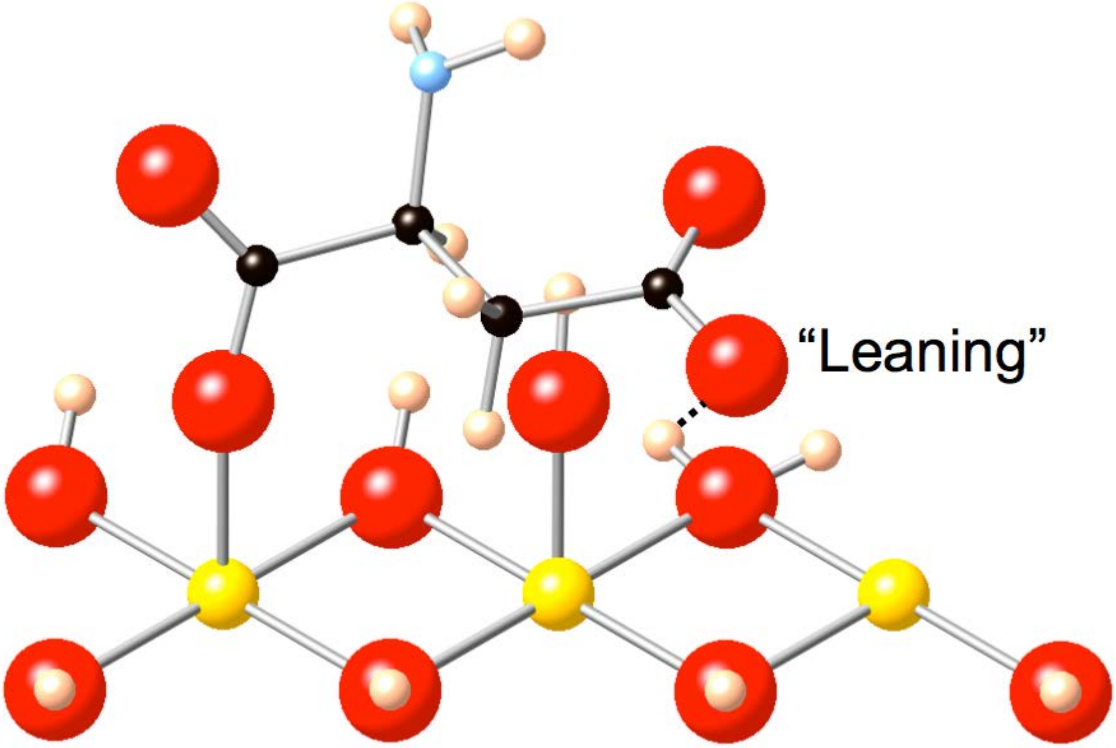

Fig. 7. Equilibrium constant, or log$[Mg^{2+}]/[H+]^2$ as a function of solution pH following brucite/water and brucite/aspartate batch experiments in the presence of (a) a low Mg^{2+} concentrations ($[Mg^{2+}]=0.7x10^{-3}$ M) and (b) both a low and high Mg^{2+} concentrations ($[Mg^{2+}]=0.7x10^{-3}$ M and $[Mg^{2+}]=5.8x10^{-3}$, respectively). The symbols represent experimental data and the vertical error bars are one standard deviation of each dataset.

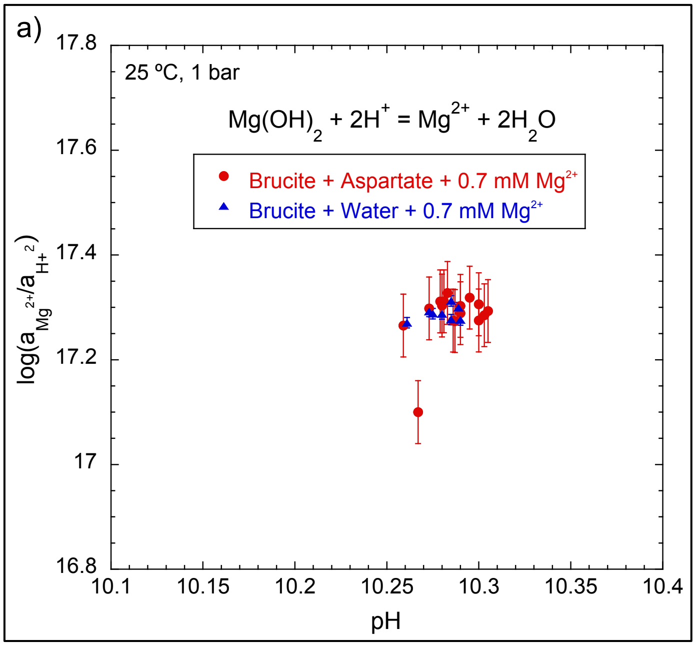

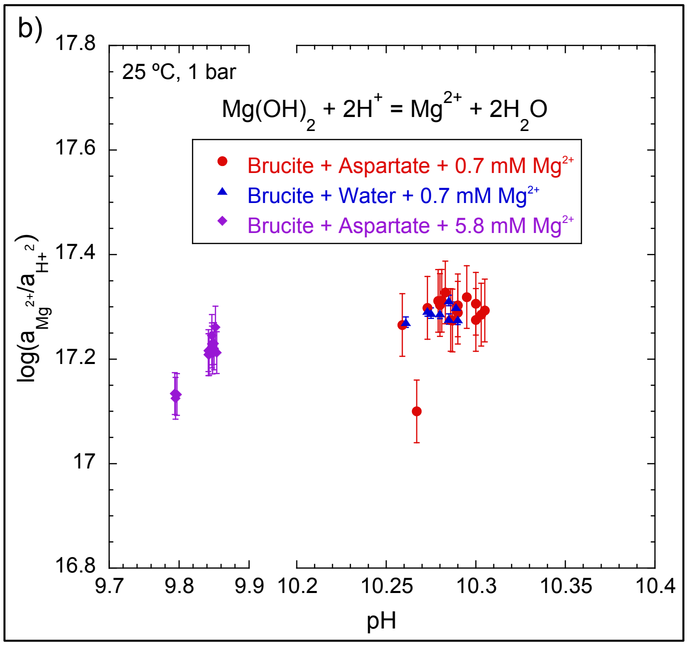

Fig. 8. (a) Adsorption of aspartate onto brucite as a function of aspartate concentration remaining in solution at low Mg^{2+} concentrations ($[Mg^{2+}]=0.7\times10^{-3}$ M) and high Mg^{2+} concentrations ($[Mg^{2+}]=5.8\times10^{-3}$ M) and (b) theoretical models of aspartate adsorption calculated with the parameters in Table 2 at the same electrolyte concentration and at pH= 10.3 and pH=9.9, respectively. Symbols represent the average of a triplicate of experimental data and horizontal and vertical error bars are ±1 standard error from the average. Dashed curves represent the model fits to the experimental data.

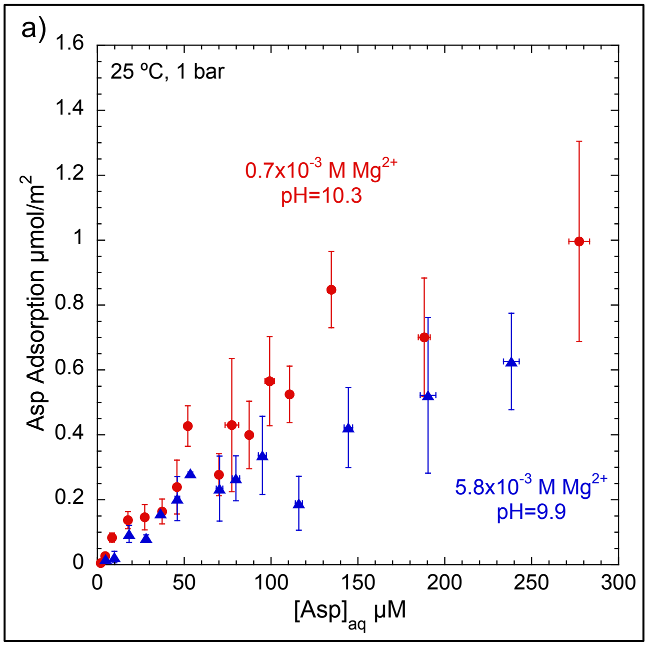

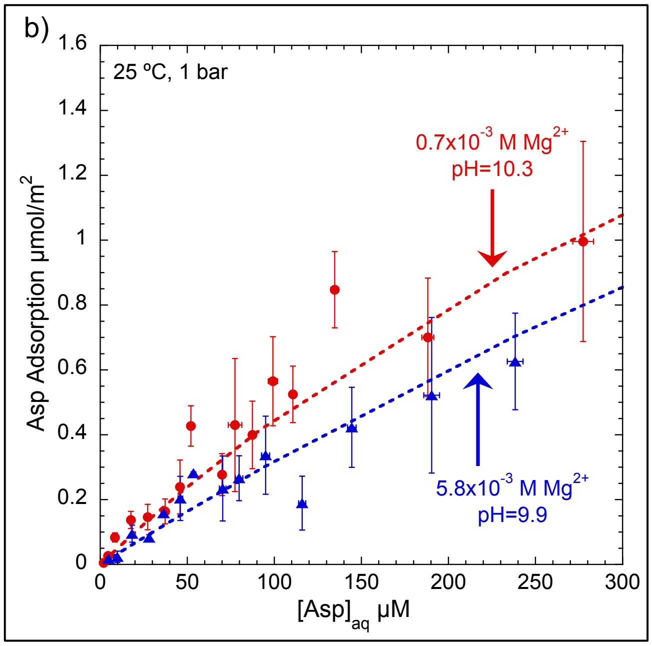

Fig. 9. (a) Adsorption of aspartate onto brucite as a function of aspartate concentration remaining in solution at low Ca^{2+} concentrations ($[Ca^{2+}]=1.0\text{x}10^{-3}$ M, $[Mg^{2+}]=0.9\text{x}10^{-3}$ M) and high Ca^{2+} concentrations ($[Ca^{2+}]=4.0\text{x}10^{-3}$ M, $[Mg^{2+}]=1.0\text{x}10^{-3}$ M) and (b) theoretical models of aspartate adsorption calculated with the parameters in Table 2 at low and high Ca^{2+} concentrations and pH=10.2 and pH=10.3, respectively. Symbols represent the average of a triplicate of experimental data and horizontal and vertical error bars are ±1 standard error from the average. Dashed curves represent the model fits to the experimental data.

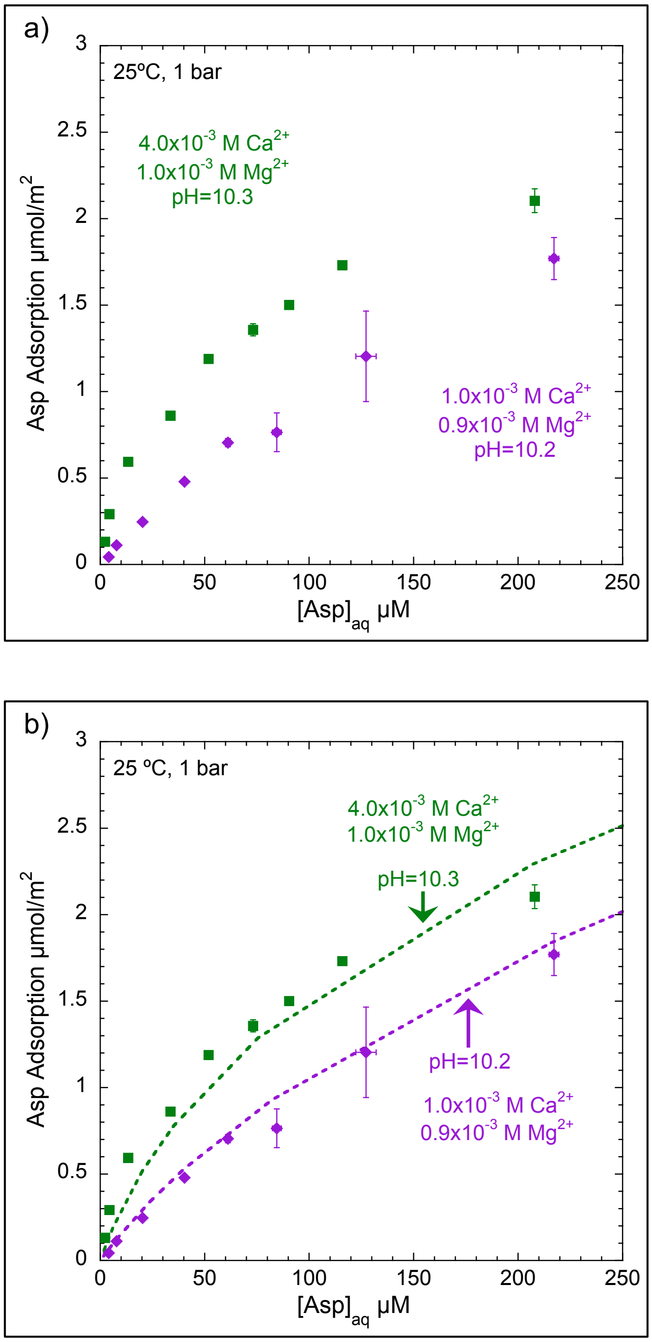

Fig. 10. (a) Adsorption of Ca^{2+} onto brucite as a function of initial aspartate concentration at low Ca^{2+} concentrations ($[Ca^{2+}]=1.0\times10^{-3}$ M, $[Mg^{2+}]=0.9\times10^{-3}$ M) high Ca^{2+} concentrations ($[Ca^{2+}]=4.0\times10^{-3}$ M, $[Mg^{2+}]=1.0\times10^{-3}$ M) and (b) theoretical models of Ca^{2+} adsorption calculated with the parameters in Table 2 at low and high Ca^{2+} concentrations at pH=10.2 and pH=10.3, respectively. Symbols represent experimental data and vertical error bars represent an error of 0.08. Dashed curves represent the model fits to the experimental data.

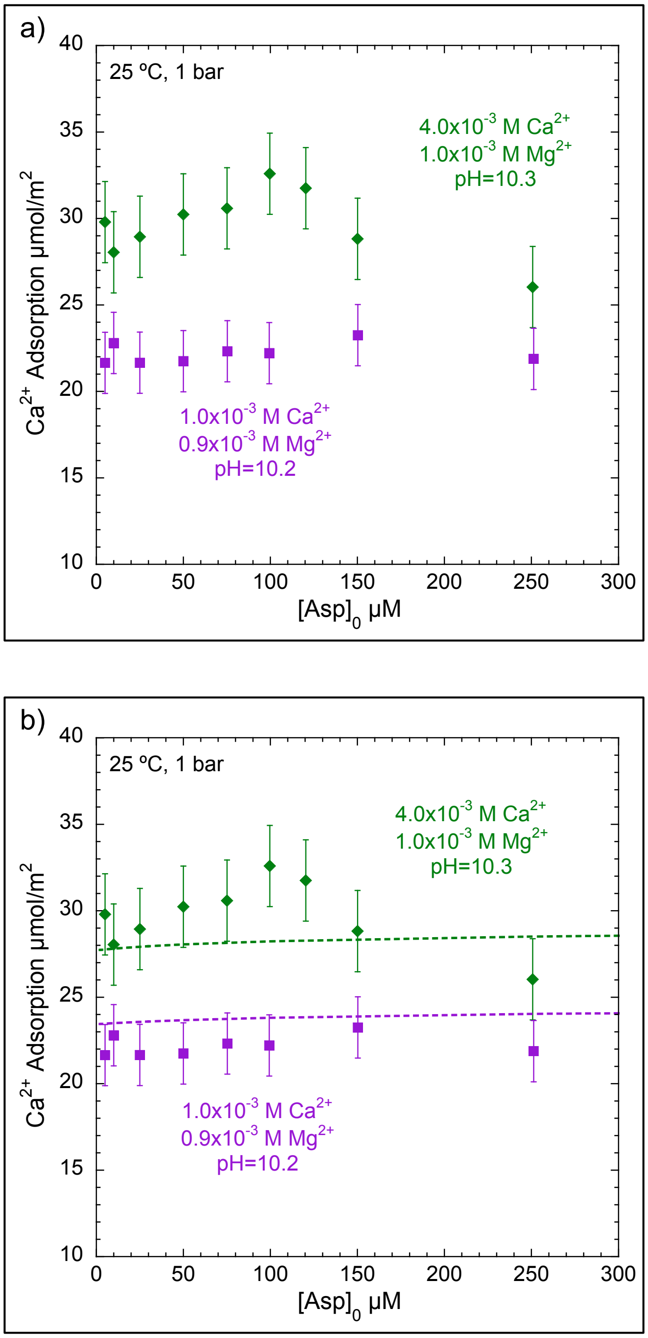

Fig. 11. Possible representation of surface species predicted by surface complexation calculations using the parameters in Table 2. (a) Attachment of a calcium-aspartate complex to the (100) surface forming a monodentate outer-sphere species through an electrostatic interaction between a surface oxygen atom and the calcium atom (>SO···Ca-O-C). (b) Attachment of a hydrated calcium molecule to the brucite surface forming a monodentate outer-sphere species through a hydrogen bond between a positively-charged surface site and the hydroxyl functional group (>SOH···OH-CaOH). Red spheres represent oxygen, yellow spheres are magnesium, tan spheres are hydrogen, large light blue spheres are calcium, small pale blue spheres are nitrogen and black spheres are carbon atoms.

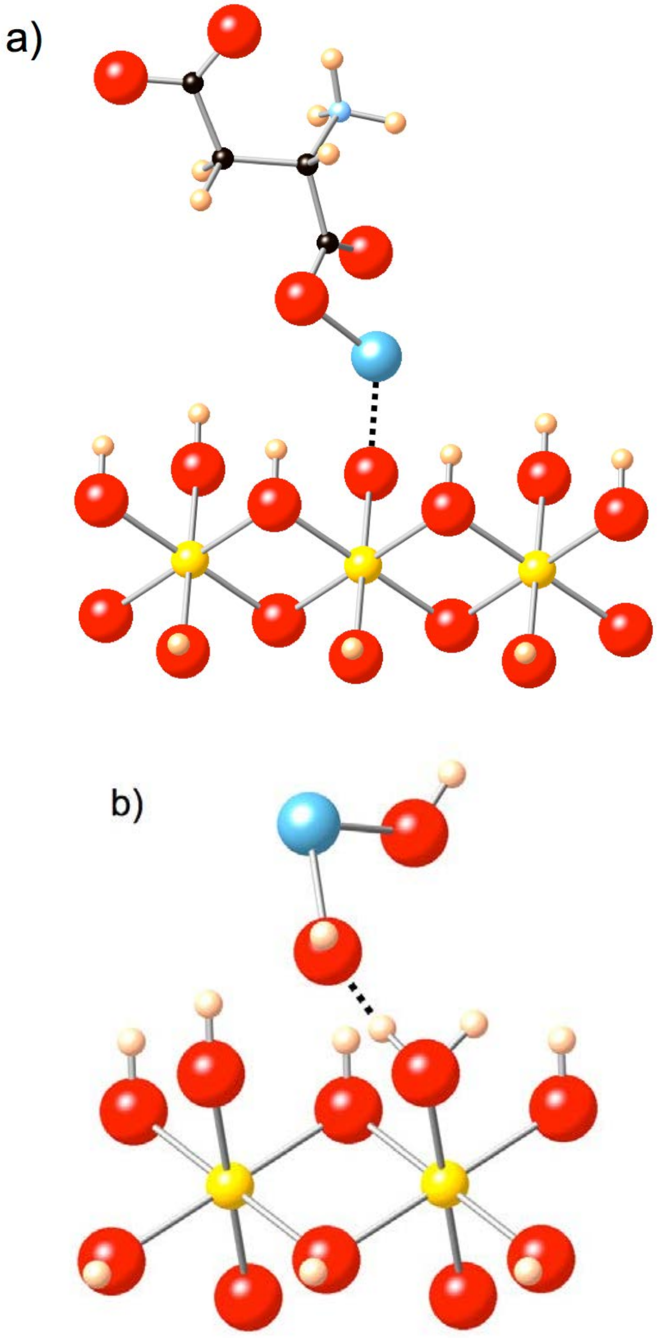

Fig. 12. ζ-potential (mv), or particle surface charge, predicted by surface complexation calculations with parameters in Table 2 as a function of initial aspartate concentration in the presence of a low Mg^{2+} concentrations ($[Mg^{2+}]=0.7x10^{-3}$ M, pH=10.3), high Mg^{2+} concentrations ($[Mg^{2+}]=5.8x10^{-3}$ M, pH=9.9), low Ca^{2+} concentrations ($[Ca^{2+}]=1.0x10^{-3}$ M, $[Mg^{2+}]=0.9x10^{-3}$ M, pH=10.2) and high Ca^{2+} concentrations ($[Ca^{2+}]= 4.0x10^{-3}$ M, $[Mg^{2+}]=1.0x10^{-3}$, pH=10.3). Dashed curves represent theoretical model predictions.

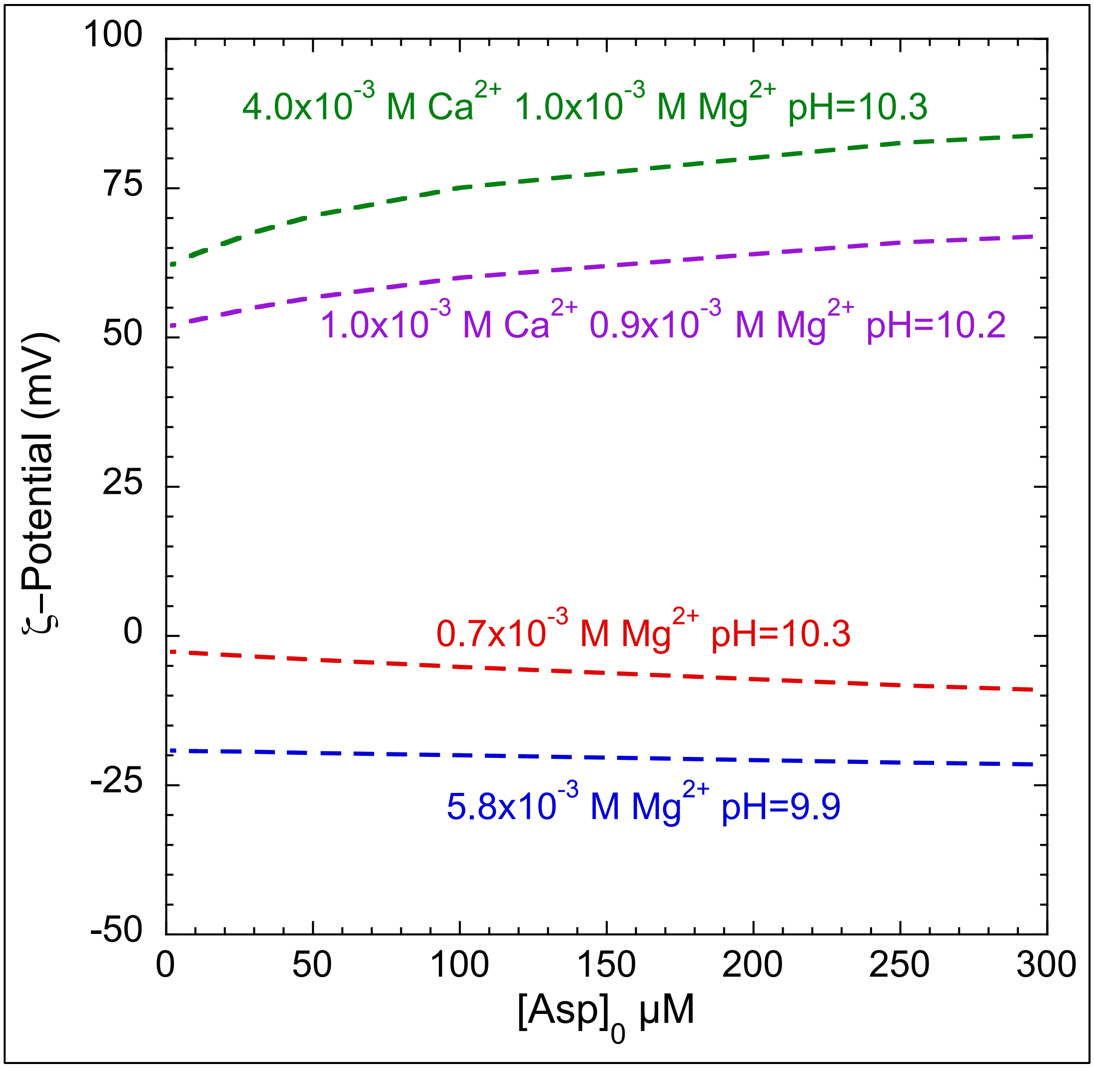

Fig. 13. Predicted surface speciation of aspartate on brucite as a function of initial aspartate concentration at (a) low Ca^{2+} concentrations ($[Ca^{2+}]=1.0\times10^{-3}$ M, $[Mg^{2+}]=0.9\times10^{-3}$ M, pH=10.2) and (b) high Ca^{2+} concentrations ($[Ca^{2+}]= 4.0\times10^{-3}$ M, $[Mg^{2+}]=1.0\times10^{-3}$, pH=10.3). The "leaning" and outer-sphere species refer to Fig. 6 and Fig. 10a, and reaction stoichiometries in Eqs. (7) and (11), respectively. Dashed curves represent the individual species and the solid curve represents the total aspartate adsorption.

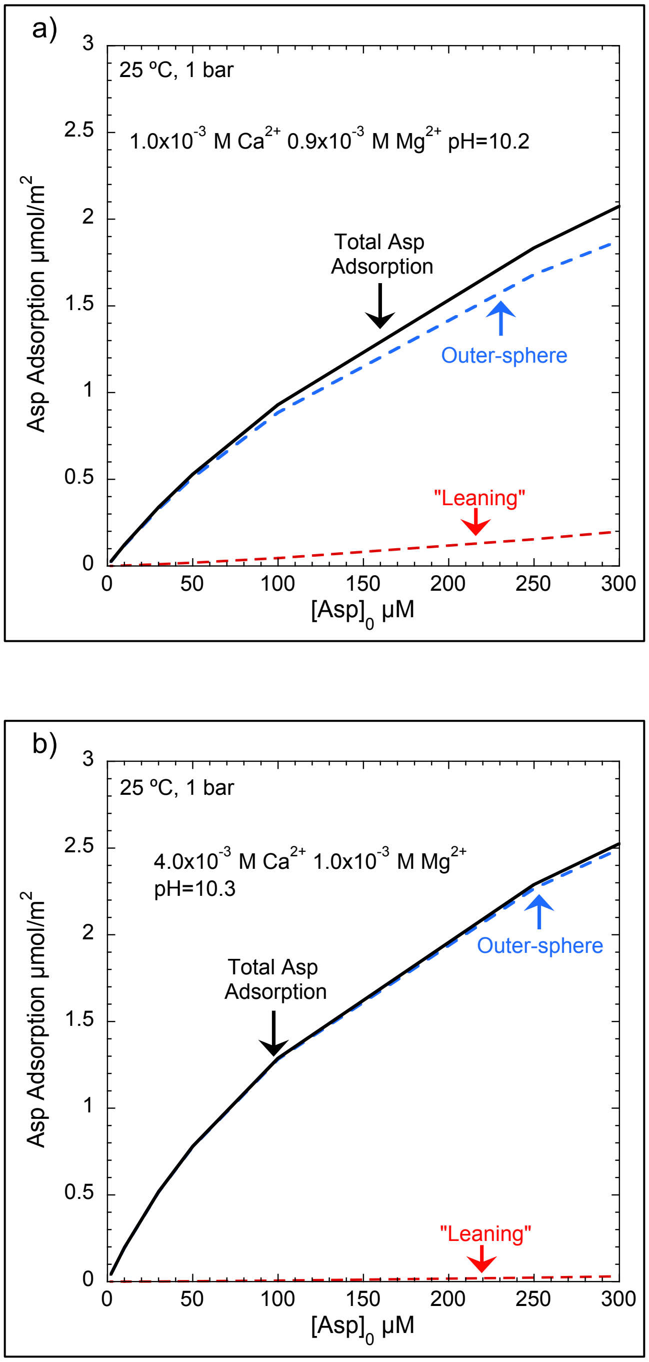

Fig. 14. Predicted distribution (%) of aspartate aqueous species that can be represented by calcium-aspartate complexes, including the species CaH_2Asp^{2+}, $CaHAsp^+$, and CaAsp as a function of initial aspartate concentration in the presence of a) low Ca^{2+} concentrations and b) high Ca^{2+} concentrations. Dashed curves indicate the predicted distribution for each aqueous species.

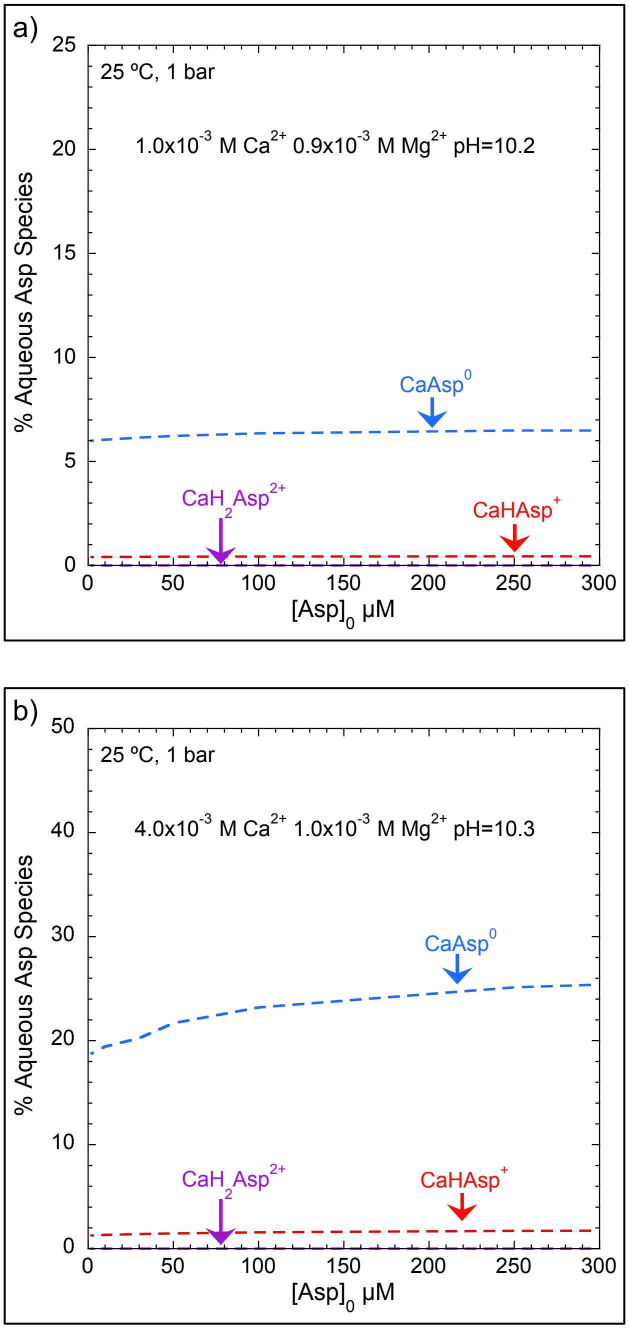

Fig. 15. Predicted aspartate surface adsorption on brucite as a function of aspartate remaining in solution in the presence of Lost City-type fluids at 25 ºC and 1 bar. Aspartate adsorption is calculated with the parameters in Table 2 in the presence of $[Na^+]$=0.485 M $[Cl^-]$= 0.549 M $[Ca^{2+}]$= 23.3x10^{-3} M and $[SO_4^{2-}]$= 12.9x10^{-3} M at pH=9.8 (Kelley et al., 2002) and pH=10.2. Solid curves represent calculated predictions.

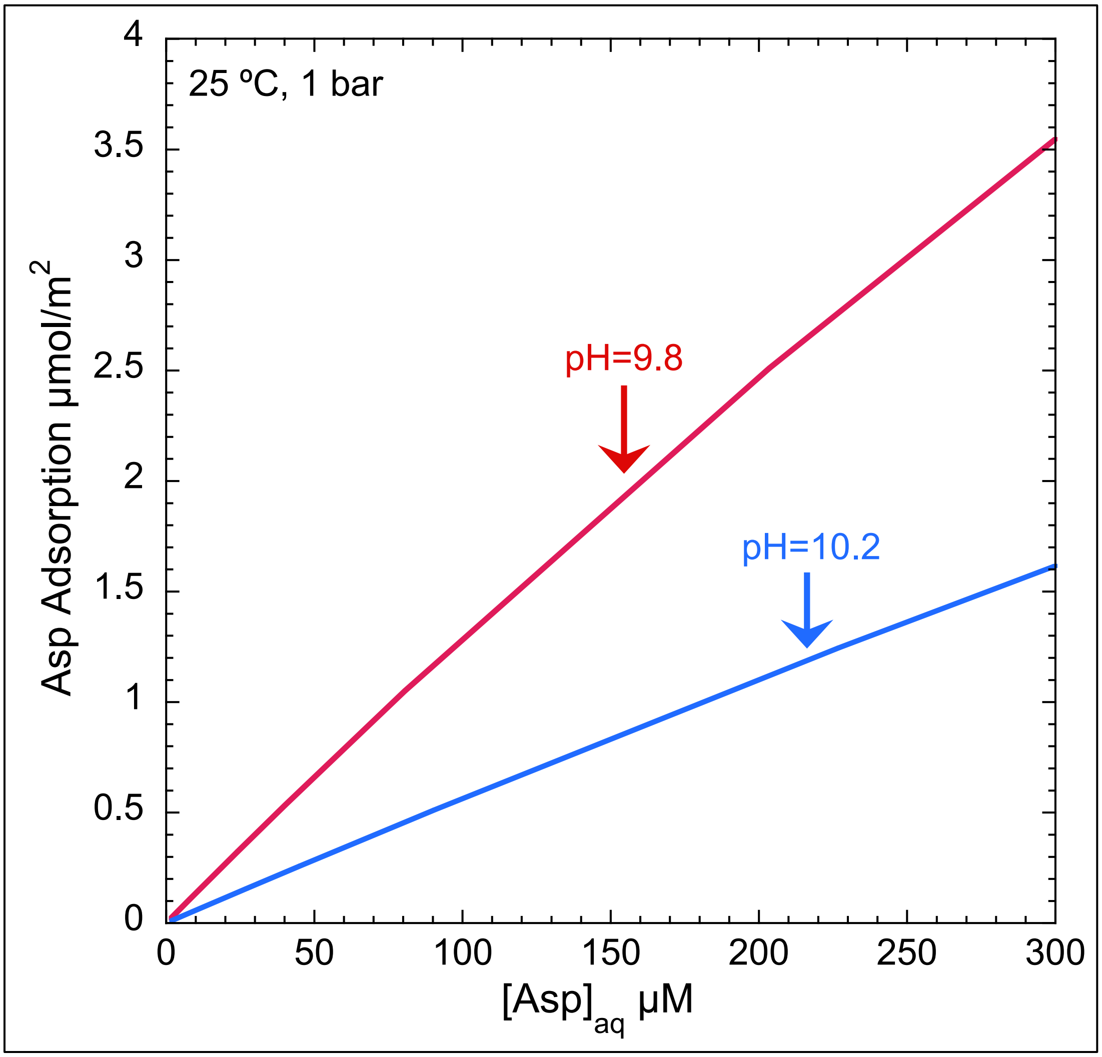

Table 1. Main parameters obtained from the application of the DIS method to argon adsorption at 77 K on brucite sample.

	Peak Position $\ln(P/P_0)$	**ω (kT)**	**V_m (cm^3•g^{-1})**	**SSA Ar (m^2•g^{-1})**
Local isotherm 1	-2.9	2.2	3.62	13.5
Local isotherm 2	-4	1.1	1.14	4.2
Local isotherm 3	-6.1	0	0.5	1.9
Local isotherm 4	-10	0	0.05	0.2

Table 2. Aqueous aspartate properties[a], characteristics of brucite[b] [$Mg(OH_2)$], and extended triple-layer model parameters for proton electrolyte and aspartate adsorption onto brucite.

Reaction Type	**Reaction**	**log K**
Aqueous aspartate equilibria	$Asp^{2-} + H^+ = HAsp^-$	10.01
	$HAsp^- + H^+ = H_2Asp$	3.88
	$H_2Asp + H^+ = H_3Asp^+$	1.92
	$HAsp^- + Cl^- + 2H^+ = H_3AspCl$	5.3
	$HAsp^- + Na^+ = NaHAsp$	-0.3
	$HAsp^- + Na^+ = NaAsp^- + H^+$	-9.6
	$HAsp^- + Ca^{2+} + H^+ = CaH_2Asp^{2+}$	-4.43
	$HAsp^- + Ca^{2+} = CaHAsp^+$	1.43
	$HAsp^- + Ca^{2+} = CaAsp + H^+$	-7.49
Surface equilibria	Hypothetical 1.0 m standard state	
$\log K_1^0$	$>SOH + H^+ = >SOH_2^+$	9.60
$\log K_2^0$	$>SO^- + H^+ = >SOH$	11.40
$\log {}^*K_{Na^+}^0$	$>SOH + Na^+ = >SO^-\_Na^+ + H^+$	-9.00
$\log {}^*K_{Cl^-}^0$	$>SOH + Cl^- + H^+ = >SOH_2^+\_Cl^-$	11.80
$\log {}^*K_{>SOH_2^+>SAsp^-}^0$	$2>SOH + H^+ + HAsp^- = >SOH_2^+>SAsp^- + H_2O$	16.08
$\log {}^*K_{>SO^-\_CaHAsp^+}^0$	$>SOH + Ca^{2+} + HAsp^- = >SO^-\_CaHAsp^+ + H^+$	-3.73
$\log {}^*K_{>SOH_2^+\_Ca(OH)_2}^0$	$>SOH + Ca^{2+} + 2H_2O = >SOH_2^+\_Ca(OH)_2 + H^+$	-5.20
Surface equilibria[c]	Site-occupancy standard states	
$\log K_{>SOH_2^+>SAsp^-}^{\theta}$	$2>SOH_2^+ + HAsp^- = >SOH_2^+>SAsp^- + H_2O + H^+$	18.80
$\log K_{>SO^-\_CaHAsp^+}^{\theta}$	$>SO^- + Ca^{2+} + HAsp^- = >SO^-\_CaHAsp^+$	-5.34
$\log K_{>SOH_2^+\_Ca(OH)_2}^{\theta}$	$>SOH_2^+ + Ca^{2+} + 2H_2O = >SOH_2^+\_Ca(OH_2) + H^+$	-3.87

[a] Protonation constants and electrolyte ion pair constants from (De Robertis et al., 1991; Jonsson et al., 2010)

[b] Brucite properties are N_s= 38 sites•nm^{-2}, A_s= 1.9 m^2•g^{-1}, C_1= 190 μF•cm^{-2}, C_2= 190 μF•cm^{-2}, pH_{PPZC}= 10.5, ΔpK^{θ}_n=2.08, $\log K^{\theta}1$= 9.46, $\log K^{\theta}_2$= 11.54, $\log^{\theta} K_{Na^+}$= -9.14 $\log^{\theta}_{Cl^-}$= 11.66

[c] Equilibrium constants relative to site occupancy standard states can be written relative to charged surface sites calculated using the equations: $\log K_{>SOH_2^+>SAsp^-}^{\theta} = \log {}^*K_{>SOH_2^+>SAsp^-}^0 + \log(N_sA_sC_s)/100$; $\log K_{>SO^-\_CaHAsp^+}^{\theta} = \log {}^*K_{>SO^-\_CaHAsp^+}^0 + \log(N_sA_s)/100$; $\log K_{>SOH_2^+\_Ca(OH)_2}^{\theta} = \log {}^*K_{>SOH_2^+\_Ca(OH)_2}^0 + \log(N_sA_s)/100$, where N_s is site density, A_s is BET edge surface area m^2•g^{-1}, and C_s is solid concentration g•L^{-1}.

Table 3. A summary of site densities calculated from idealized lateral brucite surfaces using the estimation procedures described by (Koretsky et al., 1998), where each broken bond at every possible termination of a surface is considered one site per unit area.

Surface	**N_s (Broken Bonds, sites•nm^{-2})**
(100)	20.0
	13.4
	20.0
(010)	20.0
	13.4
	20.0
(110)	15.4
	11.6
(111)	12.9
	12.9
	9.7

.

Table 4a. Aspartate adsorption data observed for low-Mg^{2+} and high-Mg^{2+} batch experiments.

Batch Experiment	**$[Asp]_{aq}$ (μM)**	**Γ_{ads} (μmol•m^{-2})**	**% Ads**
Low Mg^{2+}	4.5	0.03	10.2
	17.6	0.14	12.9
	37.3	0.16	7.8
	45.8	0.24	9.0
	70.0	0.28	7.4
	110.7	0.52	8.3
	134.7	0.85	10.8
	188.2	0.70	6.7
	1.9	0.01	3.6
	8.5	0.08	16.4
	27.3	0.15	11.6
	52.1	0.43	13.8
	77.4	0.43	9.8
	87.4	0.40	8.5
	99.2	0.57	10.3
	277.4	1.00	8.1
High Mg^{2+}	4.8	0.02	4.0
	9.8	0.02	4.5
	18.3	0.09	9.4
	46.1	0.20	8.1
	70.4	0.23	6.1
	95.0	0.34	6.6
	144.5	0.42	3.8
	190.4	0.52	5.0
	53.6	0.28	9.5
	36.4	0.16	7.7
	28.1	0.08	5.5
	238.4	0.63	4.3
	116.0	0.19	2.5
	79.8	0.27	5.4

Table 4b. Aspartate adsorption data observed for low-Ca^{2+} and high-Ca^{2+} batch experiments.

Batch Experiment	**$[Asp]_{aq}$ (μM)**	**Γ_{ads} (μmol•m^{-2})**	**% Ads**
Low Ca^{2+}	217.2	1.77	13.6
	127.2	1.20	15.3
	84.6	0.76	14.9
	61.1	0.71	18.8
	40.4	0.48	19.3
	20.3	0.25	18.8
	7.9	0.11	21.5
	4.2	0.04	17.3
High Ca^{2+}	90.4	1.50	24.8
	208.0	2.10	17.1
	115.9	1.73	22.8
	73.2	1.36	26.6
	51.9	1.19	30.9
	33.6	0.86	32.8
	13.4	0.59	46.4
	4.4	0.29	56.4
	2.4	0.13	52.7

Table 5. Ca^{2+} adsorption data observed for the low-Ca^{2+} and high-Ca^{2+} batch experiments.

Batch Experiment	**$[Ca^{2+}]$ (µM)**	**Γ_{ads} ($\mu mol \bullet m^{-2}$)**	**% Ads**
Low Ca^{2+}	614.1	21.88	40.7
	591.2	23.25	42.9
	605.0	22.21	41.6
	586.2	22.32	43.4
	597.4	21.75	42.3
	622.9	21.66	39.8
	597.3	22.80	42.3
	601.7	21.65	41.9
High Ca^{2+}	3416.5	31.75	15.6
	3519.4	26.04	13.1
	3479.0	28.83	14.1
	3411.7	32.59	15.7
	3451.2	30.59	14.8
	3473.5	30.24	14.2
	3482.4	28.94	14.0
	3505.0	28.05	13.4
	3453.3	29.79	14.7

Chapter 3

Enhanced and inhibited adsorption of D-ribose with Ca^{2+} and Mg^{2+} onto brucite [$Mg(OH)_2$]

The adsorption of biomolecules containing sugar functional groups at mineral surfaces is of interest for a wide variety of topics ranging from understanding microbial attachment to minerals to the evolution of nucleosides and nucleotides on early Earth. We conducted batch adsorption experiments between D-ribose and brucite [$Mg(OH)_2$] over variable initial ribose concentrations and four ionic strengths resulting from different Mg^{2+} and Ca^{2+} concentrations in the aqueous phase. Ribose adsorption occurred up to 0.3 $\mu mol \bullet m^{-2}$ at pH~10.3 with low Mg^{2+} concentrations present. It decreased to 4.9×10^{-2} $\mu mol \bullet m^{-2}$ when Mg^{2+} concentrations increased to 5.8×10^{-3} M at pH= 9.8. However, ribose adsorption increased when Ca^{2+} was added to the system, up to 0.4 $\mu mol \bullet m^{-2}$ at Ca^{2+} concentrations of 4.2×10^{-3} M. Calcium adsorbed to a great extent onto brucite at 21.3 ± 1.3 $\mu mol \bullet m^{-2}$ (39.9 ± 2.8 %) at low Ca^{2+} concentrations and at 22.7 ± 3.5 $\mu mol \bullet m^{-2}$ (10.4 ± 1.6 %) at high Ca^{2+} concentrations. We characterized the interactions between ribose, Ca^{2+}, and the brucite surface by constructing a surface complexation model of the adsorption data. Using the extended triple-layer model (ETLM), we proposed two reaction schemes consistent with the experimental data. Both contain three surface reactions involving 1) a bidentate outer-sphere or a “standing” surface species, 2) a monodentate calcium-ribose outer-sphere species, and 3) a monodentate calcium outer-sphere species. Our ETLM prediction of the brucite particle surface charge suggests that the surface is negative at low Mg^{2+} concentrations and surface charge further decreases at high Mg^{2+} concentrations, which may indicate why ribose adsorbs in low amounts as a deprotonated species, Rib^{-}. We predict that brucite becomes positively charged with the addition of Ca^{2+}, which may be a consequence of the large amount of Ca^{2+} adsorption. The increase in ribose adsorption with Ca^{2+} is likely driven by Ca^{2+} adsorption and the formation of a cooperative calcium-ribose outer-sphere species, which is predicted by the ETLM to predominate over the "standing" species on brucite at both Ca^{2+} concentrations. Our model of the ribose-brucite system established by a combination of batch adsorption experiments and surface complexation modeling has enabled predictions of ribose adsorption over a wide range of pH conditions. The results of this study establish a novel understanding of ribose adsorption behavior and the cooperative and inhibiting effects of Ca^{2+} and Mg^{2+}, respectively.

This paper will be submitted to Geochimica et Cosmochimica Acta.

Authors: Charlene F. Estrada, Alyssa K. Adcock, Dimitri A. Sverjensky, Manuel Pelletier,

Angélina Razafitianamaharavo, and Robert M. Hazen

1. Introduction

The adsorption of biomolecules onto protonated and deprotonated surface sites at the mineral-water interface holds implications for the global carbon cycle (Ittekkot et al., 1992), the sequestration of environmental contaminants (Biester et al., 2002; Graydon et al., 2009), microbial attachment to minerals, and the origin of life on early Earth (Schoonen et al., 2004; Hazen, 2006; Cleaves et al., 2012). The emergence of complex organic molecules such as RNA and DNA from simpler compounds, including nucleic acids and carbohydrates, is of fundamental importance in origins of life scenarios (Ferris, 1993; Hazen, 2005a). Mineral surfaces have been suggested to play a key role in this process by adsorbing and concentrating biomolecules, thereby facilitating other reactions such as polymerization. For example, the clay mineral montmorillonite has promoted the formation of ribonucleotide oligomer chains (Ferris, 1993; Huang and Ferris, 2006). The mineral-water interface may be a crucial environment in this scenario because it can provide the opportunity for an organic molecule to attach as a species that may not exist in bulk water under ambient pH conditions and salinity (Ferris, 1993; Hazen, 2005a; Hazen, 2006; Geiger, 2009; Malin et al., 2009; Cleaves et al., 2012). Thus, the mineral-water interface may increase the availability of a particular organic species that might contain more polarized or charged functional groups, and this process may facilitate reactions among other adsorbed biomolecules.

In this study, we focus on the adsorption of the pentose sugar, D-ribose, onto the clay mineral brucite [$Mg(OH)_2$]. Ribose is a monosaccharide that exists as an equilibrium mixture of five isomers: an aldose, α-ribofuranose, β-ribofuranose, α-ribopyranose, and β-ribopyranose. In water, β-ribopyranose predominates (Angyal, 1969), as does the neutral species (HRib^0, $C_5H_{10}O_5$) across the observed environmental pH range. Ribose and other monosaccharides have been synthesized in the laboratory under plausible early earth conditions (Gabel and Ponnamperuma, 1967; Reid et al., 1967; Kim et al., 2011). The formation of ribose under elevated pressures and temperatures up to 150 ºC at a bulk water composition similar to that of ultramafic hydrothermal systems (Charlou et al., 2002; Delacour et al., 2008) has also been calculated to be thermodynamically favorable (LaRowe and Regnier, 2008), which may hold implications for the evolution of more complex organic compounds from ribose within hydrothermal environments.

A number of studies have focused on the adsorption of ribonucleotides onto mineral surfaces, among them nontronite (Feuillie et al., 2013), montmorillonite (Banin et al., 1985; Ferris, 1993; Huang and Ferris, 2006; Hashizume et al., 2010; Feuillie et al., 2013), kaolinite (Rishpon et al., 1982; Hashizume et al., 2010), SiO_2 (Holland et al., 2011), $Al(OH)_3$ (Rishpon et al., 1982; Arora and Kamaluddin, 2007), manganese oxides (Bhushan et al., 2011), allophane (Hashizume and Theng, 2007), and TiO_2 (Cleaves et al., 2010). In the latter study, it was observed that ribonucleotides adsorbed onto TiO_2 to a greater extent than the deoxynucleotides, and the authors suggested that the hydroxyl groups of the ribose moiety might have enhanced adsorption by attaching to the mineral-water interface (Cleaves et al., 2010). However, there have been very few studies on the adsorption of ribose onto mineral surfaces. Notable exceptions are the studies by Hashizume and coworkers (2007; 2010), where in addition to nucleic acids, ribose was adsorbed onto the surfaces of allophane and montmorillonite. Ribose adsorption was approximately 0.01 $\mu mol \cdot m^{-2}$ on allophane, and it was generally assumed that adsorption occurred through the formation of either a weak electrostatic, hydrogen, or Van der Waals bond (Hashizume and Theng 2007).

Clay mineral surfaces have been studied extensively with ribonucleotides and to a lesser degree ribose, but the single-layer hydroxide mineral brucite [$Mg(OH)_2$] has yet to be thoroughly investigated with these organic compounds. Brucite is a thermodynamically stable phase found in serpentinite-hosted hydrothermal vents, which produce moderately hot (~70-110 ºC), alkaline, reducing fluids (Kelley et al., 2005; Proskurowski et al., 2006; Delacour et al., 2008). Holm and coworkers (2006; 2012) have proposed that a primary constituent of brucite, magnesium, may promote the self-cleavage of RNA and lead to the formation of ribozymes. Furthermore, brucite itself has been suggested to adsorb and concentrate phosphate within an alkaline environment, such as the serpentinite-hosted hydrothermal system. Brucite may also scavenge phosphate (Holm et al., 2006), which might lead to the formation of adenosine triphosphate (ATP) should ribose also adsorb at the mineral-water interface.

The brucite-water interface has been well-studied from the standpoint of constraining dissolution and precipitation kinetics of the mineral surface (Hostetler, 1963; Schott, 1981; Jordan and Rammensee, 1996; Pokrovsky and Schott, 2004; Pokrovsky et al., 2005; Kudoh et al., 2006). These studies characterized how the dissolution kinetics of brucite was affected by the addition of various biomolecules, including D-xylose, a pentose sugar that is structurally similar to ribose (Pokrovsky et al., 2005). The authors observed that xylose weakly inhibited brucite dissolution when present at concentrations greater than 0.1 M. It was also suggested that the organic species adsorbed on the brucite surface through a ligand exchange reaction, where:

$$>\mathrm{MgOH_2^+} + \mathrm{L^{n-}} = >\mathrm{MgL^{1-n}} + \mathrm{H_2O} \qquad (1)$$

in which L^{n-} represents the aqueous species of ligand, L. When adsorption is inhibited, it is possible that the biomolecule forms a binuclear complex at the surface, although it is likely that xylose did not adsorb to a great extent on brucite, as the reported equilibrium constant for Eq. (1) was $K<1$. The effect of alkali cations on brucite dissolution was also investigated, and Pokrovsky and coworkers (2005) concluded that at concentrations of about 10^{-2} M and at a pH of 4.9, Ca^{2+} increases the brucite dissolution rate. In general, the adsorption of organic and inorganic molecules in large amounts has been proposed to disrupt Mg-O bonds, thereby modifying the surface charge or the rate of exchange between water and the mineral surface and causing the brucite dissolution rate to change. The increase in brucite dissolution with Ca^{2+} is thought to be caused by the formation of bidentate or monodentate mononuclear complexes between the surface and adsorbing species (Pokrovsky et al., 2005).

We have previously examined the adsorption of the amino acid, L-aspartate, onto the surface of a synthesized brucite powder by conducting batch adsorption experiments at four distinct ionic strengths that were a result of different concentrations of Ca^{2+} and Mg^{2+} (Estrada et al., in review). We observed that aspartate adsorption decreased with increasing Mg^{2+} concentration, whereas it increased with the addition of Ca^{2+}. The enhanced adsorption with Ca^{2+} was likely due to the formation of a Ca^{2+}-aspartate complex at the brucite surface, and it may imply that Ca^{2+} could form cooperative surface complexes with other organic compounds, although the extent to which Ca^{2+} may increase surface adsorption requires further investigation. We also determined that the synthetic brucite was in equilibrium with the aqueous phase of our batch experiments with the equation:

$$Mg(OH)_2 + 2H^+ = Mg^{2+} + 2H_2O \qquad (2)$$

where the equilibrium constant, logK= 17.3 ± 0.06 (Estrada et al., in review). This figure is somewhat lower than that of a natural brucite powdered specimen, where logK= 17.6 ± 0.05 (Pokrovsky and Schott, 2004), yet we assume that the synthetic brucite is in equilibrium with the aqueous phase.

In this study we investigate the adsorption behavior of ribose at the brucite-water interface by conducting batch adsorption experiments with ribose at variable initial concentrations and ionic strengths that result from distinct concentrations of added Mg^{2+} and Ca^{2+} at 25 ºC and 1 bar. Furthermore, we characterize the interactions between ribose and brucite under these conditions by constructing a surface complexation model of the adsorption data. By establishing a fundamental model of the ribose-brucite system based on batch adsorption experiments and thermodynamic calculations, it becomes possible for us to predict the adsorption behavior of ribose over a wide range of aqueous and environmental conditions. Our goal is to attain a new understanding of the adsorption of ribose onto a mineral surface that is prevalent within serpentinite-hosted hydrothermal systems that may be important in the framework of early Earth.

2. Materials and Methods

2.1. Materials

We made all solutions in this study with Milli-Q water (Millipore, resistance= 18.2 MΩcm). We used D-Ribose (99 % Sigma) without any further purification and stored it under refrigeration at 6 ± 2 ºC. We also used sterile salt solutions including $MgCl_2$ ($25x10^{-3}$ M, Teknova) and $CaCl_2$ (0.5 M, Fluka) without any further purification to achieve [Mg^{2+}]= 5.2x10^{-3} M and [Ca^{2+}]= 1.0x10^{-3} M and 4.2x10^{-3} M, respectively. The brucite we used in the present study was from the same well-characterized batch previously detailed by Estrada and coworkers (in review). Briefly, we synthesized the microcrystalline brucite powder with a precipitation method described by previous experiments (Henrist et al., 2003; Lu et al., 2004). We subjected the precipitate to hydrothermal aging, in which we heated the brucite in Milli-Q water at 150 ºC within a sealed, PTFE-lined stainless steel reaction vessel (Col-Int-Tech) for 3 days. Powder X-ray diffraction (Bruker D2 Phaser) and scanning electron microscopy (SEM, JEOL 8500F) have revealed that hydrothermal aging improved the crystallinity and morphology of the brucite powder (Estrada et al., in review). Both methods have shown that the predominant growth face is the basal surface (001), and SEM has shown that the crystals are hexagonal (between 100-300 nm) and appear in lamellar clusters (Fig. 1).

Previous studies suggest that the (001) basal growth surface on minerals such as brucite, kaolinite, illite, gibbsite, and goethite, cannot participate in protonation/deprotonation reactions that lead to the adsorption of molecules (Prélot et al., 2003; Sayed-Hassan et al., 2006; Liu et al., 2013; Estrada et al., in review). This limitation occurs because no broken bonds are observed when these surfaces are ideally terminated. However, it can be seen with the aid of crystallographic software such as CrystalMaker (Palmer, 2009) that the lateral, or edge surfaces, of these minerals are likely to be charged in aqueous solution and are therefore probably active in adsorbing ribose.

We determined the specific surface area of the synthetic brucite powder with the multi-point BET N_2 method (Micromeritics, Norcross, GA, USA) to be 17.6 ± 0.1 $m^2 \cdot g^{-1}$.

It is likely that a high proportion of this value represents the predominant (001) basal surface of brucite, although this method is unable to elucidate the distribution of surface area between the basal and lateral faces. We characterized the edge specific surface area (ESA) with low pressure Ar adsorption, performed at the Laboratoire Interdisciplinaire des Environnements Continentaux (Vandœuvre les Nancy, France). The experimental methods of this technique have been described in detail in previous experiments (Villiéras et al., 1992; Villiéras et al., 1997; Michot and Villiéras, 2002; Eypert-Blaison et al., 2002; Sayed-Hassan et al., 2006; Perronnet et al., 2007; Estrada et al., in review). From the results of this measurement, we estimate that 89.5 % of the total specific surface area (TSA) previously reported is represented by basal brucite surfaces, whereas 10.5 % is distinguished by lateral brucite surfaces. In combination with the BET surface area, these results suggest an ESA of 1.9 $m^2 \bullet g^{-1}$ for the lateral brucite surfaces of our brucite sample.

2.2. Experimental Methods

We prepared batch samples with a 10.0 ± 0.5 $g \bullet L^{-1}$ solid concentration of brucite combined with a variable concentration of ribose, ranging from 5 to 300 μM, 15 mL sterile Falcon tubes. The brucite powder strongly buffered sample pH, and the pH of immersion (pH_{IMM}) was between pH 10.2 and 10.4 when we introduced no additional Mg^{2+} to the system. We studied four different concentrations of Mg^{2+} and Ca^{2+} that resulted in different ionic strengths throughout the course of the batch adsorption experiments:

1) a “low Mg^{2+} concentration” with no Ca^{2+} present ($[Mg^{2+}]$= 0.6x10^{-3} M, I= 1.7x10^{-3} M);

2) a “high Mg^{2+} concentration” with no Ca^{2+} present ($[Mg^{2+}]$= 5.8x10^{-3} M, I= 17.4x10^{-3} M);

3) a “low Ca^{2+} concentration” in the presence of $[Mg^{2+}]$= 0.9x10^{-3} M ($[Ca^{2+}]$= 1.0x10^{-3} M, I= 5.7x10^{-3} M); and

4) a “high Ca^{2+} concentration” in the presence of $[Mg^{2+}]$= 0.6x10^{-3} M ($[Ca^{2+}]$= 4.2x10^{-3} M, I= 14.4x10^{-3} M).

Previous studies suggested that elevated concentrations of Ca^{2+} and organic molecules (>10^{-2} M) may affect the dissolution of brucite in aqueous solution (Pokrovsky et al., 2005). Accordingly, we studied a relatively low concentration of both Ca^{2+} (≤4.0x10^{-3} M) and ribose (≤0.3x10^{-3} M) to avoid this potential complication, although we used a synthetic brucite powder as opposed to a ground natural sample (Pokrovsky and Schott, 2004). We constantly purged each sample with Ar gas during its exposure to air to avoid contamination by CO_2.

We conducted a preliminary adsorption experiment over variable time periods and determined that ribose adsorption onto brucite reaches a steady state within 2 hours. In our subsequent batch adsorption experiments, we placed the batch samples on a test tube rotator at 40 rpm (25 ± 1 ºC, 1 bar) for 4 hours to ensure that the brucite-ribose suspension had reached a steady state. We then measured the pH of the brucite-ribose suspension with a combination glass electrode (Thermo-Electron, Orion 8103BNUWP) that had been calibrated prior to the experiment with NIST standardized buffers that refer to pH values 4, 7, and 10 (Fischer Scientific). We centrifuged the samples for 10 minutes with a relative centrifugal force of 1073*g* (Fisher Scientific accuSpin 400) and separated the liquid supernatant from the solid brucite.

We analyzed the concentration of the ribose, Mg^{2+}, and Ca^{2+} in the supernatant with ion chromatography (IC). We used a Dionex ICS-5000 system equipped with a DP dual pump, AS-AP autosampler, ED electrochemical detector, and Chromeleon 6.8 software (Dionex Corporation, Sunnyvale, CA, USA). The analyte passed through an AminoPAC10 column that is packed with a hydrophobic, polymeric, pellicular resin, where gradient anion exchange separation (pH 12 to 14) removed the ribose present in the supernatant from the bulk fluid. Following separation, we determined the relative analyte concentration with integrated pulsed amperometric detection (IPAD), which irreversibly oxidizes the hydroxyl groups of ribose with the working gold electrode of the ED electrochemical detector (Clarke et al., 1999; Jandik et al., 2000). The Mg^{2+} and Ca^{2+} present in the supernatant passed through an IonPac CS12A column that is packed with a hydrophobic resin containing a carboxylate functional group that separated the ions through cation exchange (Jensen et al., 1993). A CD conductivity detector with electrolytic suppression then analyzed the cations. For each cation and carbohydrate application, a chromatogram containing a peak that is unique to ribose, Mg^{2+}, and Ca^{2+} was produced for every batch sample. We determined the concentration of the cation or ribose in the analyte from the area beneath its peak, which was integrated with the software Chromeleon 6.8. Prior to analyzing the supernatant with IC, we measured a set of standards for the cation or ribose resulting in a linear correlation between the area under the peak and analytical concentration. We standardized each set of samples within two hours of analyzing the first supernatant of the batch adsorption experiment.

We analyzed the samples with IC in triplicate and determined the mean concentration of ribose remaining in the liquid supernatant within ±1 standard error (σ_M). This step was necessary for evaluating the ribose adsorption data because preliminary experiments determined low amounts (<10 %) of ribose adsorption; therefore, analyzing in triplicate better constrained these adsorption values. In contrast, our preliminary investigation of Ca^{2+} adsorption values indicated amounts >10 % that did not vary as a function of ribose concentration. Therefore, we performed a single analysis and determined ±1 standard deviation (σ) for each batch experiment. From the analytical concentration the of ribose or cation we determined the surface adsorption (Γ_{ads}, $\mu mol \cdot m^{-2}$) of ribose or Ca^{2+} on brucite, where:

$$\Gamma_{ads} = \frac{[X]_0 - [X]_{aq}}{C_s A_s} \tag{3}$$

In which C_s is the solid concentration and A_s is the lateral edge surface area of brucite. We report Γ_{ads} as an isotherm, as a function of the $[Rib]_{aq}$, the remaining ribose concentration in the liquid supernatant.

We additionally conducted a blank batch experiment with variable initial ribose concentrations (10-50 μM) at alkaline conditions (pH= 9.9-10.4) that were attained by the addition of NaOH (Sigma) without the presence of brucite to evaluate whether or not any ribose reactions took place in the aqueous phase (e.g. polymerization). We conducted this blank experiment at low Mg^{2+} concentrations and high Ca^{2+} concentrations to reflect the conditions of the ribose-brucite experiments. We sampled the batch experiment after the steady state time for the ribose-brucite system of 4 hours and at 24 hours. Although it has been observed that sugar solutions that polymerize in water turn a distinctive brown color (Benner, 2004), we found that all the ribose samples in our blank experiment remained clear. Furthermore, our analysis of ribose concentrations after the blank experiment indicated a negligible change (<1 %) in the concentration of the ribose monomer.

2.3. Surface Complexation Modeling Approach

In this study we integrated experimental isotherm data with a predictive triple layer model that uses Born Solvation and crystal chemical theory known as the extended triple-layer model, or the ETLM (Sverjensky and Sahai, 1996; Sahai and Sverjensky, 1997; Sverjensky, 2003; Sverjensky, 2005; Sverjensky and Fukushi, 2006). Unlike other solid-water interface models, the ETLM predicts the electrical work resulting from the release of water dipoles during inner-sphere adsorption. We carried out calculations for the ETLM iteratively with the computer code GEOSURF (Sahai and Sverjensky, 1998). We estimated a pH_{PZC}= 10.5 from observations of pH_{IMM} in our batch adsorption experiments.

Ribose deprotonates into a negatively-charged species according to

$$HRib^0 = Rib^- + H^+ \tag{4}$$

Goldberg and Tewari (1989) recommend a value for the pK of 12.1. However, Sen and coworkers (2014) have experimentally determined a pKa of 11.8 with a likely uncertainty (estimated by us) of ±0.2. We chose to use a pKa of 12.0, which is within uncertainty of both sources of data. Additionally, we included a speciation constant involving the complexation of ribose to Ca^{2+} (Morel et al., 1986). Through our previous work characterizing the adsorption of aspartate onto the same batch of brucite, we obtained both protonation and electrolyte adsorption parameters for the brucite surface (Estrada et al., in review). We obtained these parameters by regression fitting of titration data with the ETLM that had been collected for another brucite sample (Pokrovsky and Schott, 2004) and recalculated for a site density of N_s= 31 sites•nm^{-2} according to the methods outlined in previous publications (Sverjensky, 2003; Sverjensky, 2005). These parameters, along with speciation reactions involving ribose, are displayed in Table 1.

In our previous study of the same brucite batch, we obtained a site density of 38 sites•nm^{-2} for the brucite-aspartate system by regression of the experimental adsorption data. The difference with the value adopted in the present study may reflect a number of possibilities. One is that the more acidic or negatively-charged aspartate adsorbing to the surface may promote dissolution of the brucite surface, thereby increasing the site density. Pokrovsky and coworkers (2005) suggested that different biomolecules could affect brucite dissolution in water, although the authors observed dissolution to occur at concentrations of at least 10^{-2} M. Another possibility is that our batch of pure synthetic brucite is more susceptible to dissolution by the adsorption of biomolecules than the natural ground brucite sample used by Pokrovsky et al., and the difference between ribose and aspartate is sufficient to affect surface atoms to such an extent that the site density is different in each system.

With the protonation and electrolyte adsorption parameters established (Table 1), we proposed surface reactions for the adsorption of ribose onto brucite in a hypothetical 10^{-3} M NaCl system and fit the reactions to the experimental data. We have collected the data at four ionic strengths with different dissolved ions present and a variable pH range, thus thoroughly testing our proposed surface reactions and permitting the selection of a small number of reactions to successfully predict the adsorption of ribose onto brucite.

3. Results and Discussion

3.1. Ribose Adsorption onto Brucite at Low Mg^{2+} Concentrations

The adsorption data for ribose onto brucite as a function of $[Rib]_{aq}$ at low Mg^{2+} concentrations ($0.6x10^{-3}$ M) is displayed in Fig. 2a. Ribose adsorption at a pH between 10.3 and 10.4 increases steadily as a function of $[Rib]_{aq}$, where the initial ribose concentration was between $[Rib]_0$= 5 and 200 μM. The error reported in Fig. 2 is ±1 σ_M of the mean Γ_{ads} and $[Rib]_{aq}$ values reported. The amount of ribose adsorption lies between $1.5x10^{-3}$ and 0.3 $\mu mol \bullet m^{-2}$. This range of surface adsorption generally corresponds with 3.9 to 0.4 % of ribose adsorption, where the percentage of adsorbed ribose decreases with increasing surface adsorption. Therefore, the reported error increases with Γ_{ads} and $[Rib]_{aq}$. All adsorption data for the ribose-brucite batch adsorption experiments is reported in Table 2.

While we only consider the lateral brucite surfaces active in the adsorption of ribose, we cannot determine if a particular surface plays a more prominent role than another. In our previous study of the brucite-aspartate system, we examined the idealized lateral surfaces and determined that there are two different types of sites resulting from the termination of the hydroxyl group: a geminal site ($>Mg(OH)_2$) where two bonds were broken, and a bridging site (>MgOH), where a single bond was broken at the surface (Estrada et al., in review). Whether the ribose molecule binds at a geminal or bridging reaction site cannot be distinguished by the ETLM because there is no difference in the electrical work that results from the proposed surface reactions in Table 1 at either site. Therefore, to avoid ambiguity, we will display surface reactions occurring at the (100) brucite plane as an example surface only, and henceforth regard the neutral brucite surface as ">SOH".

Analysis of the data in Fig. 2a with the ETLM has suggested two possible surface reactions. The primary difference between the two proposed reactions is the number of protonated surface sites that result from the formation of the surface species, where only one surface site is protonated as represented by the first reaction stoichiometry:

$$2{>}\mathrm{SOH} + \mathrm{HRib} = {>}\mathrm{SOH_2}^{+}{>}\mathrm{SOH\_Rib}^{-} \qquad (5)$$

and two surface sites are protonated in the second reaction stoichiometry:

$$2{>}\mathrm{SOH} + \mathrm{H}^{+} + \mathrm{HRib} = 2({>}\mathrm{SOH_2}^{+})\mathrm{\_Rib}^{-} \qquad (6)$$

It can be seen in Fig. 2b that these reactions both result in close fits to the adsorption data within experimental uncertainty. Both surface reactions may result in a bidentate outer-sphere complex or a “standing” complex at the brucite surface, which is illustrated in Fig. 3. Ribose is represented as the β-ribopyranose isomer, which is the most abundant isomer among the five possible forms of ribose in water (Angyal, 1969). While neither our experiments nor our surface complexation modeling suggests that this ribose isomer is attaching onto brucite instead of one of the other isomers, we will depict the ribose molecule as β-ribopyranose. In Fig. 3, the ribose molecule is hydrogen-bonded between its deprotonated hydroxyl group and the protonated surface, resulting in the bond $>\mathrm{SOH_2}^{+\cdots}\mathrm{O}$-C. For the surface reaction proposed in Eq. (5), the second hydrogen bond may occur between a neutral surface site and a neutral ribose hydroxyl group, resulting in the bond $>\mathrm{SOH}^{\cdots}(\mathrm{OH})$-C, as shown in Fig. 3a. In contrast, for the surface reaction proposed in Eq. (5), the second hydrogen bond may occur between a protonated surface site and the hydroxyl group resulting in another $>\mathrm{SOH_2}+^{\cdots}(\mathrm{OH})$-C bond (Fig. 3b).

It should be noted that we can formulate an alternative way of writing Eq. (5)

corresponding to the formation of an inner-sphere complex. If we express the neutral ribose molecule as H_2Rib, we can rewrite Eq. (5) as

$$2{>}SOH + H_2Rib = {>}SOH_2^{+}{>}SRib^{-} + H_2O \qquad (5a)$$

which is stoichiometrically and electrostatically identical to Eq. (5). Our ETLM cannot distinguish between the two possibilities. However, given the relatively weak adsorption of ribose on the surface of brucite, it seems perhaps less likely that an inner-sphere complex is formed on the surface.

The reactions in Eqs. (5-6) correspond with the equilibrium constants

$$^{*}K^{0}_{>SOH_2^{+}>SOH\_Rib^{-}} = \frac{a_{>SOH_2^{+}>SOH\_Rib^{-}}}{a^{2}{}_{>SOH}\, a_{HRib}}\, 10^{\frac{F\Delta\psi_{r,5}}{2.303RT}} \qquad (7)$$

and

$$^{*}K^{0}_{2(>SOH_2^{+})\_Rib^{-}} = \frac{a_{2(>SOH_2^{+})\_Rib^{-}}}{a^{2}{}_{>SOH}\, a_{HRib}\, a_{H^{+}}}\, 10^{\frac{F\Delta\psi_{r,6}}{2.303RT}} \qquad (8)$$

where the superscript “*” indicates the reaction is expressed relative to the neutral >SOH surface and “0” refers to a hypothetical 1.0 molal standard state (Sverjensky, 2003). The values $\Delta\psi_{r,5}$ and $\Delta\psi_{r,6}$ represent the electrical work involved in Eqs. (5) and (6), respectively. The electrical work includes a contribution from the movement of water dipoles off the brucite surface according to $\Delta\psi_{r} = -n_{H2O}(\psi_{0} - \psi_{\beta})$, where n_{H2O} is the number of water molecules on the right-hand side of the reaction. In both Eqs. (5-6), $n_{H2O} = 0$, which results in $\Delta\psi_{r,5} = \psi_{0} - \psi_{\beta}$ and $\Delta\psi_{r,6} = 2\psi_{0} - \psi_{\beta}$.

3.2. Ribose Adsorption onto Brucite at High Mg^{2+} Concentrations

We have previously characterized the equilibrium between brucite and the aqueous phase with Eq. (2) where the equilibrium constant can be expressed as:

$$\mathrm{logK} = \frac{a_{Mg^{2+}}}{a_{H^+}^2} \quad (9)$$

For our synthetic brucite powder, we calculated an equilibrium constant of logK= 17.3 ± 0.06 for suspensions of brucite and aspartate. In this study, we calculated an average equilibrium constant of logK= 17.4 ± 0.1 from the brucite-ribose batch experiments ($[Mg^{2+}]$= 0.6x10^{-3} M). Both of these values for the logK are close to the value of 17.6 ± 0.05 previously determined for a ground natural brucite sample (Pokrovsky and Schott, 2004). In Fig. 4a, we plot the steady-state activity ratio determined from the brucite-water, brucite-aspartate and brucite-ribose batch experiments and an ETLM calculation of the activity coefficient for Mg^{2+} as a function of solution pH. We observe that the activity ratio does not significantly change, and therefore we assume that the brucite used in the previous publication and this study is in equilibrium with the aqueous phase. If brucite is in equilibrium with water, then the addition of Mg^{2+} to a brucite-ribose batch experiment should decrease solution pH while the equilibrium constant remains unchanged, as illustrated by Fig. 4a. In Fig. 4b, we plot the activity ratios obtained by brucite-ribose and brucite-aspartate batch adsorption experiments conducted in the presence of 5.8x10^{-3} M Mg^{2+} (5.2x10^{-3} M $MgCl_2$ plus 0.6x10^{-3} M Mg^{2+} dissolved from brucite) as a function of solution pH. As predicted, pH decreases (pH_{imm}= 9.8 ± 0.05). The average activity ratio for aspartate and ribose is lower at 17.2 ± 0.02 and 17.1 ± 0.01, respectively, but close to the previously calculated logK values.

The ribose surface adsorption data for the batch experiment conducted at the high Mg^{2+} concentration is displayed as an isotherm along with the data from the low Mg^{2+} batch experiment in Fig. 5a. Ribose adsorption at the high Mg^{2+} concentration occurs at an ionic strength of 17.4 x 10^{-3} M and lies between 2.6x10^{-3} and 4.9x10^{-2} μmol•m^{-2}. This

Γ_{ads} generally corresponds with <1.3 to 0.1 % ribose adsorption. In comparison with the adsorption data obtained under low Mg^{2+} concentrations, ribose surface adsorption significantly decreases, and it is possible that adsorption is negligible. Using the model developed above with the surface reactions in Eq. (5) or (6), we obtained a fit to both the high and low Mg^{2+} data at pH= 9.8 and pH= 10.4, respectively, in Fig. 5b. For both surface reactions, the amount of predicted ribose adsorption does not exceed 0.5 %, which is consistent with our observation that very little or no surface adsorption has occurred between ribose and brucite at high Mg^{2+} concentrations. Additionally, we observed little variation between the predicted curves at both Mg^{2+} concentrations and the experimental data within uncertainty (Fig. 5b). Here, the "standing" ribose species from Eqs. (5) and (6) are consistent with experimental data at two ionic strengths resulting from different experimental Mg^{2+} concentrations, which lends support to the use of either surface reaction in Eq. (5) or (6).

3.3. Ribose Adsorption onto Brucite in the Presence of Ca^{2+}

Isotherms of ribose surface adsorption onto brucite in the presence of low and high Ca^{2+} concentrations are shown in Fig. 6a. The low Ca^{2+} experiments refer to a Ca^{2+} concentration of $1.0 \text{x} 10^{-3}$ M together with a Mg^{2+} concentration of $0.9 \text{x} 10^{-3}$ M at a pH of 10.2 ± 0.03. Surface adsorption is between $1.0 \text{x} 10^{-2}$ and 0.4 $\mu mol \bullet m^{-2}$. High Ca^{2+} experiments refer to a Ca^{2+} concentration of $4.2 \text{x} 10^{-3}$ M and a Mg^{2+} concentration of $0.6 \text{x} 10^{-3}$ M at a pH of 10.3 ± 0.06. We observe surface adsorption to slightly increase at high Ca^{2+} concentrations, where Γ_{ads} is between $4.8 \text{x} 10^{-2}$ and 0.4 $\mu mol \bullet m^{-2}$. This range of Γ_{ads} corresponds to between 11.4 and 3.8 % ribose adsorption, respectively.

Ribose surface adsorption is greater in the presence of Ca^{2+} compared with the batch adsorption experiments conducted with only Mg^{2+} (see Fig. 2a) although total surface adsorption does not exceed 12 %. We observed significant amounts of Ca^{2+} adsorption onto brucite independent of $[Rib]_{aq}$ as illustrated by Fig. 7a. The amount of Ca^{2+} surface adsorption averages 21.3 ± 1.3 $\mu mol \cdot m^{-2}$ (39.9 ± 2.8 %) for the low Ca^{2+} experiments and 22.7 ± 3.5 $\mu mol \cdot m^{-2}$ (10.4 ± 1.6 %) for the high Ca^{2+} experiments. The reported error in Fig. 6 corresponds to $\pm 1\ \sigma$. All Ca^{2+} adsorption data is reported in Table 3.

We proposed two surface reactions in combination with either reaction in Eq. (5) or (6) to represent the adsorption of Ca^{2+} and/or ribose and obtain a fit to the experimental data in Fig. 6a and 7a. The first surface reaction involves the formation of a calcium-ribose surface complex:

$$>SOH + HRib + Ca^{2+} = >SOH\_CaRib^{+} + H^{+} \tag{10}$$

We can interpret this reaction to involve the adsorption of a monodentate outer-sphere species, on the brucite surface, which is represented in Fig. 8a. The second reaction involves the adsorption of a hydrated calcium complex:

$$>SOH + Ca^{2+} + 2H_2O = >SOH_2^{+}\_\ Ca(OH)_2 + H^{+} \tag{11}$$

This reaction also involves a monodentate outer-sphere surface species illustrated in Fig. 8b.

In Fig. 8a, the calcium-ribose outer-sphere species may attach through a hydrogen bond between a deprotonated ribose hydroxyl group and the neutral brucite surface resulting in the bond $>SOH\cdots O\text{-}C$. The calcium ion is electrostatically attracted to the ribose oxygen atoms in the 3’, 4’ and 5’ positions as suggested by previous studies on

Ca^{2+}-ribose aqueous complexes (Angyal, 1973; Morel et al., 1986). This calcium ribose species adsorbs in addition to the "standing" ribose species represented in Fig. 3. The equilibrium constant of the surface reaction in Eq. (10) can be expressed as

$$^{*}K^{0}_{>SOH\_Ca(Rib)^{+}} = \frac{a_{>SOH\_Ca(Rib)^{+}}\, a_{H^{+}}}{a_{>SOH}\, a_{HRib}\, a_{Ca^{2+}}}\, 10^{\frac{F\Delta\psi_{r,10}}{2.303RT}} \tag{12}$$

where $\Delta\psi_{r,10} = +\psi_{\beta}$.

In Fig. 8b, the calcium outer-sphere species attaches to a protonated surface site by a single hydrogen bond through the hydroxyl group (>SOH$\cdots$OH-CaOH). Here, we can express the equilibrium constant of the surface reaction proposed in Eq. (11) as

$$^{*}K^{0}_{>SOH_2^{+}\_Ca(OH)_2} = \frac{a_{>SOH_2^{+}\_Ca(OH)_2}\, a_{H^{+}}}{a_{>SOH}\, a_{Ca^{2+}}\, a^{2}_{H_2O}}\, 10^{\frac{F\Delta\psi_{r,11}}{2.303RT}} \tag{13}$$

where $\Delta\psi_{r,11} = +\psi_0$. We have proposed the reaction in Eq. (11) in a previous study of the brucite-aspartate system (Estrada et al., in review). Because the same batch of brucite was used in this study, we have adopted the same equilibrium constant recalculated for the decreased site density of $N_s = 31$ sites•nm^{-2}.

We combined the surface reactions in Eq. (5) or (6) and Eqs. (10-11) to fit the ribose adsorption data at low and high Ca^{2+} concentrations at pH= 10.2 and pH= 10.3, respectively, in Fig. 6b. The calculated curves are consistent with almost all the adsorption data collected at low and high Ca^{2+} concentrations within analytical uncertainty. The proposed surface reactions also predict curves for Ca^{2+} adsorption percentage as a function of initial ribose concentration, $[Rib]_0$, as represented in Fig. 7b. The predicted curves in this figure average 38.2 % for low Ca^{2+} concentrations, and 10.5 % for the high Ca^{2+} concentrations, which are in acceptable agreement with the bulk of the data, where the average Ca^{2+} adsorption values were 39.9 ± 2.8 % and 10.4 ± 1.6 %

for the low and high Ca^{2+} experiments, respectively. Therefore, we consider the models predicted by the surface reactions in Eq. (5) or (6) and Eqs. (10-11) to sufficiently characterize ribose adsorption and Ca^{2+} adsorption at the brucite-water interface at different ionic strengths, pH conditions, ribose concentrations, and divalent cation concentrations.

3.4. Prediction of Brucite Particle Surface Charge

We may explain the decrease in ribose surface adsorption with increased Mg^{2+} and its increased adsorption with added Ca^{2+} by examining the electrostatic environment at the brucite-water interface. We predicted the particle surface charge (ζ-potential) of brucite, which we assume is equal to Ψ_D, the potential beginning at the diffuse layer of the ETLM. This prediction is shown in Fig. 9 for the four ionic strengths investigated in this study, and it reveals that the ζ-potential is slightly negative at low Mg^{2+} concentrations. The particle surface charge decreases by 20 mV for the high Mg^{2+} experiments. The shift in ζ-potential may be a result of the decrease in pH that is required to maintain equilibrium between the brucite and aqueous solution when Mg^{2+} is added expressed by Eq. (2). In both Mg^{2+} experiments, the ζ-potential reflects our proposed surface reaction in Eq. (5) or (6), in which Rib^- adsorbs onto brucite. However, our prediction of more negative particle surface charge could also reflect our observations of decreased ribose adsorption with increasing Mg^{2+} as the negatively-charged brucite surface is electrostatically inhibited from adsorbing ribose.

In contrast to the Mg^{2+} experiments, we predicted that the ζ-potential significantly increases toward positive values of 55 mV and 65 mV for the low Ca^{2+} and high Ca^{2+}

experiments, respectively. For both Ca^{2+} experiments, we observed a high degree of Ca^{2+} adsorption, and these observations in addition to our proposed surface reactions in Eqs. (10-11) influence the increase in the ζ-potential. Additionally, we observed a small increase in ribose adsorption in our Ca^{2+} experiments, and this increase may have been promoted by the formation of a calcium-ribose complex at the surface. This conclusion is supported by our prediction of the distribution of the ribose species on brucite at low Ca^{2+} concentrations and high Ca^{2+} concentrations as shown by Fig. 10. At both concentrations, we predict the calcium-ribose outer-sphere species predominates over the "standing" species on the brucite surface.

In our previous investigation of the brucite-aspartate system, we observed a significantly greater increase in aspartate adsorption onto brucite under similar Ca^{2+} concentrations (Estrada et al., in review). The difference in the amount of surface adsorption between aspartate and ribose with Ca^{2+} illustrates how a calcium-ligand complex is affected by different biomolecules. It is possible that ribose forms a weaker attachment to Ca^{2+} than the aspartate molecule, as indicated by the multiple bonding sites required to form the calcium-ribose complex and the low equilibrium constant for the formation of the aqueous calcium-ribose complex (Morel et al., 1986). Moreover, the ribose molecule, rather than the calcium ion, is likely attaching onto brucite as shown in Fig. 8a. These factors, when considered together, may have limited the increase in ribose adsorption in the Ca^{2+} experiments compared to aspartate. Should a neutral or positively-charged biomolecule adsorb onto the brucite surface along with added Ca^{2+}, it is possible that it will compete with the Ca^{2+} ion for adsorption onto the brucite surface.

3.5. Prediction of Ribose Adsorption as a Function of pH

We have extended our model of the ribose-brucite system to predict ribose adsorption onto brucite under the four ionic strengths we investigated over the pH range of 5 to 12. Because pH is dependent on the concentration of Mg^{2+} for brucite to maintain equilibrium with the aqueous phase (Eq. 2), it is unlikely that these ionic strengths would naturally persist at this pH range. Nevertheless, this prediction may provide a fundamental estimation of the magnitude of ribose adsorption in different environments. As illustrated by Fig. 11, there is a significant amount of ribose surface adsorption at low and high Mg^{2+} concentrations at highly alkaline pH conditions (between 11 and 12) where Γ_{ads}= 3.0 μmol•m^{-2} when $[Rib]_0$ is at 500 μM. Additionally, we predicted ribose adsorption up to 3.4 μmol•m^{-2} at high Ca^{2+} concentrations and a pH value of 9 when $[Rib]_0$ is at 500 μM. This prediction may indicate that ribose adsorption is favorable on brucite in an alkaline environment with elevated Ca^{2+} concentrations.

Fluids within serpentinite-hosted hydrothermal environments have high Ca^{2+}/Mg^{2+} ratios and alkaline pH. We therefore predicted the adsorption of ribose onto the brucite surface in the presence of Lost City-type fluids at ambient temperatures and pressures. We obtained the major ion composition of Lost City vent fluids from a previous study, where pH= 9.8, $[Ca^{2+}]$= 23.3x10^{-3} M, and $[Mg^{2+}]$= 0 M (Kelley et al., 2002). In Fig. 12, we predicted the extent of ribose adsorption onto brucite at pH values of 9.8 and 10.2. We predicted that ribose adsorption does not exceed 0.3 μmol•m^{-2}, or approximately <2 %, on brucite under these conditions. This predicted amount of adsorption is the same magnitude that we observed in our experiments, however, the low extent of surface adsorption indicates that serpentinite-hosted hydrothermal environments are unlikely to play an important role in concentrating ribose when brucite alone is considered. It may be possible that a localized, hyperalkaline aqueous system would act as a suitable environment for ribose adsorption, although it is unlikely that this type environment is prevalent, either among modern or ancient aqueous systems.

4. Concluding Remarks

We conducted batch adsorption experiments to characterize the adsorption of ribose onto brucite at low Mg^{2+} ($0.6x10^{-3}$ M), high Mg^{2+} ($5.8x10^{-3}$ M), low Ca^{2+} ($1.0x10^{-3}$ M) and high Ca^{2+} ($4.2x10^{-3}$ M) concentrations at 25 ºC and 1 bar. Our results revealed that the adsorption of ribose increased when Ca^{2+} is added to the system, whereas it decreased with the addition of Mg^{2+}. We obtained a thermodynamic characterization of ribose adsorption onto brucite using the ETLM. We constructed two possible models that describe the experimental data. Both models contain three fundamental types of surface reactions that involve 1) a bidentate outer-sphere, or “standing” ribose species, 2) a calcium-ribose complex attaching as a monodentate outer-sphere species, and 3) the hydrated calcium ion attaching as a monodentate outer-sphere species.

We tested our surface complexation models against the data collected at four different ionic strengths, variable initial ribose concentrations, and different pH conditions depending on the amount of Mg^{2+} in the system. We also tested the models with the Ca^{2+} adsorption data we collected as a function of initial ribose concentration. In each case, the three surface reactions we proposed with the ETLM were consistent with the experimental data within analytical uncertainty. Our success in representing the data with both models has provided strong support that these three types of surface reactions accurately depict ribose and Ca^{2+} adsorption onto brucite.

The two possible surface complexation models constructed with these three surface reactions predict that ribose adsorption significantly decreases when Mg^{2+} is added because the brucite particle charge, or the ζ-potential, becomes more negative. This addition of Mg^{2+} creates an unfavorable electrostatic environment for the negatively-charged ribose molecule to adsorb as a "standing" species. In contrast, we predict a reversal in brucite particle surface charge with the addition and subsequent adsorption of Ca^{2+}, and the observed increase in ribose adsorption may be due to the formation of a cooperative calcium-ribose complex. The surface complexation model predicts that the calcium-ribose outer-sphere species predominates over the "standing" species at both Ca^{2+} concentrations. However, we observe only a small increase in ribose surface adsorption when Ca^{2+} is added, and this may be a consequence of the weak attachment of ribose to Ca^{2+} or the assumption that the calcium-ribose outer-sphere species is attaching onto brucite through a deprotonated site of ribose, rather than the calcium ion.

We have used our surface complexation model to predict the adsorption of ribose onto brucite at a wide pH range of 5 to 12. This model reveals that ribose surface adsorption may significantly increase at highly alkaline conditions (Fig. 11). This prediction also indicates that a greater amount of ribose surface adsorption might occur at a pH of 9 at high Ca^{2+} concentrations, which could hold implications for ribose adsorption and concentration at serpentinite-hosted hydrothermal environments. However, when we applied our model to a system with a bulk water composition similar to the Lost City Hydrothermal Field (Kelley et al., 2002), we predicted that ribose surface adsorption is consistent with the observations of our high Ca^{2+} experiments. These results are likely to be relevant for serpentinite-hosted hydrothermal vents. Compared with aspartate, ribose does not adsorb onto brucite to a great extent. Even though adsorption levels are low, we have characterized the ribose-brucite system with batch adsorption experiments and surface complexation modeling, and we have further used these techniques to predict the behavior of this system in other environments. This model provides us with a novel understanding of ribose surface adsorption behavior and the role that both the brucite surface and Ca^{2+} might contribute to the evolution of prebiotic chemistry in early Earth aqueous systems.

Acknowledgements

We thank Cécile Feuillie, Namhey Lee, George Cody, Timothy Strobel, Dionysis Foustoukos, Paul Goldey, John Armstrong, Adrian Villegas-Jimenez, Stephen Hodge and Steven Coley for their invaluable expertise and advice throughout this project. We thank the National Science Foundation, the NASA Astrobiology Institute, the Deep Carbon Observatory, and the Carnegie Institution for Science for support of this research.

References

Angyal S. J. (1973) Complex formation between sugars and metal ions. *Pure Appl. Chem.* **35**, 131–146.

Angyal S. J. (1969) The composition and conformation of sugars in solution. *Angew. Chem. Int. Ed. Engl.* **8**, 157–166.

Arora A. K. and Kamaluddin (2007) Interaction of ribose nucleotides with zinc oxide and relevance in chemical evolution. *Colloids Surf., A* **298**, 186–191.

Banin A., Lawless J. G., Mazzurco J., Church F. M., Margulies L. and Orenberg J. B. (1985) pH profile of the adsorption of nucleotides onto montmorillonite. *Orig. Life Evol. Biosph.* **15**, 89–101.

Benner S. A. (2004) Understanding nucleic acids using synthetic chemistry. *Acc. Chem. Res.* **37**, 784–797.

Bhushan B., Shanker U. and Kamaluddin (2011) Adsorption of ribose nucleotides on manganese oxides with varied Mn/O ratio: Implications for chemical evolution. *Orig. Life Evol. Biosph.* **41**, 469–482.

Biester H., Müller G. and Schöler H. F. (2002) Binding and mobility of mercury in soils contaminated by emissions from chlor-alkali plants. *Sci. Total Environ.* **284**, 191-203.

Charlou J., Donval J., Fouquet Y., Jean-Baptiste P. and Holm N. G. (2002) Geochemistry of high H_2 and CH_4 vent fluids issuing from ultramafic rocks at the Rainbow hydrothermal field (36 14'N, MAR). *Chem. Geol.* **191**, 345–359.

Clarke A. P., Jandik P., Rocklin R. D., Liu Y. and Avdalovic N. (1999) An integrated amperometry waveform for the direct, sensitive detection of amino acids and amino sugars following anion-exchange chromatography. *Anal. Chem.* **71**, 2774–2781.

Cleaves H. J. II, Jonsson C. M., Jonsson C. L., Sverjensky D. A. and Hazen R. M. (2010) Adsorption of nucleic acid components on rutile (TiO2) surfaces. *Astrobiology* **10**, 311–323.

Cleaves H. J., Michalkova Scott A., Hill F. C., Leszczynski J., Sahai N. and Hazen R. M. (2012) Mineral–organic interfacial processes: Potential roles in the origins of life. *Chem. Soc. Rev.* **41**, 5502.

Delacour A., Früh-Green G. L., Bernasconi S. M., Schaeffer P. and Kelley D. S. (2008) Carbon geochemistry of serpentinites in the Lost City Hydrothermal System (30°N, MAR). *Geochim. Cosmochim. Acta* **72**, 3681–3702.

Estrada C. F., Sverjensky D. A., Pelletier M., Razafitianamaharavo A. and Hazen R. M. (2014) Interaction between L-aspartate and the brucite [Mg(OH)2]-water interface

Geochim. Cosmochim. Acta. In Review.

Eypert-Blaison C., Villiéras F., Michot L. J., Pelletier M., Humbert B., Ghanbaja J. and Yvon J. (2002) Surface heterogeneity of kanemite, magadiite and kenyaite: A high-resolution gas adsorption study. *Clay Miner.* **37**, 531–542.

Ferris J. P. (1993) Catalysis and prebiotic RNA synthesis. *Orig. Life Evol. Biosph.* **23**, 307–315.

Feuillie C., Daniel I., Michot L. J. and Pedreira-Segade U. (2013) Adsorption of nucleotides onto Fe–Mg–Al rich swelling clays. *Geochim. Cosmochim. Acta* **120**, 97–108.

Gabel N. W. and Ponnamperuma C. (1967) Model for origin of monosaccharides. *Nature* **216**, 453–455.

Geiger F. M. (2009) Second harmonic generation, sum frequency generation, and χ (3): Dissecting environmental interfaces with a nonlinear optical swiss army knife. *Annu. Rev. Phys. Chem.* **60**, 61–83.

Goldberg, R. N. and Tewari, Y. B. (1989) Thermodynamic and transport properties of carbohydrates and their monophosphates - the pentoses and hexoses. *J. Phys. Chem. Ref. Data* **18**, 809–880.

Graydon J. W., Zhang X., Kirk D. W. and Jia C. Q. (2009) Sorption and stability of mercury on activated carbon for emission control. *J. Hazard. Mater.* **168**, 978-982.

Hashizume H. and Theng B. K. G. (2007) Adenine, adenosine, ribose and 5′-AMP adsorption to allophane. *Clay Clay Miner* **55**, 599–605.

Hashizume H., Van der Gaast S. and Theng B. K. G. (2010) Adsorption of adenine, cytosine, uracil, ribose, and phosphate by Mg-exchanged montmorillonite. *Clay Miner.* **45**, 469–475.

Hazen R. M. (2005a) Genesis: Rocks, minerals, and the geochemical origin of life. *Elements* **1**, 135–137.

Hazen R. M. (2005b) *Genesis: The Scientific Quest for Life's Origin*, Joseph Henry Press, Washington, DC.

Hazen R. M. (2006) Presidential address to the mineralogical society of america, Salt Lake City, October 18, 2005: Mineral surfaces and the prebiotic selection and organization of biomolecules. *Am. Mineral.* **91**, 1715–1729.

Henrist C., Mathieu J., Vogels C., Rulmont A. and Cloots R. (2003) Morphological study of magnesium hydroxide nanoparticles precipitated in dilute aqueous solution. *J. Cryst. Growth* **249**, 321–330.

Holland J. G., Malin J. N., Jordan D. S. and Geiger F. M. (2011) Specific and nonspecific metal ion−nucleotide interactions at aqueous/solid interfaces functionalized with adenine, thymine, guanine, and cytosine oligomers. *J. Am. Chem. Soc.* **133**, 2567–2570.

Holm N. G. (2012) The significance of Mg in prebiotic geochemistry. *Geobiology* **10**, 269–279.

Holm N. G., Dumont M., Ivarsson M. and Konn C. (2006) Alkaline fluid circulation in ultramafic rocks and formation of nucleotide constituents: A hypothesis. *Geochem. Trans.* **7**, 1–13.

Hostetler P. B. (1963) The stability and surface energy of brucite in water at 25 degrees C. *Am. J. Sci.* **261**, 238–258.

Huang W. and Ferris J. P. (2006) One-step, regioselective synthesis of up to 50-mers of RNA oligomers by montmorillonite catalysis. *J. Am. Chem. Soc.* **128**, 8914–8919.

Ittekkot V., Haake B., Bartsch M., Nair R. R. and Ramaswamy V. (1992) Organic carbon removal in the sea: The continental connection. *Geol. Soc. London Spec. Pub.* **64**, 167–176.

Jandik P., Pohl C., Barreto V. and Avdalovic N. (2000) Anion exchange chromatography and integrated amperometric detection of amino acids. In *Amino acid analysis protocols* Humana Press, New Jersey. pp. 63–85.

Jensen D., Weiss J., Rey M. A. and Pohl C. A. (1993) Novel weak acid cation-exchange column. *J. Chromatogr., A* **640**, 65–71.

Jordan G. and Rammensee W. (1996) Dissolution rates and activation energy for dissolution of brucite (001) : A new method based on the microtopography of crystal surfaces. *Geochim. Cosmochim. Acta* **60**, 5055–5062.

Kelley D. S., Baross J. A. and Delaney J. R. (2002) Volcanoes, fluids, and life at mid-ocean ridge spreading centers. *Annu. Rev. Earth Planet. Sci.* **30**, 385–491.

Kelley D. S., Karson J. A., Fruh-Green G. L., Yoerger D. R., Shank T. M., Butterfield D. A., Hayes J. M., Schrenk M. O., Olson E. J., Proskurowski G., Jakuba M., Bradley A., Larson B., Ludwig K., Glickson D., Buckman K., Bradley A.S., Brazelton W.J., Roe K., Elend M.J., Delacour A., Bernasconi S.M., Lilley M.D., Baross J.A., Summons R.T., and Sylva S.P. (2005) A serpentinite-hosted ecosystem: the Lost City hydrothermal field. *Science* **307**, 1428-1434.

Kim H.-J., Ricardo A., Illangkoon H. I., Kim M. J., Carrigan M. A., Frye F. and Benner S. A. (2011) Synthesis of carbohydrates in mineral-guided prebiotic cycles. *J. Am. Chem. Soc.* **133**, 9457–9468.

Kudoh Y., Kameda J. and Kogure T. (2006) Dissolution of brucite on the (001) surface at neutral pH: In situ atomic force microscopy observations. *Clay Clay Miner* **54**, 598–604.

LaRowe D. E. and Regnier P. (2008) Thermodynamic potential for the abiotic synthesis of adenine, cytosine, guanine, thymine, uracil, ribose, and deoxyribose in hydrothermal systems. *Orig. Life Evol. Biosph.* **38**, 383–397.

Liu X., Cheng J., Sprik M., Lu X. and Wang R. (2013) Understanding surface acidity of gibbsite with first principles molecular dynamics simulations. *Geochim. Cosmochim. Acta* **120**, 487–495.

Lu J., Qiu L. and Qu B. (2004) Controlled growth of three morphological structures of magnesium hydroxide nanoparticles by wet precipitation method. *J. Cryst. Growth* **267**, 676–684.

Malin J. N., Holland J. G. and Geiger F. M. (2009) Free energy relationships in the electric double layer and alkali earth speciation at the fused silica/water interface. *J. Phys. Chem., C* **113**, 17795–17802.

Michot L. J. and Villiéras F. (2002) Assessment of surface energetic heterogeneity of synthetic Na-saponites. The role of layer charge. *Clay Miner.* **37**, 39–57.

Morel J.-P., Lhermet C. and Morel-Desrosiers N. (1986) Interactions between cations and sugars. II. Enthalpies, heat capacities, and volumes of aqueous solutions of Ca^{2+}– D-ribose and Ca^{2+}– D-arabinose at 25 °C. *Can. J. Chem.* **64**, 996–1001.

Palmer D. (2009) CrystalMaker for Mac OS X, 8.2.2. *CrystalMaker Software Limited: Oxfordshire*.

Perronnet M., Villiéras F., Jullien M., Razafitianamaharavo A., Raynal J. and Bonnin D. (2007) Towards a link between the energetic heterogeneities of the edge faces of smectites and their stability in the context of metallic corrosion. *Geochim. Cosmochim. Acta* **71**, 1463–1479.

Pokrovsky O. S. and Schott J. (2004) Experimental study of brucite dissolution and precipitation in aqueous solutions: Surface speciation and chemical affinity control. *Geochim. Cosmochim. Acta* **68**, 31–45.

Pokrovsky O. S., Schott J. and Castillo A. (2005) Kinetics of brucite dissolution at 25°C in the presence of organic and inorganic ligands and divalent metals. *Geochim. Cosmochim. Acta* **69**, 905–918.

Prélot B., Villiéras F., Pelletier M., Gérard G., Gaboriaud F., Ehrhardt J.-J., Perrone J., Fedoroff M., Jeanjean J., Lefèvre G., Mazerolles L., Pastol J.-L., Rouchaud J.-C. and Lindecker C. (2003) Morphology and surface heterogeneities in synthetic goethites. *J. Colloid Interface Sci.* **261**, 244–254.

Proskurowski G., Lilley M. D., Kelley D. S. and Olson E. J. (2006) Low temperature volatile production at the Lost City Hydrothermal Field, evidence from a hydrogen stable isotope geothermometer. *Chem. Geol.* **229**, 331–343.

Reid C., Orgel L. E. and Ponnamperuma C. (1967) Nucleoside synthesis under potentially prebiotic conditions. *Nature* **216**, 936–936.

Rishpon J., O'Hara P. J., Lahav N. and Lawless J. G. (1982) Interaction between ATP, metal ions, glycine, and several minerals. *J Mol Evol* **18**, 179–184.

Sahai N. and Sverjensky D. A. (1998) GEOSURF: A computer program for modeling adsorption on mineral surfaces from aqueous solution. *Comput. Geosci.* **24**, 853–873.

Sahai N. and Sverjensky D. A. (1997) Solvation and electrostatic model for specific electrolyte adsorption. *Geochim. Cosmochim. Acta* **61**, 2827–2848.

Sayed-Hassan M., Villiéras F., Gaboriaud F. and Razafitianamaharavo A. (2006) AFM and low-pressure argon adsorption analysis of geometrical properties of phyllosilicates. *J. Colloid Interface Sci.* **296**, 614–623.

Schoonen M., Smirnov A. and Cohn C. (2004) A perspective on the role of minerals in prebiotic synthesis. *AMBIO* **33**, 539–551.

Schott H. (1981) Electrokinetic studies of magnesium hydroxide. *J. Pharm. Sci.* **70**, 486–489.

Sen S., Pal U. and Maiti N. C. (2014) pKa Determination of F-Ribose by Raman Spectroscopy. *J. Phys. Chem. B* **118**, 909–914.

Sverjensky D. A. (2005) Prediction of surface charge on oxides in salt solutions: Revisions for 1:1 (M+L−) electrolytes. *Geochim. Cosmochim. Acta* **69**, 225–257.

Sverjensky D. A. (2003) Standard states for the activities of mineral surface sites and species. *Geochim. Cosmochim. Acta* **67**, 17–28.

Sverjensky D. A. and Fukushi K. (2006) A predictive model (ETLM) for As(III) adsorption and surface speciation on oxides consistent with spectroscopic data. *Geochim. Cosmochim. Acta* **70**, 3778–3802.

Sverjensky D. A. and Sahai N. (1996) Theoretical prediction of single-site surface-protonation equilibrium constants for oxides and silicates in water. *Geochim. Cosmochim. Acta* **60**, 3773–3797.

Villiéras F., Cases J. M., François M., Michot L. J. and Thomas F. (1992) Texture and surface energetic heterogeneity of solids from modeling of low pressure gas adsorption isotherms. *Langmuir* **8**, 1789–1795.

Villiéras F., Michot L. J., Bardot F., Cases J. M., François M. and Rudziński W. (1997) An improved derivative isotherm summation method to study surface heterogeneity of clay minerals. *Langmuir* **13**, 1104–1117.

Fig. 1. SEM image of synthesized brucite after hydrothermal treatment. Hexagonal platelets are in lamellar clusters where the basal (001) is predominant (scale= 1 μM). The blue arrow indicates the (001) surface.

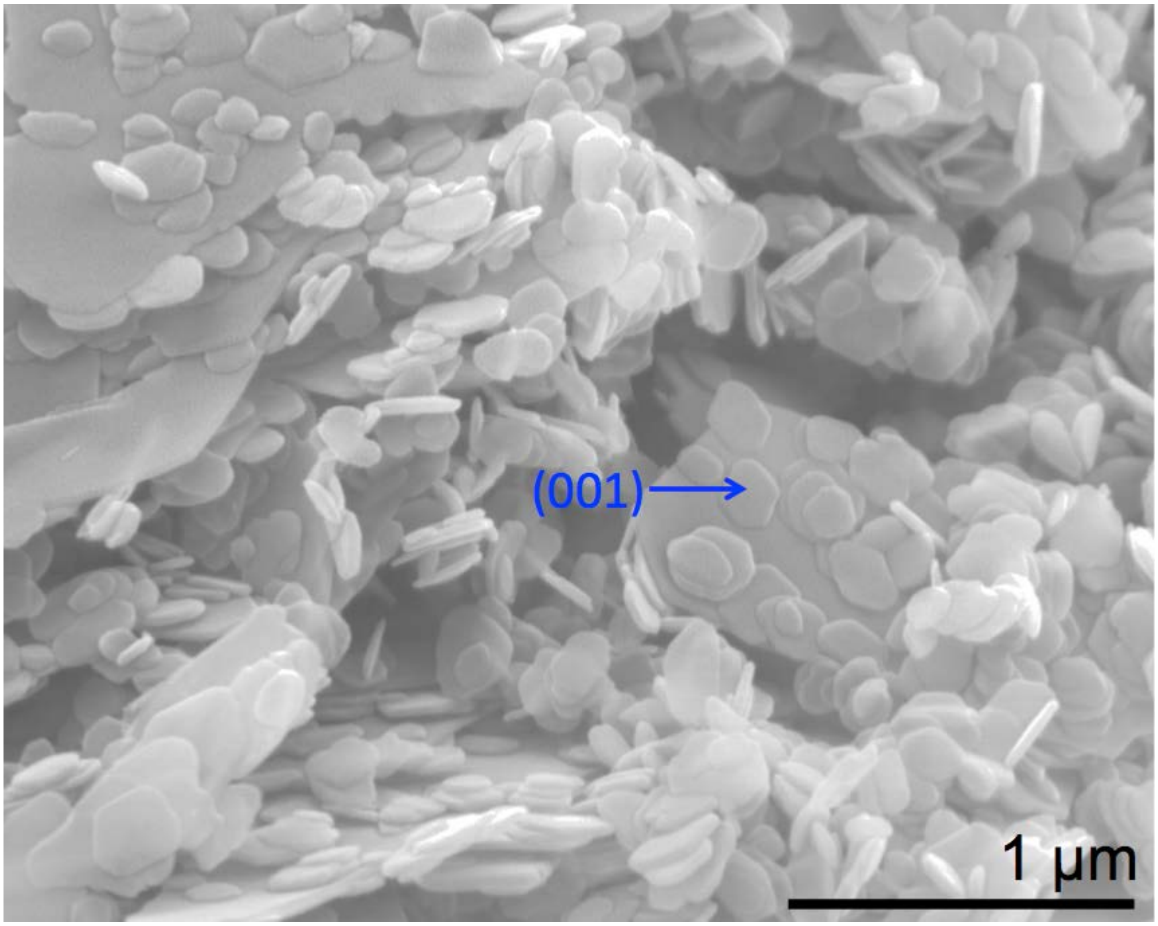

Fig. 2. a) Adsorption of ribose on brucite as a function of ribose concentration remaining in solution in the presence of a low Mg^{2+} concentration (Mg^{2+}= 0.6x10^{-3} M) and (b) predicted ribose adsorption at pH= 10.4 calculated using the parameters in Table 1. Symbols represent experimental data that are the average of a triplicate run and vertical error bars are ±1 standard error from the average and horizontal error bars fall within the data symbols. Dashed and dotted curves represent the calculated fits to the data with surface reactions in Eqs. (5) and (6), respectively.

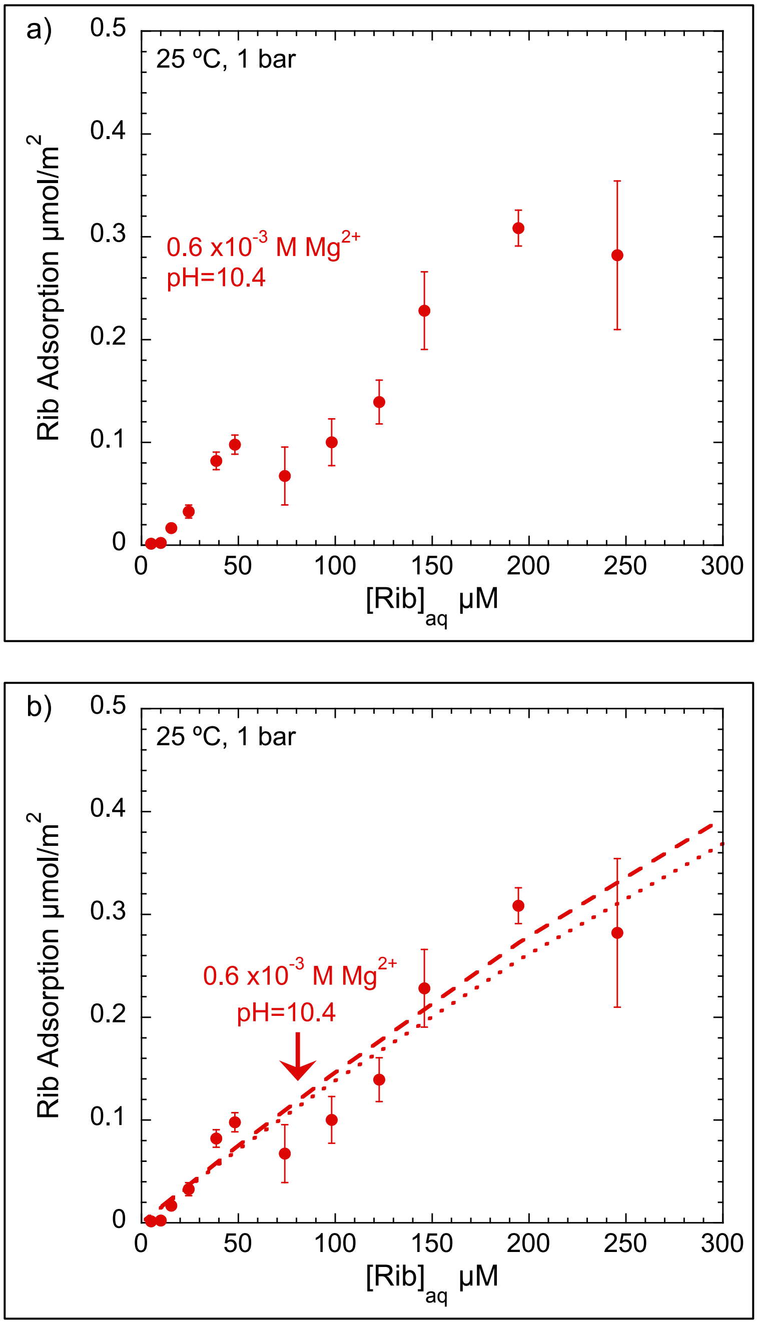

Fig. 3. Two possible representation of the surface species predicted by surface complexation calculations using the parameters in Table 1 where ribose attaches onto brucite as a bidentate outer-sphere, or "standing" species. Ribose attaches onto (100) brucite through a hydrogen bond between the protonated surface and a deprotonated –OH group ($>SOH_2^{+\cdots}O\text{-}C$) and a hydrogen bond between the ribose –OH group and either (a) the neutral surface ($>SOH^{\cdots}OH\text{-}C$) or (b) another protonated surface ($>SOH_2^{+\cdots}O\text{-}C$). Red spheres represent oxygen, yellow spheres are magnesium, pale tan spheres are hydrogen, and black spheres are carbon atoms.

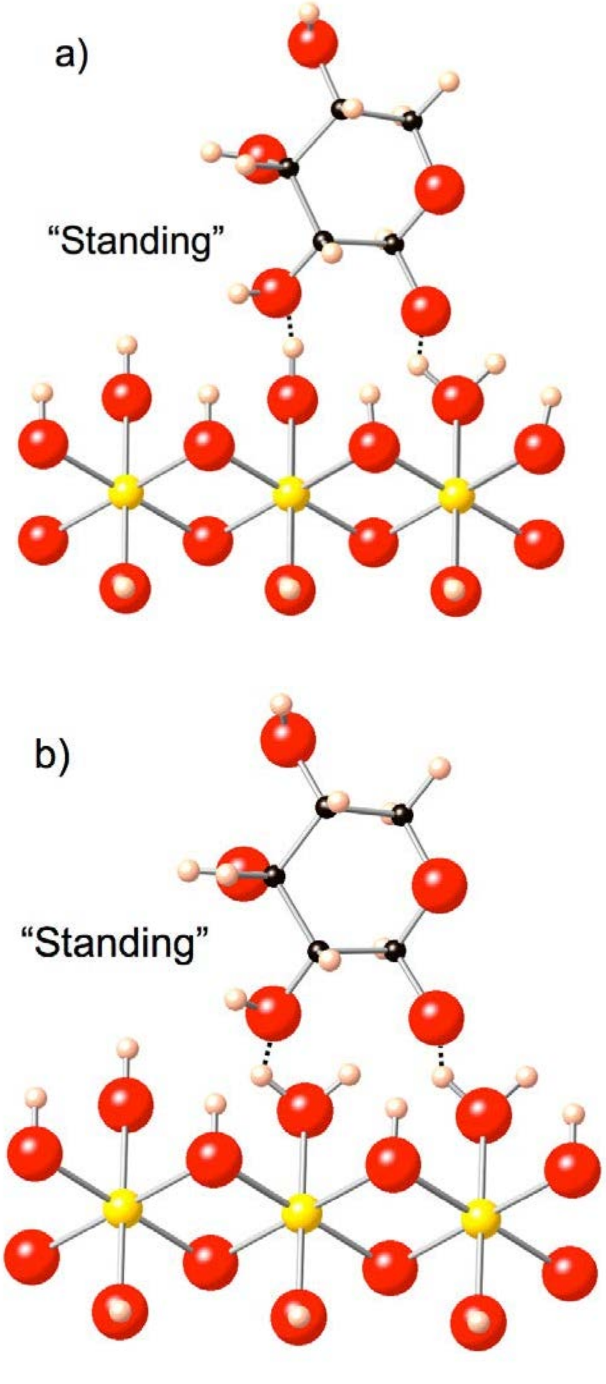

Fig. 4. Equilibrium constant, assumed to be equivalent to log[Mg^{2+}]/[H+]^2, as a function of solution pH following brucite/water and brucite/ribose batch experiments in the presence of (a) a low Mg^{2+} concentrations ([Mg^{2+}]= 0.6x10^{-3} M) and (b) both a low and high Mg^{2+} concentrations ([Mg^{2+}]= 0.6x10^{-3} M and [Mg^{2+}]= 5.8x10^{-3}, respectively) plotted alongside adsorption data for aspartate on the same batch of brucite. Symbols represent experimental data and vertical error bars represent ±1 standard deviation.

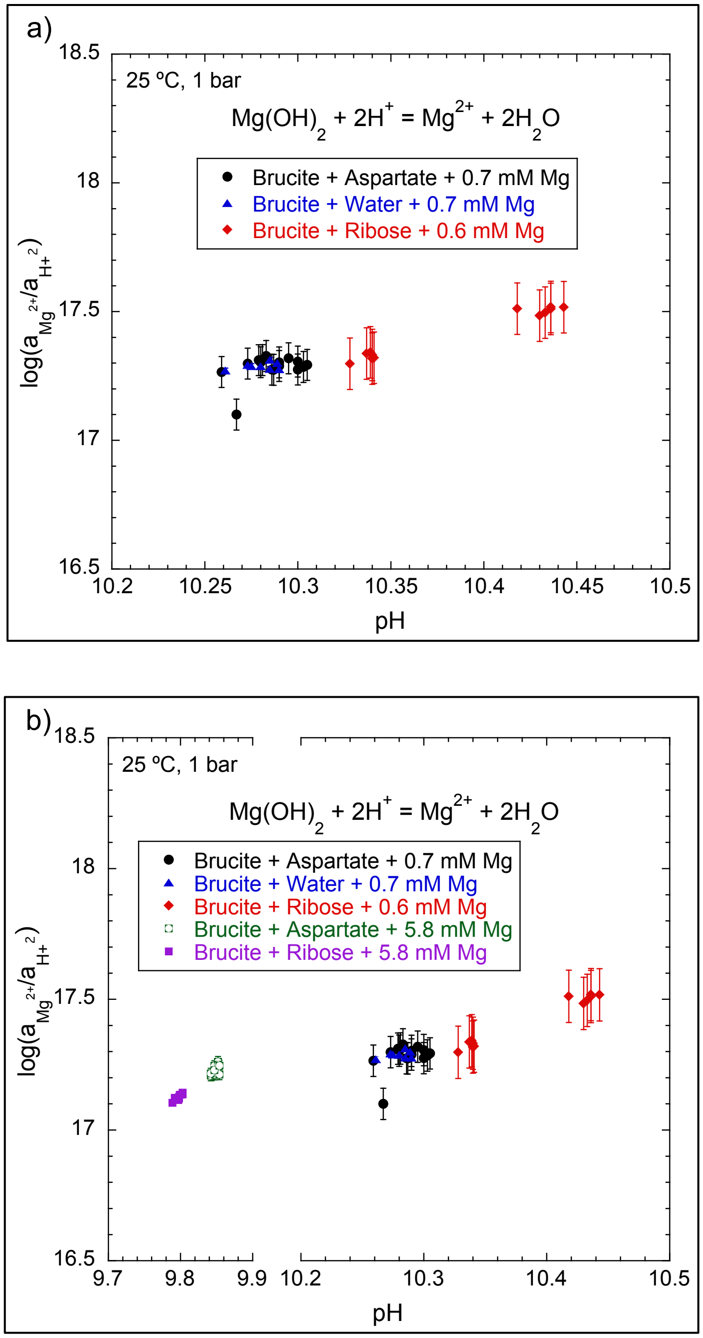

Fig. 5. (a) Adsorption of ribose onto brucite as a function of ribose concentration remaining in solution at low Mg^{2+} concentrations ($[Mg^{2+}]= 0.6x10^{-3}$ M) and high Mg^{2+} concentrations ($[Mg^{2+}]= 5.8x10^{-3}$ M) and (b) predicted ribose adsorption calculated with the parameters in Table 1 at the same electrolyte concentration and at pH= 10.4 and pH= 9.8, respectively. Symbols represent experimental data that are the average of a triplicate run and vertical error bars are ±1 standard error from the average and horizontal error bars fall within the data symbols. Dashed and dotted curves represent the calculated fits to the data with surface reactions in Eqs. (5) and (6), respectively.

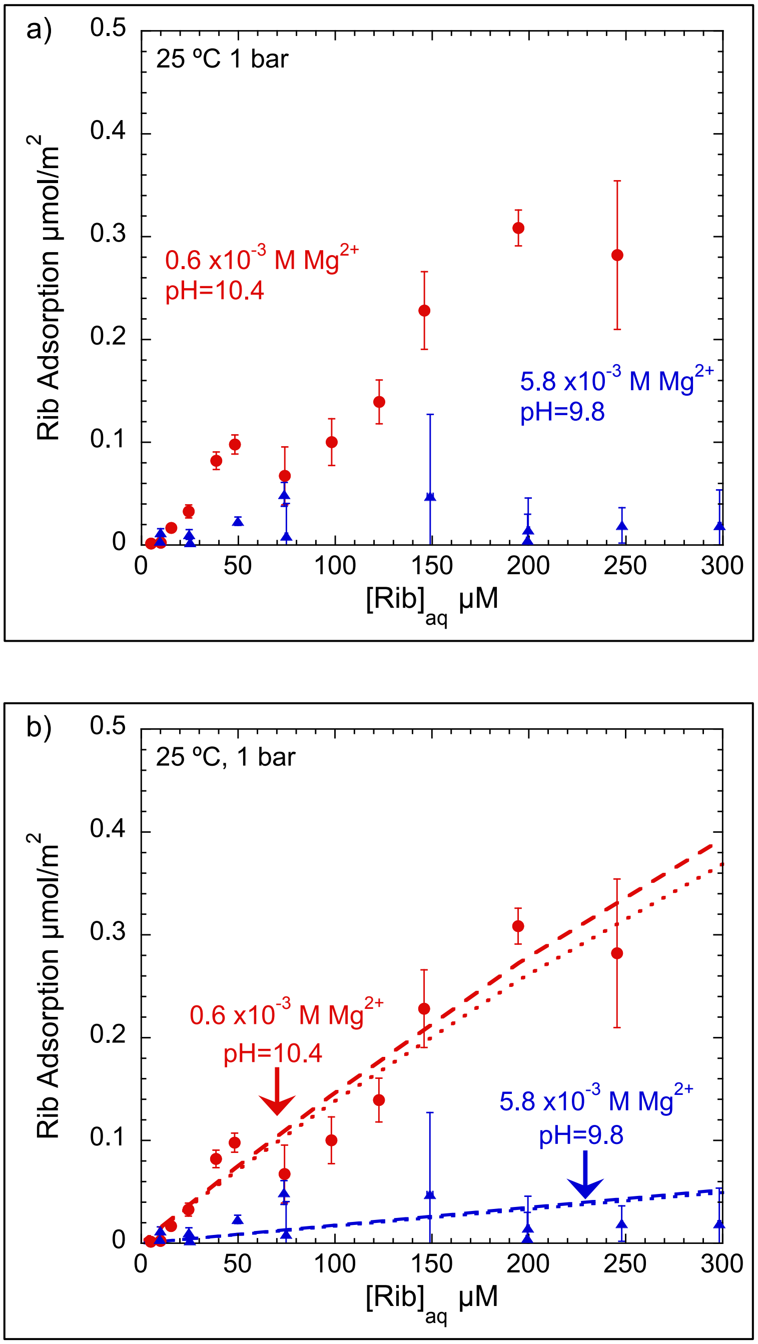

Fig. 6. (a) Adsorption of ribose onto brucite as a function of ribose concentration remaining in solution at low Ca^{2+} concentrations ($[Ca^{2+}]= 1.0\times10^{-3}$ M, $[Mg^{2+}]= 0.9\times10^{-3}$ M) and high Ca^{2+} concentrations ($[Ca^{2+}]= 4.2\times10^{-3}$ M, $[Mg^{2+}]= 0.6\times10^{-3}$ M) and (b) predicted ribose adsorption calculated with the parameters in Table 1 at low and high Ca^{2+} concentrations and pH= 10.2 and pH= 10.3, respectively. Symbols represent experimental data that are the average of a triplicate run and vertical error bars are ±1 standard error from the average and horizontal error bars fall within the data symbols. Dashed and dotted curves represent the calculated fits to the data with surface reactions in Eqs. (5) and (6), respectively.

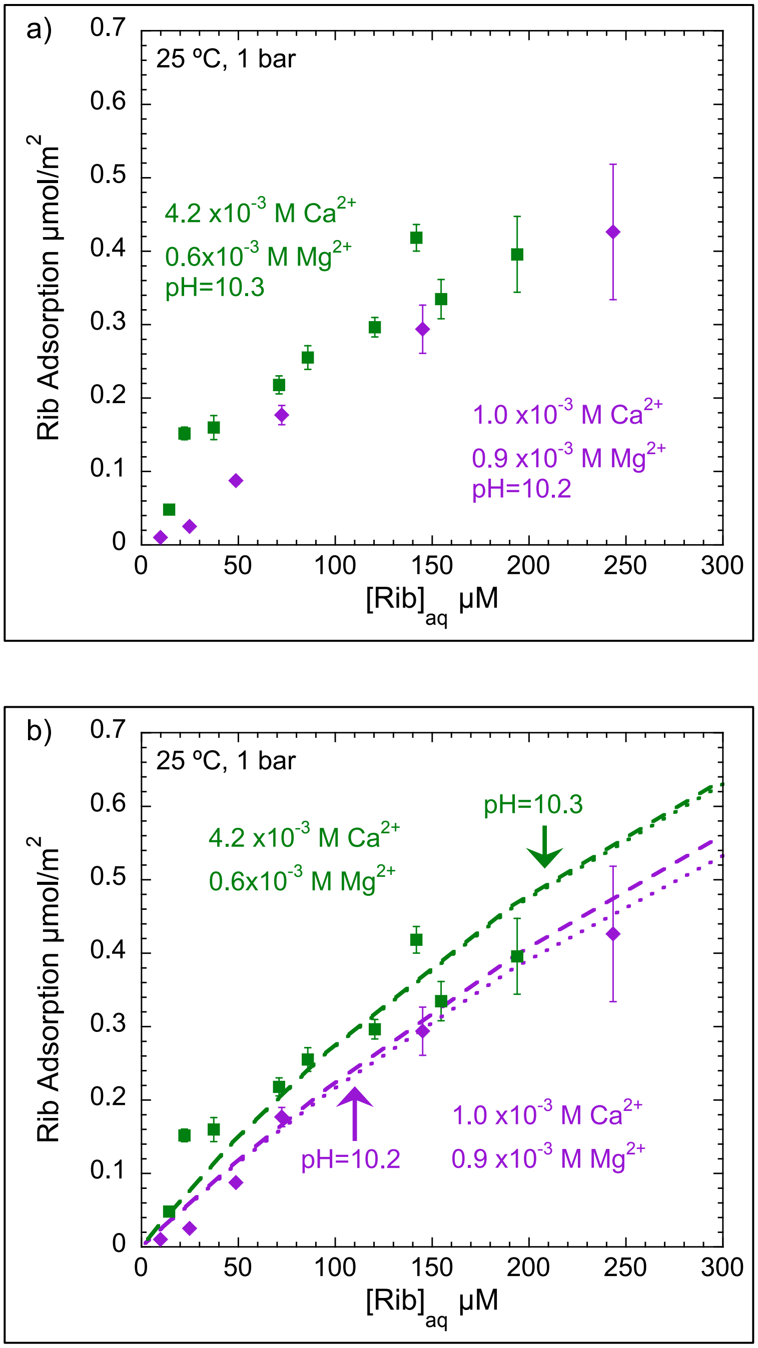

Fig. 7. (a) Adsorption of Ca^{2+} onto brucite as a function of initial ribose concentration at low Ca^{2+} concentrations ($[Ca^{2+}]$= 1.0x10^{-3} M, $[Mg^{2+}]$= 0.9x10^{-3} M); high Ca^{2+} concentrations ($[Ca^{2+}]$= 4.2x10^{-3} M, $[Mg^{2+}]$= 0.6x10^{-3} M); and (b) predicted Ca^{2+} adsorption calculated with the parameters in Table 1 at low and high Ca^{2+} concentrations at pH= 10.2 and pH= 10.3, respectively. Symbols represent experimental data and vertical error bars represent one standard deviation. Dashed curves represent the calculated fits to the data where curves from surface reactions in Eqs. (5) and (6) overlay one another.

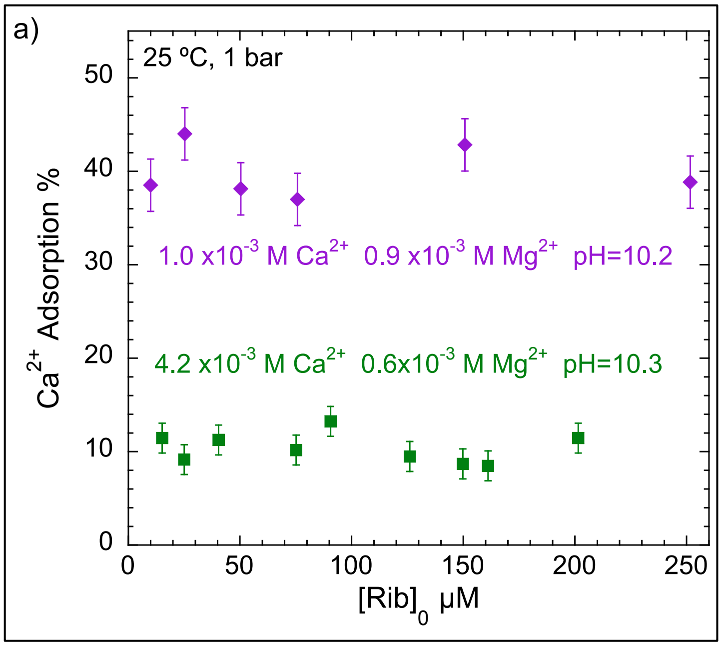

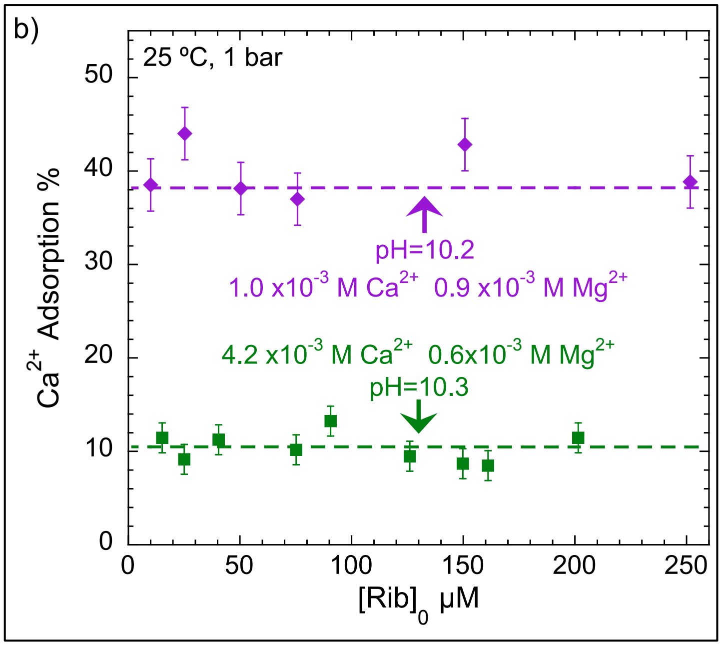

Fig. 8. Possible representation of surface species predicted by surface complexation calculations using the parameters in Table 1. (a) Attachment of a calcium-ribose complex to the (100) surface forming a monodentate outer sphere species that attaches through a hydrogen bond between the neutral surface and a deprotonated ribose hydroxyl group (>SOH$^{\cdots}$O-C). (b) Attachment of a hydrated calcium molecule to the brucite surface forming a monodentate outer-sphere species through a hydrogen bond between a positively charged surface site and the hydroxyl functional group (>SOH$^{\cdots}$OH-CaOH). Red spheres represent oxygen, yellow spheres are magnesium, pale tan spheres are hydrogen, large light blue spheres are calcium, and black spheres are carbon atoms.

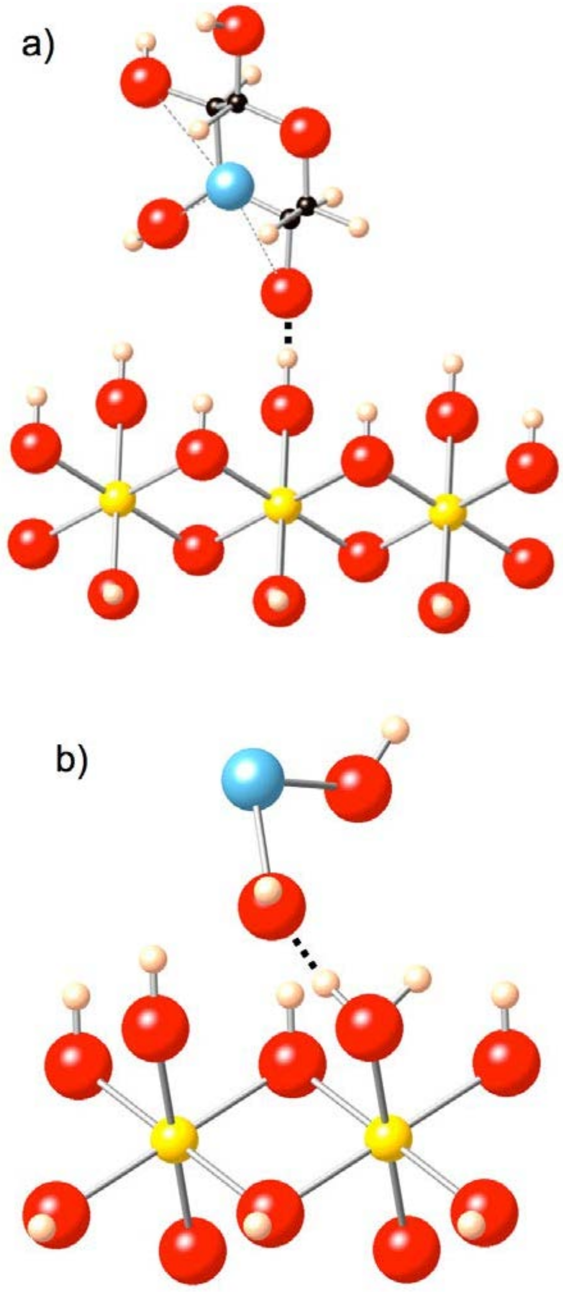

Fig. 9. ζ-potential (mv), or particle surface charge, predicted by surface complexation calculations with parameters in Table 1 as a function of initial ribose concentration in the presence of low Mg^{2+} concentrations ($[Mg^{2+}]= 0.6x10^{-3}$ M, pH= 10.4), high Mg^{2+} concentrations ($[Mg^{2+}]= 5.8x10^{-3}$ M, pH= 9.80), low Ca^{2+} concentrations ($[Ca^{2+}]= 1.0x10^{-3}$ M, $[Mg^{2+}]= 0.9x10^{-3}$ M, pH= 10.2) and high Ca^{2+} concentrations ($[Ca^{2+}]= 4.2x10^{-3}$ M, $[Mg^{2+}]= 0.6x10^{-3}$, pH= 10.3). Dashed curves represent the calculated fits to the data where curves from surface reactions in Eqs. (5) and (6) overlay one another.

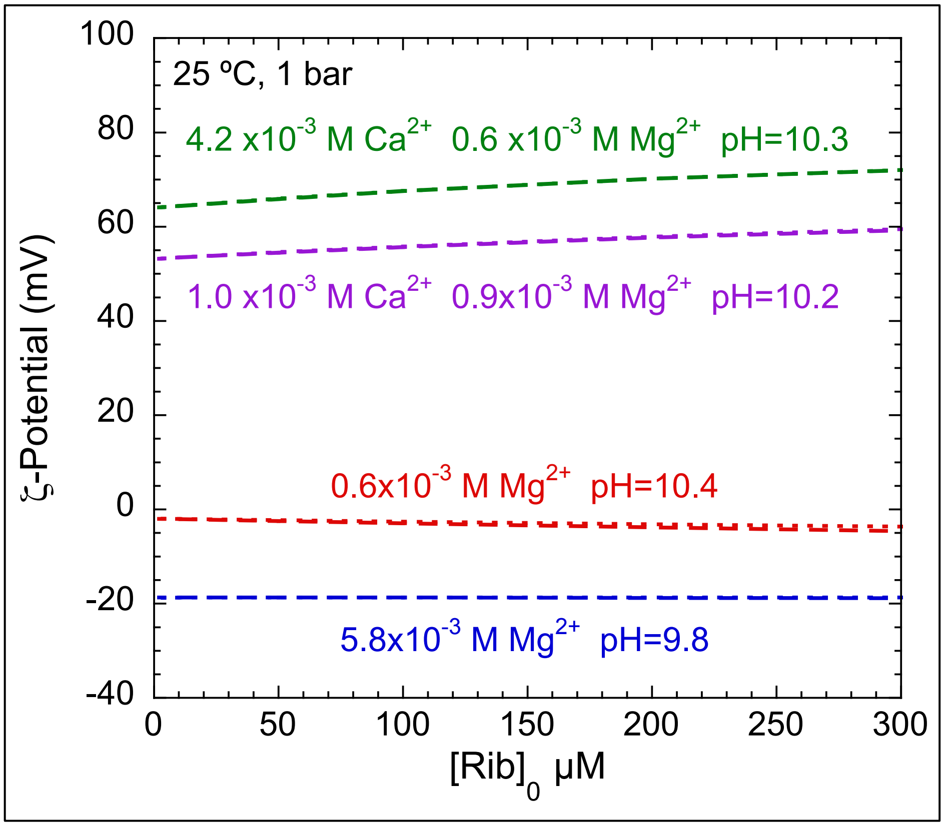

Fig. 10. Predicted surface speciation of ribose on brucite as a function of initial ribose concentration at (a) low Ca^{2+} concentrations ($[Ca^{2+}]$= 1.0x10^{-3} M, $[Mg^{2+}]$= 0.9x10^{-3} M, pH= 10.2), and (b) high Ca^{2+} concentrations ($[Ca^{2+}]$= 4.2x10^{-3} M, $[Mg^{2+}]$= 0.6x10^{-3}, pH= 10.3). The "standing" and outer-sphere species refer to Fig. 3 and Fig. 8a, and reaction stoichiometries in Eqs. (6-7) and (10), respectively, where predictions for Eq. (6) and (7) overlay one another. Colored curves represent the individual species and the black curve represents the total ribose adsorption.

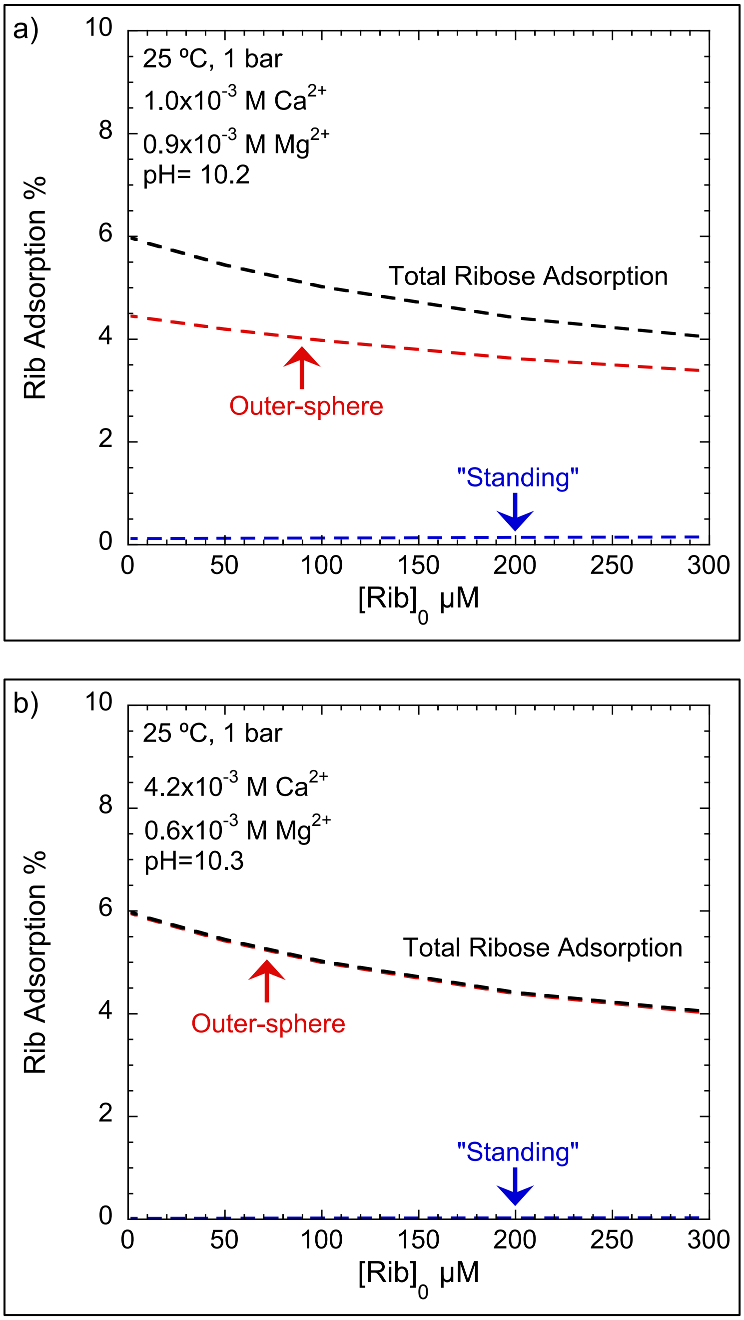

Fig. 11. Predicted ribose surface adsorption as a function of pH at low Mg^{2+} concentrations ($[Mg^{2+}]= 0.6x10^{-3}$ M) in red, high Mg^{2+} concentrations ($[Mg^{2+}]= 5.8x10^{-3}$ M) in blue, low Ca^{2+} concentrations ($[Ca^{2+}]= 1.0x10^{-3}$ M, $[Mg^{2+}]= 0.9x10^{-3}$ M) in purple, and high Ca^{2+} concentrations ($[Ca^{2+}]= 4.2x10^{-3}$ M, $[Mg^{2+}]= 0.6x10^{-3}$ M) in green with an initial ribose concentration of a) 100 µM and b) 500 µM. Dashed and dotted curves were calculated with the surface reactions in Eqs. (5) and (6), respectively.

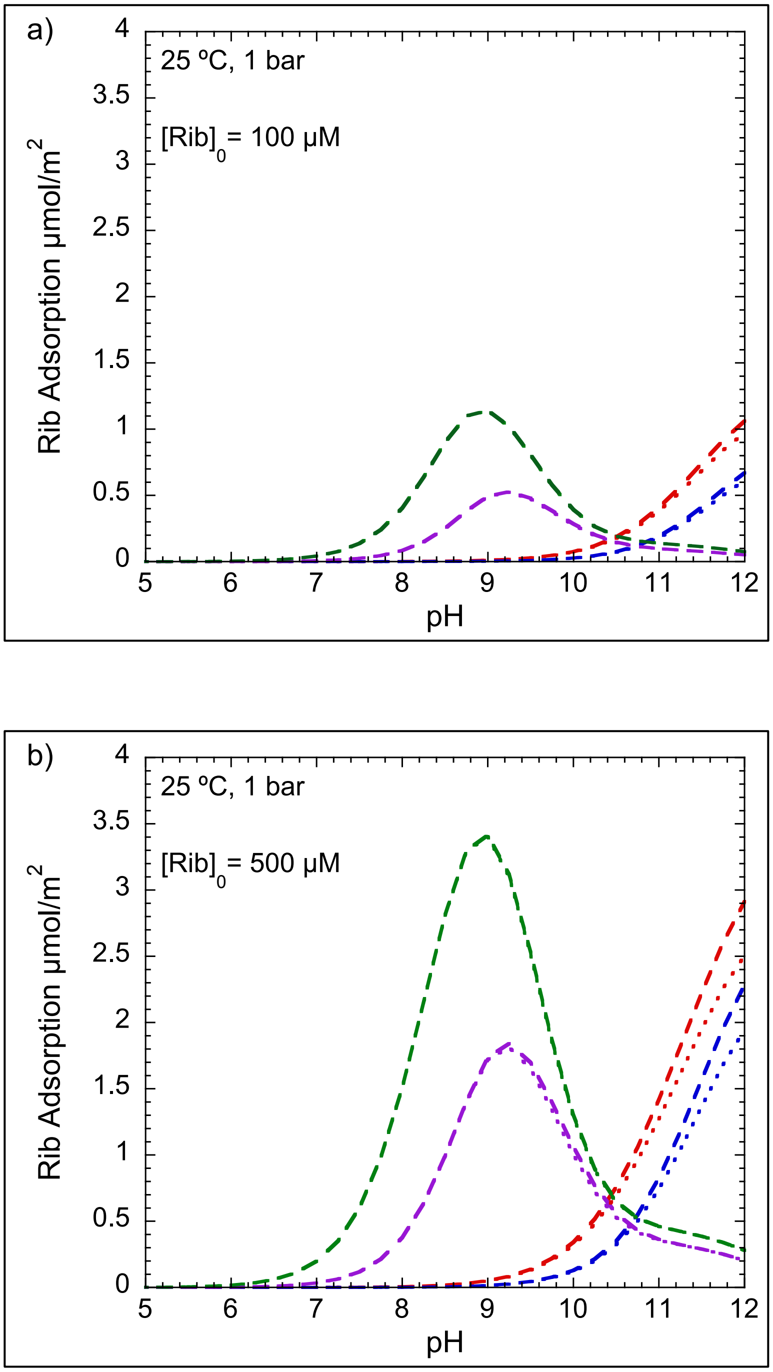

Fig. 12. Predicted ribose surface adsorption on brucite as a function of ribose concentration remaining in solution in the presence of Lost City-type fluids at 25 ºC and 1 bar. Ribose adsorption is calculated with the parameters in Table 1 in the presence of [Na^+]= 0.485 M, [Cl^-]= 0.549 M, [Ca^{2+}]= 23.3×10^{-3} M, and [SO_4^{2-}]= 12.9×10^{-3} M at pH= 9.8[a] and pH= 10.2[b]. Dashed curves represent the calculated fits to the data where curves from surface reactions in Eqs. (5) and (6) overlay one another.

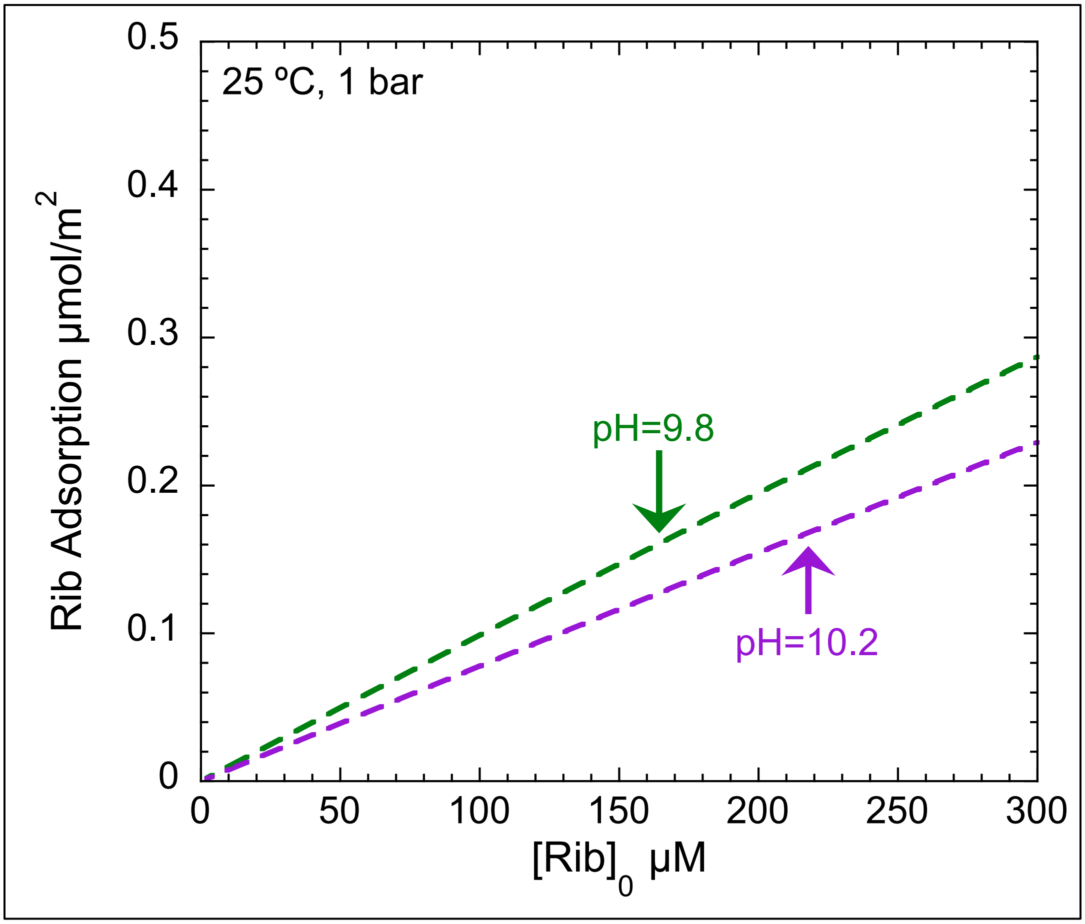

Table 1. Aqueous ribose properties, characteristics of brucite[a] [$Mg(OH_2)$], and extended triple-layer model parameters for proton electrolyte and ribose adsorption onto brucite.

Reaction Type	Reaction	log K
Aqueous ribose equilibria	$Rib^- + H^+ = HRib^0$	12.00
	[b]$HRib^0 + Ca^{2+} = HRibCa^{2+}$	-0.85
Surface equilibria	Hypothetical 1.0 m standard state	
$\log K_1^0$	$>SOH + H^+ = >SOH_2^+$	9.69
$\log K_2^0$	$>SO^- + H^+ = >SOH$	11.31
$\log {}^*K^0_{Na^+}$	$>SOH + Na^+ = >SO^-\_Na^+ + H^+$	-8.91
$\log {}^*K^0_{Cl^-}$	$>SOH + Cl^- + H^+ = >SOH_2^+\_Cl^-$	11.89
$\log {}^*K^0_{>SOH>SOH_2^+\_Rib^-}$	$2>SOH + HRib^0 = >SOH>SOH_2^+\_Rib^-$	4.97
$\log {}^*K^0_{2>SOH_2^+\_Rib^-}$	$2>SOH + H^+ + HRib^0 = 2>SOH_2^+\_Rib^-$	15.45
$\log {}^*K^0_{>SOH\_CaRib^+}$	$>SOH + Ca^{2+} + HRib^0 = >SOH\_CaRib^+ + H^+$	-3.43
$\log {}^*K^0_{>SOH_2^+\_Ca(OH)_2}$	$>SOH + Ca^{2+} + 2H_2O = >SOH_2^+\_Ca(OH)_2 + H^+$	-5.11
Surface equilibria[c]	Site-occupancy standard states	
$\log K^{\theta}_{>SOH>SOH_2^+\_Rib^-}$	$2>SOH_2^+ + HRib^0 = >SOH>SOH_2^+\_Rib^- + 2H^+$	7.51
$\log K^{\theta}_{2>SOH_2^+\_Rib^-}$	$2>SOH_2^+ + HRib^0 = 2>SOH_2^+\_Rib^- + H^+$	17.99
$\log K^{\theta}_{>SOH\_CaRib^+}$	$>SOH + Ca^{2+} + HRib^0 = >SOH\_CaHRib^+$	-3.66
$\log K^{\theta}_{>SOH_2^+\_Ca(OH)_2}$	$>SOH_2^+ + Ca^{2+} + 2H_2O = >SOH_2^+\_Ca(OH_2) + H^+$	-5.34

[a] Protonation constants and electrolyte ion pair constants modified from Pokrovsky et al. (2004) by Estrada and coworkers (in review).

[b] From Morel et al. (1986)

[c] Equilibrium constants relative to site occupancy standard states can be written relative to charged surface sites calculated using the equations: $\log K^{\theta}_{>SOH>SOH_2^+\_Rib^-} = \log {}^*K^0_{>SOH>SOH_2^+\_Rib^-} + \log(N_sA_sC_s)/100$; $\log K^{\theta}_{2>SOH_2^+\_Rib^-} = \log {}^*K^0_{2>SOH_2^+\_Rib^-} + \log(N_sA_sC_s)/100$; $\log K^{\theta}_{>SOH\_CaRib^+} = \log {}^*K^0_{>SOH\_CaRib^+} + \log(N_sA_s)/100$; $\log K^{\theta}_{>SOH_2^+\_Ca(OH)_2} = \log {}^*K^0_{>SOH_2^+\_Ca(OH)_2} + \log(N_sA_s)/100$, where N_s is site density, A_s is BET edge surface area $m^2 \bullet g^{-1}$, and C_s is solid concentration $g \bullet L^{-1}$.

Table 2. Ribose adsorption data observed for the low Mg^{2+}, high Mg^{2+}, low Ca^{2+} and high Ca^{2+} batch experiments.

Batch Experiment	**$[Rib]_{aq}$ (μM)**	**Γ_{ads} (μmol•m^{-2})**	**% Ads**
Low Mg^{2+}	5.0	<0.01	0.6
	15.4	0.02	2.0
	38.6	0.08	3.9
	122.7	0.14	2.1
	194.5	0.31	3.0
	245.6	0.28	2.1
	10.0	<0.01	0.4
	24.3	0.03	2.5
	48.2	0.10	3.7
	74.0	0.07	1.7
	98.1	0.10	1.9
	146.0	0.23	3.1
High Mg^{2+}	9.6	<0.01	0.8
	25.1	<0.01	0.2
	49.8	0.02	0.9
	74.8	0.01	0.2
	149.0	0.05	0.6
	199.6	0.01	0.1
	9.9	0.01	0.1
	24.7	0.01	0.8
	73.7	0.05	1.3
	199.2	<0.01	0.0
	247.9	0.02	0.1
	298.3	0.02	0.1
Low Ca^{2+}	9.8	0.01	2.0
	24.8	0.03	2.0
	48.7	0.09	3.3
	72.4	0.18	4.4
	145.1	0.29	3.8
	243.4	0.43	3.3
High Ca^{2+}	22.2	0.15	11.4
	71.0	0.22	5.5
	141.9	0.42	5.3
	14.3	0.05	6.1
	37.3	0.16	7.6
	85.8	0.26	5.3
	120.4	0.30	4.4
	154.6	0.33	4.0
	193.9	0.40	3.8

Table 3. Ca^{2+} adsorption data observed for the low Ca^{2+} and high Ca^{2+} batch experiments.

Batch Experiment	**$[Ca^{2+}]_{aq}$ (µM)**	**Γ_{ads} (µmol•m^{-2})**	**% Ads**
Low Ca^{2+}	636.3	21.88	40.7
	579.4	23.25	42.9
	640.3	22.21	41.6
	652.1	22.32	43.4
	591.7	21.75	42.3
	633.0	21.66	39.8
High Ca^{2+}	3896.7	20.35	9.1
	3923.2	22.41	10.2
	3925.5	19.12	8.7
	3701.7	25.00	11.5
	3737.7	24.20	11.3
	3798.1	29.33	13.2
	3806.5	20.89	9.5
	3835.8	18.24	8.5
	3730.5	24.92	11.5

Chapter 4

Selective adsorption of calcium-aspartate ligands onto brucite [$Mg(OH)_2$]: Implications for calcium in prebiotic chemistry

Calcium is a biologically essential element and the emergence of calcium-binding proteins on Early Earth may have been a significant innovation in the origin of life. Their assembly may have been facilitated by the selective adsorption of constituent calcium-amino acid complexes onto mineral surfaces within calcium-rich environments, such as serpentinite-hosted hydrothermal vents, although the interactions of these metal-ligand complexes with the mineral-water interface are not well known. We conducted batch adsorption experiments with an equimolar mixture of the amino acids aspartate, glycine, lysine, leucine, and phenylalanine onto powdered brucite [$Mg(OH_2]$, a thermodynamically stable phase during serpentinization, at pH~10.2. We performed the batch experiments in triplicate both without and with $4.1x10^{-3}$ M Ca^{2+}. In experiments without Ca^{2+}, we observed up to 8.9 % of aspartate and no greater than 5 % each of the remaining four amino acids adsorbed onto brucite. When Ca^{2+} was added, we found up to 37.3 % of aspartate adsorbed onto brucite, whereas the other amino acids each did not exceed 3.5 %. Aspartate is selectively adsorbed in the presence of Ca^{2+} relative to the other amino acids. Additionally, an average of 15.9 % of calcium adsorbed onto brucite. We used calculations of the brucite-water interface with the extended triple-layer model to predict that brucite particle surface charge is slightly negative without added Ca^{2+}, but reverses to strongly positive values in the presence of 4.1×10^{-3} M Ca^{2+}. Our results suggest that calcium is predominantly adsorbed on the brucite surface, and it preferentially complexes to aspartate, the most negatively charged amino acid at pH~10.2, to form an electrostatically favorable metal-ligand surface complex. The selective complexation of aspartate to calcium reflects a similar preference in calcium-binding proteins. The conditions of this study may hold implications for the importance of calcium-rich aqueous environments, such as the serpentinite-hosted hydrothermal environments, in the evolution of fundamental proteins in the origin of life.

This paper will be submitted to Astrobiology for publication.

Authors: Charlene F. Estrada, Dimitri A. Sverjensky, and Robert M. Hazen

1. Introduction

Calcium is a ubiquitous element in all living organisms that performs a wide variety and number of essential biochemical processes including glycolysis, cell signaling, ion transport, and apoptosis (Forsén and Kordel, 1994). Calcium-binding proteins (CaBPs) play a fundamental role in many of these processes. They occur in eukaryotes, as well as in the prokarya and archaea domains of life (Swan et al., 1987; Zhou et al., 2006; Barnwal et al., 2009). The emergence of macromolecules such as these proteins on early Earth may have occurred through the prebiotic synthesis of constituent amino acids through a variety of plausible pathways (Miller, 1953; Ponnamperuma and Pering, 1966; Hennet et al., 1992; Cleaves et al., 2008). The complexation of calcium to amino acid carboxylate groups has been observed in aqueous systems and may possibly occur in natural systems with elevated dissolved Ca^{2+} concentrations (De Robertis et al., 1991; Fox et al., 2007; Kurochkin et al., 2011). The selection and concentration of such metal-ligand complexes at mineral-water interfaces available within these environments could have led to the polymerization of primordial CaBPs as a crucial process in the origin of life.

The mineral-water interface undergoes protonation or deprotonation reactions depending on the pH of the aqueous environment relative to the mineral's point of zero charge, or PZC (Sverjensky and Sahai, 1996). When the pH of the aqueous phase is above the PZC, the mineral surface is net-negative and below the PZC, it is net-positive. The extent of amino acid adsorption onto mineral surfaces has been generally observed to correlate with the difference between the PZC and a corresponding property for amino acids, the isoelectric point (pI) determined as

$$\mathrm{pI} = \frac{\mathrm{pK_{a1}} + \mathrm{pK_{a2}}}{2} \qquad (1)$$

where $\mathrm{pK_{a1}}$ and $\mathrm{pK_{a2}}$ are the aqueous protonation constants of the amino acid. For instance, Churchill and coworkers (2004) observed the mineral calcite (PZC= 9.5) to adsorb aspartate (pI=2.98) to a greater extent than lysine (pI= 9.74) because negatively-charged, aqueous aspartate was widely available to adsorb onto the positively-charged calcite surface over the pH range of 3.0 to 9.5. The electrostatic environment at the mineral-water interface may therefore adsorb and concentrate one charged biomolecule while another is repelled and remains dilute in bulk water.

Clay mineral surfaces have been thoroughly investigated because of their high surface area compared with other minerals that may enable the adsorption of large amounts of organic material. Among clay minerals, montmorillonite and kaolinite have been studied with respect to organic adsorption (Lahav et al., 1978; Rishpon et al., 1982; Ferris, 1993; Ikhsan et al., 2004; Ferris, 2005; Huang and Ferris, 2006; Hashizume et al., 2010). Franchi and coworkers (2003) investigated the interaction of nucleic acids both these clay mineral surfaces and observed that adsorption increases significantly in the presence of the divalent cations Mg^{2+} and Ca^{2+}. The authors attributed the increase in adsorption to the formation of a cation-ligand complex where the M^{2+} cation acts as a bridge between the clay surface and the nucleic acid. Similarly, our investigations on the surface of the double-layered clay brucite, $Mg(OH)_2$, discovered that the adsorption of aspartate was enhanced in the presence of Ca^{2+} and surface complexation modeling has proposed that a cooperative calcium-aspartate complex adsorbs at the brucite-water interface via the "cation-bridge" configuration (Estrada et al., in review).

These previous investigations may hold implications for the cooperative effect between mineral surfaces and the dissolved ion profile of aquatic environments in concentrating organic species that are significant to prebiotic chemistry. For instance, ferro-brucite [$Mg_{0.75}Fe_{0.25}(OH)_2$] is another thermodynamically stable phase during serpentinization, which is formed during hydration of magnesium-rich olivine in serpentinite-hosted hydrothermal vents (Bach et al., 2006). In the serpentinite-hosted Lost City Hydrothermal Field, Ca^{2+} has been reported in elevated concentrations of 22.5×10^{-3} M relative to seawater where $[Ca^{2+}] = 10 \times 10^{-3}$ M (Kelley et al., 2001; Kelley et al., 2002; Kelley et al., 2005). There are greenstone sequences that suggest serpentinite-hosted hydrothermal activity on Earth's surface as early as 3.8 Ga in the Isua Formation (Dymek et al., 1988) and 3.5 Ga on the Pilbara Craton (Van Kranendonk et al., 2007). Thus it is plausible that the brucite-water interface and a calcium-rich serpentinite-hosted hydrothermal environment were relevant on early Earth prior to the emergence of cellular life ca. 3.48 Ga (Noffke et al., 2013).

In this study, we investigate the adsorption of aqueous solutions of the five amino acids aspartate, glycine, lysine, leucine, and phenylalanine in equimolar mixtures in the presence of the brucite. The five amino acids, depicted in Fig. 1., have diverse side chains (R) where R= CH_2COO^-, H, $(CH_2)_4NH_3^+$, $CH_2CH(CH_3)_2$, and CH_2Ph for aspartate, glycine, lysine, leucine, and phenylalanine, respectively. The adsorption of aspartate has been previously characterized on TiO_2, kaolinite, γ-Al_2O_3, calcite, and brucite (Roddick-Lanzilotta and McQuillan, 2000; Hazen et al., 2001; Ikhsan et al., 2004; Jonsson et al., 2010; Greiner et al., 2014; Estrada et al., in review). Glycine has primarily been investigated in the context of peptide condensation onto kaolinite and montmorillonite surfaces (Lahav and Chang, 1976; Lahav et al., 1978; Rishpon et al., 1982) although there have been adsorption studies involving alumina, silica, and Cr_2O_3 (Stievano et al., 2007; Arrouvel et al., 2007; Garrain et al., 2010; Costa et al., 2011). Lysine adsorption has been previously studied on silica, montmorillonite, silica, and TiO_2 (Roddick-Lanzilotta et al., 1998; Vlasova and Golovkova, 2004; Stievano et al., 2007; Parbhakar et al., 2007; Kitadai et al., 2009). Few studies have quantitatively characterized the adsorption behavior of phenylalanine and leucine at the mineral-water interface although there have been investigations of phenylalanine adsorption onto zeolite-β (Krohn and Tsapatsis, 2005) and onto rutile (Bahri et al., 2011). Theoretical calculations of the interactions between the amino acid zwitterions with Ca^{2+} in water have determined that a bidentate chelating-structure between the carboxylate group and the Ca^{2+} ion is the most stable configuration (Qin et al., 2014). There have also been studies elucidating the thermodynamic properties of Ca-aspartate, Ca-leucine, and Ca-glycine complexes (De Robertis et al., 1991; Shock and Koretsky, 1993; Kurochkin et al., 2011). Klevenz and coworkers (2010) report that, with the exception of phenylalanine, there are elevated concentrations of these amino acids at the Logatchev serpentinite-hosted hydrothermal field, and Hennet and coworkers (1992) synthesized both aspartate and glycine at mineral-buffered, hydrothermal conditions.

The goal of our investigation is to evaluate the extent to which brucite adsorbs the five amino acids as a function of the initial concentration of the amino acid mixture. We further characterize the adsorption of an equimolar amino acid mixture in the presence of Ca^{2+} to determine whether adsorption may be amplified through the formation of cooperative calcium-ligand complexes. It is also possible that competitive adsorption may occur between the amino acids, and the addition of Ca^{2+} may enhance those effects. We determine quantitatively whether these differences in adsorption occur on the brucite surface and evaluate our results in the context of chemical evolution and the possible role that the mineral-water interface, in coordination with the dissolved ion content of a surrounding environment, might play in this process.

2. Materials and Methods

2.1. Brucite Synthesis

We prepared all solutions with 18.2 MΩcm Milli-Q water (Millipore). Throughout the batch adsorption experiments we used a synthetic brucite powder. We synthesized brucite using a precipitation method reported by Henrist and coworkers (2003) and Lu and coworkers (2004) where we added 2.0 M $MgCl_2$ (99.99% Alfa Aesar dry ampoules under Ar gas) dropwise to a stirred reaction vessel containing 2.0 M NH_4OH at 45 ± 3 ºC. Following precipitation of the brucite powder, we cooled the reaction vessel at room temperature for 3 days and dried the powder with a hot plate (Corning PC-420D). We then carried out a hydrothermal aging process, which has been suggested by previous studies to improve crystallinity and morphology (Henrist et al., 2003; Lu et al., 2004), on the brucite by sealing the precipitate in Milli-Q water within a PTFE-lined stainless steel reaction vessel (Col-Int-Tech). We heated the vessel at 150 ºC for 3 days (Fisher Scientific Isotherm oven ±2 ºC), cooled the suspension to room temperature, and dried the powder using a Corning hot plate. We stored the hydrothermally-aged product in a glass vial under Ar gas at 25 ºC.

We imaged the brucite powder before and after the hydrothermal-aging process with SEM (JEOL 8500F), and we observed that rosettes of circular to oblong platelets characterized the untreated brucite (Fig. 2a). In contrast, the hydrothermally-aged brucite had a lamellar crystal habit defined by smaller clusters of hexagonal platelets (Fig. 2b). Compared with that of the untreated brucite, the powder XRD pattern (Bruker D2 Phaser) of the hydrothermally-treated brucite (Fig. 3) had reduced peak intensities for the reflections (100), (101), and (111) and greater intensity for (001), which is consistent with brucite powder XRD patterns archived at the International Centre for Diffraction Data (http://icdd.com). Both SEM and powder XRD suggested that the hydrothermal aging process improved the morphology and crystallinity of the synthetic brucite. Therefore, we performed our adsorption experiments on the hydrothermally-aged brucite powder.

2.2. Batch Adsorption Experiments

We prepared equimolar mixtures of aspartate, glycine, lysine, leucine, and phenylalanine at four concentrations of 10, 50, 75 and 150×10^{-6} M. We added each solution to a 15 mL sterile Falcon tube containing 10.0 ± 0.5 g•L^{-1} powdered brucite. We placed the batch samples on a test tube rotator at 40 rpm (25 ± 1 ºC, 1 bar) for 24 hours. We then measured the pH of the brucite-amino acid suspension with a combination glass electrode (Thermo-Electron, Orion 8103BNUWP) that had been calibrated with NIST standardized buffers of pH values 4, 7, and 10 (Fischer Scientific). The brucite powder strongly buffered the pH of each sample, and the pH of immersion was approximately

10.2. The corresponding amount of Mg^{2+} that dissolved from the brucite surface ranged from 0.9×10^{-3} M to 1.1×10^{-3} M according to the dissolution equation

$$Mg(OH)_2 + 2H^+ = Mg^{2+} + 2H_2O \tag{2}$$

where the brucite powder is assumed to reach equilibrium with the aqueous solution after 24 hours. We determined the equilibrium constant for this batch of synthetic brucite powder in a previous surface adsorption study where logK= 17.3 ± 0.06 (Estrada et al., in review). We purged all batch samples with Ar gas during their exposure to air to avoid surface contamination by CO_2. We centrifuged the samples for 10 minutes with a relative centrifugal force of 1073 x g (Fisher Scientific accuSpin 400) and separated the liquid supernatant from the solid brucite.

We repeated the procedure described above for a second set of experiments in the presence of 4.1×10^{-3} M Ca^{2+} that we added to the amino acid mixtures as $CaCl_2$ (Fluka Analytical). A previous investigation of brucite surface dissolution kinetics by Pokrovsky and coworkers (2005) suggested that over 10^{-2} M of Ca^{2+} and some organic species may either increase or decrease dissolution of brucite in aqueous solution. We therefore investigated low concentrations of Ca^{2+} ($\leq 4.1 \times 10^{-3}$ M) and the amino acids ($\leq 0.15 \times 10^{-3}$ M) to avoid such changes in the brucite dissolution rate. The batch adsorption experiment involving adsorption of the equimolar amino acid mixture onto brucite in the presence of Ca^{2+} was performed in triplicate concurrently with the experiments without added Ca^{2+} to ensure the reproducibility of the results.

We determined the concentration of the five amino acids, Mg^{2+}, and Ca^{2+} in the supernatant with ion chromatography (IC). We used a Dionex ICS-5000 system equipped with a DP dual pump, AS-AP autosampler, ED electrochemical detector and Chromeleon

6.8 software (Dionex Corporation, Sunnyvale, CA, USA). During analysis, the supernatant passed through an AminoPAC10 column, which is packed with a hydrophobic, polymeric, pellicular resin, where gradient anion exchange separation at pH 12 to 14 removed the amino acids within the bulk supernatant. Following separation, integrated pulsed amperometric detection (IPAD), which irreversibly oxidizes the amino and hydroxyl groups of the amino acids that are then detected with the working gold electrode of the ED electrochemical detector, determined the relative analyte concentration (Clarke et al., 1999; Jandik et al., 2000). The Mg^{2+} and Ca^{2+} present in the supernatant passed through an IonPac CS12A column packed with a hydrophobic resin containing a carboxylate functional group that separated the ions through cation exchange (Jensen et al., 1993). The CD conductivity detector then analyzed the cations with electrolytic suppression. Following analysis using the cation or amino acid IC application, a chromatogram containing a peak that is unique to the cation or amino acid of interest was produced for every batch sample. We determined the concentration of the cation or amino acid in the supernatant from the area beneath the chromatogram peak, which was integrated with the software Chromeleon 6.8.

Prior to analyzing the supernatant with the IC, we measured a set of standards for the equimolar amino acid mixture, Mg^{2+}, and Ca^{2+} resulting a linear correlation between the area under the peak and molar concentration. We standardized for each set of samples by calibrating with IC within two hours of analyzing the first supernatant of the batch adsorption experiment.

We analyzed the samples with IC in triplicate and determined the mean concentration of aspartate, glycine, lysine, leucine, and phenylalanine remaining in the liquid supernatant within ±1 standard error (σ_M). It was necessary for us to analyze the samples containing the mixture of five amino acids in triplicate because we initially detected low amounts of adsorption (<10 %) for all the amino acids in the experiments without added Ca^{2+}, and collecting data in triplicate better determined an accurate representation of amino acid adsorption values. It was not necessary for us to analyze Ca^{2+} adsorption data in triplicate because our initial measurements found that Ca^{2+} adsorbed onto brucite in large amounts (>10 %), and we calculated that ±1 standard deviation (σ) was equal to about 8 % of the adsorption data. From the analytical concentrations we determined with IC, we reported the percentage of Ca^{2+}, aspartate, glycine, lysine, leucine, and phenylalanine adsorption on brucite.

In addition to carrying out the experiments described above, we also performed a blank adsorption experiment where initial concentrations of 10, 50, 75 and $150\text{x}10^{-6}$ M of an equimolar mixture of aspartate, glycine, lysine leucine, and phenylalanine were each added to 15 mL Falcon tubes without brucite powder. Initial pH values of the amino acid mixtures were increased to approximately 10.2 to 10.3 using small volumes of 0.1 M NaOH (Sigma-Aldrich). The experiment was performed without Ca^{2+} and with approximately $4.0\text{x}10^{-3}$ M Ca^{2+} for each of the initial amino acid concentrations. The purpose of the experiment was to evaluate whether or not a difference could be detected in the supernatant between the initial concentration and the concentration after 24 hours due to either polymerization at alkaline conditions or the formation of complexes between the multiple amino acid species. We analyzed the solutions with IC after they had mixed over 24 hours, and we found that the concentrations in the supernatant were equal to the initial concentrations for each amino acid.

2.3. Surface Complexation Modeling

In a previous study we characterized the surface of our synthetic brucite powder and the brucite-aspartate system with batch adsorption experiments and a predictive triple layer model that uses Born solvation and crystal chemical theory known as the extended triple-layer model or ETLM (Sverjensky and Sahai, 1996; Sahai and Sverjensky, 1997; Sverjensky, 2003; Sverjensky, 2005; Sverjensky and Fukushi, 2006). The ETLM predicts the electrical work resulting from the release of water dipoles during adsorption of a species directly at the mineral surface. We used the computer code GEOSURF (Sahai and Sverjensky, 1998) to perform iterative calculations for the ETLM that fit our experimental data obtained for the brucite-calcium system as well as data obtained for the brucite-aspartate system in a previous study (Estrada et al., in review). The parameters we obtained for the ETLM are displayed in Table 1.

In this study, we investigate the adsorption of structurally similar biomolecules onto the same batch of synthetic brucite; therefore we assume that the parameters in Table 1 are applicable to our adsorption experiments with mixtures of amino acids. In Table 2 we have listed known speciation reactions from previous investigations involving aqueous aspartate, glycine, lysine, leucine, phenylalanine, and where applicable, electrolyte ion pair reactions with Ca^{2+} (De Robertis et al., 1991; Shock and Koretsky, 1993; Jonsson et al., 2010; Kurochkin et al., 2011; Haynes, 2014). We incorporated the parameters in Tables 1 and 2 into the ETLM to predict the sign of the particle surface charge, by examining the ζ-potential, of brucite in the presence of the amino acid-mixture at variable initial concentrations and the two different ionic strengths ($I = 2.7 \times 10^{-3}$ M where [Ca^{2+}]= 0 M and [Mg^{2+}]= 0.9x10^{-3} M and I= 15.6x10^{-3} M where [Ca^{2+}]= 4.1x10^{-3} M and [Mg^{2+}]= 1.1x10^{-3} M). During our calculations, we assumed that the ζ-potential is equal to the potential at the beginning of the diffuse layer, denoted as Ψ_d, in the ETLM.

3. Results and Discusion

3.1. Surface Adsorption without Ca^{2+}

The average adsorption data for aspartate, glycine, lysine, leucine, and phenylalanine onto the brucite surface as a function of the initial concentration of the amino acid mixture at [Mg^{2+}]= 0.9x10^{-3} M are displayed in Fig. 4. All adsorption data are reported in Table 3. In Fig. 4, surface adsorption does not exceed 9 % for each of the five amino acids, regardless of initial amino acid concentration. We observe glycine, lysine, leucine, and phenylalanine adsorb onto brucite in comparable amounts from 2.6 to 5.3 % when initial amino acid concentrations are 10 and 150 x10^{-6} M, respectively. In contrast, aspartate adsorbs to a greater extent on brucite, in amounts from 5.3 to 8.9 % at the same conditions. The standard error displayed in Fig. 4 typically increases when the percentage of amino acid adsorption decreases as there is less confidence in the analysis of low amounts of adsorption.

3.2. Surface Adsorption with Added Ca^{2+}

The average percentage of amino acid adsorption onto brucite in the presence of 4.1x10^{-3} M Ca^{2+} and 1.1x10^{-3} M Mg^{2+} following three experimental runs is displayed in Fig. 5 as a function of initial amino acid concentration. When Ca^{2+} is added to the brucite-amino acid system, the amount of aspartate adsorption substantially increases to between 37.3 and 20.6 % when the initial amino acid concentration is between 10 and $150\text{x}10^{-6}$ M, respectively. In comparison, the adsorption of glycine, lysine, leucine, and phenylalanine do not exceed 3.6 % each at all initial concentrations, such that the amount of aspartate adsorbed onto brucite with Ca^{2+} is from 5.7 to 20 times greater than the adsorption of the other amino acids in this study. All adsorption data for the experiments are displayed in Table 3.

In addition to the amino acids, a significant amount of calcium adsorbed onto the surface of brucite, which is shown in Fig. 6. On average, we observed that 15.9 % of the initial $4.1\text{x}10^{-3}$ M Ca^{2+} adsorbed at the brucite-water interface. This amount did not vary more than 0.6 % with initial amino acid concentration. We have observed comparable amounts of calcium adsorption (14.4 %) onto brucite in the brucite-aspartate system when $[Ca^{2+}]= 4.0\text{x}10^{-3}$ M (Estrada et al., in review). In this previous study, we fit calcium adsorption data with the ETLM and proposed that calcium adsorbed onto brucite with the reaction stoichiometry

$$>SOH + Ca^{2+} + 2H_2O = >SOH_2^{+}\_Ca(OH)_2 + H^{+} \qquad (3)$$

where ">SOH" denotes the brucite surface, and the adsorbing hydrated calcium complex was a monodentate outer-sphere surface species (Fig. 7a). We include the reaction in Eq. (3) in our ETLM characterization of the brucite-calcium system. When we fit the calcium adsorption data in Fig. 6 with the ETLM, we predict that, an average of 12.7 % of the initial Ca^{2+} added adsorbs at all amino acid concentrations. Considering the surface species predicted by Eq. (3) alone, the ETLM slightly underestimates the amount of calcium adsorption onto brucite. This discrepancy may possibly be explained by the existence of additional calcium species at the brucite-water interface, including calcium-amino acid complexes.

3.3. Selective Adsorption of Aspartate onto Brucite

We observed that aspartate adsorbs to a greater extent on the brucite surface compared with the other four amino acids present in the system under all initial concentrations and ionic strengths investigated in this study. However, when we introduced Ca^{2+} to the system, aspartate adsorption was at least 5.7 times greater, and as much as 20 times greater, than each of the other amino acids. Both observations provide insight into the behavior of the brucite-water interface and its role in selecting aspartate over the other amino acids present. Churchill and coworkers (2004) concluded that the charge of the mineral surface relative to that of the adsorbing molecule in bulk aqueous solution determines the extent to which the mineral-water interface may select an amino acid for adsorption. However, previous studies have determined that a molecular surface species is not always the predominant aqueous species (Malin et al., 2009; Jonsson et al., 2010; Estrada et al., in review).

We used the ETLM established with the parameters in Tables 1 and 2 to determine the sign of the brucite particle surface charge (ζ-potential) at variable concentrations of the amino acid mixture in the presence of (1) 0.9×10^{-3} M Mg^{2+} and (2) with concentrations of 4.1×10^{-3} M Ca^{2+} and 1.1×10^{-3} M Mg^{2+}. The results of our prediction indicate that the brucite surface has a slightly negative charge at all amino acid concentrations when no Ca^{2+} is added to the system (Fig. 8). Nevertheless, aspartate, which is more negatively-charged in aqueous solution at pH 10.2, adsorbs at the brucite-water interface to the greatest extent relative to the other four amino acids. It is likely that at pH 10.2 positively-charged functional groups exist at the brucite surface with almost equal abundances as negatively-charged, deprotonated surface groups resulting in a slightly negative ζ-potential. Therefore, these positively-charged functional groups may adsorb aspartate in greater amounts compared with less polar and less negatively-charged amino acids such as glycine and lysine. It may also be possible that the speciation of the doubly-deprotonated aspartate species in water enhances the amount of aspartate surface adsorption relative to the other four amino acids.

With the addition of $4.1\text{x}10^{-3}$ M Ca^{2+}, we determined that brucite particle surface charge significantly reverses from slightly negative to strongly positive values at all initial amino acid concentrations (Fig. 8). This reversal may demonstrate the considerable extent to which calcium adsorbs onto brucite, and it reflects our predicted surface reaction in Eq. (3). In this surface reaction, calcium adsorbs at the brucite-water interface to form a positively-charged, calcium outer-sphere species; hence, as more calcium adsorbs onto brucite, we predict that the surface will become more positively-charged. This electrostatic environment alone would be conducive toward the adsorption of a negatively-charged amino acid such as aspartate. However, as the predominant surface species, calcium might be expected to limit the number of surface sites available for amino acid adsorption. Additionally, the slight underestimation of the amount of calcium adsorption by the ETLM when incorporating the reaction proposed in Eq. (3) may also indicate that in addition to adsorbing directly onto the brucite surface, aspartate forms a cooperative metal-ligand complex with calcium. We propose that such an interaction at the brucite surface could occur through the reaction stoichiometry

$$>SOH + Ca^{2+} + HAsp^{-} = >SO^{-}\_CaHAsp^{+} + H^{+} \qquad (4)$$

where the aspartate molecule attaches onto brucite via an electrostatic interaction with Ca^{2+} (Fig. 7b), which is similar to the "cation bridge" configuration suggested by Franchi and coworkers (2003) for clay minerals and nucleic acids. Therefore, we propose that calcium surface adsorption plays a prominent role in both the reversal of brucite particle surface charge and the selective adsorption of aspartate.

At pH 10.2, aspartate is the most negatively-charged, electronegative molecule among the five amino acids in the aqueous phase. This characteristic improves the likelihood that aspartate, a hard Lewis base, will form strong electrostatic bonds with Ca^{2+}, a hard Lewis acid, that result in a metal-ligand complex. Simultaneously, the possibility of the other four amino acids forming metal-ligand complexes decreases as surface-bound calcium becomes less available. Aspartate-calcium complexes can also be neutral ($CaAsp^0$) and positively-charged ($CaAsp^+$) in water, whereas calcium complexes with the other four amino acids can only be positively-charged, and this restriction may limit the amount to which these complexes adsorb on the brucite surface. Moreover, both calcium and aspartate adsorb in significant amounts, resulting in decreased availability of surface sites on brucite for the attachment of other amino acids. This competitive effect may account for the slight decrease, on average, of glycine, lysine, leucine, and phenylalanine adsorption onto brucite when 4.1×10^{-3} M Ca^{2+} is added.

Our results indicate that a natural aqueous environment with a high total dissolved Ca^{2+} concentration and minerals with high PZCs such as brucite may prove ideal in selectively adsorbing negatively-charged organic species from a suite of molecules. Serpentinite-hosted hydrothermal vents contain a number of minerals, including brucite and calcite, as major phases within an aqueous environment with over twice the total calcium concentration (22.5×10^{-3} M) of ambient seawater (Kelley et al., 2001; 2002; 2005). On the early Earth, it is possible that any number of organic species, including amino acids, may have formed abiotically due to the disequilibria established when cold, CO_2-enriched seawater mixes with hot, CH_4-rich hydrothermal fluids (Shock and Canovas, 2010). If these organic species came into contact with minerals such as brucite within Ca^{2+}-rich waters, serpentinite-hosted hydrothermal vents could have possibly played a role in life's origins by acting as host environments for selective adsorption. The preferential adsorption of calcium-aspartate complexes onto a mineral-water interface could be significant for the evolution of CaBPs, which are known to selectively bind the calcium ion to the negatively-charged amino acids, glutamate and aspartate (Harding, 2004; Fox et al., 2007). The concentration of calcium-aspartate complexes at the mineral surface may serve as a precursor to the formation of CaBPs as a fundamental step in the emergence of life on early Earth.

Our observations of competitive and cooperative adsorption effects demonstrate that the geochemical complexity reflected by the total dissolved ion composition of the aqueous environment combined with mineral surfaces may influence the availability of biomolecules. Hazen and Sverjensky (2010) suggested that in order to evaluate molecular complexification it was necessary to conduct experiments that attempt to reproduce prebiotic complexities (e.g., multiple organic species, biomolecule concentrations, and electrolytes). We have focused specifically on the addition of Ca^{2+}, in the presence of Mg^{2+}, as a first step in approaching complex geochemical conditions while assessing molecular interactions at the mineral surface. Molecular self-organization may emerge within a system as organic species, such as aspartate, are selectively adsorbed and concentrated at the mineral-water interface, whereas other biomolecules remain dilute within bulk water (Hazen and Sverjensky, 2010). The selective pressure exerted by the brucite surface during the addition of Ca^{2+} may hold implications for the transition between a dilute, unorganized "prebiotic soup" to a concentrated, systematic suite preceding molecular complexification.

4. Concluding Remarks

We investigated the attachment of an equimolar mixture of the five biologically essential amino acids aspartate, glycine, lysine, leucine, and phenylalanine onto brucite both with and without the presence of Ca^{2+} at pH 10.2. Aspartate adsorbs to a slightly greater extent without Ca^{2+} compared with the other amino acids, but in experiments where we added $4.1x10^{-3}$ M Ca^{2+}, aspartate adsorption is 5.7 to 20 times greater than that of glycine, lysine, leucine, or phenylalanine onto brucite alone. Moreover, we observed that an average of 15.9 % of the initial Ca^{2+} added adsorbed at the brucite-water interface. We used the ETLM to characterize the brucite-calcium system by fitting calcium adsorption data. Our results, combined with data from a previous study of the interactions between aspartate and brucite, suggest that calcium attaches onto brucite as a hydrated, monodentate outer-sphere species. The ETLM also predicts that the brucite particle surface charge (represented as ζ-potential) is slightly negative without Ca^{2+}, and it reverses to strongly positive values in the presence of $4.1x10^{-3}$ M Ca^{2+}, which may indicate that calcium predominantly adsorbs onto brucite. We conclude that the considerable increase in aspartate adsorption onto brucite with the addition of Ca^{2+} is a result of the adsorption of a calcium-aspartate surface complex where aspartate, as the most negatively-charged amino acid at pH 10.2, forms the strongest bond with surface calcium.

The adsorption of calcium-aspartate complexes onto the surface may hold implications for the formation of CaBPs as there exists a preferred attachment of calcium to the carboxylate groups of glutamate and aspartate in these macromolecules. Furthermore, in addition to playing a prominent role in modern biological functions, calcium may promote the adsorption of key biomolecules in an otherwise electrostatically unfavorable environment by reversing the charge at the mineral-water interface. The conditions of this study underscore the importance of the dissolved ion content of some aqueous environments on early Earth, such as the calcium-rich serpentinite-hosted hydrothermal vents that may promote biomolecule interactions with the surfaces of mineral assemblages, and thereby behave as ideal host environments for the emergence of complex organic species.

Acknowledgements

We thank Cécile Feuillie, Namhey Lee, Alyssa K. Adcock, Timothy Strobel, Dionysis Foustoukos, Paul Goldey, John Armstrong, Adrian Villegas-Jimenez, Stephen Hodge, and Steven Coley for their invaluable expertise and advice throughout this project. We thank the National Science Foundation, the NASA Astrobiology Institute, the Deep Carbon Observatory, and the Carnegie Institution for Science for support of this research.

References

Arrouvel C., Diawara B., Costa D. and Marcus P. (2007) DFT periodic study of the adsorption of glycine on the anhydrous and hydroxylated (0001) surfaces of α-alumina. *J. Phys. Chem., C* **111**, 18164–18173.

Bach W., Paulick H., Garrido C. J., Ildefonse B., Meurer W. P. and Humphris S. E. (2006) Unraveling the sequence of serpentinization reactions: Petrography, mineral chemistry, and petrophysics of serpentinites from MAR 15°N (ODP Leg 209, Site 1274). *Geophys. Res. Lett.* **33**, 1–4.

Barnwal R. P., Jobby M. K., Devi K. M. and Sharma Y. (2009) Solution structure and calcium-binding properties of M-crystallin, a primordial βγ-crystallin from Archaea. *J. Mol. Biol.* **386**, 675-689.

Churchill H., Teng H. and Hazen R. M. (2004) Correlation of pH-dependent surface interaction forces to amino acid adsorption: Implications for the origin of life. *Am. Mineral.* **89**, 1048–1055.

Clarke A. P., Jandik P., Rocklin R. D., Liu Y. and Avdalovic N. (1999) An integrated amperometry waveform for the direct, sensitive detection of amino acids and amino sugars following anion-exchange chromatography. *Anal. Chem.* **71**, 2774–2781.

Cleaves H. J., Chalmers J. H., Lazcano A., Miller S. L. and Bada J. L. (2008) A reassessment of prebiotic organic synthesis in neutral planetary atmospheres. *Orig. Life Evol. Biosph.* **38**, 105–115.

Costa D., Garrain P. A., Diawara B. and Marcus P. (2011) Biomolecule−biomaterial interaction: A DFT-D study of glycine adsorption and self-assembly on hydroxylated Cr_2O_3 surfaces. *Langmuir* **27**, 2747–2760.

De Robertis A., De Stefano C. and Gianguzza A. (1991) Salt effects on the protonation of L-histidine and L-aspartic acid: A complex formation model. *Thermochim Acta* **177**, 39–57.

Dymek R. F., Brothers S. C. and Schiffries C. M. (1988) Petrogenesis of ultramafic metamorphic rocks from the 3800 Ma Isua Supracrustal Belt, West Greenland. *J. Petrol.* **29**, 1353–1397.

Estrada C. F., Sverjensky D. A., Pelletier M., Razafitianamaharavo A. and Hazen R. M. (2014) Interaction between L-aspartate and the brucite [$Mg(OH)_2$]-water interface. *Geochim. Cosmochim. Acta*. In Review.

Ferris J. P. (1993) Catalysis and prebiotic RNA synthesis. *Orig. Life Evol. Biosph.* **23**, 307–315.

Ferris J. P. (2005) Mineral catalysis and prebiotic synthesis: Montmorillonite-catalyzed formation of RNA. *Elements* **1**, 145–149.

Forsén S. and Kordel J. (1994) Calcium in biological systems. In *Bioinorganic chemistry* (eds. I. Bertini, H. B. Gray, S. J. Lippard, and J. S. Valentine). University Science Books, Mill Valley, California. pp. 107–166.

Fox S., Büsching I., Barklage W. and Strasdeit H. (2007) Coordination of biologically important α-Amino Acids to Calcium (II) at high pH: Insights from crystal structures of calcium α-aminocarboxylates. *Inorg. Chem.* **46**, 818–824.

Franchi M., Ferris J. P. and Gallori E. (2003) Cations as mediators of the adsorption of nucleic acids on clay surfaces in prebiotic environments. *Orig. Life Evol. Biosph.* **33**, 1–16.

Garrain P. A., Costa D. and Marcus P. (2010) Biomaterial− biomolecule interaction: DFT-D study of glycine adsorption on Cr_2O_3. *J. Phys. Chem., C* **115**, 719–727.

Greiner E., Kumar K., Sumit M., Giuffre A., Zhao W., Pedersen J. and Sahai N. (2014) Adsorption of L-glutamic acid and L-aspartic acid to γ-Al_2O_3. *Geochim. Cosmochim. Acta* **133**, 142–155.

Harding M. M. (2004) The architecture of metal coordination groups in proteins. *Acta Crystallogr D Biol Crystallogr* **60**, 849–859.

Hashizume H., van der Gaast S. and Theng B. K. G. (2010) Adsorption of adenine, cytosine, uracil, ribose, and phosphate by Mg-exchanged montmorillonite. *Clay Miner.* **45**, 469–475.

Haynes W. M. (2014) *CRC Handbook of Chemistry and Physics*. 95 ed., Taylor & Francis, Boca Raton, FL.

Hazen R. M., Filley T. and Goodfriend G. (2001) Selective adsorption of L- and D-amino acids on calcite: Implications for biochemical homochirality. *PNAS* **98**, 5487–5490.

Hennet R., Holm N. G. and Engel M. H. (1992) Abiotic synthesis of amino-acids under hydrothermal conditions and the origin of life - a perpetual phenomenon. *Naturwissenschaften* **79**, 361–365.

Henrist C., Mathieu J., Vogels C., Rulmont A. and Cloots R. (2003) Morphological study of magnesium hydroxide nanoparticles precipitated in dilute aqueous solution. *J. Cryst. Growth* **249**, 321–330.

Huang W. and Ferris J. P. (2006) One-step, regioselective synthesis of up to 50-mers of RNA oligomers by montmorillonite catalysis. *J. Am. Chem. Soc.* **128**, 8914–8919.

Ikhsan J., Johnson B. B., Wells J. D. and Angove M. J. (2004) Adsorption of aspartic acid on kaolinite. *J. Colloid Interface Sci.* **273**, 1–5.

Jandik P., Pohl C., Barreto V. and Avdalovic N. (2000) Anion exchange chromatography and integrated amperometric detection of amino acids. In *Amino acid analysis* *protocols* Humana Press, New Jersey. pp. 63–85.

Jensen D., Weiss J., Rey M. A. and Pohl C. A. (1993) Novel weak acid cation-exchange column. *J. Chromatogr. A* **640**, 65–71.

Jonsson C. M., Jonsson C. L., Estrada C. F., Sverjensky D. A., Cleaves H. J. II and Hazen R. M. (2010) Adsorption of L-aspartate to rutile (α-TiO_2): Experimental and theoretical surface complexation studies. *Geochim. Cosmochim. Acta* **74**, 2356–2367.

Kelley D. S., Baross J. A. and Delaney J. R. (2002) Volcanoes, fluids, and life at mid-ocean ridge spreading centers. *Annu. Rev. Earth Planet. Sci.* **30**, 385–491.

Kelley D. S., Karson J. A., Fruh-Green G. L., Yoerger D. R., Shank T. M., Butterfield D. A., Hayes J. M., Schrenk M. O., Olson E. J., Proskurowski G., Jakuba M., Bradley A., Larson B., Ludwig K., Glickson D., Buckman K., Bradley A.S., Brazelton W.J., Roe K., Elend M.J., Delacour A., Bernasconi S.M., Lilley M.D., Baross J.A., Summons R.T., and Sylva S.P. (2005) A serpentinite-hosted ecosystem: The Lost City hydrothermal field. *Science* **307**, 1428-1434.

Kelley D. S., Karson J., Blackman D., Frueh-Green G., Butterfield D., Lilley M., Olson E., Schrenk M., Roe K., Lebon G., Rivizzigno P., and the AT3-60 Shipboard Party (2001) An off-axis hydrothermal vent field near the Mid-Atlantic Ridge at 30 degrees N. *Nature* **412**, 145–149.

Kitadai N., Yokoyama T. and Nakashima S. (2009) In situ ATR-IR investigation of L-lysine adsorption on montmorillonite. *J. Colloid Interface Sci.* **338**, 395–401.

Klevenz V., Sumoondur A., Ostertag-Henning C. and Koschinsky A. (2010) Concentrations and distributions of dissolved amino acids in fluids from Mid-Atlantic Ridge hydrothermal vents. *Geochem. J.* **44**, 387–397.

Krohn J. E. and Tsapatsis M. (2005) Amino acid adsorption on zeolite β. *Langmuir* **21**, 8743–8750.

Kurochkin V. Y., Chernikov V. V. and Orlova T. D. (2011) The thermodynamic characteristics of complex formation between calcium ions and L-leucine in aqueous solution. *Russ. J. Phys. Chem.* **85**, 598–602.

Lahav N. and Chang S. (1976) The possible role of solid surface area in condensation reactions during chemical evolution: Reevaluation. *J. Mol. Evol.* **8**, 357–380.

Lahav N., White D. and Chang S. (1978) Peptide formation in the prebiotic era: Thermal condensation of glycine in fluctuating clay environments. *Science* **201**, 67–69.

Lu J., Qiu L. and Qu B. (2004) Controlled growth of three morphological structures of magnesium hydroxide nanoparticles by wet precipitation method. *J. Cryst. Growth* **267**, 676–684.

Malin J. N., Holland J. G. and Geiger F. M. (2009) Free energy relationships in the electric double layer and alkali earth speciation at the fused silica/water interface. *J. Phys. Chem., C* **113**, 17795–17802.

Miller S. L. (1953) A production of amino acids under possible primitive Earth conditions. *Science* **117**, 528–529.

Noffke N., Christian D., Wacey D. and Hazen R. M. (2013) Microbially induced sedimentary structures recording an ancient ecosystem in the ca. 3.48 billion-year-old Dresser Formation, Pilbara, Western Australia. *Astrobiology* **13**, 1103–1124.

Parbhakar A., Cuadros J., Sephton M. A., Dubbin W., Coles B. J. and Weiss D. (2007) Adsorption of L-lysine on montmorillonite. *Colloids Surf., A* **307**, 142–149.

Pokrovsky O. S., Schott J. and Castillo A. (2005) Kinetics of brucite dissolution at 25°C in the presence of organic and inorganic ligands and divalent metals. *Geochim. Cosmochim. Acta* **69**, 905–918.

Ponnamperuma C. and Pering K. (1966) Possible abiogenic origin of some naturally occurring hydrocarbons. *Nature* **209**, 979–982.

Qin P., Lü W., Qin W., Zhang W. and Xie H. (2014) Theoretical studies on complexes of calcium ion with amino acids. *Chem. Res. Chin. Univ.* **30**, 125–129.

Rishpon J., O'Hara P. J., Lahav N. and Lawless J. G. (1982) Interaction between ATP, metal ions, glycine, and several minerals. *J. Mol. Evol.* **18**, 179–184.

Roddick-Lanzilotta A. D. and McQuillan A. J. (2000) An in situ Infrared spectroscopic study of glutamic acid and of aspartic acid adsorbed on TiO_2: Implications for the biocompatibility of titanium. *J. Colloid Interface Sci.* **227**, 48–54.

Roddick-Lanzilotta A. D., Connor P. A. and McQuillan A. J. (1998) An in situ Infrared spectroscopic study of the adsorption of lysine to TiO_2 from an aqueous solution. *Langmuir* **14**, 6479–6484.

Sahai N. and Sverjensky D. A. (1998) GEOSURF: A computer program for modeling adsorption on mineral surfaces from aqueous solution. *Comput. Geosci.* **24**, 853–873.

Sahai N. and Sverjensky D. A. (1997) Solvation and electrostatic model for specific electrolyte adsorption. *Geochim. Cosmochim. Acta* **61**, 2827–2848.

Shock E. L. and Canovas P. (2010) The potential for abiotic organic synthesis and biosynthesis at seafloor hydrothermal systems. *Geofluids* **10**, 161–192.

Shock E. L. and Koretsky C. M. (1993) Metal-organic complexes in geochemical processes: Calculation of standard partial molal thermodynamic properties of aqueous acetate complexes at high pressures and temperatures. *Geochim. Cosmochim. Acta* **57**, 4899–4922.

Stievano L., Yu Piao L., Lopes I., Meng M., Costa D. and Lambert J.-F. (2007) Glycine and lysine adsorption and reactivity on the surface of amorphous silica. *Eur. J. Mineral.* **19**, 321–331.

Sverjensky D. A. (2005) Prediction of surface charge on oxides in salt solutions: Revisions for 1:1 (M^+L^-) electrolytes. *Geochim. Cosmochim. Acta* **69**, 225–257.

Sverjensky D. A. (2003) Standard states for the activities of mineral surface sites and species. *Geochim. Cosmochim. Acta* **67**, 17–28.

Sverjensky D. A. and Fukushi K. (2006) A predictive model (ETLM) for As(III) adsorption and surface speciation on oxides consistent with spectroscopic data. *Geochim. Cosmochim. Acta* **70**, 3778–3802.

Sverjensky D. A. and Sahai N. (1996) Theoretical prediction of single-site surface-protonation equilibrium constants for oxides and silicates in water. *Geochim. Cosmochim. Acta* **60**, 3773–3797.

Swan D. G., Hale R. S., Dhillon N. and Leadlay P. F. (1987) A bacterial calcium-binding protein homologous to calmodulin. *Nature* **329**, 84–85.

Van Kranendonk M. J., Hugh Smithies R., Hickman A. H. and Champion D. C. (2007) Review: Secular tectonic evolution of Archean continental crust: Interplay between horizontal and vertical processes in the formation of the Pilbara Craton, Australia. *Terra Nova* **19**, 1–38.

Vlasova N. N. and Golovkova L. P. (2004) The adsorption of amino acids on the surface of highly dispersed silica. *Colloid J.* **66**, 657–662.

Zhou Y., Yang W., Kirberger M., Lee H.-W., Ayalasomayajula G. and Yang J. J. (2006) Prediction of EF-hand calcium-binding proteins and analysis of bacterial EF-hand proteins. *Proteins* **65**, 643–655.

Fig. 1. Illustration of the five amino acids, a) aspartate, b) glycine, c) lysine, d) leucine, and e) phenylalanine investigated in this study where red, black, tan, and light blue spheres represent oxygen, carbon, hydrogen, and nitrogen atoms, respectively.

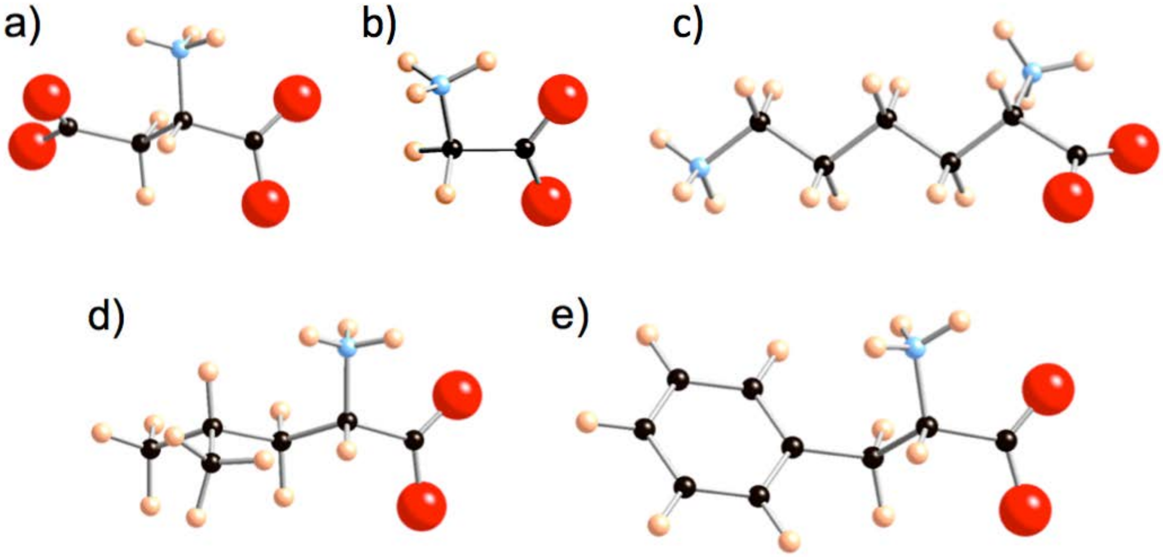

Fig. 2. SEM image of synthesized brucite (a) before hydrothermal treatment where oblong platelets are clustered in rosettes and (b) after hydrothermal treatment where platelets are hexagonal in lamellar clusters (scale= 1 μM).

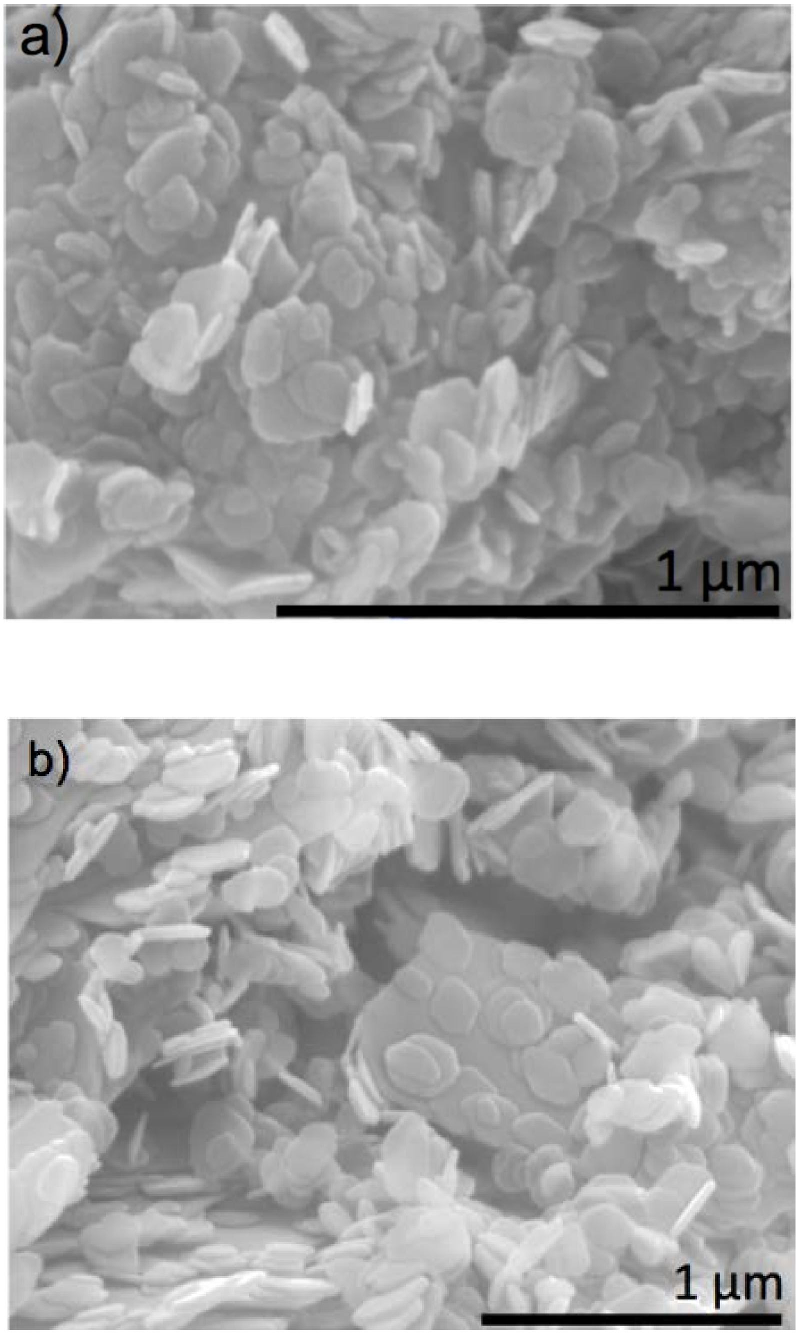

Fig. 3. Power XRD pattern of synthesized brucite that has been untreated (blue) and hydrothermally-treated (black). *(hkl)* reflections are indexed by the red symbols.

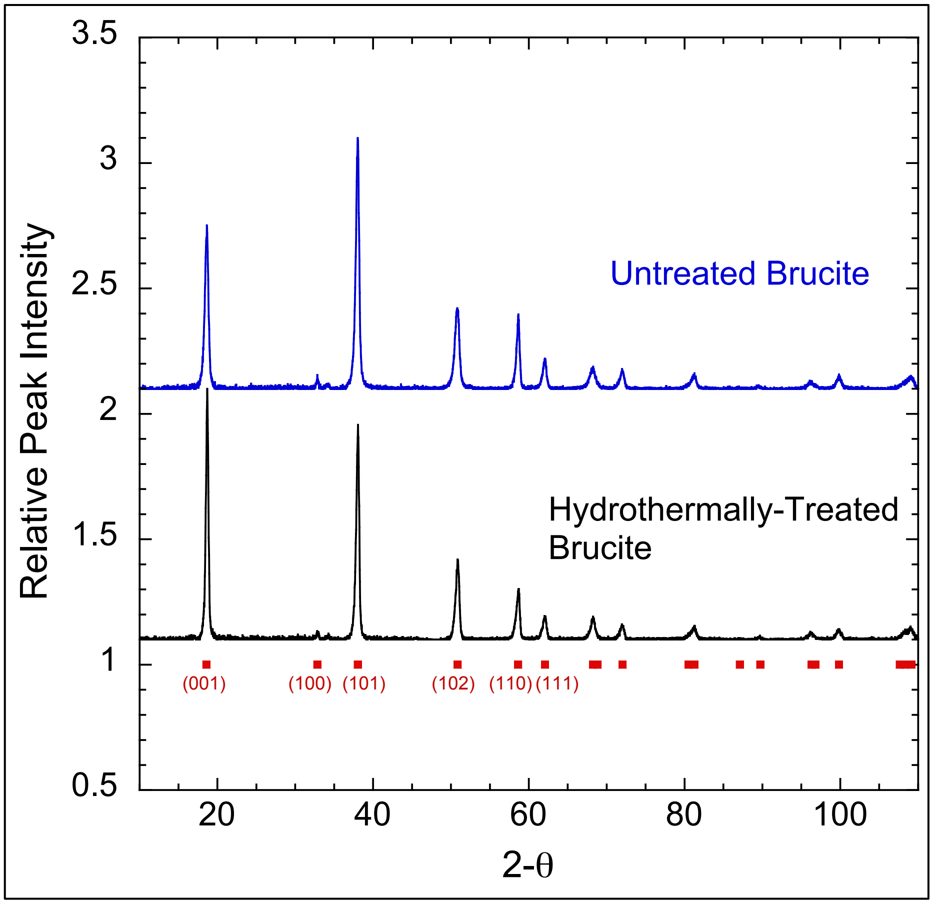

Fig. 4. Average adsorption (%) of aspartate, glycine, lysine, leucine, and phenylalanine onto brucite as a function of the initial concentration of the amino acid mixture following three batch experiments with [Mg^{2+}]=0.9x10^{-3} M and no Ca^{2+} present at pH 10.2. Vertical error bars represent the standard error calculated from all measured adsorption values.

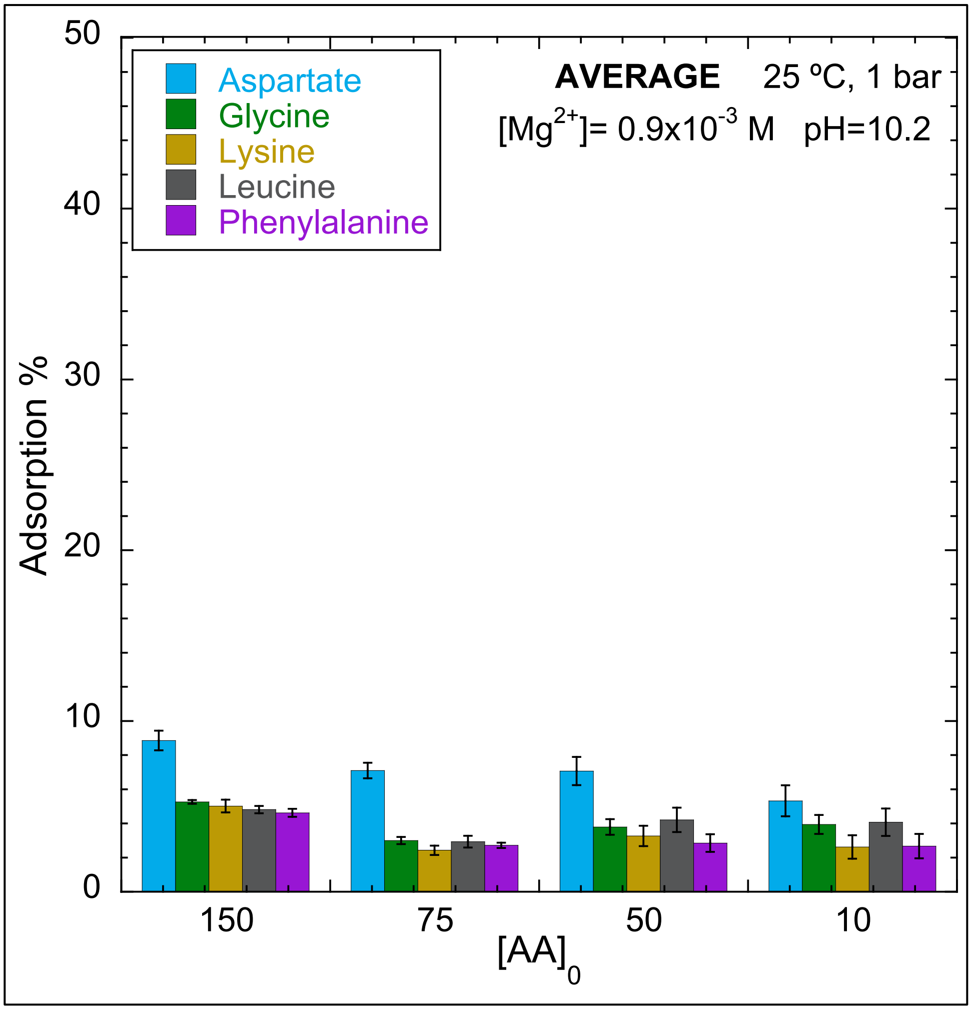

Fig. 5. Average adsorption (%) of aspartate, glycine, lysine, leucine, and phenylalanine onto brucite as a function of the initial concentration of the amino acid mixture following three batch experiments with [Mg^{2+}]=0.9x10^{-3} M and [Ca^{2+}]=4.1x10^{-3} M present at pH 10.2. Vertical error bars represent the standard error calculated from all measured adsorption values.

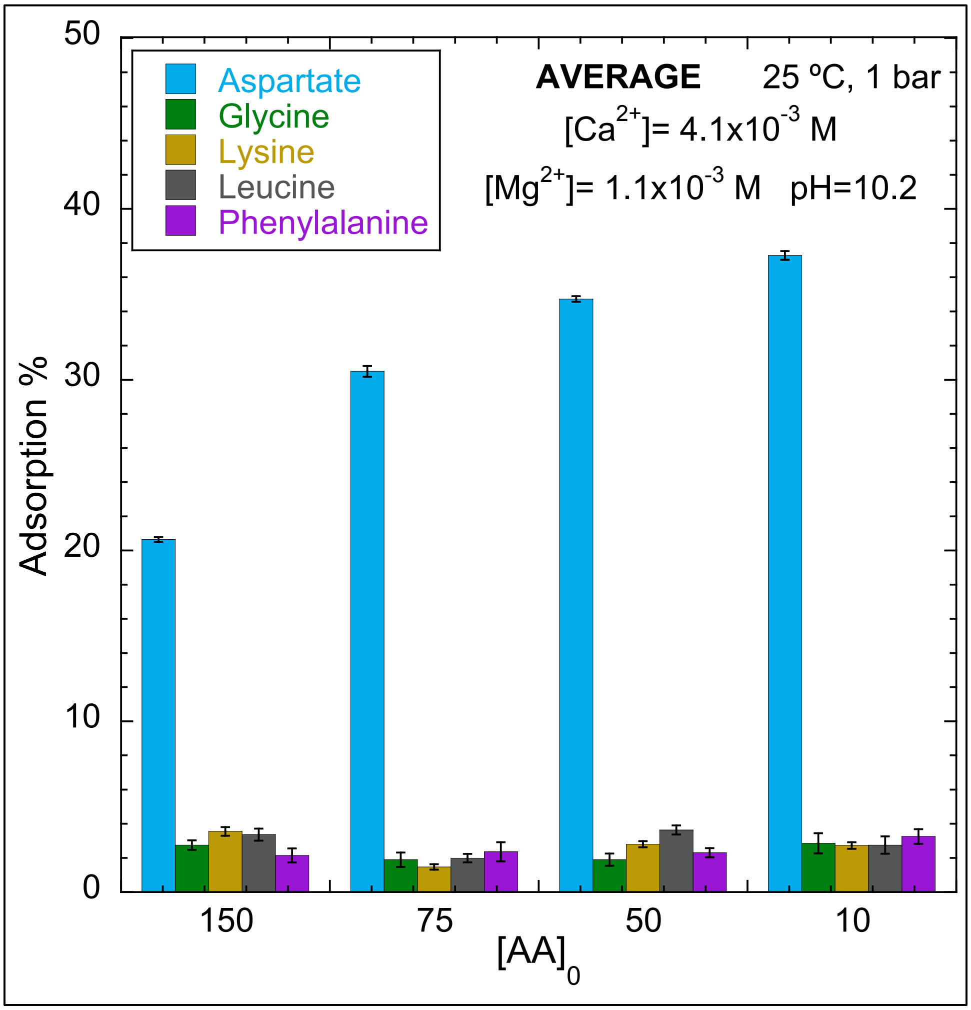

Fig. 6. Adsorption (%) of calcium onto brucite as a function of the initial concentration of the amino acid mixture at the three batch experiments with $[Mg^{2+}]=0.9x10^{-3}$ M and $[Ca^{2+}]=4.1x10^{-3}$ M present at pH 10.2. Vertical error bars represent standard error observed in each experiment. Adsorption data predicted with the proposed reaction in Eq. (3) and the parameters in Tables 1 and 2 using surface complexation modeling are represented by striped bars.

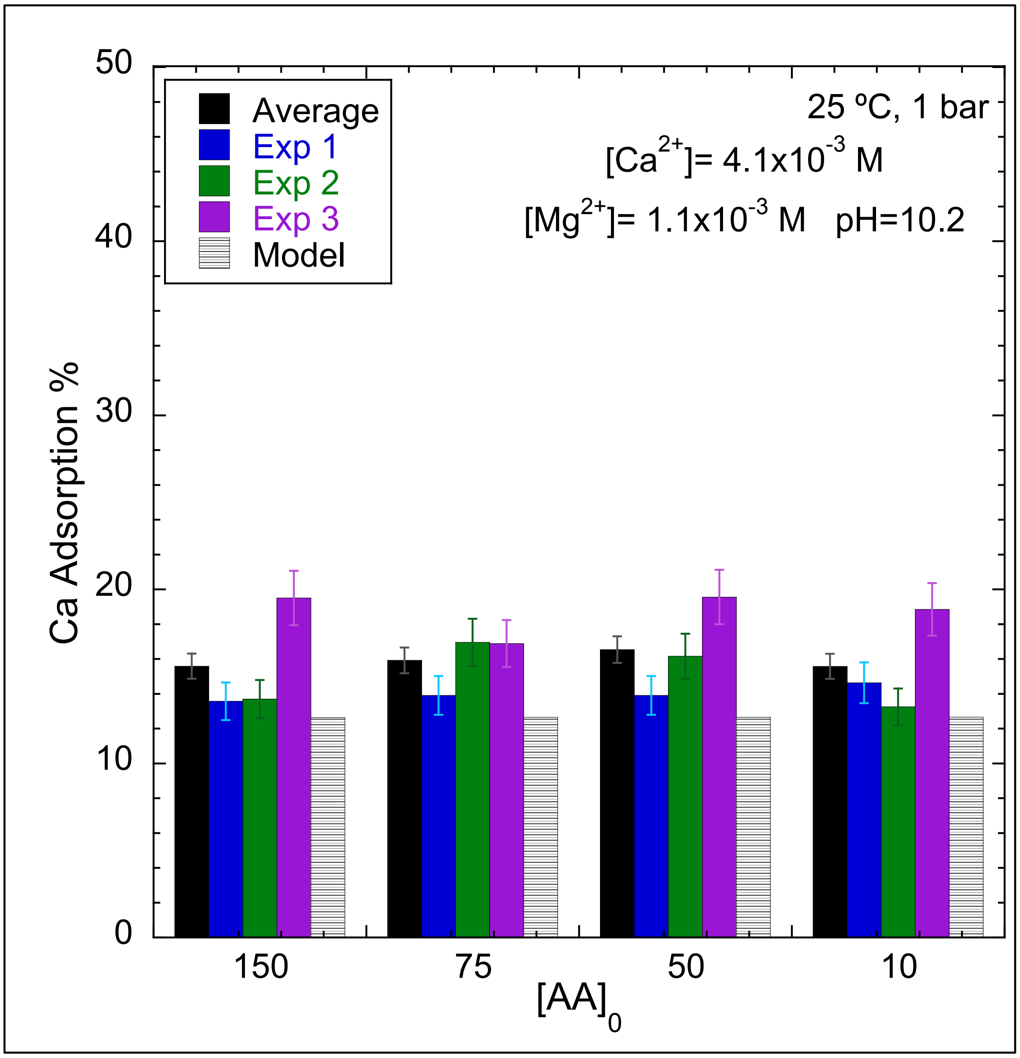

Fig. 7. Possible representation of surface species predicted by surface complexation calculations using the parameters in Tables 1 and 2 and in unpublished data investigating the brucite-aspartate system. (a) Attachment of a hydrated calcium molecule to the brucite surface forming a monodentate outer-sphere species through a hydrogen bond between a positively-charged surface site and the hydroxyl functional group (>SOH···OH-CaOH). (b) Attachment of a calcium-aspartate complex to the (100) surface forming a monodentate outer-sphere species through an electrostatic interaction between a surface oxygen atom and the calcium atom (>SO···Ca-O-C). Red spheres represent oxygen, yellow spheres are magnesium, tan spheres are hydrogen, large light blue spheres are calcium, small pale blue spheres are nitrogen, and black spheres are carbon atoms.

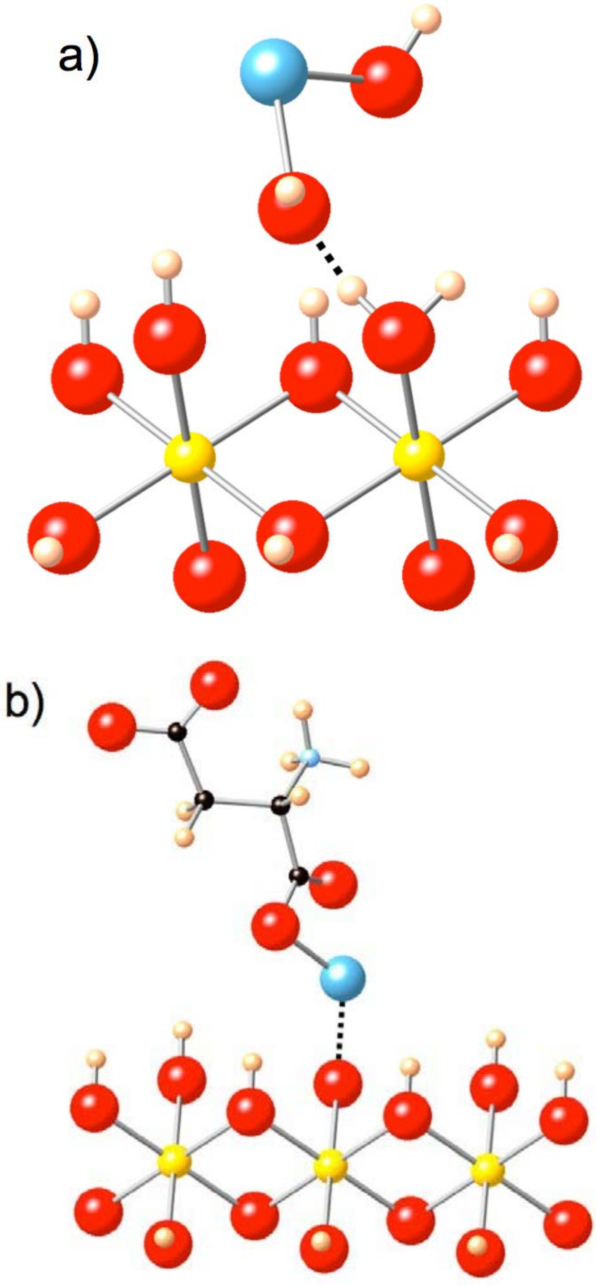

Fig. 8. ζ-potential (mv), or particle surface charge, predicted by surface complexation calculations with parameters in Tables 1 and 2 as a function of the initial concentration of the amino acid mixture in the presence of [Mg^{2+}]=0.9x10^{-3} M and no Ca^{2+} and [Mg^{2+}]=1.1x10^{-3} M and [Ca^{2+}]=4.1x10^{-3} M at pH 10.2.

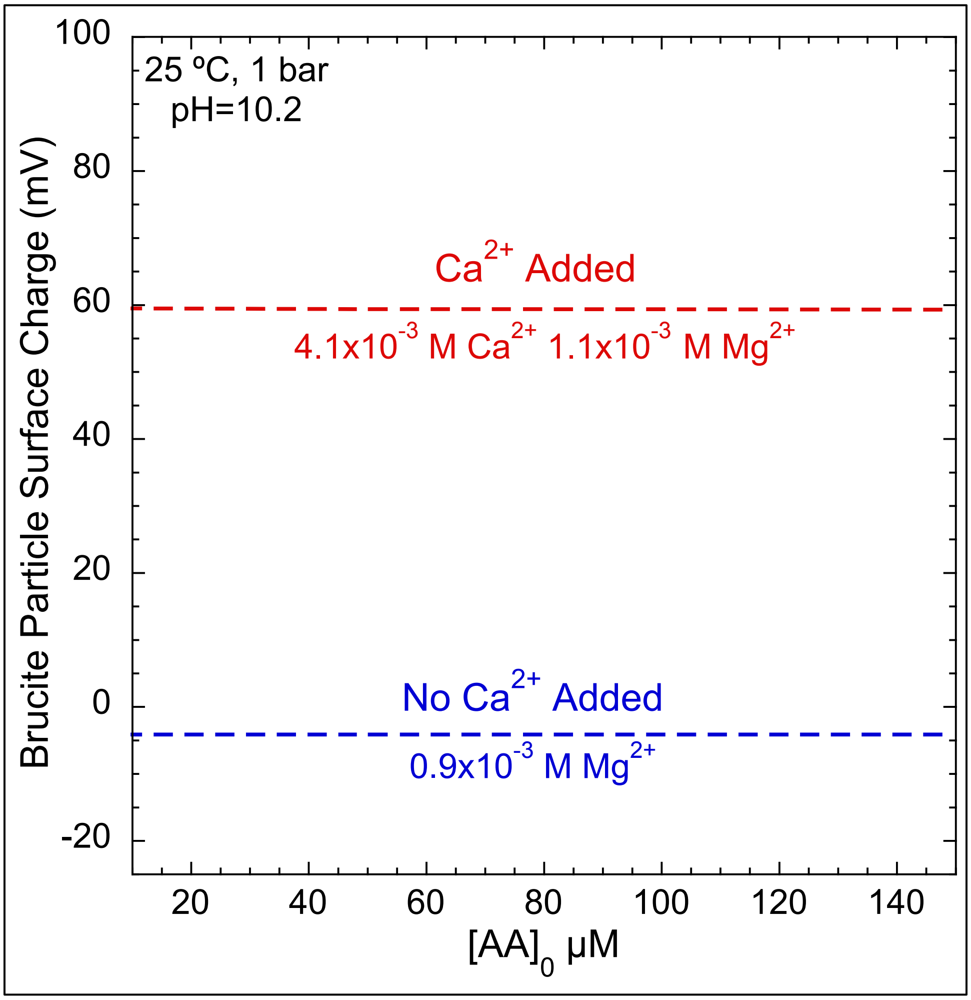

Table 1. Characteristics of brucite[a] [$Mg(OH_2)$], and extended triple-layer model parameters for proton and electrolyte adsorption onto brucite.

Reaction Type	**Reaction**	**log K**
Surface equilibria	Hypothetical 1.0 m standard state	
$\log K_1^0$	$>SOH + H^+ = >SOH_2^+$	9.60
$\log K_2^0$	$>SO^- + H^+ = >SOH$	11.40
$\log {}^*K_{Na^+}^0$	$>SOH + Na^+ = >SO^-\_Na^+ + H^+$	-9.00
$\log {}^*K_{Cl^-}^0$	$>SOH + Cl^- + H^+ = >SOH_2^+\_Cl^-$	11.80
$\log {}^*K_{>SOH_2^+\_Ca(OH)_2}^0$	$>SOH + Ca^{2+} + 2H_2O = >SOH_2^+\_Ca(OH)_2 + H^+$	-5.20
Surface equilibria[b]	Site-occupancy standard state	
$\log K_{>SOH_2^+\_Ca(OH)_2}^\theta$	$>SOH_2^+ + Ca^{2+} + 2H_2O = >SOH_2^+\_Ca(OH_2) + H^+$	-3.87

[a] Brucite properties are N_s= 38 sites•nm^{-2}, A_s= 1.9 m^2•g^{-1}, C_1= 190 µF•cm^{-2}, C_2= 190 µF•cm^{-2}, pH_{PPZC}= 10.5, ΔpK^θ_n=2.08, $\log K^\theta 1$= 9.46, $\log K^\theta_2$= 11.54, $\log^\theta K_{Na}$+= -9.14 $\log^\theta{}_{Cl}$-= 11.66

[b] Equilibrium constants relative to site occupancy standard states can be written relative to charged surface sites calculated using the equations: $\log K_{>SOH_2^+\_Ca(OH)_2}^\theta = \log {}^*K_{>SOH_2^+\_Ca(OH)_2}^0 + \log(N_sA_s)/100$, where N_s is site density, A_s is BET edge surface area m^2•g^{-1}, and C_s is solid concentration g•L^{-1}.

Table 2. Aqueous amino acid properties incorporated into ETLM calculations.

Reaction Type	**Reaction**	**log K**
Aqueous aspartate equilibria[a]	$Asp^{2-} + H^+ = HAsp^-$	10.01
	$HAsp^- + H^+ = H_2Asp$	3.88
	$H_2Asp + H^+ = H_3Asp^+$	1.92
	$HAsp^- + Cl^- + 2H^+ = H_3AspCl$	5.3
	$HAsp^- + Na^+ = NaHAsp$	-0.3
	$HAsp^- + Na^+ = NaAsp^- + H^+$	-9.6
	$HAsp^- + Ca^{2+} + H^+ = CaH_2Asp^{2+}$	-4.43
	$HAsp^- + Ca^{2+} = CaHAsp^+$	1.43
	$HAsp^- + Ca^{2+} = CaAsp + H^+$	-7.49
Aqueous glycine equilibria[b,c]	$HGly^- + H^+ = H_2Gly$	9.58
	$H_2Gly + H^+ = H_3Gly^+$	2.34
	$H_2Gly + Ca^{2+} = CaHGly^+ + H^+$	-8.43[c]
Aqueous lysine equilibria[b]	$HLys^- + H^+ = H_2Lys$	10.67
	$H_2Lys + H^+ = H_3Lys^+$	9.16
	$H_3Lys^+ + H^+ = H_4Lys^{2+}$	2.15
Aqueous leucine equilibria[b,d]	$HLeu^- + H^+ = H_2Leu$	9.58
	$H_2Leu + H^+ = H_3Leu^+$	2.32
	$H_2Leu + Ca^{2+} = CaH_2Leu^{2+}$	1.36[d]
Aqueous phenylalanine equilibria[b]	$HPhe^- + H^+ = H_2Phe$	9.09
	$H_2Phe + H^+ = H_3Phe^+$	2.18

[a] Protonation constants and electrolyte ion pair constants from (De Robertis et al., 1991; Jonsson et al., 2010)

[b] Protonation constants from (Haynes, 2014)

[c] Electrolyte ion pair constant from (Shock and Koretsky, 1993)

[d] Electrolyte ion pair constant from (Kurochkin et al., 2011)

Table 3. Amino acid adsorption data observed for batch experiments with no Ca^{2+} and 4.1×10^{-3} M Ca^{2+} added.

Batch Experiment	**$[AA]_0$ (μM)**	**% Asp Ads**	**% Gly Ads**	**% Lys Ads**	**% Leu Ads**	**% Phe Ads**
No Ca^{2+} Added #1	10	5.7	4.9	3.3	3.4	1.3
	50	6.7	3.8	4.0	4.2	1.7
	75	7.5	3.3	2.9	2.6	2.2
	150	12.9	9.0	8.9	8.4	7.8
No Ca^{2+} Added #2	10	3.9	1.1	0.7	2.2	1.3
	50	8.3	1.2	1.5	2.5	1.0
	75	8.1	2.3	0.7	2.0	1.2
	150	10.6	3.8	3.2	3.6	2.9
No Ca^{2+} Added #3	10	6.3	3.1	4.0	6.6	5.4
	50	6.2	3.3	4.3	6.0	5.9
	75	5.7	6.4	3.8	4.2	4.8
	150	3.0	5.8	2.9	2.5	3.2
Average	*10*	*5.3*	*4.0*	*2.6*	*4.0*	*2.7*
	50	*7.1*	*3.8*	*3.3*	*4.2*	*2.9*
	75	*7.1*	*3.0*	*2.4*	*2.9*	*2.7*
	150	*8.9*	*5.3*	*5.0*	*4.8*	*4.6*
Ca^{2+} Added #1	10	38.4	3.5	0.8	0.7	3.1
	50	34.2	1.1	0.8	2.4	0.3
	75	30.2	0.8	0.8	0.6	0.8
	150	20.7	1.9	2.3	2.3	1.2
Ca^{2+} Added #2	10	39.0	2.6	6.0	5.7	5.3
	50	36.1	3.5	5.5	4.5	3.5
	75	30.2	4.2	1.9	2.9	2.4
	150	20.1	3.9	5.0	3.5	2.2
Ca^{2+} Added #3	10	34.4	2.5	1.4	1.9	1.4
	50	33.9	1.1	2.1	4.1	3.2
	75	31.0	0.6	1.7	2.5	3.9
	150	21.1	2.5	3.3	4.4	3.0
Average	*10*	*37.3*	*2.9*	*2.7*	*2.8*	*3.2*
	50	*34.7*	*1.9*	*2.8*	*3.6*	*2.3*
	75	*30.5*	*1.9*	*1.5*	*2.0*	*3.4*
	150	*20.6*	*2.8*	*3.6*	*3.4*	*2.1*

Chapter 5

Aspartate transformation at 200 °C with brucite [Mg(OH)$_2$], NH$_3$, and H$_2$: Implications for prebiotic molecules in hydrothermal vents

The role of hydrothermal systems in the evolution of prebiotic chemistry on early Earth has been debated due to the perceived instability of amino acids at high temperatures. However, little is known about the stability of amino acids in the presence of mineral surfaces and reducing conditions, which reflect the geochemical complexities of hydrothermal environments such as serpentinite-hosted hydrothermal vents. We therefore investigated the decomposition of 25 mM aspartate at 200 ºC and 15.5 bars (P_{SAT}) in gold tubes both with and without brucite [Mg(OH)$_2$], a stable mineral during serpentinization, and reducing conditions (NH_4Cl and $H_{2(aq)}$). We observed that the reaction kinetics of aspartate are complex and vary significantly with the initial reaction conditions. Fluids containing aspartate alone decomposed to fumarate, maleate, malate, acetate, and minor amounts of succinate and glycine. However, under reducing conditions (2.4 ± 0.6 mM NH_4Cl and 13 ± 10 mM $H_{2(aq)}$), the main product was succinate (8 mM). We also found a total of ~1 mM total of the amino acids glycine, α-alanine, β-alanine, and glycine. In the presence of brucite, we detected up to 2.6 mM α-alanine plus

glycine, but no β-alanine, which suggests that the addition of a mineral surface could play a stereoselective role in the formation of α-alanine. The presence of brucite was also associated with a decrease in the fumarate concentration by a factor of three while maleate concentration decreased by over a factor of ten, leading to an overall increase in the fumarate-to-maleate ratio from 0.9 to 4.5. This increase in the cis/trans ratio might have been caused by stereoselective adsorption, a pH shift, or increased Mg^{2+} concentrations. The results of this study provide clear evidence that the fundamental properties of a hydrothermal system, including mineral assemblages, reducing conditions, and dissolved species concentrations, may directly influence the fate of amino acids at high temperatures. The complicated behavior of amino acids under more geochemically complex reaction conditions may potentially provide a diverse array of biologically relevant organic compounds at hydrothermal systems, and particularly serpentinite-hosted hydrothermal fields, for life's origins.

Authors: Charlene F. Estrada, Irena Mamajanov, Jihua Hao, Dimitri A. Sverjensky

George D. Cody, and Robert M. Hazen

1. Introduction

The potential role of hydrothermal vents as host environments for the emergence of prebiotic compounds may be of critical importance for theories of life's origins on early Earth. Previous studies have successfully synthesized biomolecules including lipids, amino acids, and oligopeptides under laboratory-simulated hydrothermal conditions (Hennet et al., 1992; McCollom et al., 1999; Tsukahara et al., 2002; Kawamura and Shimahashi, 2008; Lemke et al., 2009). Moreover, thermodynamic calculations by Shock and coworkers have predicted that kinetic barriers preventing the equilibration of methane may lead to metastable equilibrium between oxidizing and reducing species within the C-H-O-N system at modern hydrothermal temperatures and pressures and thereby permit an array of biologically useful organic species to form spontaneously (Shock, 1990; Shock and Canovas, 2010). Recent studies of glutamic acid under hydrothermal conditions are consistent with the concept of metastable equilibrium amongst glutamate, glutaconate, α-hydroxyglutarate, and α-ketoglutarate in the presence of dissolved H_2 over timescales of ~40 minutes (Lee et al., 2014a, b). Despite suggestions to the contrary (White, 1984; Bernhardt et al., 1984; Miller and Bada 1988; Bada et al., 1995; Aubrey et al., 2008), it is possible that if biomolecules synthesized at hydrothermal vents achieve metastable equilibrium under high-temperature, high-pressure conditions over geologic periods of time, hydrothermal systems may well represent a significant source of early Earth's organic species.

Numerous studies have indicated that mineral surfaces catalyze transformation pathways of organic molecules under hydrothermal conditions (Wächtershäuser, 1988; Andersson and Holm, 2000; Cody et al., 2004; Foustoukos and Seyfried, 2004; de

Aldecoa et al., 2013) Recently, Shipp and coworkers (2014) demonstrated a very specific, well-characterized catalytic conversion in the presence of sphalerite. The normally slow conversion between *cis* and *trans* stereoisomers of 1,2-dimethylcyclohexane was rapidly accelerated in the presence of sphalerite (ZnS_2) at 300 ºC and 1000 bars. Another strong effect of minerals was indicated by the interaction of pyruvate with the transition metal sulfides pyrrhotite, troilite, marcasite, arsenopyrite, or pyrite both at 25 ºC and 110 ºC (Novikov and Copley 2013). The decomposition products of pyruvate varied compared to those experiments when no mineral was added. Furthermore, the addition of certain minerals selectively facilitated some reaction pathways over others, thereby leading to increased concentrations of biomolecules specific to the mineral. For instance, the highest concentration of lactate, produced from the reduction of pyruvate, occurred when pyrrhotite was added (Novikov and Copley, 2013). These studies reflect the potential of mineral surfaces to induce a complex mixture of biomolecules to follow specific reaction pathways. These mineral-guided organic reaction pathways may lead to greater concentrations of only a few specific products. In this way, the presence of minerals may induce an organic system to self-organize (Hazen and Sverjensky, 2010). However, the above experiments neither directly controlled the redox state nor measured the concentration of dissolved H_2.

In this study, we have investigated the reaction pathways of a previously well-studied amino acid, l-aspartate, in the presence of reducing conditions and ammonia by adding $H_{2(aq)}$ and NH_4Cl, and in the presence of brucite [$Mg(OH)_2$]. Brucite is a major phase in serpentinite-hosted hydrothermal vents (Kelley et al., 2001; Kelley et al., 2005; Bach et al., 2006). Serpentinite-hosted hydrothermal vents involve the hydration of olivine at temperatures of 110 to 150 ºC, which results in the production of up to 19 mM $H_{2(aq)}$ (Kelley et al., 2005; Proskurowski et al., 2006). Ferro-brucite $[(Fe^{2+},Mg)(OH)_2]$ initially precipitates as a product from serpentinization although, as the reaction progresses over long periods of time, the magnesium end-member brucite precipitates as hydrogen activity decreases (Bach et al., 2006; McCollom and Bach, 2009).

We have previously investigated surface chemical interactions between a synthetic brucite powder and biomolecules, including ribose and the amino acids glycine, lysine, leucine, phenylalanine, and aspartate (Estrada et al, in review; in prep. a; in prep. b). We found that at 25 ºC and 1 bar up to 1.0 $\mu mol \bullet m^{-2}$ aspartate adsorbed onto the brucite surface. We also established that brucite attains a steady state with the aqueous phase after 16 hours. We assumed that the reaction

$$Mg(OH)_2 + 2H^+ = Mg^{2+} + H_2O \qquad (1)$$

reaches equilibrium at the steady state with a calculated equilibrium constant of logK= 17.3 ± 0.06. This value is consistent with the equilibrium constant logK= 17.6 ± 0.5 that was previously calculated in an investigation of a powdered natural brucite sample by Pokrovsky and Schott (2004). If we assume that brucite is in equilibrium with the aqueous phase, then we can calculate pH with the known concentration of Mg^{2+} and the equilibrium constant from Eq. (1).

The stability and reaction pathways of aspartate in water at hydrothermal temperatures and pressures have previously been studied in detail (Bada and Miller, 1969; Bada and Miller, 1970; Andersson and Holm, 2000; Sato et al., 2004; Cox and Seward, 2007; Faisal et al., 2007). Of these studies only Cox and Seward (2007) used gold reaction vessels. Their study was particularly relevant because they demonstrated the catalytic effect of container materials other than gold and directly correlated this previously unrecognized effect with measured differences in the kinetics of aspartate decomposition reactions. The reactions in Fig. 1 outline some of the decomposition pathways that have been proposed for aspartate at temperatures from 60 ºC to 260 ºC. Bada and Miller (1970) reported that aspartate predominantly decomposes to fumarate and approximately equal concentrations of its *–cis* isomer, maleate, with a reversible deamination reaction according to

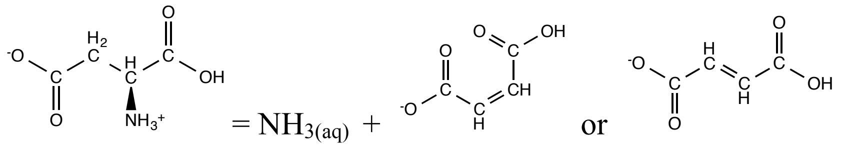

(2)

This reaction has also been reported by Cox and Seward (2007), particularly at temperatures greater than 170 ºC and 20 bars, and Sato et al. (2004), Faisal et al. (2007) at 200 to 260 ºC and 200 bar.

Numerous studies also reported that malate forms reversibly as a hydration product of fumarate and maleate according to the reaction

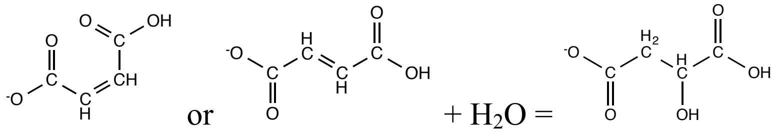

(3)

However, malate was not detected by Cox and Seward (2007), presumably because of the relatively short reaction times used (~several hours).

Citric acid cycle pathways suggest that malate may oxidize to oxaloacetate (Thauer, 1988; Meléndez-Hevia et al., 1996; Cody et al., 2001; Dalla-Betta and Schulte, 2009). Oxaloacetate then rapidly decarboxylates to form pyruvate (Krebs and Johnson 1937; Thauer, 1988; Meléndez-Hevia et al., 1996; Cody et al., 2001; Dalla-Betta and

Schulte, 2009), which undergoes a second decarboxylation reaction that results in acetate according to

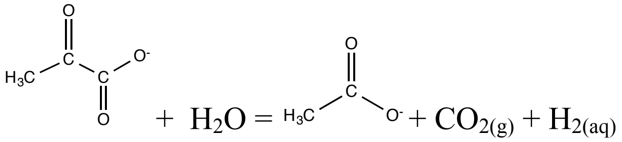

(4)

These reactions, illustrated in Fig. 1, suggest that fumarate, maleate, malate, pyruvate, acetate, and $CO_{2(g)}$ are the predominant decomposition products of aspartate in water at high temperatures. Previous characterizations of aspartate stability at temperatures above 200 ºC suggest that aspartate is one of the most unstable amino acids, with a half-life as limited as several hours (White, 1984; Bada et al., 1995; Sato et al., 2004; Faisal et al., 2007). Nevertheless, Cox and Seward (2007) have reported the formation of diaspartate, particularly at temperatures of 120 to 170 ºC, suggesting the transformation pathways of aspartate may be more complex than previously assumed. This potential complexity was also observed by Holm and Andersson (2000), who found that aspartate decomposition rates decreased in the presence of a sulfide mineral assemblage. It may therefore be possible to increase the stability of aspartate relative to its decomposition products by increasing hydrogen fugacity and/or adding minerals.

In the present study we investigate the stability of aspartic acid under hydrothermal conditions with the addition of both $NH_{3(aq)}$ and $H_{2(aq)}$, with and without brucite, in gold reaction capsules. Fig. 2 illustrates that aspartate is thermodynamically stable relative to oxaloacetate at $[NH_{3(aq)}]= 10^{-2}$ to 10^{-6} M when $[H_{2(aq)}]$ is greater than 10^{-6} and 10^{-1} M, respectively. In our study, we therefore investigated the stability of aspartate under reducing conditions of approximately 2 mM NH_4Cl and 10 to 20 mM $H_{2(aq)}$ for comparison with experiments involving aspartate only. These conditions are consistent with those detected at serpentinite-hosted hydrothermal vents where [$H_{2(aq)}$] has been reported up to 19 mM and [$NH_{3(aq)}$]= 1 to 3 mM (Kelley et al., 2001; Kelley et al., 2002; Kelley et al., 2005). The goal of these experiments is to characterize aspartate stability under hydrothermal temperatures of 200 ºC and determine whether geochemical variables, such as $NH_{3(aq)}$ and $H_{2(aq)}$ and the addition of a mineral surface, may promote specific reaction products. These experiments therefore represent a first step toward understanding the complexities of hydrothermal systems and their associated mineral assemblages and redox conditions in the evolution of prebiotic chemistry on early Earth.

2. Materials and Methods

2.1. Brucite Synthesis

We used a laboratory-synthesized brucite powder that we have previously characterized with batch adsorption studies (Estrada et al., in review; in prep.a; in prep.b). Our preparation method followed similar procedures to those reported previously (Henrist et al., 2003; and Lu et al., 2004). Briefly, we added 2.0 M $MgCl_2$ (99.99% Alfa Aesar dry ampoules under Ar gas) dropwise to a stirred reaction vessel containing 2.0 M NH_4OH at 45 ± 3 ºC. Following precipitation of the brucite powder, we cooled the reaction vessel at room temperature for 3 days and dried the powder with a hot plate (Corning PC-420D). We then carried out a hydrothermal aging process to improve crystallinity and morphology (Henrist et al., 2003; Lu et al., 2004) by sealing the precipitate in 18.2 MΩ•cm Milli-Q water (Millipore) within a PTFE-lined stainless steel reaction vessel (Col-Int-Tech). We heated the vessel at 150 ºC for 3 days (Fisher-Scientific Isotherm Furnace ±2 ºC), cooled the suspension to room temperature, and dried the powder using a Corning hot plate. We stored the hydrothermally-aged product in a glass vial under Ar gas at 25 ºC. Scanning electron microscopy (JEOL 8500F) confirmed that the particles were lamellar, hexagonal-shaped platelets that were aggregated into small clusters of < 1 μm (Fig. 3).

2.2. High Temperature Reactions

In our study, we examined the reaction of l-aspartate (>99%, Sigma-Aldrich) at 200 ºC and 15.5 bars in four types of experiments:

1) Solutions containing only 25 mM aspartate.
2) Aspartate (25 mM) under reducing conditions, to which we added 2.4 ± 0.6 mM NH_4Cl and 13 ± 10 mM $H_{2(aq)}$.
3) Aspartate (25 mM) with either 10 ± 1 $g{\bullet}L^{-1}$ or 30 ± 1 $g{\bullet}L^{-1}$ brucite added.
4) Aspartate (25 mM) with brucite under reducing conditions, to which we added 10 ± 1 $g{\bullet}L^{-1}$ brucite, 2.4 ± 0.6 mM NH_4Cl, and 22 ± 10 mM $H_{2(aq)}$).

We added $H_{2(aq)}$ to experiments (2) and (4) by adding small amounts of Mg metal to the reactors, and assuming that the reaction

$$Mg_{(s)} + 2H_2O \rightarrow Mg(OH)_2 + H_{2(aq)} \tag{5}$$

proceeds to completion at 200 ºC to produce a concentration of $H_{2(aq)}$ that can be calculated from the reaction stoichiometry. We determined an uncertainty of ±10 mM for the amount of $H_{2(aq)}$ calculated for both experiments (2) and (4) due to uncertainties in weighing μg quantities of magnesium metal. We dissolved commercially available NH_4Cl (>99 % Sigma-Aldrich) in Milli-Q water to obtain a solution of approximately 2 mM NH_4Cl. Analyses of this solution by IC determined that $[NH_4^+]$ was equal to 2.4 ± 0.6 mM.

As emphasized above, previous studies have observed that the surfaces of reactors may exhibit catalytic effects on amino acid reactions at hydrothermal conditions (Cox and Seward, 2007; Lemke et al, 2009). Therefore, we conducted our experiments with inert gold reactors made from capsules 2 to 2.5 cm in length with an inner diameter of 4.1 mm and an outer diameter of 5 mm. Prior to our experiments, we boiled the capsules in a 50 % solution of 12 M HCl, rinsed them Milli-Q water, and dried them in an oven at 85 ºC for at least 1 hour. The capsules were sealed at one end using a precision welder (PUK 3s Plus Professional), and each capsule was purged with Ar gas. If an experiment required the addition of either Mg metal to create $H_{2(aq)}$ or brucite power, we loaded the solids into the capsules. We purged the aspartate solutions with Ar gas and then added between 0.15 and 0.20 mL of the solution to each capsule. We sealed the capsules within a PTFE-lined stainless steel reactor (Col-Int-Tech) with Milli-Q water, and we placed the reactor into a pre-heated furnace set at 200 ± 2 ºC. We allowed the reaction to proceed over 24 hours, including the amount of time for the reaction vessel to reach an internal temperature of 200 ºC. We assumed that the pressure within the gold capsule is equal to the pressure of water vapor at 200 ºC. The water we added to the PTFE-lined vessel pressurizes the capsule and prevents it from bursting.

After the 24-hour experimental run, we quenched the reaction vessel to room temperature by submersing it in cold water. We then removed the gold capsules from the reaction vessel and weighed each capsule to determine any mass lost due to leakage. We rinsed the capsules with Milli-Q water and froze them in liquid nitrogen. We then cut open the frozen capsules with a pre-sterilized pair of steel cutters, and placed the capsules in a glass vial filled with the volume of Milli-Q water necessary to dilute the contents by a factor of 25. We allowed the contents of the glass vial to thaw and mix for at least one hour before separating the fluid from the gold capsule. Following experiments in which we added brucite or we inferred that brucite had precipitated after we added Mg metal (Eq. 5), it was necessary to separate the mineral from the fluid by centrifugation at 4000 rpm for 10 minutes. We further separated and passed the clear fluid through 0.2 μm membrane filters before we analyzed the solutions with UPLC-MS and IC methods.

2.3. Analysis of Samples by Ultra Performance Liquid Chromatography-Mass Spectrometry

We determined the concentrations of fumarate, maleate, malate, pyruvate, and succinate present in each sample with an Acquity Ultra Performance Liquid Chromatography (UPLC-MS) system equipped with a Triple Quadrupole (TQ) detector (Waters Corporation, Manchester UK). We operated the instrument in negative ion mode with a probe capillary voltage of 2.5 kV and a sampling cone voltage of 15 V. We set the source and desolvation temperatures to 150 and 250 °C, respectively, and we set the nitrogen desolvation flow rate to 500 $L \cdot h^{-1}$. We calibrated the mass spectrometer across the 80 to 2000 m/z range using a 0.5 mM citric acid aqueous solution. We set the scan time to 0.5 s and carried out data acquisition and processing using MassLynx v4.1 software (Waters Corp.) Additionally, our UPLC-MS system was configured with a C18 (HSS T3 1.8 μm, 2.1 Å – 150 mm, Waters Corporation) column. We employed an isocratic flow rate of 0.200 $mL \cdot min^{-1}$ using H_2O and 0.15 % formic acid. We set the column temperature to 40 ºC. The UPLC-MS system detected the organic compounds of interest in single ion current mode, and we determined the concentrations of these compounds by comparing them against standard solution curves within the peak area-analyte concentration (mM) range. We used this standardization to determine the reported uncertainty (±) associated with the concentrations for each sample by calculating the absolute value of the concentration that would result if no peak area was detected for each compound. We observed that the reported error varied between the different organic acids we analyzed, and it also increased with a greater dilution factor.

2.4. Analysis of Samples by Ion Chromatography

We analyzed the concentrations of the amino acids aspartate, glycine, α-alanine, and β-alanine, and the cations Mg^{2+} and NH_4^+ with ion chromatography (IC) using a Dionex ICS-5000 system equipped with a DP dual pump, AS-AP autosampler, and Chromeleon 6.8 software (Dionex Corporation, Sunnyvale, CA, USA). We assayed the amino acid concentrations by passing the samples through an AminoPAC10 column, after which the amino groups were oxidized with integrated pulsed amperometric detection (IPAD) in order to detect them with the working gold electrode of the ED electrochemical detector (Clarke et al., 1999; Jandik et al., 2000). We determined the concentrations of NH_4^+ and Mg^{2+} present in the samples with the ICS-5000 using an IonPac CS12A column that separates the cations, which are then detected with a CD conductivity detector with electrolytic suppression.

We analyzed the concentration of acetate present in the samples with a Metrohm IC system consisting of an 813 AS autosampler unit, 709 IC pump and 752 pump units, and an 820 IC separation center with a column oven and conductivity detector connected to an 819 IC detector and 762 IC interface. We evaluated the chromatograms resulting from the separation of samples with Metrohm IC Net 2.3 software.

At least two hours prior to analyzing the samples with IC, both with the ICS-5000 and Metrohm systems, we ran standard solutions for each compound of interest. We standardized the analyte concentration-chromatogram area as a linear correlation. We used this calibration to calculate the reported uncertainty (±) associated with each compound of interest by determining the absolute value of the concentration that would be detected if no peak area was detected. We observe that this value increases as the dilution factor required for the analysis increases.

3. Results and Discussion

3.1. Mass Balance Considerations

In Fig. 4a, we compared the concentration of carbon present in the initial 25 mM aspartate with total carbon present in the concentration of the calculated organic decomposition products, which included stoichiometric estimations of $CO_{2(g)}$ (see below), and total measured concentrations of the decomposition products, which included only the products we detected with IC and UPLC-MS methods, in each experiment. Furthermore, we compared the initial concentration of nitrogen-bearing species in the initial aspartate and added NH_4Cl with the measured concentrations of nitrogen-bearing species, which include residual aspartate, additional amino acids, and free NH_4^+, for each experiment in Fig. 4b. All mass balance data for the separate experiments are displayed in Table 1. In the experiments with only aspartate, the average concentration of carbon (113

± 17 mM) appears to exceed that of the initial aspartate added to each experiment. It is possible that we have overestimated the amount of $CO_{2(g)}$ present in experiments with only aspartate, as is indicated by the measured concentration of carbon-bearing products (101 ± 15 mM). In experiments with added NH_4Cl and $H_{2(aq)}$, we determined that the average calculated concentration of carbon present in the organic decomposition products was 96 ± 17 mM and the measured amount of carbon was 89 ± 15 mM. Both values balance the initial concentration of carbon (100 mM) within analytical uncertainty.

The average calculated concentration of carbon present in the organic decomposition products for experiments with 10 $g•L^{-1}$ and 30 $g•L^{-1}$ are 75 ± 16 mM and 73 ± 17 mM, respectively (Fig. 4a). The calculated carbon concentration for both experiments is slightly lower than the initial amount of carbon in the aspartate solution. We observe a difference of approximately 40 mM between the aspartate-only experiments and those with added brucite. We observed a similar trend with the average calculated concentration of carbon in the experiments involving added NH_4Cl, $H_{2(aq)}$, and brucite (70 ± 18 mM). Although we have apparently balanced the initial and final mass, it is possible that some material may have adsorbed onto the brucite surface. This possibility may also be inferred from the mass balance of nitrogen-bearing species, shown in Fig. 4b. Experiments with aspartate only (22 ± 2 mM) and aspartate with NH_4Cl and $H_{2(aq)}$ (24 ± 2 mM) approximate the initial amount of nitrogen added to the system within error, whereas we observe that the experiments involving 10 $g•L^{-1}$, 30 $g•L^{-1}$, or brucite with NH_4Cl and $H_{2(aq)}$ have lower amounts of nitrogen (19 ± 2, 21 ± 2, and 21 ± 2 mM, respectively). The apparent mass balance deficit between the initial amount of aspartate and decomposition organic products, and particularly nitrogen-bearing products, may suggest that there is either an additional nitrogenous species that we have not detected or the brucite is effectively adsorbing species at the mineral-water interface.

3.2. Reaction of Aspartate Alone

We conducted three separate experiments in which 25 mM aspartate reacted at 200 ºC and 15.5 bars without added brucite, NH_4^+, or $H_{2(aq)}$. The concentrations of NH_4^+ and organic species are given in Figs. 5 and 6a, respectively. The concentrations of all the products we measured or estimated for the separate experiments are listed in Table 2. On average, only 0.42 ± 0.05 mM aspartate survived the reaction. The majority of initial aspartate deaminated into fumarate (9.3 ± 0.6 mM) and maleate (10.7 ± 0.5 mM). We also found significant amounts of malate (2.2 ± 1.5 mM), pyruvate (0.3 ± 0.2 mM), and acetate (2.3 ± 0.4 mM). We detected trace amounts of succinate, although the average concentration did not exceed the analytical error established for succinate with the UPLC-MS. We also found that the reaction produced small amounts of the amino acids α-alanine (0.70 ± 0.02 mM), β-alanine (0.06 ± 0.02 mM), and glycine (0.37 ± 0.01 mM). It is likely in the course of these experiments that a small amount of $CO_{2(g)}$ also formed. If we assume that stoichiometric quantities of $CO_{2(g)}$ formed with pyruvate and acetate using the reactions in Fig. 1, an average of 12.3 ± 2.3 mM $CO_{2(g)}$ may have contributed to the total concentration of organic products from aspartate decomposition.

3.3. Reaction of Aspartate with NH_4Cl and $H_{2(aq)}$

We performed two separate experiments with 25 mM aspartate at 200 ºC and 15.5 bars with 2.4 ± 0.6 mM NH_4Cl. We also added 0.06 mg Mg metal to each experiment to produce an average of 13 ± 10 mM $H_{2(aq)}$ and 0.8 ± 0.6 g•L^{-1} brucite, assuming the reaction in Eq. (5) goes to completion. Fig. 5 displays the concentrations of NH_4^+ and Mg^{2+} we detected, and Fig. 6b shows the concentrations of the organic species formed from the decomposition of aspartate. We detected an average of 11.2 ± 0.2 mM Mg^{2+}, which most likely dissolved from the surface of the brucite precipitate.

It can be seen in Fig. 6b that, relative to the aspartate only experiments (Fig. 6a), the amount of aspartate remaining (0.46 ± 0.05 mM) was the same within analytical uncertainty. However, a dramatic difference is apparent for the other organic product species. Most strikingly, we detected substantial concentrations of succinate (8.2 ± 0.8 mM), and notably less fumarate (6.3 ± 0.6 mM), maleate (3.3 ± 0.5 mM), and acetate (0.8 ± 0.3 mM). We also found greater concentrations of the decomposition products malate (2.4 ± 1.5 mM) and pyruvate (0.5 ± 0.2 mM). The concentrations of α-alanine (0.84 ± 0.02 mM), β-alanine (0.03 ± 0.02 mM), and glycine (0.44 ± 0.01 mM) were similar to the values in Fig. 6a. We calculated that an average of 7.2 ± 2.1 mM $CO_{2(g)}$ may have formed, assuming that equimolar quantities of $CO_{2(g)}$ formed with pyruvate and acetate according to the reaction in Fig. 1.

3.4. Reaction of Aspartate with Brucite

We conducted two separate experiments in which 25 mM aspartate reacted at 200 ºC and 15.5 bars, with 10 ± 1 g•L^{-1} brucite and 30 ± 1 g•L^{-1} brucite. Fig. 5 displays the concentrations of cations (NH_4^+ and Mg^{2+}), and Fig. 7a shows the concentrations of organic species. The concentrations of all the products we measured or estimated for the separate experiments are listed in Table 2. We observed that an average of 29.1 ± 0.1 and

38.8 ± 0.3 mM Mg^{2+} respectively dissolved from 10 g•L^{-1} and 30 g•L^{-1} of brucite. The average remaining concentration of aspartate slightly decreased (0.27 ± 0.05 mM and 0.33 ± 0.05 mM) relative to the aspartate-only experiments. We also found that fumarate decreased at least two-fold (4.5 ± 0.6 mM and 4.0 ± 0.6 mM), and maleate decreased more than ten-fold (1.1 ± 0.4 mM and 0.9 ± 0.5 mM) concentrations. Low amounts of succinate (1.3 ± 0.7 mM and 1.6 ± 0.7 mM) were found, and the concentrations of malate (2.8 ± 1.4 mM and 2.6 ± 1.5 mM) and glycine (0.34 ± 0.01 mM and 0.28 ± 0.01 mM) were similar to those of the aspartate-only experiment. Pyruvate concentrations increased by a factor of 2 to 3 (0.9 ± 0.2 mM and 1.2 ± 0.2 mM) as do acetate concentrations (3.0 ± 0.3 mM and 2.7 ± 0.4 mM).

Interestingly, in the experiments with added brucite it can be seen that α-alanine concentrations increased by a factor of 2.9 (2.0 ± 0.02 mM and 2.0 ± 0.02 mM) relative to the aspartate-only experiments. However, we did not detect β-alanine. Assuming that equimolar amounts of $CO_{2(g)}$ were produced with pyruvate and acetate according to the reaction stoichiometries in Fig. 1, we estimated that an average of 20.4 ± 1.9 mM and 20.3 ± 1.0 mM $CO_{2(g)}$ were produced in experiments with 10 g•L^{-1} and 30 g•L^{-1} brucite added, respectively.

3.5. Reaction of Aspartate with Brucite, NH_4Cl, and $H_{2(aq)}$

We conducted two experiments in which 25 mM aspartate reacted at 200 ºC and 15.5 bars with 10 ± 1 g•L^{-1} brucite, 2.4 ± 0.6 mM NH_4Cl, and 0.10 ± 0.04 mg Mg metal. The latter should have converted to an average of 22 ± 10 mM $H_{2(aq)}$ and 1.2 ± 0.6 g•L^{-1} brucite assuming that the reaction in Eq. (5) goes to completion. Fig. 5 displays the cation

(NH_4^+ and Mg^{2+}) concentrations, and Fig. 7b shows the concentrations of organic species. The concentrations of all the products we measured or estimated for the separate experiments are listed in Table 2. Relative to the aspartate-only experiments, we observed significantly less fumarate (5.0 ± 0.7 mM) and one-tenth of the maleate concentration (1.2 ± 0.5 mM), although we found greater amounts of malate (3.3 ± 1.5 mM). We also detected average concentrations of aspartate (0.4 ± 0.1 mM), α-alanine (0.8 ± 0.02 mM), glycine (0.34 ± 0.01 mM), and acetate (2.1 ± 0.4 mM) that were comparable with those of the asparate-only experiments. A large amount of succinate (2.7 ± 0.8 mM) formed relative to the experiments with only aspartate, but much less than in the experiments depicted in Fig. 6b. We calculated that 4.5 ± 0.9 mM of $CO_{2(g)}$ may have been present if we assume that stoichiometric amounts of $CO_{2(g)}$ formed with acetate and pyruvate in the reactions in Fig. 1. We did not detect any β-alanine in these experiments. We also found an average of 23.9 ± 0.5 mM Mg^{2+} and 19.4 ± 1.6 mM NH_4^+.

3.6. Alanine and Glycine Synthesis

We have reported the presence of smaller amino acids including α-alanine, β-alanine, and glycine in our experiments. Whereas both α-alanine and β-alanine have been previously detected in experiments involving the decomposition of aspartate at high temperatures, no investigation has reported glycine. In a study involving the decomposition of serine at 260 ºC and 200 bars, however, Sato et al. (2004) have reported that less than 1 mM glycine formed from retro-aldol condensation. In our experiments, we detected glycine in relatively constant amounts between 0.3 and 0.5 mM. We propose a retro-aldol condensation reaction in which malate decomposes to acetate and glyoxylate according to

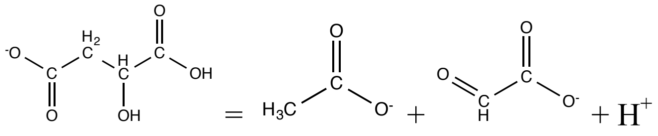

(6)

was followed by reductive amination of glyoxylate to form glycine:

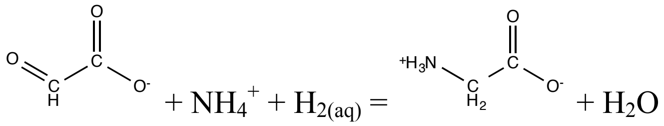

(7)

(Nakada and Weinhouse, 1953; Hafenbradl et al., 1995; White 2006). The reactions in Eqs. (6-7) are labeled as reaction pathway “I” in Fig. 8.

Previous studies (Sato et al., 2004; Faisal et al., 2007; Cox and Seward, 2007) have suggested that the α- and β-carbons of aspartate could have respectively decarboxylated to form α-alanine and β-alanine. While we cannot rule out this mechanism, Bada and Miller (1970) have argued that aspartate decarboxylation accounts for less than 0.2 % of the decomposition products. Considering its relatively low concentrations, it may follow that β-alanine could have formed from this mechanism, but we observe high concentrations of α-alanine that may suggest an additional mechanism of synthesis. Among other researchers, Morowitz (2000), Brandes et al. (1999), Hafenbradl et al. (1995), and Huber and Wächterhauser (2003) have proposed that amino acids may readily form through the reductive amination of α-keto acids such as pyruvate. We have detected both pyruvate and an excess of NH_4^+, which are necessary to achieve this reaction. We therefore propose that α-alanine forms from pyruvate with the mechanism

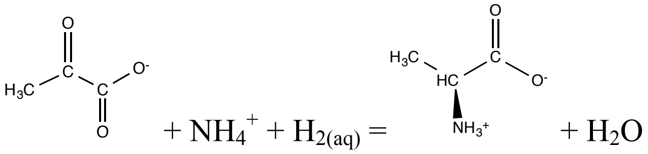

(8),

which is illustrated as reaction pathway “II” in Fig. 8. Additionally, β-alanine may have formed from pyruvate through a reductive amination reaction involving lactate and the acrylate ion, where the reactions

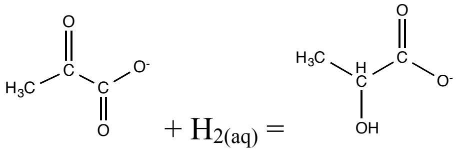

(9a),

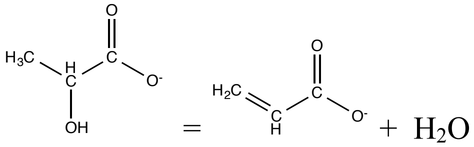

(9b),

and

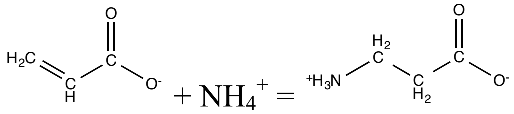

(9c).

are labeled as reaction pathway “III” in Fig. 8.

In our experiments, we observe significantly different concentrations of α- and β-alanine in the presence of brucite. When we add brucite we cannot detect β-alanine, but we observed almost three times the amount of α-alanine (2 mM) at both brucite solid concentrations of 10 g•L^{-1} and 30 g•L^{-1}. In the experiments in which we added only brucite, we also detected the highest concentrations of pyruvate. Because NH_4^+ concentrations in each experiment were relatively high, between 15 to 23 mM (Fig. 4b), we may consider pyruvate as the limiting reactant for the reactions in Eqs. (8-9). As the concentration of pyruvate increases, we expect the concentration of α-alanine to correspondingly increase as shown in Fig. 9. However, when NH_4Cl and $H_{2(aq)}$ are also added with 10 g•L^{-1} brucite, we observed that the average amount of α-alanine decreased to less than 1 mM. It may be possible that the added $H_{2(aq)}$ facilitates competing reaction pathways, and this competitive effect between brucite-favored and $H_{2(aq)}$-favored products results in an overall decrease in α-alanine.

The fact that β-alanine does not form in the presence of brucite could be attributable to either of two effects. Either the brucite surface or the release of Mg^{2+} into the aqueous phase from the dissolution of brucite might inhibit one or more of the reactions in Eqs. (9a-c). However, it is also a possibility that β-alanine formed directly from the decarboxylation of aspartate, where the reaction

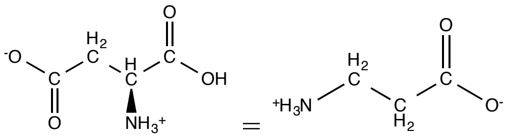

$+ CO_{2(g)}$ (10)

is labeled as pathway "IV" in Fig. 8. If β-alanine forms via decarboxylation, its disappearance could be a pH effect. After we add brucite, the pH could increase toward circumneutral to alkaline conditions near pK_{a2} of aspartate. The electrostatic charge could then strengthen the R–CO_2 bond, and thus decrease the likelihood that aspartate will decarboxylate at the β-position (Li and Brill, 2003). Novikov and Copley (2013) have observed that transition metal sulfides such as pyrrhotite, arsenopyrite, and marcasite may facilitate reductive amination of pyruvate. A similar finding has also been established by Hafenbradl and coworkers (1995) and Wang and coworkers (2011) when pyrrhotite is simultaneously oxidized to pyrite. Therefore, it is possible that brucite exhibits a direct or indirect stereoselective effect on the reductive amination pathway between alanine and pyruvate.

3.7. Succinate Synthesis under Reducing Conditions

The significant amounts of succinate formed under reducing conditions stand in marked contrast to the aspartate-only experiments, where we detected trace amounts of succinate consistent with results reported by Sato et al. (2004) and Faisal et al. (2007). This substantial increase in succinate concentration suggests that reducing conditions, and in particular the addition of $H_{2(aq)}$, may directly lead to the formation of succinate. Our conclusion is consistent with those of Sato et al. (2004) and Faisal et al. (2007), who have suggested that fumarate or maleate reduces to form succinate. Furthermore, in addition to calculating the concentrations of $H_{2(aq)}$ added to the experiment, we have determined the stoichiometric amount of $H_{2(aq)}$ expected to form with pyruvate and acetate in the reactions in Fig. 1. Fig. 10 illustrates that even in the aspartate-only experiments, small amounts of $H_{2(aq)}$ are expected to form from decomposition of aspartate. This concentration of $H_{2(aq)}$ may react with fumarate and maleate to form succinate with the reaction

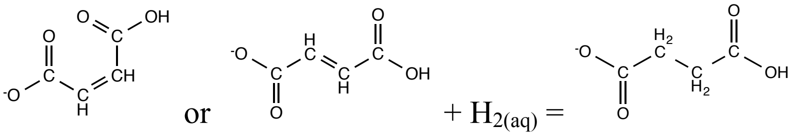

(11),

which is labeled as pathway “V” in Fig. 8.

We observed that the concentration of succinate decreased when we added brucite to the experiments with reducing conditions. We have previously discussed that the addition of $H_{2(aq)}$ to brucite may facilitate reaction pathways, such as pathway V, that compete and consequently decrease the concentration of products that could be promoted by brucite addition alone. It could be that the opposite also may also occur, by which addition of brucite may facilitate pathway II and lead to decreased amounts of succinate.

Another possibility is that brucite decreased the available reactants, fumarate and maleate (see below), or it may directly adsorb succinate. Adsorption investigations at 25 °C and 1 bar by Yao and Yeh (1996) as well as Hwang and Lenhart (2008) have determined that up to 1 $\mu mol \bullet m^{-2}$ succinate adsorbs onto δ-Al_2O_3 and hematite, respectively. These adsorption data certainly support the notion that succinate could interact with the brucite surface under hydrothermal conditions, but adsorption at a level of 1 $\mu mol \bullet m^{-2}$ is not sufficient to take millimolar amounts of succinate out of the solutions in the experiments. It is also possible that brucite has an oxidizing effect on Eq. (11), and clay minerals as well as more reducing mineral assemblages such as transition metal sulfides should be further investigated to evaluate whether mineral surfaces interfere with reducing and oxidizing reaction pathways.

The reduction of fumarate or maleate to form succinate under reducing conditions is another example of the possible reaction pathways that aspartate may follow when more complex conditions are introduced to the system. Nevertheless, we cannot completely dismiss the possibility that succinate could form directly from aspartate through reductive deamination, although we have experimentally observed that both maleate and fumarate are more stable intermediate decomposition products (Figs. 6-7). Regardless of the exact mechanism, we previously hypothesized that aspartate concentrations might increase with the addition of reducing conditions, but our results have indicated that increasing the hydrogen fugacity of the environment specifically favors the formation of succinate. We have calculated that succinate is thermodynamically stable relative to aspartate at moderately low to high hydrogen fugacities. This calculation, shown in Fig. 11, is consistent with our experimental data, which plot well within the succinate field.

3.8. Decrease in Maleate and Fumarate Concentrations

In experiments with aspartate alone, we observe high fumarate and maleate concentrations that are approximately equal to one another. This observation is consistent with that of Bada and Miller (1970). However, as we add greater amounts of brucite (and correspondingly, Mg^{2+}) to each experiment, we observe decreases in the concentrations of both maleate and fumarate. The decrease in maleate concentration is more significant and, as a result, the fumarate-to-maleate concentration ratio increases from approximately 1 to 4 as a function of brucite and $[Mg^{2+}]$, as shown in Fig. 12. Furthermore, the malate concentration is relatively constant. We are unsure whether the decrease in maleate and fumarate concentration and subsequent increase in fumarate-to-maleate ratio is a consequence of either brucite surface effects, a shift in pH, or increased Mg^{2+} concentration.

Studies by Hwang and Lenhart (2008) and Yao and Yeh (1996) have determined that maleate adsorbs in slightly greater amounts than fumarate onto hematite and hydrous δ-Al_2O_3, respectively. The former investigation by Hwang and Lenhart (2008) reported a point of zero charge (pH_{PZC}) of 9.0 for hematite, which suggests that fumarate and maleate could exhibit similar adsorption behavior with brucite (pH_{PZC}= 10.5). Fogg and coworkers (1998) have observed that an aluminum double layered hydroxide, such as $[LiAl_2(OH)_6]Cl{\bullet}H_2O$, selectively intercalates fumarate over maleate. Brucite may therefore selectively adsorb maleate. In Fig. 12a, we have plotted the increase in fumarate-to-maleate ratio from 0.9 to 4.5 as the brucite solid concentration increases. We observe this concentration ratio levels off in the presence of 10 g•L^{-1} brucite or more, which may indicate that if maleate and fumarate adsorb onto brucite, the maximum surface coverage has been reached. Nevertheless, our previous considerations of the brucite surface indicate that significant concentrations between 9 to 10 mM of maleate are unlikely to adsorb onto the brucite surface due to a limited availability of surface sites (Estrada et al., in review). Therefore, it is likely that surface adsorption alone is not causing the dramatic shift in the fumarate-to-maleate concentration ratio.

An alternative explanation for the increase in the fumarate-to-maleate ratio could be a shift in the experimental pH with increasing brucite solid concentration. The reaction in Eq. (1) illustrates the relationship between the dissolution of Mg^{2+} from brucite and solution pH. In Table 3, we have calculated the equilibrium constant of this reaction at 200 ºC and 15.5 bars (logK = 10.3). Furthermore, we also calculated the deprotonation constants, pk_{a1} and pk_{a2}, that result in the formation of the singly- and doubly-deprotonated fumarate and maleate ions at 200 ºC and 15.5 bars (Table 3) by referencing the constants at ambient conditions (Dalla-Betta and Schulte, 2009). Assuming that the brucite is in equilibrium with the aqueous phase after 24 hours, we calculated the experimental pH at 200 ºC and 15.5 bars with the detected concentrations of Mg^{2+} (Fig. 13). We determined that the pH is approximately circumneutral (5.9 to 6.1) in the presence of brucite. These values coincide with the second deprotonation of fumarate ($pK_{a2} = 5.4$) and approach that of maleate ($pK_{a2} = 6.3$). It is possible that the $Male^{2-}$ ion is unstable in aqueous solution due to the proximity of two charged carboxylate groups (Elving and Teitelbaum, 1949). Due to this inherent instability, $Male^{2-}$ may spontaneously isomerize to Fum^{2-} (Davies and Evans, 1956; Font et al., 1988), although at the pH conditions we have calculated in Fig. 13, no more than 20 % of the reported maleate is expected speciate to $Male^{2-}$. We observe that the fumarate-to-maleate concentration ratio decreases with increasing pH, which contradicts the trend that would be expected if maleate converted to fumarate at higher pH conditions. Furthermore, this hypothesis does not explain the net decrease in both fumarate and maleate concentration.

In Fig. 12b, we demonstrate that the fumarate-to-maleate concentration ratio also increases with increasing Mg^{2+} concentration. Mg^{2+} concentration increases with brucite solid concentration, as we have demonstrated with the experimental data in Fig. 14. It is possible that maleate may form stronger complexes with metal ions in water compared with fumarate (Choppin et al. 1973; Naidu and Harter, 1988). While these experiments have focused on lanthanide and cadmium ions with markedly different properties from Mg^{2+}, we cannot dismiss the possibility that Mg^{2+} is complexing to maleate and fumarate (and their decomposition products) to different extents at 200 ºC. Whether the decrease in maleate and fumarate concentration and increase in the fumarate-to-maleate ratio is specifically an effect of the brucite surface, a pH increase, or increased Mg^{2+} concentrations requires further investigation of the maleate to fumarate isomerization reaction with these variables.

4. Concluding Remarks

We investigated the reaction pathways of aspartate at 200 ºC and 15.5 bars, both with and without the presence of brucite (10 to 30 $g \bullet L^{-1}$) and reducing conditions involving 2.4 ± 0.6 mM NH_4Cl and 13 to 22 ± 10 mM $H_{2(aq)}$ in gold capsules over a reaction period of 24 hours. Our main observations and inferences include:

(1) Experiments involving aspartate only resulted in major production of fumarate and maleate, lesser amounts of malate and acetate, and minor amounts of glycine, α- and β-alanine, succinate, and residual aspartate.

(2) In experiments in which we added NH_4Cl and $H_{2(aq)}$, succinate concentrations increased to about 8 mM, and the amounts of fumarate and maleate significantly decreased. We also found small amounts of the amino acids glycine, α-alanine, and β-alanine, which are likely products of retro-aldol condensation, reductive amination, and decarboxylation, respectively (Fig. 8).

(3) When we studied aspartate in the presence of brucite without NH_4Cl or $H_{2(aq)}$, we observed a dramatic decrease in the production of fumarate and maleate compared to the experiments with aspartate alone and an increase in the fumarate-to-maleate ratio. Whether this is an effect of stereoselective adsorption onto brucite, a pH increase, or increases in Mg^{2+} concentration is currently unknown. The presence of brucite also appeared to promote the α-alanine reaction pathway, but inhibit the β-alanine pathway (Fig. 8).

(4) Experiments in which we added NH_4Cl, $H_{2(aq)}$, and brucite resulted in amounts of succinate (about 3 mM) that were greater compared to experiments with aspartate alone, but less than experiments with reducing conditions and no brucite present. We observed that the fumarate-to-maleate ratio also increased as a function of added brucite, a shift in pH, or an increase in Mg^{2+} concentration. We found amounts of α-alanine that were similar to the experiments with NH_4Cl

and $H_{2(aq)}$ added to aspartate without brucite. However, we did not detect β-alanine, which is consistent with experiments involving only aspartate in the presence of brucite. The results of this experiment may suggest competing effects between the brucite surface and the added NH_4Cl and $H_{2(aq)}$.

Overall, we have observed a wide range of reaction pathways following the decomposition of aspartate, and each pathway is favored to a different extent under a varying initial reaction conditions. Although the decomposition of aspartate has been frequently studied, it has been observed by Cox and Seward (2007) that the reaction kinetics of amino acids at hydrothermal conditions are likely more complicated than previously assumed. A comparison between Figs. 1 and 8 supports this conclusion, although in this study our attempts to introduce more geochemically complex initial conditions are only a first step. The significant changes in product concentrations with added brucite and reducing conditions, which are relevant for serpentinite-hosted hydrothermal conditions, indicate that aspartate reaction pathways may be strongly dependent on the mineral surfaces and redox conditions present in the environment. It is necessary to explore the effect of these complexities in future studies in order to assess the potential wealth of biomolecules that hydrothermal systems may have contributed to the prebiotic Earth.

Acknowledgements

We would like to thank Dionysis Foustoukos, Bjørn Mysen, Chris Glein, Robert Martin, Paul Goldey, John Armstrong, Stephen Hodge, and Steven Coley for their invaluable advice throughout this project. We thank the National Science Foundation, the NASA

Astrobiology Institute, the Deep Carbon Observatory, Johns Hopkins University, and the Carnegie Institution for Science for support of this research.

References

Andersson E. and Holm N. G. (2000) The stability of some selected amino acids under attempted redox constrained hydrothermal conditions. *Orig. Life Evol. Biosph.* **30**, 9–23.

Aubrey A. D., Cleaves H. J. and Bada J. L. (2008) The role of submarine hydrothermal systems in the synthesis of amino acids. *Orig. Life Evol. Biosph.* **39**, 91–108.

Bach W., Paulick H., Garrido C. J., Ildefonse B., Meurer W. P. and Humphris S. E. (2006) Unraveling the sequence of serpentinization reactions: petrography, mineral chemistry, and petrophysics of serpentinites from MAR 15°N (ODP Leg 209, Site 1274). *Geophys. Res. Lett.* **33**, 1–4.

Bada J. L. and Miller S. L. (1969) Kinetics and mechanism of the nonenzymatic reversible deamination of aspartic acid. *J. Am. Chem. Soc.* **91**, 3946–3948.

Bada J. L. and Miller S. L. (1970) Kinetics and mechanism of the reversible nonenzymic deamination of aspartic acid. *J. Am. Chem. Soc.* **92**, 2774–2782.

Bada J. L., Miller S. L. and Zhao M. (1995) The stability of amino acids at submarine hydrothermal vent temperatures. *Orig. Life Evol. Biosph.* **25**, 111–118.

Bernhardt G., Lüdemann, H. D., Jaenicke R., König H. and Stetter K. O. (1984) Biomolecules are unstable under "black smoker" conditions. *Naturwissenschaften* **71**, 583–586.

Brandes J. A., Boctor N. Z., Hazen R. M. and Yoder H. S. Jr (1999) Prebiotic amino acid synthesis pathways via a-keto acids: An alternative to the Strecker synthesis. In *Perspectives in Amino Acid and Protein Geochemistry.* 41–47.

Choppin G. R., Dadgar A. and Stampfli R. (1973) The thermodynamics of lanthanide complexing by fumarate and maleate. *J. Inorg. Nucl. Chem.* **35**, 875-880.

Clarke A. P., Jandik P., Rocklin R. D., Liu Y. and Avdalovic N. (1999) An integrated amperometry waveform for the direct, sensitive detection of amino acids and amino sugars following anion-exchange chromatography. *Anal. Chem.* **71**, 2774–2781.

Cody G. D., Boctor N. Z., Brandes, J. A., Filley, T. R., Hazen R. M. and Yoder H. S. Jr. (2004). Assaying the catalytic potential of transition metal sulfides for abiotic carbon fixation. *Geochim. Cosmochim. Acta* **68**, 2185-2196.

Cody G. D., Boctor N. Z., Hazen R. M. and Brandes J. A. (2001) Geochemical roots of autotrophic carbon fixation: hydrothermal experiments in the system citric acid, H2O-(±FeS)−(±NiS). *Geochim. Cosmochim. Acta* **65**, 3557-3576.

Cox J. S. and Seward T. M. (2007) The hydrothermal reaction kinetics of aspartic acid. *Geochim. Cosmochim. Acta* **71**, 797–820.

Dalla-Betta P. and Schulte M. (2009) Calculation of the aqueous thermodynamic properties of citric acid cycle intermediates and precursors and the estimation of high temperature and pressure equation of state. *Int. J. Mol. Sci.* **10**, 2809-2837.

Davies M. and Evans F. P. (1956) The isomerization of maleic acid in aqueous solutions. *Trans Faraday Soc*. **52**, 74-80.

de Aldecoa, A. L. I., Roldán, F. V., and Menor-Salván, C. (2013) Natural pyrrhotite as a catalyst in prebiotic chemical evolution. *Life* **3**, 502-517.

Elving P. J. and Teitelbaum C. (1949) Polarographic Behavior of organic compounds. I. The maleate and fumarate species. *J. Am. Chem. Soc.* **71**, 3916–3921.

Estrada, C. F., Adcock, A. K., Sverjensky, D. A., Pelletier, M., Razafitianamharavao, A., and Hazen, R. M. (2014) Enhanced and inhibited adsorption of D-ribose with Ca^{2+} and Mg^{2+} onto brucite [$Mg(OH)_2$]. *Geochim. Cosmochim. Acta,* In Prep.a.

Estrada, C. F., Sverjensky, D. A., and Hazen, R. M. (2014) Selective adsorption of calcium-aspartate ligands onto [Mg(OH)2] brucite: Implications for calcium in prebiotic chemistry. *Astrobiology*, In Prep.b.

Estrada C. F., Sverjensky D. A., Pelletier M., Razafitianamaharavo A. and Hazen R. M. (2014) Interaction between L-aspartate and the brucite [$Mg(OH)_2$]-water interface. *Geochim. Cosmochim. Acta.* In Review.

Faisal M., Sato N., Quitain A. T., Daimon H. and Fujie K. (2007) Reaction kinetics and pathway of hydrothermal decomposition of aspartic acid. *Int. J. Chem. Kinet.* **39**, 175–180.

Fogg A. M., Dunn J. S., Shyu S.-G., Cary D. R. and O'Hare D. (1998) Selective ion-exchange intercalation of isomeric dicarboxylate anions into the layered double hydroxide [$LiAl_2(OH)_6$]$Cl\cdot H_2O$. *Chem. Mater.* **10**, 351–355.

Font R., Gomez D. and Rubio A. (1988) Kinetics of isomerization of maleic acid in concentrated solutions. *Ind. Eng. Chem. Res.* **27**, 774–779.

Foustoukos, D. I. and Seyfried, W .E. Jr. (2004). Hydrocarbons in hydrothermal vent fluids: The role of chromium-bearing catalysts. *Science* **304**, 1002-1005.

Goldberg R. N., Kishore N. and Lennen R. M. (2002) Thermodynamic quantities for the ionization reactions of buffers. *J. Phys. Chem. Ref. Data* **31**, 231–370.

Hafenbradl D., Keller M., Wächtershäuser G. and Stetter K. O. (1995) Primordial amino acids by reductive amination of α-oxo acids in conjunction with the oxidative formation of pyrite. *Tetrahedron Lett.* **36**, 5179–5182.

Hazen R. M. and Sverjensky D. A. (2010) Mineral surfaces, geochemical complexities, and the origins of life. *Cold Spring Harbor Perspectives in Biology* **2**, 1-21.

Hennet R., Holm N. G. and Engel M. H. (1992) Abiotic synthesis of amino-acids under hydrothermal conditions and the origin of life - a perpetual phenomenon. *Naturwissenschaften* **79**, 361–365.

Henrist C., Mathieu J., Vogels C., Rulmont A. and Cloots R. (2003) Morphological study of magnesium hydroxide nanoparticles precipitated in dilute aqueous solution. *J. Cryst. Growth* **249**, 321–330.

Huber C. and Wächtershäuser G. (2003) Primordial reductive amination revisited. *Tetrahedron Lett*. **44**, 1695-1697.

Hwang Y. S. and Lenhart J. J. (2008) Adsorption of C4-dicarboxylic acids at the hematite/water interface. *Langmuir* **24**, 13934–13943.

Jandik P., Pohl C., Barreto V. and Avdalovic N. (2000) Anion exchange chromatography and integrated amperometric detection of amino acids. In *Amino acid analysis protocols* Humana Press, New Jersey. pp. 63–85.

Kawamura K. and Shimahashi M. (2008) One-step formation of oligopeptide-like molecules from Glu and Asp in hydrothermal environments. *Naturwissenschaften* **95**, 449–454.

Kelley D. S., Baross J. A. and Delaney J. R. (2002) Volcanoes, fluids, and life at mid-ocean ridge spreading centers. *Annu. Rev. Earth Planet. Sci.* **30**, 385–491.

Kelley D. S., Karson J. A., Blackman D. K., Früh-Green G. L., Butterfield D. A., Lilley M. D., Olson E. J., Schrenk M. O., Roe K. K., Lebon G. T., Rivizzigno P. and the AT3-60 Shipboard Party (2001) An off-axis hydrothermal vent field near the Mid-Atlantic Ridge at 30[deg] N. *Nature* **412**, 145–149.

Kelley D. S., Karson J., Fruh-Green G., Yoerger D., Shank T., Butterfield D., Hayes J., Schrenk M., Olson E., Proskurowski G., Jakuba M., Bradley A., Larson B., Ludwig K., Glickson D., Buckman K., Bradley A., Brazelton W., Roe K., Elend M., Delacour A., Bernasconi S., Lilley M., Baross J., Summons R. and Sylva S. (2005) A serpentinite-hosted ecosystem: The Lost City Hydrothermal Field. *Science* **307**, 1428–1434.

Krebs, H. A. and Johnson, W. A. (1937) Metabolism of ketonic acids in animal tissues. *Biochem. J.* **31**, 645-660.

Lee. N., Foustoukos, D. I., Sverjensky, D. A., Hazen, R. M., and Cody, G. D. (2014a) Hydrogen enchances the stability of glutamic acid in hydrothermal environments. *Chem. Geol.* **386**,184-189.

Lee, N., Foustoukos, D. I., Sverjensky, D. A., Cody, G. D., Hazen, R. M., (2014b). The effects of temperature, pH and redox state on the stability of glutamic acid in hydrothermal fluids. *Geochim. Cosmochim. Acta*. In Press.

Lemke K. H., Rosenbauer R. J. and Bird D. K. (2009) Peptide synthesis in early Earth hydrothermal systems. *Astrobiology* **9**, 141–146.

Li J. and Brill T. B. (2003) Spectroscopy of hydrothermal reactions, part 26: Kinetics of decarboxylation of aliphatic amino acids and comparison with the rates of racemization. *Int. J. Chem. Kinet.* **35**, 602–610.

Lu J., Qiu L. and Qu B. (2004) Controlled growth of three morphological structures of magnesium hydroxide nanoparticles by wet precipitation method. *J. Cryst. Growth* **267**, 676–684.

McCollom T. M. and Bach W. (2009) Thermodynamic constraints on hydrogen generation during serpentinization of ultramafic rocks. *Geochim. Cosmochim. Acta* **73**, 856–875.

McCollom T. M., Ritter G. and Simoneit B. R. T. (1999) Lipid synthesis under hydrothermal conditions by Fischer- Tropsch-Type Reactions. *Orig. Life Evol. Biosph.* **29**, 153–166.

Meléndez-Hevia E., Waddell T. G. and Cascante M. (1996) The puzzle of the Krebs citric acid cycle: assembling the pieces of chemically feasible reactions, and opportunism in the design of metabolic pathways during evolution. *J. Mol. Evol.* **43**, 293–303.

Miller S. L. and Bada J. L. (1988) Submarine hot springs and the origin of life. *Nature* **334**, 609–611.

Morowitz H. J., Kostelnik J. D., Yang J. and Cody G. D. (2000) The origin of intermediary metabolism. *PNAS* **97**, 7704–7708.

Naidu R. and Harter R. D. (1998) Effect of different organic ligands on cadmium sorption by and extractability from soils. *Soil Sci. Soc. Am. J.* **62**, 644–650.

Nakada H. I. and Weinhouse S. (1953) Non-enzymatic transamination with glyoxylic acid and various amino acids. *J. Biol. Chem*. **204**, 831-836.

Novikov Y. and Copley S. D. (2013) Reactivity landscape of pyruvate under simulated hydrothermal vent conditions. *PNAS* **110**, 13283–13288.

Orlova T. D. and Bychkova S. A. (2007) The heat effects of dissociation of maleic and fumaric acids. *Russ. J. Phys. Chem.* **81**, 693–695.

Pokrovsky O. S. and Schott J. (2004) Experimental study of brucite dissolution and precipitation in aqueous solutions: surface speciation and chemical affinity control. *Geochim. Cosmochim. Acta* **68**, 31–45.

Proskurowski G., Lilley M. D., Kelley D. S. and Olson E. J. (2006) Low temperature volatile production at the Lost City Hydrothermal Field, evidence from a hydrogen stable isotope geothermometer. *Chem. Geol.* **229**, 331–343.

Sato N., Quitain A. T., Kang K., Daimon H. and Fujie K. (2004) Reaction kinetics of amino acid decomposition in high-temperature and high-pressure water. *Ind. Eng. Chem. Res.* **43**, 3217–3222.

Shipp J. A., Gould I. R., Shock E. L., Williams L. B. and Hartnett H. E. (2014) Sphalerite is a geochemical catalyst for carbon−hydrogen bond activation. *PNAS* **111**, 11642-11645.

Shock E. L. (1990) Geochemical constraints on the origin of organic compounds in hydrothermal systems. *Orig. Life Evol. Biosph.* **20**, 331–367.

Shock E. L. and Canovas P. (2010) The potential for abiotic organic synthesis and biosynthesis at seafloor hydrothermal systems. *Geofluids* **10**, 161–192.

Thauer R. K. (1988) Citric-acid cycle, 50 years on: Modifications and an alternative pathway in anaerobic bacteria. *Eur. J. Biochem.* **176**, 497–508.

Tsukahara H., Imai E., Honda H., Hatori K. and Matsuno K. (2002) Prebiotic oligomerization on or inside lipid vesicles in hydrothermal environments. *Orig. Life Evol Biosph* **32**, 13–21.

Wächtershäuser, G. (1988). Before enzymes and templates: Theory of surface metabolism. *Microbiol. Rev.* **52**, 452-484.

Wang W., Yang B., Qu Y., Liu X. and Su W. (2011) FeS/S/FeS_2 redox system and its oxidoreductase-like chemistry in the iron-sulfur world. *Astrobiology* **11**, 471–476.

White R. H. (2006) A simple synthesis of (RS)-[2-2H] glycine by the reductive amination of glyoxylic acid. *J. Label. Compd. Radiopharm.* **20**, 787–790.

White R. H. (1984) Hydrolytic stability of biomolecules at high temperatures and its implication for life at 250 °C. *Nature* **310**, 430–432.

Yao H.-L. and Yeh H.-H. (1996) Fumarate, maleate, and succinate adsorption on hydrous δ-Al_2O_3. 1. Comparison of the adsorption maxima and their significance. *Langmuir* **12**, 2981–2988.

Fig. 1. Decomposition pathways of aspartate previously established (Bada and Miller, 1970, Sato et al., 2004, Faisal et al., 2007; Cox and Seward, 2007). Aspartate undergoes a reversible deamination reaction to form maleate and fumarate, which hydrate to form malate. Malate is oxidized to oxaloacetate, which decarboxylates to pyruvate. Pyruvate undergoes a second decarboxylation reaction to product acetate.

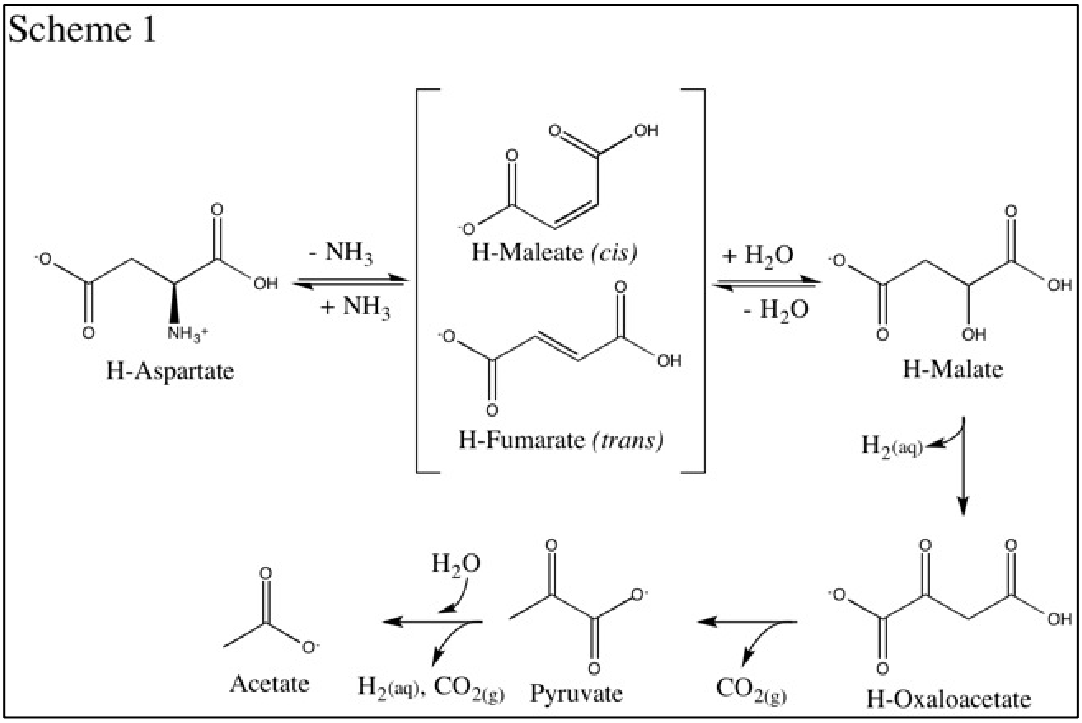

Fig. 2. The calculated stability field of aspartate relative to oxaloacetate plotted as the log of $NH_{3(aq)}$ concentration as a function of $H_{2(aq)}$ fugacity. The solid line indicates the field assuming that equal concentrations of aspartate and oxaloacetate form, whereas the dashed line indicates the field where 1 mole aspartate forms with every 10 moles of oxaloacetate.

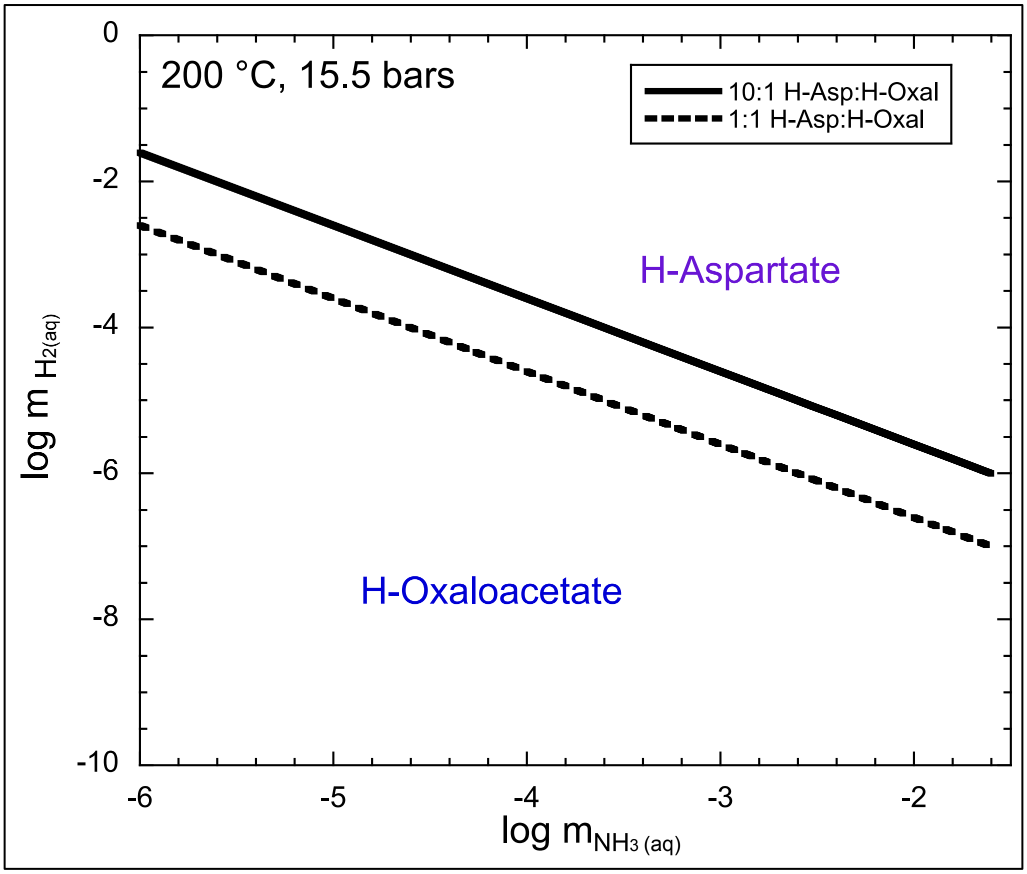

Fig. 3. Scanning electron microscopy image of synthetic brucite powder. Lamellar, hexagonal platelets occur in < 1 μm aggregates.

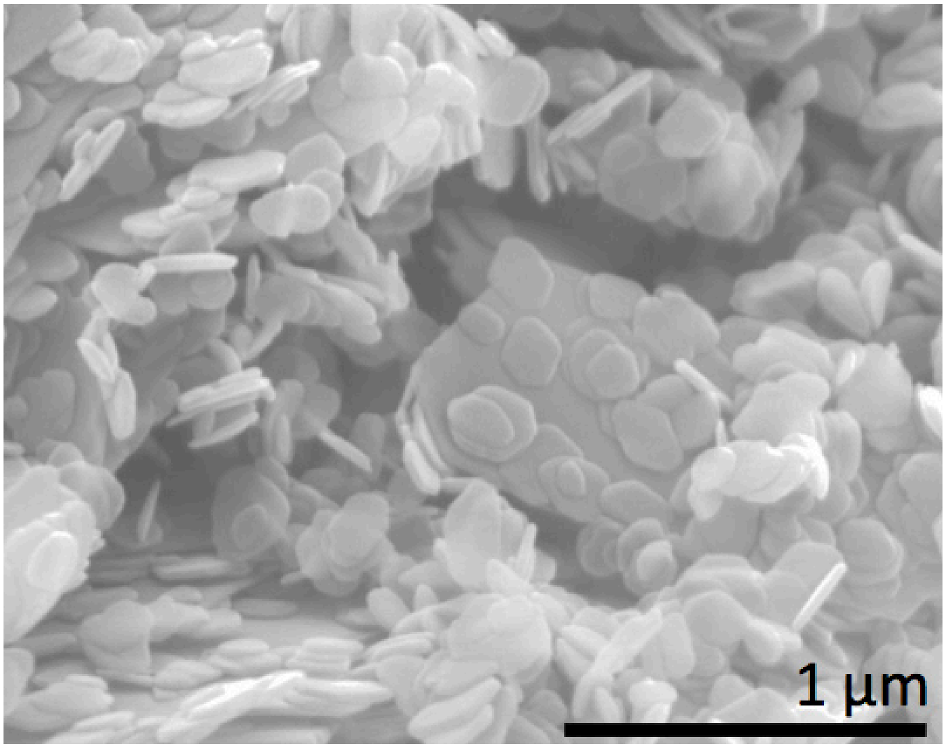

Fig. 4. a) A comparison between the initial amount of carbon in aspartate (black), the total calculated amount of carbon (blue), and the total measured amount of carbon (red). b) The total measured concentration of nitrogen-bearing products (purple) compared with the amount of nitrogen in the initial aspartate (black). The total measured concentration of products includes only the species that could be detected with IC and UPLC-MS methods. The vertical error bars represent the sum of the uncertainties encountered when analyzing each product by either IC or UPLC-MS.

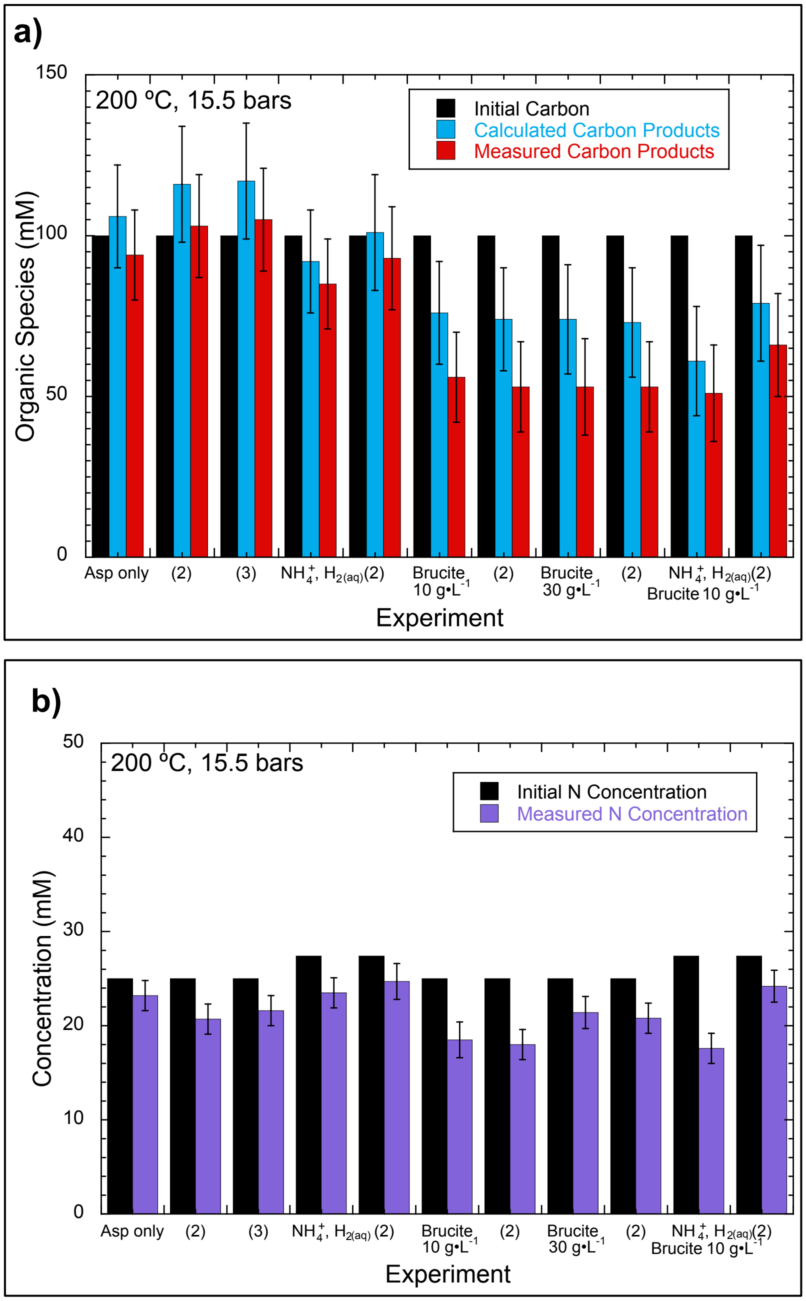

Fig. 5. The Mg^{2+} (orange) and NH_4^+ (purple) concentrations (mM) detected in each experiment. The vertical error bars represent the uncertainty encountered during IC analysis.

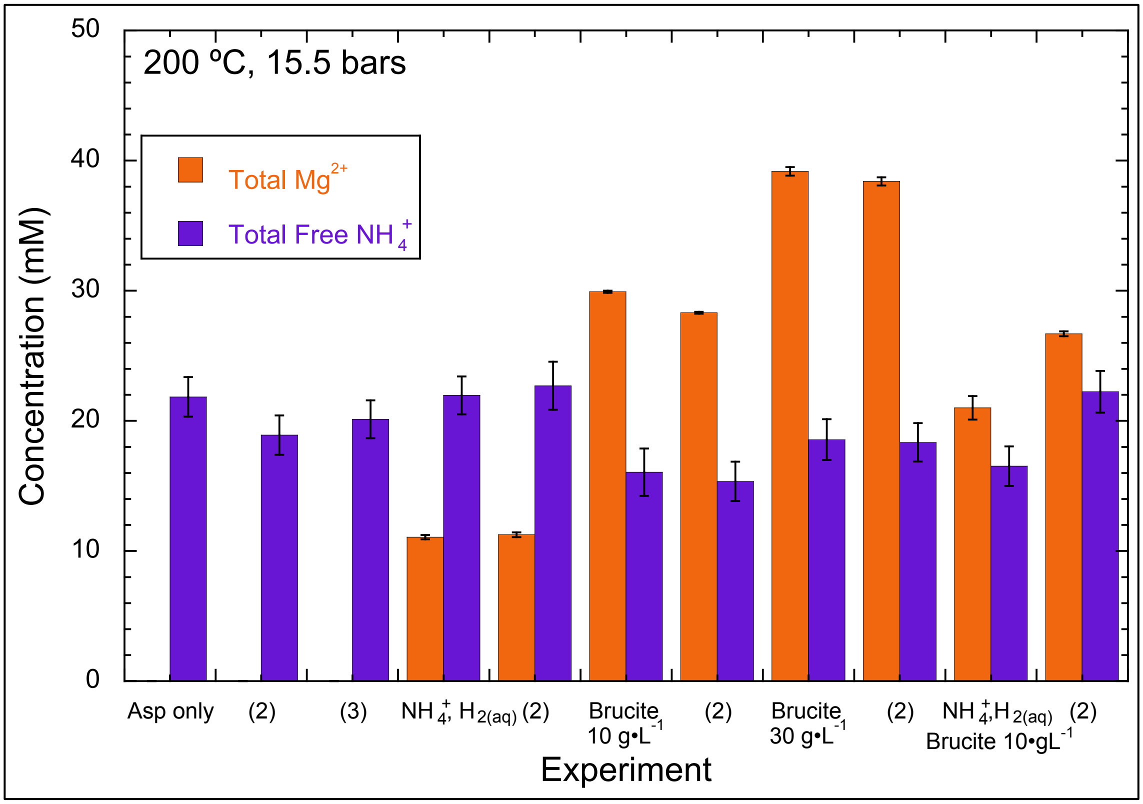

Fig. 6. Concentration of the decomposition products of aspartate after a 24-hour reaction at 200 ºC and 15.5 bars when: a) only aspartate is been added to the experiments, and b) when 2.4 ± 0.6 mM NH_4Cl and 13 ± 10 mM $H_{2(aq)}$ are added to aspartate. Vertical error bars represent the uncertainty specific to each compound encountered with IC and UPLC-MS analysis.

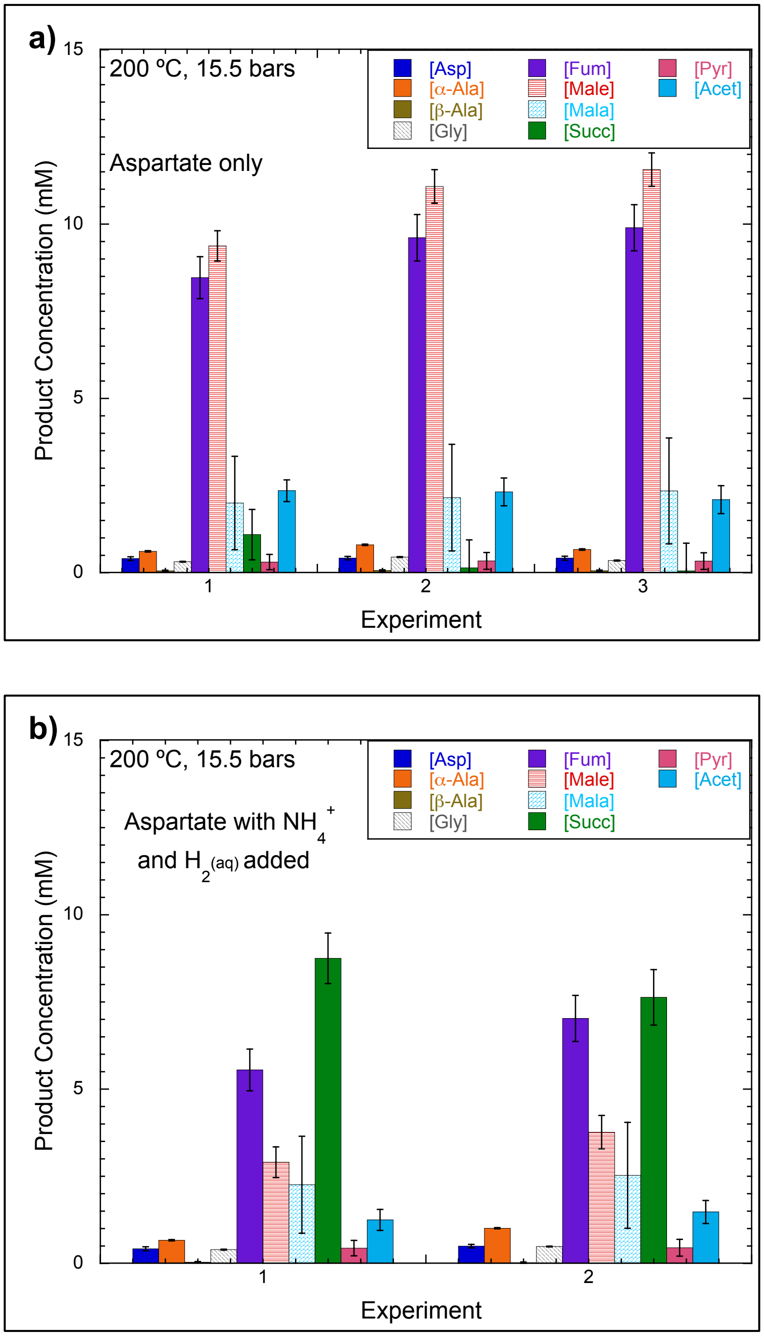

Fig. 7. Concentration of the decomposition products of aspartate after a 24-hour reaction at 200 ºC and 15.5 bars when: a) 10 g•L^{-1} and 30 g•L^{-1} brucite are added to aspartate, and b) when 2.4 ± 0.6 mM NH_4Cl, 22 ± 10 mM $H_{2(aq)}$, and 10 g•L^{-1} brucite are added to aspartate. Vertical error bars represent the uncertainty specific to each compound encountered with IC and UPLC-MS analysis.

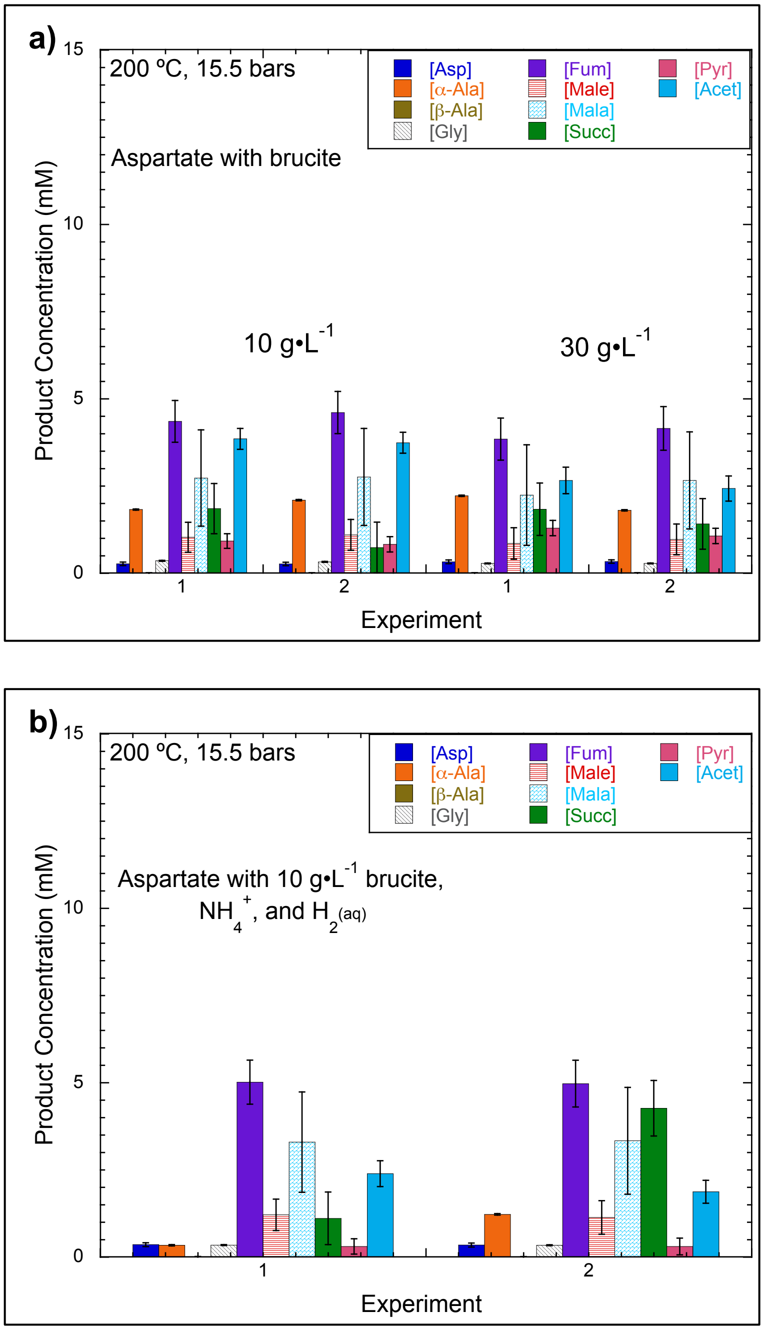

Fig. 8. Proposed reaction pathways following the decomposition of aspartate at 200 ºC and 15.5 bars for this study. Aspartate forms fumarate, maleate, malate, oxaloacetate, pyruvate, and acetate as previously established with Fig. 1. Malate undergoes retro-aldol condensation to produce glycine in pathway I (Eqs 6-7). Pyruvate undergoes reductive amination to form either α-alanine with pathway II (Eq. 8) or β-alanine with pathway III (Eq. 9). β-alanine could alternatively form via decarboxylation from aspartate with pathway IV (Eq. 10). Succinate forms from the reduction of either fumarate or maleate (pathway V, Eq. 11).

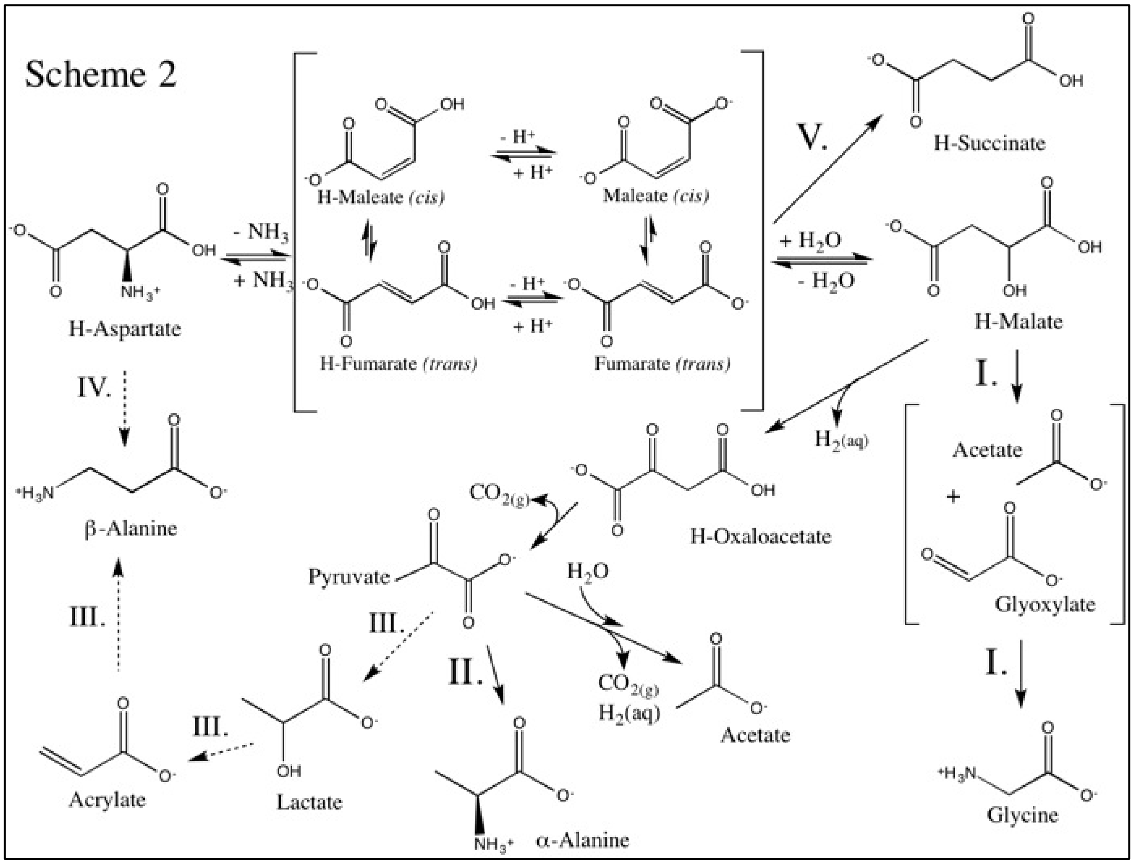

Fig. 9. Detected α-alanine concentrations plotted as a function of pyruvate concentration after aspartate is reacted at 200 ºC and 15.5 bars. The symbols represent the initial conditions of the experiments, including aspartate only (red circles), aspartate with 2.4 ± 0.6 mM NH_4Cl and 13 ± 10 mM $H_{2(aq)}$ (purple diamonds), aspartate with brucite (blue squares), and aspartate with 2.4 ± 0.6 mM, NH_4Cl, 22 ± 10 mM $H_{2(aq)}$, and brucite (green triangles). Vertical and horizontal error bars represent the uncertainty specific to α-alanine and pyruvate, respectively, encountered during IC and UPLC-MS analysis.

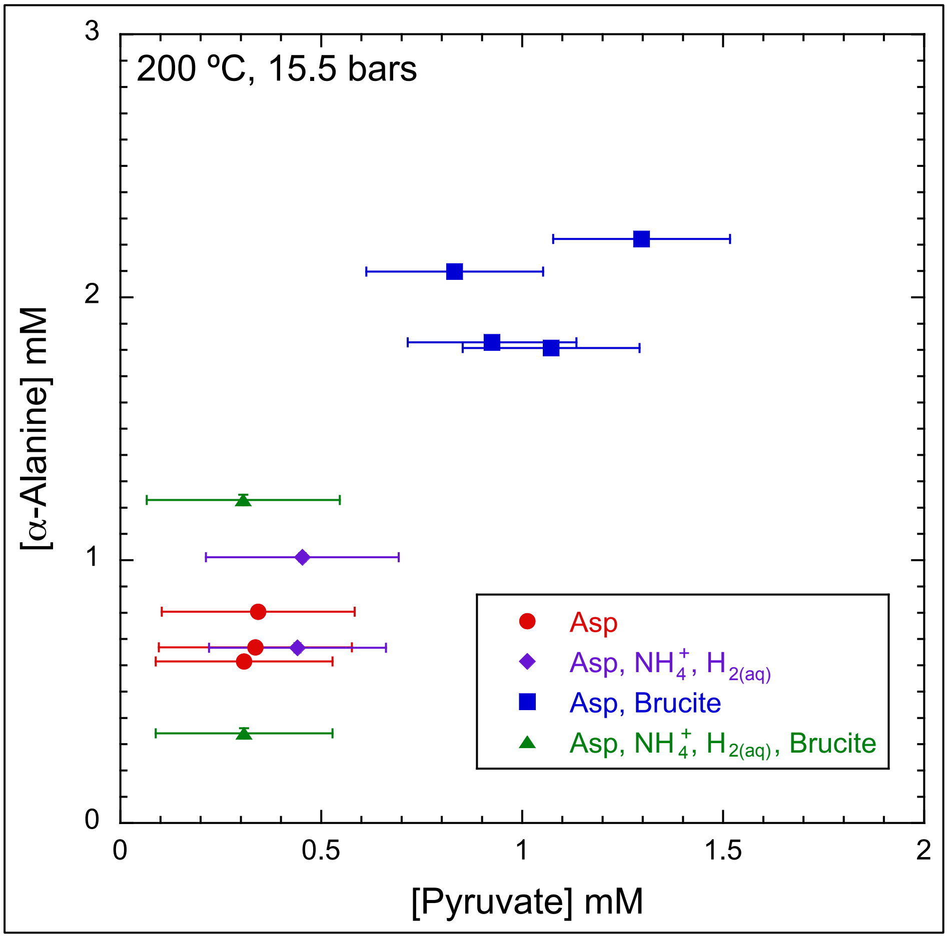

Fig. 10. The detected concentrations of succinate plotted as a function of calculated total [$H_{2(aq)}$] produced after aspartate is reacted at 200 ºC and 15.5 bars. $H_{2(aq)}$ is calculated using known mass of Mg metal added to the experiments and the detected concentrations of pyruvate and acetate using the reaction stoichiometries in Fig. 8. The symbols represent the initial conditions of the experiments, including: aspartate only (red circles), aspartate with 2.4 ± 0.6 mM NH_4Cl and 13 ± 10 mM $H_{2(aq)}$ (purple diamonds), aspartate with brucite (blue squares), and aspartate with 2.4 ± 0.6 mM, NH_4Cl, 22 ± 10 mM $H_{2(aq)}$, and brucite (green triangles). Vertical error bars represent the uncertainty specific to succinate encountered during UPLC-MS analysis, whereas horizontal error bars indicate uncertainty in the measurement of Mg metal used to produce $H_{2(aq)}$.

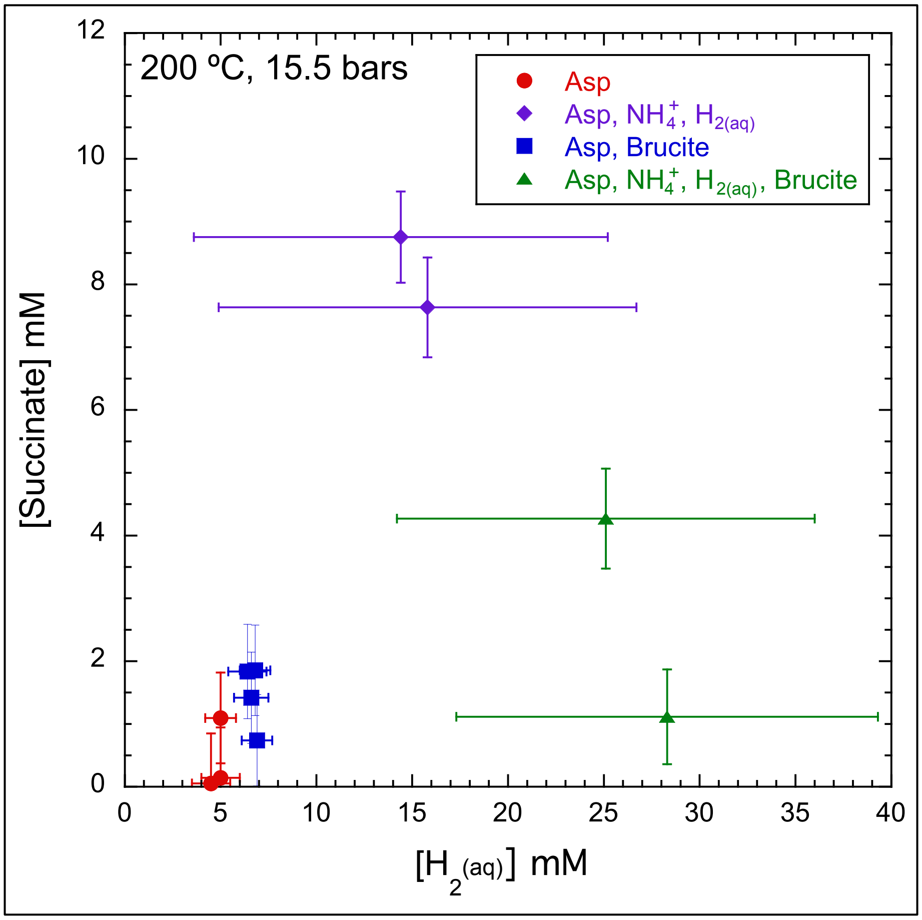

Fig. 11. The calculated stability field of succinate relative to aspartate plotted as the log of $NH_{3(aq)}$ concentration as a function of $H_{2(aq)}$ fugacity. The solid line indicates the field, assuming that equal concentrations of succinate and aspartate form, whereas the dotted line indicates the field where 10 moles of succinate forms with each mole of aspartate.

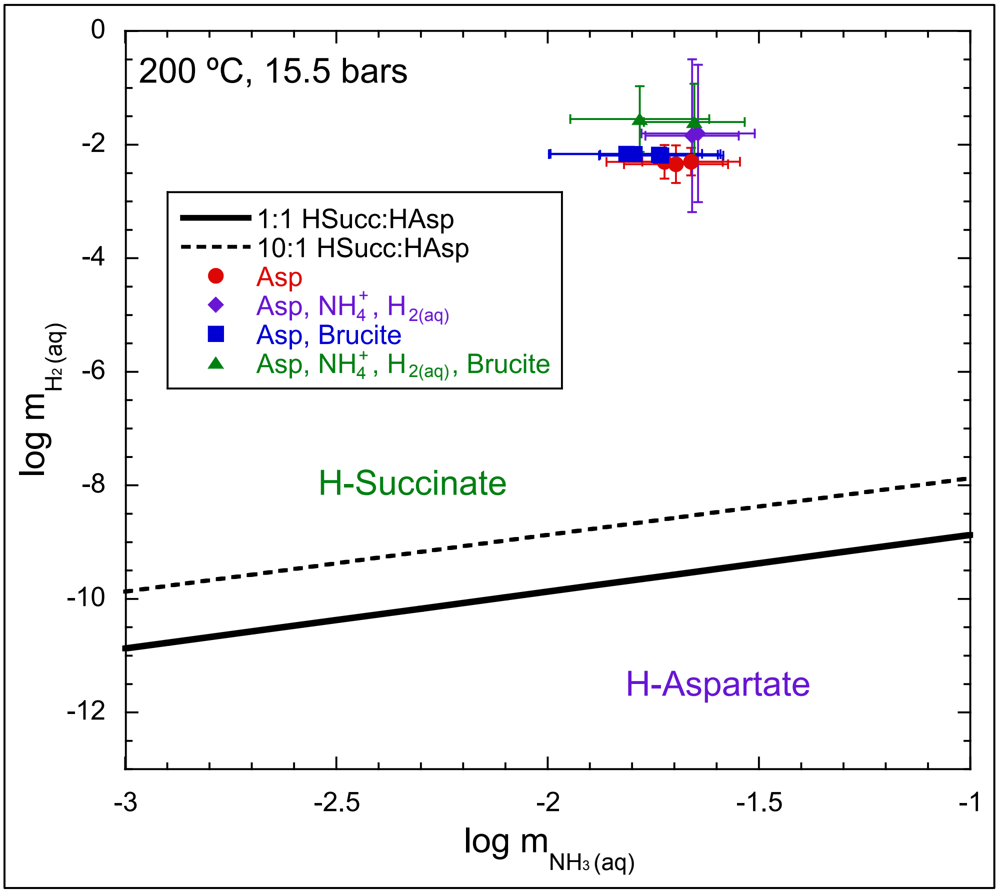

Fig. 12. The fumarate-to-maleate concentration ratio plotted as a function of: a) brucite solid concentration, and b) Mg^{2+} concentration after aspartate reacts at 200 ºC and 15.5 bars. The symbols represent the initial conditions of the experiments, including: aspartate only (red circles); aspartate with 2.4 ± 0.6 mM NH_4Cl and 13 ± 10 mM $H_{2(aq)}$ (purple diamonds); aspartate with brucite (blue squares); and aspartate with 2.4 ± 0.6 mM, NH_4Cl, 22 ± 10 mM $H_{2(aq)}$, and brucite (green triangles). Vertical error bars represent the uncertainty specific to fumarate and maleate encountered during UPLC-MS analysis and horizontal error bars represent the uncertainty specific to Mg^{2+} encountered during IC analysis.

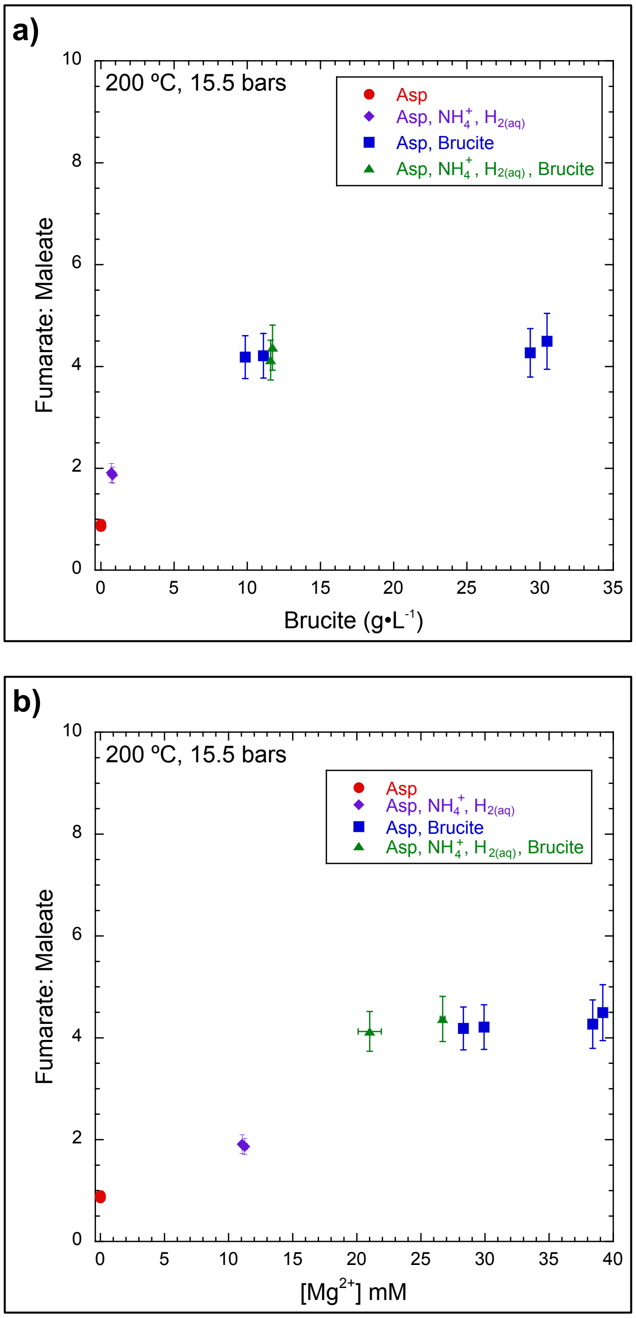

Fig. 13. The fumarate-to-maleate concentration ratio plotted as a function of calculated solution pH after aspartate reacted at 200 °C and 15.5 bars. Solution pH was calculated from the detected Mg^{2+} concentrations and equations and equilibrium constants in Table 3 with the assumption that the brucite added and precipitated in each experiment are in equilibrium with the aqueous phase. The symbols represent the initial conditions of the experiments, including: aspartate only (red circles); aspartate with 2.4 ± 0.6 mM NH_4Cl and 13 ± 10 mM $H_{2(aq)}$ (purple diamonds); aspartate with brucite (blue squares); and aspartate with 2.4 ± 0.6 mM, NH_4Cl, 22 ± 10 mM $H_{2(aq)}$, and brucite (green triangles). Vertical error bars represent the uncertainty specific to fumarate and maleate encountered during UPLC-MS analysis.

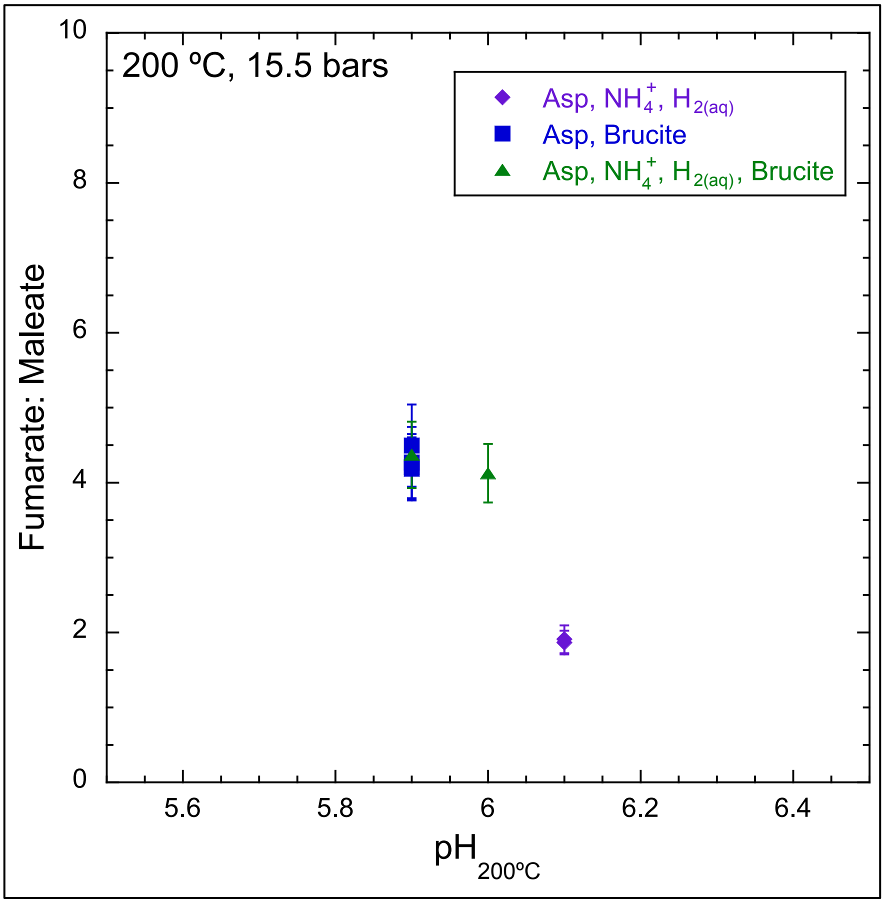

Fig. 14. Concentrations of Mg^{2+} plotted as a function of brucite solid concentration added to each experiment after aspartate reacts at 200 ºC and 15.5 bars. The symbols represent the initial conditions of the experiments, including: aspartate only (red circles); aspartate with 2.4 ± 0.6 mM NH_4Cl and 13 ± 10 mM $H_{2(aq)}$ (purple diamonds); aspartate with brucite (blue squares); and aspartate with 2.4 ± 0.6 mM, NH_4Cl, 22 ± 10 mM $H_{2(aq)}$, and brucite (green triangles). Vertical error bars represent the uncertainty specific to fumarate and maleate encountered during UPLC-MS analysis.

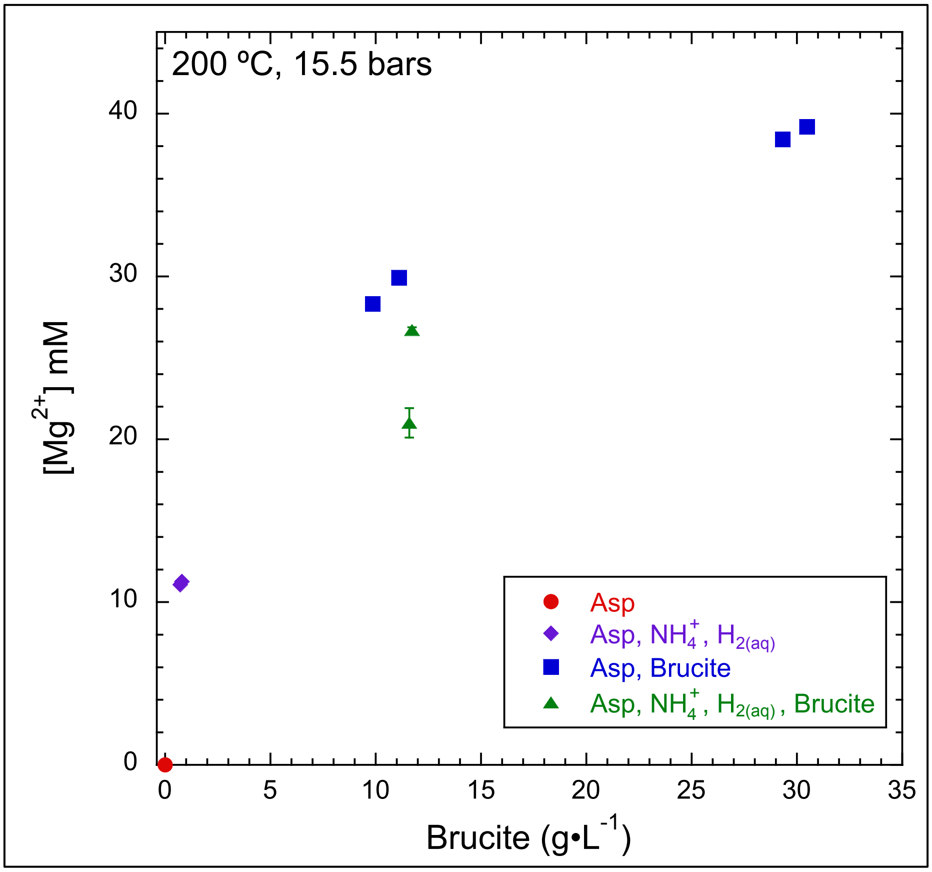

Table 1. Total concentration (mM) of carbon and nitrogen products relative to the initial 25 mM aspartate reacted at 200 ºC and 15.5 bars for 24 hours. Total calculated amount of carbon includes the amount of $CO_{2(g)}$ estimated to form during the experiments, whereas the total measured amount includes only the products detected by IC and UPLC-MS methods.

Sample	**Total C_{calc} (mM)**	**Total C_{meas} (mM)**	**Total $[N]_{meas}$ (mM)**	**% N of Initial Asp**
Asp only (1)	106 ± 16	94 ± 14	23 ± 2	93 ± 6
Asp only (2)	116 ± 18	103 ± 16	21 ± 2	83 ± 6
Asp only (3)	117 ± 18	105 ± 16	22 ± 2	86 ± 6
NH_4^+, $H_{2(aq)}$ (1)	92 ± 16	85 ± 14	23 ± 2	86 ± 6
NH_4^+, $H_{2(aq)}$ (2)	101 ± 18	93 ± 16	25 ± 2	90 ± 7
Brucite 10 g•L^{-1} (1)	76 ± 16	56 ± 14	19 ± 2	74 ± 8
Brucite 10 g•L^{-1} (2)	74 ± 16	53 ± 14	18 ± 2	72 ± 6
Brucite 30 g•L^{-1} (1)	74 ± 17	53 ± 15	21 ± 2	86 ± 7
Brucite 30 g•L^{-1} (2)	73 ± 17	53 ± 14	21 ± 2	83 ± 6
NH_4^+, $H_{2(aq)}$, Brucite 10 g•L^{-1} (1)	61 ± 15	51 ± 15	18 ± 2	64 ± 6
NH_4^+, $H_{2(aq)}$, Brucite 10 g•L^{-1} (2)	79 ± 18	66 ± 16	24 ± 2	88 ± 6

Table 2. Concentration (mM) of decomposition products after aspartate reacted at 200 ºC and 15.5 bars for 24 hours.

Sample	**[Asp]**	**[α-Ala]**	**[β-Ala]**	**[Gly]**	**[Fum]**	**[Male]**	**[Mal**	**[Succ]**
Asp only (1)	0.41 ± 0.05	0.62 ± 0.02	0.05 ± 0.02	0.32 ± 0.01	8.5 ± 0.6	9.4 ± 0.44	2.0 ± 1.3	1.1 ± 0.7
Asp only (2)	0.42 ± 0.05	0.80 ± 0.02	0.07 ± 0.02	0.45 ± 0.01	9.6 ± 0.7	11.1 ± 0.5	2.2 ± 1.5	0.1 ± 0.8
Asp only (3)	0.42 ± 0.06	0.67 ± 0.02	0.06 ± 0.02	0.35 ± 0.01	9.9 ± 0.7	11.6 ± 0.5	2.3 ± 1.5	0.1 ± 0.8
NH_4^+, $H_{2(aq)}$ (1)	0.42 ± 0.06	0.67 ± 0.02	0.04 ± 0.02	0.40 ± 0.01	5.6 ± 0.6	2.9 ± 0.4	2.3 ± 1.4	8.8 ± 0.7
NH_4^+, $H_{2(aq)}$ (2)	0.50 ± 0.05	1.01 ± 0.02	0.02 ± 0.02	0.49 ± 0.01	7.0 ± 0.7	3.8 ± 0.5	2.5 ± 1.5	7.6 ± 0.8
Brucite 10 g•L^{-1} (1)	0.27 ± 0.05	1.83 ± 0.02	n.d.	0.36 ± 0.01	4.4 ± 0.6	1.0 ± 0.4	2.7 ± 1.4	1.9 ± 0.7
Brucite 10 g•L^{-1} (2)	0.27 ± 0.05	2.10 ± 0.02	n.d.	0.33 ± 0.01	4.6 ± 0.6	1.1 ± 0.4	2.8 ± 1.4	0.7 ± 0.7
Brucite 30 g•L^{-1} (1)	0.33 ± 0.05	2.22 ± 0.02	n.d.	0.28 ± 0.01	3.9 ± 0.6	0.9 ± 0.5	2.2 ± 1.4	1.8 ± 0.8
Brucite 30 g•L^{-1} (2)	0.34 ± 0.05	1.81 ± 0.02	n.d.	0.28 ± 0.01	4.2 ± 0.6	1.0 ± 0.4	2.7 ± 1.4	1.4 ± 0.7
NH_4^+, $H_{2(aq)}$, Brucite 10 g•L^{-1} (1)	0.36 ± 0.06	0.34 ± 0.02	n.d.	0.35 ± 0.01	5.0 ± 0.6	1.2 ± 0.5	3.3 ± 1.4	1.1 ± 0.8
NH_4^+, $H_{2(aq)}$, Brucite 10 g•L^{-1} (2)	0.35 ± 0.06	1.23 ± 0.02	n.d.	0.34 ± 0.01	5.0 ± 0.7	1.1 ± 0.5	3.3 ± 1.5	4.3 ± 0.8

Table 2., (cont.) Concentration (mM) of decomposition products after aspartate reacted at 200 ºC and 15.5 bars for 24 hours.

Sample	**[Pyr]**	**[Acet]**	**[$CO_{2(g)}$]^{a}**	**[$H_{2(aq)}$]^{a}**	**[pH]^{c}**	**[Mg^{2+}]**	**[NH_4^+]**	**Fum:Male**
Asp only (1)	0.3 ± 0.2	2.4 ± 0.3	12.4 ± 2.0	5.0 ± 0.8	n/a	n.d.	21.9 ± 1.5	0.9 ± 0.1
Asp only (2)	0.3 ± 0.2	2.3 ± 0.4	12.9 ± 2.4	5.0 ± 1.0	n/a	n.d.	18.9 ± 1.5	0.9 ± 0.1
Asp only (3)	0.3 ± 0.2	2.1 ± 0.4	11.6 ± 2.4	4.5 ± 1.0	n/a	n.d.	20.1 ± 1.5	0.9 ± 0.1
NH_4^+, $H_{2(aq)}$ (1)	0.4 ± 0.2	0.8 ± 0.3	6.7 ± 2.0	14.4 ± 10.8	6.1	11.1 ± 0.2	22.0 ± 1.5	1.9 ± 0.2
NH_4^+, $H_{2(aq)}$ (2)	0.5 ± 0.2	0.8 ± 0.3	7.7 ± 2.1	15.8 ± 10.9	6.1	11.3 ± 0.2	22.7 ± 1.9	1.9 ± 0.2
Brucite 10 g•L^{-1} (1)	0.9 ± 0.2	2.9 ± 0.3	20.0 ± 1.9	6.8 ± 0.8	5.9	29.9 ± 0.1	16.1 ± 1.8	4.2 ± 0.4
Brucite 10 g•L^{-1} (2)	0.8 ± 0.2	3.0 ± 0.3	20.9 ± 1.9	6.9 ± 0.8	5.9	28.3 ± 0.1	15.4 ± 1.5	4.2 ± 0.4
Brucite 30 g•L^{-1} (1)	1.3 ± 0.2	2.6 ± 0.4	20.8 ± 2.2	6.4 ± 1.0	5.9	39.2 ± 0.3	18.6 ± 1.6	4.5 ± 0.5
Brucite 30 g•L^{-1} (1)	1.1 ± 0.2	2.8 ± 0.4	19.8 ± 2.2	6.6 ± 0.9	5.9	38.4 ± 0.3	18.4 ± 1.5	4.3 ± 0.5
NH_4^+, $H_{2(aq)}$, Brucite 10 g•L^{-1} (1)	0.3 ± 0.2	2.1 ± 0.4	10.3 ± 2.2	28.3 ± 11.0	6.0	21.0 ± 0.9	16.5 ± 1.5	4.1 ± 0.4
NH_4^+, $H_{2(aq)}$, Brucite 10 g•L^{-1} (2)	0.3 ± 0.2	2.1 ± 0.3	13.0 ± 2.1	28.3 ± 10.9	5.9	26.7 ± 0.2	22.2 ± 1.6	4.4 ± 0.4

---

[a] $CO_{2(g)}$ concentrations were calculated with the concentrations of pyruvate and acetate and using the reaction stoichiometries in Fig. 1.

[b] Total $H_{2(aq)}$ concentrations have been estimated from the amount of Mg metal initially added to experiments to produce $H_{2(aq)}$ according to Eq. (5), the amounts of pyruvate and acetate, and the reaction stoichiometries in Fig 1.

[c] pH was estimated from the concentration of Mg^{2+} and the equilibrium constant reported for Eq.(1) at 200 ºC (Table 3).

Table 3. Equilibrium constants for the dissolution of brucite and deprotonation reactions involving fumarate and maleate at 25ºC and 1 bar, and 200 ºC and 15.5 bars.

Reaction Type	**Reaction**	**log K**
Brucite dissolution at 25 ºC	$Mg(OH)_2 + 2H^+ = Mg^{2+} + H_2O$	17.3
Brucite dissolution at 200 ºC	$Mg(OH)_2 + 2H^+ = Mg^{2+} + H_2O$	10.3
Reaction Type	**Reaction**	**pK**
Aqueous fumarate equilibria at 25 ºC [a]	$H_2Fum = HFum^- + H^+$	3.1
	$HFum^- = Fum^{2-} + H^+$	4.6
Aqueous fumarate equilibria at 200 ºC	$H_2Fum = HFum^- + H^+$	3.7
	$HFum^- = Fum^{2-} + H^+$	5.4
Aqueous maleate equilibria at 25 ºC [b,c]	$H_2Male = HMale^- + H^+$	1.9
	$HMale^- = Male^{2-} + H^+$	6.1
Aqueous maleate equilibria at 200 ºC	$H_2Male = HMale^- + H^+$	2.0
	$HMale^- = Male^{2-} + H^+$	6.3

[a] Deprotonation constants for fumarate at 25 ºC by Dalla-Betta and Schulte (2009).

[b] Deprotonation constants at 25 ºC for $HMale^-$ by Goldberg (2002) and $Male^{2-}$ by Orlova and Bychkova 2007).

Chapter 6

Conclusions

In these studies I report the interactions between organic molecules and the brucite-water interface at multiple electrolyte and biomolecule concentrations, pH conditions, and temperatures that reflect the geochemical complexities of serpentinite-hosted hydrothermal vents. I characterized brucite, a major mineral phase of serpentinization, in order to evaluate the suitability of serpentinite-hosted hydrothermal systems as host environments for biochemical evolution during life's origins. I conducted batch adsorption experiments to assess the adsorption of the amino acid aspartate onto synthetic brucite at variable initial aspartate concentrations, pH conditions, and four ionic strengths that were determined by the concentrations of Mg^{2+} and Ca^{2+} in the system. When low concentrations of Mg^{2+} ($0.7x10^{-3}$ M) were present in system, I observed up to 1.0 μmol aspartate adsorb per m^2 brucite. This amount of adsorption decreased to 0.6 $\mu mol \bullet m^{-2}$ when the amount of Mg^{2+} increased to $5.8x10^{-3}$ M, and it resulted in a pH value of 9.8. Moreover, I observed that aspartate adsorption significantly increased up to 2.0 $\mu mol \bullet m^{-2}$ with $4.0x10^{-3}$ M Ca^{2+} added, whereas substantial amounts of calcium (29.6 $\mu mol \bullet m^{-2}$) also adsorbed at the brucite surface.

I characterized the interactions of aspartate and Ca^{2+} between brucite with surface complexation modeling using the extended triple-layer model (ETLM). When only Mg^{2+} was present within the system, I predicted that aspartate attached onto brucite as an inner-sphere bidentate, or “leaning” species. In the presence of Ca^{2+}, I proposed two additional species: a monodentate, calcium-aspartate outer-sphere species and a monodentate, calcium outer-sphere species. My calculations with the ETLM determined that brucite particle surface charge became more negative with increasing Mg^{2+}. This negative charge likely created an unfavorable electrostatic environment for the negatively-charged aspartate molecule to adsorb at the brucite-water interface. In the presence of Ca^{2+}, brucite particle surface charge became positive. The reversal in brucite particle surface charge reveals that calcium predominantly adsorbed onto brucite. These calculations, in addition to the cooperative effect of Ca^{2+} on aspartate adsorption, demonstrate the importance of geochemically complex aqueous systems in selecting key biomolecules at mineral surfaces. Furthermore, this experiment establishes the first detailed results and theoretical predictions for biomolecule adsorption at a wide range of conditions onto a mineral relevant for serpentinite-hosted hydrothermal vents.

Ribose has been significant in discussions of nucleotide formation mediated by serpentinite-hosted hydrothermal systems, although there have been limited studies that characterize its adsorption on mineral surfaces. In my second study, I analyzed the attachment of ribose onto brucite with batch adsorption experiments in the presence of different pH conditions, as well as initial concentrations of ribose, Mg^{2+}, and Ca^{2+}. At low Mg^{2+} concentrations (0.6×10^{-3} M) and pH 10.3, I observed that ribose adsorbed onto brucite up to 0.3 $\mu mol \bullet m^{-2}$. After I increased Mg^{2+} concentrations to 5.8×10^{-3} M, ribose surface adsorption decreased to negligible values. When I added 4.2×10^{-3} M Ca^{2+}, I observed an increase in ribose adsorption up to 0.4 $\mu mol \bullet m^{-2}$. Calcium also adsorbed in substantial amounts onto brucite, up to 22.7 μmol•m^{-2}, as I have previously observed in the brucite-aspartate study.

I applied the ETLM predictions that I established for the brucite-water interface during aspartate attachment to this study. When Mg^{2+} was the only electrolyte present, I proposed that ribose adsorbs onto brucite as a bidentate, outer-sphere, or "standing" surface species. When Ca^{2+} was added, I proposed the formation of a calcium-ribose outer-sphere species at the brucite surface in addition to the "standing" species. Because I characterized the same batch of synthetic brucite in both studies, I predicted that the same calcium outer-sphere species I proposed in the previous aspartate study also applies to the ribose-brucite system. I additionally used the ETLM to predict that brucite particle surface charge was negative when only Mg^{2+} was present, but it became positive with the addition of Ca^{2+}, which may reflect calcium adsorption onto brucite.

I conducted two detailed studies involving the adsorption of two biomolecules, an amino acid and a sugar, at the brucite-water interface at a four ionic strengths governed by Mg^{2+} and Ca^{2+} concentrations. The wide range of experimental conditions I investigated has enabled me to evaluate the attachment of both biomolecules onto brucite with a unique set of reaction stoichiometries with the ETLM. Because I have characterized the aspartate and ribose interactions with brucite with the ETLM, I further predicted surface adsorption of both molecules at a wide range of pH and total dissolved ion concentrations. For instance, I proposed that ribose adsorption might increase at the brucite surface at highly alkaline conditions. Moreover, in both studies I predicted that the extent of aspartate and ribose adsorption observed with Ca^{2+} might reflect values at Lost City-type fluids. Thus, the results I report in these studies may hold significance for biomolecule adsorption at more geochemically complex, serpentinite-hosted hydrothermal environments.

The enhanced adsorption of both ribose and aspartate with Ca^{2+} is a cooperative effect that may reflect a process where a complex geochemical system may induce a molecular domain to self-organize. I further investigated the potential cooperative effect of Ca^{2+} on organic species adsorbing at the brucite-water interface with a more diverse molecular system including equimolar mixtures of five biologically important amino acids, aspartate, glycine, lysine, leucine, and phenylalanine. I observed that when Ca^{2+} was added, aspartate selectively adsorbed onto brucite at 5.7 to 20 times more than the other four amino acids. As I have observed in the previous two studies, a significant amount of calcium adsorbs at the brucite surface, and thus the ETLM predicted that the brucite particle surface charge with added Ca^{2+} was positive. As the most negative and polar amino acid at the pH of immersion (10.2), aspartate likely forms the strongest complex with calcium at the surface. Furthermore, I have observed that the extent of glycine, lysine, leucine, and phenylalanine adsorption decreased when Ca^{2+} was added, which may indicate that the calcium-aspartate surface species was competing with the other amino acids for adsorption.

These results may suggest that the complexities of a geochemical system (e.g., dissolved ion content, mineral particle surface charge, and multiple dissolved organic species) may enhance the selection of specific prebiotic molecules from a molecular array. The selective adsorption of a narrow set of organic species may eventually lead to their concentration and possible polymerization into biologically relevant macromolecules at the mineral surface. For instance, calcium-binding proteins are present in all three domains of life and often include sites where negative amino acids, such as aspartate, bind to the central calcium ion. Thus, the calcium-aspartate surface complex may serve as a possible precursor molecule to this essential protein. Additionally, the cooperative and competitive effects that have led to the selective adsorption of this calcium-aspartate complex were observed in geochemical conditions approximating those of calcium-rich, serpentinite-hosted hydrothermal conditions. While the more complex conditions would more accurately represent molecule-mineral interactions within serpentinite-hosted environments, this experiment is an important first step toward understanding the effect of geochemical complexity on molecular systems.

The results of my previous investigations have characterized the interactions between prebiotic molecules and brucite at 25 ºC, although in order to better evaluate these interactions in the context of hydrothermal systems it was necessary to conduct experiments at higher temperatures. In my final study, I observed the transformation pathways of aspartate at 200 ºC and 15.5 bars over 24 hours in inert gold capsules. These experiments were conducted with: 1) 25 mM aspartate only; 2) 2.4 mM NH_4Cl and 10 to 20 mM $H_{2(aq)}$ added; 3) either 10 $g \bullet L^{-1}$ or 30 $g \bullet L^{-1}$ brucite added; and 4) with both 10 $g \bullet L^{-1}$ brucite, 2.4 mM NH_4Cl, and 10 to 20 mM $H_{2(aq)}$ added. I observed that the concentration of organic species that formed from aspartate decomposition varied significantly with these initial conditions. When I added NH_4Cl and $H_{2(aq)}$ to aspartate, I observed that a large amount of succinate formed (8 mM) relative to the experiments with aspartate alone. When I added only brucite to aspartate, I observed that large amounts (2 mM) of α-alanine formed, whereas no β-alanine formed. Additionally, the fumarate-to-maleate concentration ratio increased when I added brucite as a result of a selective decrease in maleate concentration. Whether this result is an effect of brucite surface adsorption, increased Mg^{2+} concentration, or a shift in pH is not known. I also observed possible competitive effects between NH_4^+, $H_{2(aq)}$, and the brucite surface. For instance, a greater amount of succinate formed (3 mM) than in experiments with only aspartate, but less than in experiments with only NH_4Cl and $H_{2(aq)}$ added to aspartate. Likewise, I observed that slightly more α-alanine (0.8 mM) formed in these experiments compared to those with aspartate alone, but less than experiments with only brucite added to aspartate.

These observations indicate that the decomposition of aspartate might be strongly influenced by brucite, the dissolved ions present in the aqueous phase, and hydrogen fugacity. The complex decomposition behavior of aspartate suggests that serpentinite-hosted hydrothermal fields could have supported a wealth of prebiotic organic species. Moreover, it is possible that mineral surfaces present in these systems may selectively promote and inhibit reaction pathways during amino acid decomposition pathways, as I have observed with the formation of α-alanine and the suppression of β-alanine. The results of this study serve as an added example that geochemically complex conditions, including temperature, ionic strength, redox conditions, and the presence of a mineral, can dramatically change the narrative on prebiotic chemistry on early Earth.

Vita

Charlene Fae Estrada
Date of Birth: 01/21/1987
Place of Birth: Tucson, AZ, USA

Research Interests

Mineral surface chemistry; interactions between organic molecules and mineral surfaces; surface complexation modeling; serpentinite-hosted hydrothermal systems; prebiotic chemistry; mineral evolution; Early Earth; Raman spectroscopy

Education

PhD. Geochemistry, September 2014
Department of Earth and Planetary Sciences, Johns Hopkins University
M.A. Geochemistry, May 2011
Department of Earth and Planetary Sciences, Johns Hopkins University
B.S. Geosciences, May 2009 (Summa Cum Laude, Honors)
Department of Geosciences, University of Arizona

Professional Experience

06/2011-10/2014	**Predoctoral Fellow**, Carnegie Institution of Washington, Geophysical Laboratory, Washington, DC
08/2009-10/2014	**Research Assistant,** Johns Hopkins University, Baltimore, MD
03/2014-09/2014	**Laboratory Manager**, Johns Hopkins University, Baltimore, MD
06/2010-06/2013	**NSF Graduate Research Fellow,** Johns Hopkins University, Baltimore, MD
05/2006-05/2009	**RRUFF Project Student Employee**, The University of Arizona, Tucson, AZ
08/2008-05/2009	**NASA/UA Space Grant Intern**, The University of Arizona, Tucson, AZ
06/2008-08/2008	**Summer Intern**, Carnegie Institution of Washington Geophysical Laboratory, Washington, D.C.

Analytical Skills

Ion Chromatography
Extended Triple Layer Model (GEOSURF)
EQ3, EQ6
SUPCRT92
Deep Earth Water (DEW) Model

Mineral Synthesis
Raman Spectroscopy
Sum Frequency Generation Spectroscopy
UV-Vis Spectrometry
Powder X-ray Diffraction
Mineral Photography

Honors & Awards

National Science Foundation Graduate Research Fellowship Program, 2010-2013

University of Arizona Outstanding Senior Award in Geosciences, College of Science, May 2009

NASA University of Arizona Space Grant Internship, Aug 2008

University of Arizona National Hispanic Scholarship, 2005-2009

Association for Women Geoscientists Minority Scholarship, 2007-2008

Publications

Estrada, C. F. Adcock, A. K., Sverjensky, D. A., Pelletier, M., Razafitianamaharavo, A., Hazen, R. M. Enhanced and inhibited adsorption of d-ribose with Ca^{2+} and Mg^{2+} onto brucite [$Mg(OH)_2$]**.** *In Prep., A.*

Estrada, C. F., Sverjensky, D. A., Hazen, R. M. Selective adsorption of calcium-aspartate ligands onto brucite [$Mg(OH)_2$]: Implications for calcium in prebiotic chemistry. *In Prep., B.*

Estrada, C. F., Mamajanov, I., Hao, J., Sverjensky, D. A., Cody, G. D., and Hazen, R. M. Aspartate transformation at 200 °C with brucite [$Mg(OH)_2$], NH_3, and H_2: Implications for prebiotic molecules in hydrothermal vents. *In Prep., C.*

Estrada, C. F., Sverjensky, D. A., Pelletier, M., Razafitianamaharavo, A., Hazen, R. M. (2014). Attachment of L-aspartate onto brucite [$Mg(OH)_2$]: an experimental and surface complexation modeling approach. *Geochim. Cosmochim. Acta* In Review.

Hazen, R. M., Liu, X., Downs, R. T., Golden, J., Grew, E. S., Hystad, G., Estrada, C., Sverjensky, D. A. (2014). Mineral evolution: episodic metallogenesis, the supercontinental cycle, and the co-evolving geosphere and biosphere. *Society of Economic Geology Special Publication* **18**, 1-15.

Jonsson, C. M., Jonsson, C. J., Estrada, C. F., Sverjensky, D. A., Cleaves, H. J. Hazen, R. M. (2010). Adsorption of L-aspartate to rutile (α-TiO_2): experimental and theoretical surface complexation studies. *Geochim. Cosmochim. Acta*, 74, 2356-2367.

Estrada, C. F. (2007). Changing the science of mineralogy: The use of Raman spectroscopy in mineral identification and the RRUFF project. *Outcrop, Newsletter of the Rocky Mountain Association of Geologists* 55, 1-8.

Abstracts

Estrada, C. F., Sverjensky, D. A., Hazen, R. M. (2014) Selective adsorption of L-aspartate onto [$Mg(OH)_2$] brucite with Ca^{2+}. *Goldschmidt. Poster.*

Estrada, C. F., Sverjensky, D. A., Hazen, R. M. (2013). Attachment of aspartic acid at the brucite [$Mg(OH)_2$]-water interface. *Goldschmidt*. *Oral.*

Estrada, C. F., Chen, E. H., Geiger, F. M., Sverjensky, D. A., Hazen, R. M. (2012). Probing the interactions between glutamic acid and diopside. *Goldschmidt*. *Oral.*

Estrada, C. F., Chen, E. H., Geiger, F. M., Sverjensky, D. A., Hazen, R.M. (2012). The interaction between glutamic acid and diopside determined by sum frequency generation spectroscopy. *Gordon Research Conference on Vibrational Spectroscopy*.

Estrada, C. F., Sverjensky, D. A. (2011). Predictions of silica adsorption and surface speciation at the mineral-water interface. *AGU*, Fall Meet. Suppl., Abstract PP41A-1735.

Estrada, C. F., Jonsson, C. M., Jonsson, C. F., Sverjensky, D. A., Hazen, R. M. (2008). Adsorption of aspartic acid onto rutile: Implications for biochirality. *AGU*, Fall Meet. Suppl., Abstract V23B-2143.